



Probing the Biology of Zinc Alpha2-Glycoprotein

Justin Greig

Thesis submitted in fulfilment of the requirements for the Degree of Doctor of

Philosophy

2024

Strathclyde Institute of Pharmacy and Biomedical Sciences

University of Strathclyde

Authors Declaration

This thesis is the result of the author's original research. It has been composed by the author and has not been previously submitted for examination which has led to the award of a degree. All experimental, *in silico* and imaging work in this thesis was performed by the candidate unless otherwise stated.


The copyright of this thesis belongs to the author under the terms of the United Kingdom Copyright Acts as qualified by the University of Strathclyde Regulation 3.50. Due acknowledgment must always be made of the use of any material contained in, or derived from this thesis.

Signed: J C Greig

Date: 06/11/24

Page of Declaration

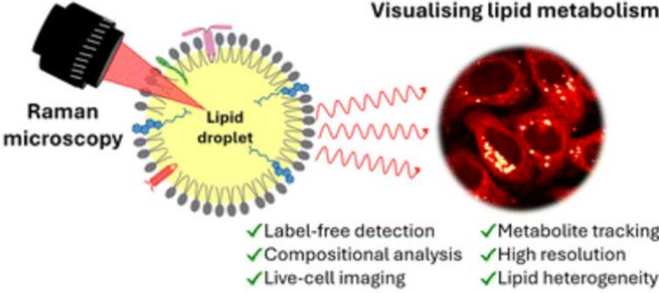
This thesis includes material from the following published paper:

 Minireview

New insights into lipid and fatty acid metabolism from Raman spectroscopy

Justin C. Greig, William J. Tipping, Duncan Graham, Karen Faulds and Gwyn W. Gould

Raman microscopy can reveal metabolic signatures and heterogeneity at the single cell level.



From the themed collection: [Analyst Review Articles 2024](#)

The article was first published on 05 Sep 2024

Analyst, 2024, **149**, 4789-4810

<https://doi.org/10.1039/D4AN00846D>

[Download PDF](#) [Article HTML](#)

Citation: *Analyst*, 2024,149, 4789-4810

Link to Published Article: <https://doi.org/10.1039/D4AN00846D>

Sections in thesis:

5.0 Developing a Workflow to Study Adipocyte Heterogeneity Using Stimulated Raman Spectroscopy

Permission: This article is included, in part, in this thesis with permission from *Analyst*.

The original source has been attributed as required by the publisher.

Abstract

Zinc Alpha 2-Glycoprotein (AZGP1;ZAG) is a ~40-kDa single-chain polypeptide protein thought to contribute to the regulation of weight and body fat through lipid and glucose metabolism. In healthy individuals, ZAG exerts a homeostatic effect by inducing lipolysis of adipose tissue to help reduce fat storage and overall weight. ZAG is upregulated in various carcinomas; cancer patients with upregulated ZAG lose weight rapidly and there is a clear link between ZAG and cancer cachexia. The crystal structure of ZAG revealed an MHC-Class I-like protein fold which has been proposed to act as a potential lipid binding site that could be important for ZAG's function.

The work in this thesis aimed to produce an *in silico* docking approach to identify ligand(s) which may bind this groove, and to understand the key interactions between them and ZAG. Using PLANTS software and the protein visualisation software UCSF Chimera, we identified candidate ligands for binding in ZAGs pocket that have equalled or outscored previous identified ligands which can now be incorporated into competition binding assays to test their affinity for ZAG. In parallel, we developed approaches to produce recombinant ZAG using bacterial and mammalian expression systems, confirmed their structure using fluorescence spectroscopy and outline initial work to show that the recombinant protein is functional and can promote lipolysis in fat cells.

Because a key target of ZAG action is adipocytes, methods were developed to utilise Stimulated Raman Scattering (SRS) to provide a workflow that allows for a label-free, high throughput, single cell analysis to investigate heterogenous metabolic activity of adipocytes. Specifically, the approach described allows measurement of lipid droplet numbers, size and quantifying glucose metabolism using glucose-d₇. We have demonstrated the validity of our method in 3T3-L1 adipocytes incubated in culture for different periods as a model of adipocyte

hypertrophy. Lastly, we adapted a mitochondrial isolation assay to separate cytosolic and peridroplet mitochondria from 3T3-L1 adipocytes.

In sum, this study provided tools and insight to help progress the knowledge and understanding of ZAG biology, signalling mechanisms and for the investigation of both phenotypic and metabolic adipocyte heterogeneity.

Table of Contents

Authors Declaration	2
Page of Declaration	3
Abstract	4
Table of Contents	6
List of Tables	10
List of Figures	11
Acknowledgements	15
List of Abbreviations	17
1.0 Introduction	22
1.1 Cancer, Diabetes and Cardiovascular Disease	22
1.2 Adipocyte Biology and Their Role in Metabolism	27
1.3 Zinc Alpha 2-Glycoprotein	50
1.4 Aims of the Project	67
2.0 Materials and Methods	68
2.1 Materials	68
2.1.1 List of General Suppliers	68
2.1.2 Solutions	68
2.1.3 Bacterial Strains and Eukaryotic Cell Lines	71
2.1.4 Primary Antibodies	72
2.1.5 Secondary antibodies	73
2.1.6 Plasmids	74
2.1.7 Lentivirus Particles	74
2.1.8 Commercial ZAG	74
2.2 Methods	75
2.2.1 Cell Lines	75
2.2.2 Bacterial Transformation	75
2.2.3 Miniprep	76
2.2.4 Restriction Digest	77
2.2.5 Protein Purification	77
2.2.6 Cell Culture	78
2.2.6.1 Cell Culture of HEK293 Cells	78
2.2.6.2 Cell Culture of 3T3-L1 Fibroblasts	79
2.2.6.3 3T3-L1 Adipocyte Differentiation	79
2.2.6.4 3T3-L1 Adipocyte Treatments	80

2.2.6.5	Measuring Lipolysis of 3T3-L1 Cells	80
2.2.6.6	Measuring Glucose Uptake in 3T3-L1 Cells.....	81
2.2.7	HEK Transfection	81
2.2.7.1	Lentivirus Transduction of HEK293 Cells	82
2.2.8	Harvesting Cells and Supernatants for SDS-PAGE	83
2.2.9	Western Blotting.....	84
2.2.10	Fluorescence Spectroscopy	85
2.2.11	Mitochondrial Isolation	85
2.2.12.1	Fixing Cells for Imaging	86
2.2.12.2	Stimulated Raman Scattering Microscopy (SRS)	86
2.2.12.3	Hyperspectral SRS Imaging.	87
2.2.12.4	Spectral Phasor Analysis.	87
2.2.13	Data Analysis of Lipid Droplets	88
2.2.14	In Silico Ligand Docking	89
2.2.15	Data and Statistical Analysis	90
3.0	Investigating Zinc Alpha 2-Glycoprotein Ligand Binding Through Computational Techniques	92
3.1.1	Introduction	92
3.1.2	Validation of Ligand Docking Programme PLANTS.....	97
3.1.3	Ligand Screening to Identify Suitable Ligand Candidates for ZAG	99
3.1.4	Evaluating the Degree in which ZAG Residue Mutations Effect Lipid Binding....	104
3.1.5	Expanding Ligand Binding Simulations with Other ZAG Mutants	116
3.1.6	Investigating A Reported Second Binding Site Within ZAG's Groove	122
3.2	Discussion	124
3.2.1	Establishing ZAGs Biochemistry with in silico Docking Work	124
3.2.2	Further Investigation into the ZAG Ligand Binding Pocket	126
3.2.3	New Insights or Conflicting Information?.....	128
4.0	ZAG Expression Methodology	135
4.1.1	Introduction	135
4.1.2	Conformation of pQE60 and pCDNA3.1 Plasmid Construction.....	139
4.1.3	Optimising the Conditions for ZAG Expression in E. coli.	142
4.1.4	Releasing ZAG from Inclusion Bodies in BL21 Cells.	145
4.1.5	Denaturing and Refolding ZAG	147
4.1.6	Evaluating Methods for Purifying ZAG	149
4.1.7	Validating the Refolding Procedure of ZAG.....	151

4.1.8	Testing the Biological Activity of ZAG	155
4.1.9	Transfection of HEK293 Cells to Establish a ZAG Expressing Cell Line	157
4.1.10	Transducing HEK293 Cells for ZAG Production	159
4.1.11	Testing the Biological Activity of Mammalian ZAG	165
4.2	Discussion	167
4.2.1	Optimizing ZAG Expression and Purification	167
5.0	Developing a Workflow to Study Adipocyte Heterogeneity Using Stimulated Raman Spectroscopy	171
5.1.1	Introduction	171
5.1.2	Development of SRS Techniques to Investigate Adipocyte Heterogeneity	179
5.1.3	Raman Can be Exploited to Study Metabolic Readouts	182
5.1.4	3T3-L1 Adipocytes Undergo Hypertrophy with Increased Incubation	185
5.1.5	Demonstrating This Heterogeneity in Single Cells	187
5.1.6	SRS and Phasor Combination Allows for Cell Image Segmentation	189
5.1.7	Using Chemical Probes to Study Adipocyte Biology	192
5.1.8	Developing an Approach to Lipid Droplet Segmentation	198
5.1.9	Investigating Differences in the Adipocyte Life Cycle	203
5.1.10	Understanding Adipocyte Heterogeneity Further with Droplet and Whole Cell Segmentation	209
5.2	Discussion	218
5.2.1	A New Route for Adipocyte Metabolic Investigation	218
5.2.2	Limitations of the Current Study	220
5.2.3	Lots of Potential - Future Work	222
6.0	Investigating the Impact of Zinc Alpha 2-Glycoprotein in Adipose Browning Biology	225
6.1.1	Introduction	225
6.1.2	Examining Mitochondrial Distribution in 3T3-L1 Adipocytes	226
6.1.3	Assessing Adipocyte Metabolic Rate with ZAG Stimulation.	231
6.1.4	Investigating Adipocyte Browning Signalling Pathways	234
6.2	Discussion	237
6.2.1	No change observed	237
7.0	Discussion and Conclusion	240
7.1	Key Work and Conclusions	240
8.0	References	247
	Supplementary Material	275

List of Tables

Table 2.1. List of Primary Antibodies ... 71

Table 2.2. List of Secondary Antibodies ... 72

Table 3.1. Candidate Ligands for Docking Simulations in ZAG ... 100

Table 3.2. Common Residues That are Interacting with Successful Ligand Candidates ... 102

Table 3.3. RMSD Scores of Candidate Ligands Docked in Native and Mutated ZAG ... 114

Table 3.4. RMSD Scores of 8,11-Eicosadiynoic acid Docked in Mutant ZAG Variants in Comparison to Native ZAG ... 118

Table 3.5. RMSD Scores of Arachidic acid Docked in Mutant ZAG Variants in Comparison to Native ZAG ... 120

Table 3.6. Critical Micelle Formation Index ... 130

Supplementary Table 1: List of Candidate Ligands for Docking Experiments ... 275

List of Figures

- Figure 1. 1.** The Link Between Insulin and Glucose Homeostasis ... 24
- Figure 1. 2.** Overview of Adipose Distribution and Function ... 30
- Figure 1. 2.** Two Mechanisms to Accommodate for Increased Lipid Storage ... 36
- Figure 1. 3.** A Conserved Mechanism to Store Lipids in Lipid Droplet Organelles ... 40
- Figure 1. 4.** Whole Body Glucose Homeostasis and Dysfunction ... 42
- Figure 1. 6.** The Interplay Between Lipids and Mitochondria for Energy Production ... 45
- Figure 1. 7.** Exposure to Cold Results in Adipocyte and Mitochondria Remodelling ... 48
- Figure 1. 8.** An Overview of ZAGs Metabolic Activity ... 51
- Figure 1. 9.** A Whole Body Cachexia Overview ... 56
- Figure 1. 10.** Crystal Structure of Zinc Alpha-2 Glycoprotein (ZAG) ... 63
- Figure 1. 11.** Crystal Structure of Zinc Alpha-2 Glycoprotein (ZAG) with native ligand Hexaethylene Glycol (P6G) ... 64
- Figure 3. 1.** Research and Experimental Design for *in silico* Ligand Docking ... 96
- Figure 3. 2.** Initial Ligand Docking Simulation in ZAG Alpha Helix Groove ... 98
- Figure 3. 3.** Protein Modelling of Successful Candidate Ligand Dockings in ZAG ... 102
- Figure 3. 4.** Protein Modelling of Successful Candidate Ligand Dockings in Mutated Tryptophan 148 ZAG ... 108
- Figure 3. 5.** Protein Modelling of Successful Candidate Ligand Dockings in Mutated Arginine 73 ZAG ... 109
- Figure 3. 6.** Protein Modelling of Successful Candidate Ligand Dockings in Mutated Threonine 80 ZAG ... 110
- Figure 3. 7.** Protein Modelling of Successful Candidate Ligand Dockings in Mutated Phenylalanine 101 ZAG ... 111

Figure 3. 8. Protein Modelling of Successful Candidate Ligand Dockings in Mutated Isoleucine 76 ZAG ...	112
Figure 3. 9. Protein Modelling of Successful Candidate Ligand Dockings in Mutated Tyrosine 117 ZAG ...	113
Figure 3. 10. Protein Modelling of Successful Candidate Ligand Dockings in Mutated Glutamic Acid 80 ZAG ...	114
Figure 3. 11. Selection of Protein Docking Models in Tryptophan 148 Mutation Simulations ...	118
Figure 3. 12. Selection of Protein Docking Models in Arginine 73 Mutation Simulations ...	120
Figure 3. 13. Proposed Binding Site of BODIPY C16 ...	123
Figure 3. 14. Representation of Micelle Formation ...	130
Figure 3. 15. Proposed Secondary Binding Site in ZAG ...	133
Figure 4. 1. Restriction Digest of pQE60 and pCDNA3.1Plasmids ...	140
Figure 4. 2. Effects of Time and IPTG Induction on ZAG Expression in Transformed DH5- α and BL21 Competent Cells ...	143
Figure 4. 3. Effects of Subsequent Triton-x-100 Wash Steps on the Cleanliness of ZAG Expression ...	146
Figure 4. 4. Effects on ZAG Expression After Denaturing and Refolding Treatment of Resultant Triton X-100 Wash Step Pellet ...	148
Figure 4. 5. ZAG Expression Cleanliness After Vivaspin Centrifugation ...	150
Figure 4. 6. Fluorescence Spectroscopy Experiments Verify ZAG Refolding ...	153
Figure 4. 7. Glycerol is Released from 3T3-L1 Adipocytes After ZAG Stimulation ...	156
Figure 4. 8. ZAG Protein Expression in Cell and Supernatant Samples After pCDNA3.1 Transfection of HEK293 Cells ...	158

Figure 4. 9. Determining the Effective Dose of Blasticidin S for Transduced HEK293 Cell Selection ...	161
Figure 4. 10. Successful Lentivirus Transduction of HEK293 Cells to Express ZAG ...	163
Figure 4. 11. Stable HEK293-ZAG Transduced Cell Lines Secrete ZAG in a Titre Dependent Manner ...	164
Figure 4. 12. Glycerol is Released from 3T3-L1 Adipocytes After Mammalian ZAG Stimulation ...	166
Figure 5. 1. Understanding the Key Differences in Raman Spectroscopy ...	176
Figure 5. 2. Representative Raman Spectrum of Biological Specimens ...	178
Figure 5. 3. Acquisition Capabilities of SRS ...	181
Figure 5. 4. Lipid Droplet Expansion Observed in 3T3-L1 Adipocytes with Prolonged Incubation ...	186
Figure 5. 5. Heterogeneity in 3T3-L1 Adipocytes ...	188
Figure 5. 6. Cellular Characteristics Have Their Own Phasor Plots ...	190
Figure 5. 7. Images of Particular Subcellular Compartments ...	191
Figure 5. 8. Utilising Tools in SRS ...	193
Figure 5. 9. Measuring Glucose-d7 Uptake in 3T3-L1 Adipocytes ...	195
Figure 5. 10. Glucose Metabolism is Affected by Insulin and Adipocyte Size ...	196
Figure 5. 11. Spectral Phasor Allows for Lipid Segmentation ...	200
Figure 5. 12. Spectral Phasor Allows for Lipid Quantification ...	202
Figure 5. 13. Evident Hypertrophy of Lipid Droplets in Lengthened Cultured 3T3-L1 Adipocytes ...	205
Figure 5. 14. Lipid Droplet Content Characterization Possible Through SRS ...	206
Figure 5. 15. Lipid Droplet Composition Changes Observed with Increased Incubation Periods ...	208

Figure 5. 16.	Post Image Unmixing as an Alternative for Lipid Droplet Analysis ...	212
Figure 5. 17.	Individual Lipid Droplet Interrogation Possible with Spectral Phasor ...	214
Figure 5. 18.	Implementing Spectral Phasor for Total Cell Analysis ...	216
Figure 5. 19.	Glucose Uptake with Increasing 3T3-L1 Adipocyte Incubation Periods ...	219
Figure 5. 20.	Bottleneck for High Throughput on Lipid Composition ...	229
Figure 6. 1.	Mitochondrial Protein Expression in Adipocytes at Varied Cultured Periods ...	228
Figure 6. 2.	Mitochondrial Protein Expression After Recombinant ZAG Stimulation ...	229
Figure 6. 3.	Mitochondrial Protein Expression After Mammalian ZAG Stimulation ...	230
Figure 6. 4.	Investigating Metabolic Activity Changes in 3T3-L1 Adipocytes via Glucose Uptake After ZAG Stimulation ...	232
Figure 6. 5.	Browning Protein Expression in ZAG Treated 3T3-L1 Adipocytes ...	235
Supplementary Figure 1:	Lenti-ORF Plasmid Map ...	274

Acknowledgements

Although my name is on the front page here, the skills and personal qualities I have acquired over the years to complete this thesis are an accumulation of all of life's challenges and the people who have supported me through those. It is always easy to think of the most recent people when remembering people to thank. However, many people from teachers, coaches, mentors, family members, friends, loved ones and lecturers will all have played their part - big or small - over the years and I am grateful for their positive impact.

More recently, I would like to thank Medical Research Scotland and Moleculomics for their funding and support during my PhD and The University of Strathclyde for lab space to conduct this project.

To the lab. There have been many comings and goings since starting, but I would just like to thank everyone; Shaun, Holly, Laura, Angeline, Rod and Shannan. Thank you for creating a supportive environment for conducting research and an insightful and learning one with constant communication in our science in both labs and group meetings.

To Margaret. You have been very busy furthering your own career but have always given me time and have been an honest voice which is hugely important to me. Thank you for all your belief and support. And to Marco and Zainab. Thank you for your support and memories during these 4 years. I have made two dear friends.

Malcolm, Jonathan, Karl and William: thank you for all the knowledge and insight you have provided in this multifaceted project. Without all your expertise, this work couldn't have gotten far.

The Biggies

The Boss. Thank you for your mentorship, support and still ongoing belief in myself. I have heard some terrible tales from people regarding a PhD, but I have not had those same experiences and I am grateful to have undertaken my studies here. Since writing, I have missed a coffee and a chat with you and I think that says a lot. A card with more thoughts will follow.

To my late Gran. You were very supportive of me and my studies, and I loved visiting and sharing this with you and I miss that dearly. Unfortunately I can't share this with you, but your hilarious stories and support are still with me.

Luke. Whilst you have been off conquering your own difficult task, it is great having someone to support and root for. I am very proud of you and we have grown a lot together. Keep swinging that stick and thank you for being a crackin' brother.

A special thanks to my Mum and Dad. There is no doubt you have made decisions at a time I have been too young to understand that have allowed me to be here today. There will have been many personal sacrifices on your part to provide me with the best chance possible to try my hand at many things. We might have thought football would have been the breakthrough, but here we are. Thank you for your love and support.

And to my Beautiful Wife Rhona. In short, without you I wouldn't be writing this. It may be the wrong conclusion, but despite all this has taken out of me getting to the end of this thesis, being your Husband is my greatest and proudest achievement. Wee fresh faced Justin and Rhona in 2nd year of Uni have come a long way; 2024 in particular has been wild! You are my rock and my best friend and I am blessed to do life with you. Mwaahhh x.

Love you all very much,

J

List of Abbreviations

2YT - 2x Yeast Extract Tryptone Media

ACC - Acetyl-CoA Carboxylase

AGK - Acylglycerol Kinase

AKT – Protein Kinase B

ALDP - Adipocyte Lipid-Binding Protein

AOC3 - Amine Oxidase Copper-Containing 3

ATCC - American Type Culture Collection

ATGL - Adipose Triglyceride Lipase

β_3 AR - Beta-3 Adrenergic Receptor

BAT – Brown Adipose Tissue

BEVS - Baculovirus Expression Vector System

BSA - Bovine Serum Albumin

cAMP - Cyclic Adenosine Monophosphate

CARS - Coherent Raman Scattering

CD - Circular Dichroism

CHO - Chinese Hamster Ovary

CM - Cytosolic Mitochondria

CMC - Critical Micelle Formation Index

CPT1A - Carnitine Palmitoyltransferase I

DAGT - Diacylglycerol Acyltransferases

DAUDA - 11-(Dansylamino)Undecanoic Acid

DMEM - Dulbecco's Modified Eagle's Medium

DTT – Dithiothreitol

E. coli - *Escherichia coli*

ECM - Extracellular Matrix

ER - Endoplasmic Reticulum

ETC - Electron Transport Chain

FAS - Fatty Acid Synthase

FBS - Foetal Bovine Serum

FFA - Free Fatty Acids

FIT - Fat Storage-Inducing Transmembrane

G6Pase - Glucose-6-Phosphatase

GAPDH - Glyceraldehyde-3-Phosphate Dehydrogenase

GSV – Glucose Storage Vesicle

HEK293 - Human Embryonic Kidney Cells

HOMA-IR - Homeostatic Model Assessment of Insulin Resistance

HSL - Hormone-Sensitive Lipase

IBMX - 3-Isobutyl-1-Methylxanthine

IL-1 – Interleukin-1

IL-6 - Interleukin-6

IR - Insulin Receptor

IRS1 – Insulin Receptor Substrate 1

LASSO - Least Absolute Shrinkage and Selection Operator

LIF – Leukaemia Inhibitory Factor

LMF - Lipid Mobilizing Factor

MEFs - Mouse Embryonic Fibroblasts

MCP-1 - Monocyte Chemoattractant Protein-1

MGL - Monoglyceride Lipase

MHC - Major Histocompatibility Complex

MFN2 – Mitofusin 2

MOI - Multiplicity of Infection

Na₄P₂O₇ - Sodium Pyrophosphate

NaCl - Sodium Chloride

NAFLD - Non-Alcoholic Fatty Liver Disease

NASH - Non-Alcoholic Steatohepatitis

NCS - Newborn Calf Serum

NE - Norepinephrine

NEFAs - Non-Esterified Fatty Acids

NRF1/2 - Nuclear Respiratory Factors 1 and 2

NRZ - NAG-RINT1-ZW10

P6G - Hexaethylene Glycol

PBS - Phosphate Buffered Saline

PBST - Phosphate Buffered Saline with Tween

PDB - Protein Data Bank

PDM - Peridroplet Mitochondria

PEPCK - Phosphoenolpyruvate Carboxykinase

PFA - Paraformaldehyde

PGC-1 α - PPAR γ Coactivator 1-alpha

PI3K - Phosphoinositide 3-Kinase

PKA - Protein Kinase A

PLANTS - Protein-Ligand ANT System

PLIN – Perilipins

PLIN5 - Perilipin 5

PPAR γ - Peroxisome Proliferator-Activated Receptor Gamma

PRDM16 - co-factor PR Domain-Containing 16

PTMs - Post-Translational Modifications

POMC - Proopiomelanocortin

Rab18 - Ras-Related Protein 18

RMSD - Root Mean Square Deviation

ROI - Region of Interest Tool

RRID - Research Resource Identifier

SDS - Sodium Dodecyl Sulphate

Sf9 and Sf21- *Spodoptera frugiperda*

SNARE - Syntaxin 18 , Use1, BNIP1

SNS - Sympathetic Nervous System

SRG - Stimulated Raman Gain

SRL - Stimulated Raman Loss

SRS - Stimulated Raman Scattering

TAE – Tris-Acetate-EDTA Buffer

TAGs – Triacylglycerols

TBS - Tris Buffered Saline

TBST - Tris Buffered Saline with Tween

TCA - Tricarboxylic Acid (citric acid cycle)

TCR - T-Cell Receptors

TFAM - Mitochondrial Transcription Factor A

TNF- α - Tumour Necrosis Factor-Alpha

TWEAK – TNF-Like Weak Inducer of Apoptosis

UCP - Uncoupling Proteins

UCP-1 - Uncoupling Protein 1

UPR - Unfolded Protein Response

VDAC1/3 - Voltage-Dependent-Anion-Channel 1/3

WAT – White Adipose Tissue

WB - Western Blotting

ZAG - Zinc α 2-Glycoprotein

1.0 Introduction

1.1 *Cancer, Diabetes and Cardiovascular Disease*

As of 2015, 2.5 million people in the UK are living with cancer. Since 2001, new diagnosis of cancer in patients each year has risen by 29%, with over 390,000 people newly diagnosed in 2024, and around 167,000 people die of cancer each year in the UK. Cancer can affect various organs and tissues with different areas presenting a greater mortality rate than other types. For example, pancreatic cancer patients rarely live beyond 5 years whilst women diagnosed with breast cancer have an 80% survival rate at 5 years. The area of the body that is diagnosed and the stage of the cancer at the time of diagnosis are important factors dictating survival rate. Patients diagnosed at stage 4 had a 48% decreased survival rate at 1 year compared with patients being diagnosed at stage 1 (Macmillan Cancer Report., 2019).

Cancer can be classed as a neoplasm, i.e. an abnormal uncoordinated growth of cells that surmounts the growth of regular cells. The tumour serves no purpose and manipulates the host to receive its own blood supply and nutrients to continue development. A tumour can be classed as either benign or malignant (Baba and Câtoi, 2007). A benign tumour is not cancerous. The cells are well differentiated and have similarities to the neighbouring tissue (Baba & Câtoi, 2007). They grow at a slower rate than malignant tumours and the higher differentiation levels of the cells correlate with that slower growth (Cifone, 1982). These tumours are non-invasive and do not have the capacity to metastasise. In comparison, a malignant tumour's rate of growth is greater, and its level of cell differentiation is lower and does not resemble the surrounding tissue (Angell et al., 2017). Along with these physiological changes a malignant tumour has the capacity to invade and metastasise (Patel, 2020). Cancer ultimately starts through genetic damage which can be gained through environmental factors such as carcinogenic chemicals taken in through smoking or UV light radiation from the sun (Narayanan et al., 2010; Smith,

2009). These damaged genes ultimately lead to the underlying mutations resulting in cancer progression.

Diabetes

In healthy individuals, elevated blood glucose results in glucose being transferred from the circulation into muscle and fat where it is stored until blood sugar levels fall. Insulin is the hormone of the fed state; released from the pancreas in response to elevated blood glucose, insulin triggers peripheral tissues to take up glucose. Diabetes is a metabolic disease which results in elevated blood glucose levels, characterised by a failure of insulin action. There are two main types of diabetes, type 1 and 2. Type 1 diabetes is an auto-immune disease in which your body cannot make the hormone insulin due to a cell-mediated immune response on the beta cells, resulting in damage and dysfunction within the pancreas (Roep et al., 2021). 8% of people with Diabetes have type 1 (UK, 2023). Type 2 diabetes underlying mechanism is that sufficient insulin is produced from the pancreas, but this insulin is unable to produce a typical response in target tissues; a condition referred to as insulin resistance. Extended periods of high glucose blood levels can result in long term damage, and associated complications include retinopathy, nephropathy and cardiovascular disease (UK, 2023). The insulin receptor (IR) is a transmembrane homodimer comprised of two monomers ; an alpha subunit that sits at the cell surface exposed to the circulatory system that binds the insulin, and a beta subunit that resides inside the cell that triggers the signalling cascade. When insulin binds, a conformational change results in tyrosine kinase activity autophosphorylating the receptor. This phosphorylation triggers the insulin signalling pathway resulting in the translocation of glucose transporter molecules for e.g. GLUT 4 to the cell surface via glucose storage vesicles (GSV) and exocytosis. These GSVs then dock and fuse with the plasma membrane and facilitate glucose uptake into the cell.

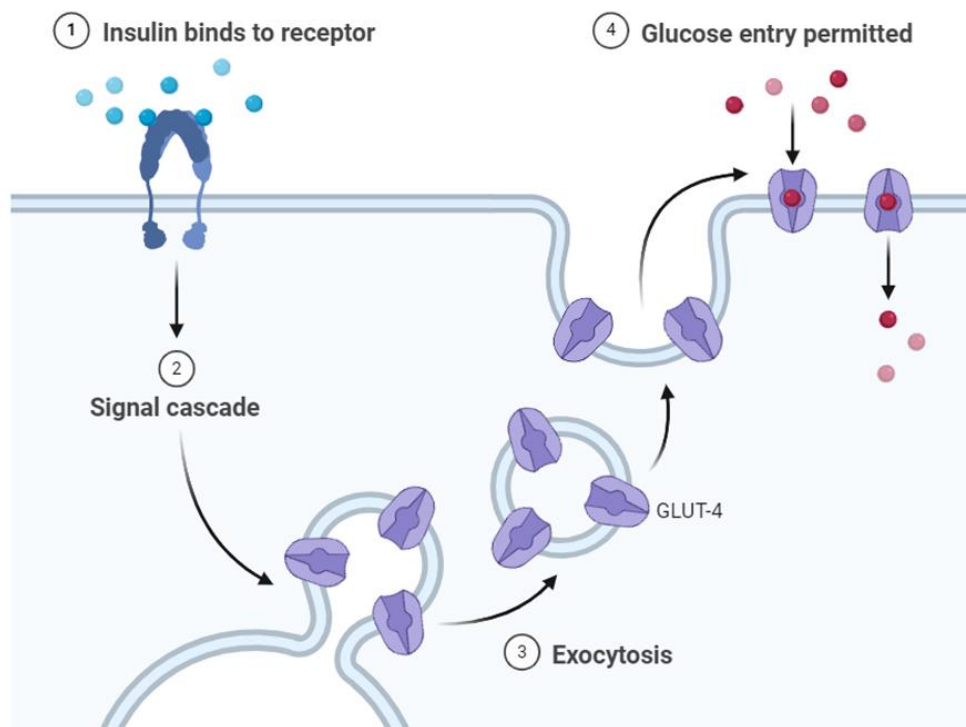
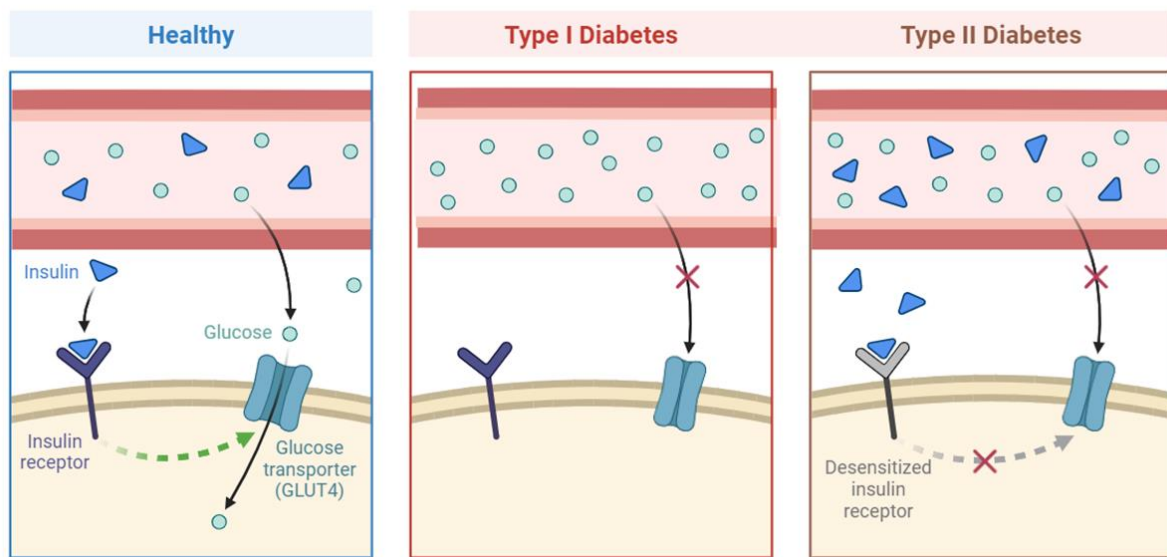


Figure 1. 1. The Link Between Insulin and Glucose Homeostasis

Glucose uptake can involve the role of insulin which recruits GLUT4 to the membrane surface and facilitates glucose homeostasis. Disruption in insulin signalling results in progression to metabolic health disorders such as Diabetes. Type 1 Diabetic individuals are unable to produce insulin and therefore insulin dependent glucose uptake cannot be undertaken resulting in upregulated

concentrations of glucose in the blood (Hyperglycemia). Type 2 Diabetic individuals can produce insulin, but the insulin signalling pathway is faulty. This results in disruption to GLUT4 translocating to the plasma membrane and again results in hyperglycemia. Healthy regulation of glucose after a meal is facilitated by this pathway. Figures are adapted from BioRender.

Healthy Glucose Regulation

Glycogenesis is the anabolic process through which glucose is converted into glycogen, a highly branched polysaccharide used for energy storage. This process occurs predominantly in the liver and muscle tissues (Han et al., 2016) (Hargreaves & Spriet, 2020), providing a mechanism to store glucose during periods of excess intake, such as after meals, ensuring a supply of energy during times of fasting or increased physical activity. While the fundamental biochemical steps in glycogenesis are conserved across tissues, the regulation, transport mechanisms, and physiological roles of glycogen in the liver and muscle differ significantly, reflecting the specialized functions of these organs in glucose homeostasis (Han et al., 2016) (Hargreaves & Spriet, 2020). In the liver, glucose is transported into hepatocytes via the insulin-independent GLUT2 transporter (Karim et al., 2012), which allows glucose to enter freely in response to fluctuations in blood glucose levels. GLUT2 has a high capacity but a low affinity for glucose (Thorens, 2015), ensuring that the liver acts as a glucose buffer after meals, storing large amounts of glycogen. Once inside the cell, glucose is phosphorylated by glucokinase to form glucose-6-phosphate, a key regulatory step in glycogenesis. Glucokinase is unique to the liver and has a higher K_m (Michaelis constant) than hexokinase, allowing it to respond efficiently to postprandial hyperglycemia without becoming saturated (De Backer et al., 2016). In muscle tissue, glucose uptake is more tightly regulated by insulin. Glucose enters myocytes via insulin-sensitive GLUT4 transporters (Richter & Hargreaves, 2013), which translocate to the cell membrane in response to insulin signalling. This ensures that glucose is taken up primarily in the fed state, when insulin levels are high. Once internalized, glucose is phosphorylated by hexokinase, which has a lower K_m than glucokinase, allowing muscle cells to rapidly utilize glucose even at lower concentrations (Chadt & Al-Hasani, 2020). Glycogen stored in muscle serves as a localized energy reserve for contraction and ATP production during exercise. Unlike the liver, muscle lacks glucose-6-phosphatase, preventing it from

releasing free glucose into the bloodstream; thus, muscle glycogen is reserved for intracellular use during physical activity. The purpose of glycogen storage in these two tissues reflects their distinct roles in metabolism. Liver glycogen acts primarily as a buffer for blood glucose levels. During periods of fasting or between meals, glycogenolysis (the breakdown of glycogen) in the liver releases glucose into the bloodstream, maintaining glucose homeostasis and providing a continuous supply of energy, particularly for glucose-dependent tissues like the brain. In contrast, muscle glycogen is utilized primarily during periods of intense physical activity, where glucose is rapidly metabolized via glycolysis to meet the immediate ATP demands of muscle contraction (Hargreaves & Spriet, 2020).

1.2 Adipocyte Biology and Their Role in Metabolism

The Adipocytes Role in Glucose Homeostasis

When glucose intake exceeds the storage capacity for glycogen, the body diverts excess glucose toward lipid synthesis via *de novo* lipogenesis in the adipose tissue (Ameer et al., 2014). Adipose tissue is a central player in metabolic regulation, governing energy storage, hormone secretion, lipid metabolism, inflammation, and thermogenesis (Luo & Liu, 2016) (Kawai et al., 2021) (Fenzl & Kiefer, 2014). It functions primarily as an energy reservoir, storing surplus energy as triacylglycerols (TAGs) within lipid droplets, which protects non-adipose tissues from harmful lipid accumulation and prevents lipotoxicity (Cusi, 2010). Adipose tissue can be broadly categorised into two types; White adipose tissue (WAT) and brown adipose tissue (BAT), which have distinct roles in energy metabolism and glucose homeostasis. While both tissues store energy in the form of lipids, their physiological functions, cellular architecture, metabolic activity, and distribution vary significantly, reflecting their distinct contributions to the body's energy balance and metabolic regulation (Rosell et al., 2014).

WAT primarily serves as the body's main energy reserve, storing excess energy in the form of triacylglycerols (TAGs). During periods of caloric surplus, white adipocytes accumulate triacylglycerols, which can later be hydrolysed to release fatty acids and glycerol when energy demand arises, such as during fasting or prolonged physical activity. This mechanism ensures that the body has access to energy during periods of deprivation. The majority of WAT is comprised of white adipocytes, professional lipid storing cells that are unilocular - containing one large lipid droplet that dominates the majority of the cell volume. This large lipid droplet allows the cell to store substantial amounts of fat efficiently. White adipocytes are relatively large cells that can expand significantly in response to excess nutrient intake (Santoro et al., 2021), enabling the tissue to accommodate increasing energy demands. White adipose tissue is distributed throughout the body, with prominent depots located subcutaneously (beneath the skin) and viscerally (around internal organs). Subcutaneous fat provides insulation and protection against external temperature fluctuations, while visceral fat plays a central role in metabolic regulation (Santoro & Kahn, 2023; Santoro et al., 2021). Conversely, BAT is comprised of brown or beige adipocytes that are specialised for heat expenditure through thermogenesis. These adipocytes are multilocular -contain multiple lipid droplets- and are densely packed with mitochondria. It is the iron contained in the high concentrations of mitochondria that results in the brown appearance of the tissue. These adipocytes are observed in vast quantities in new-born babies and their thermogenic capabilities maintain body temperature as new-borns cannot shiver to generate heat through muscular activity. The consensus was that as humans aged and gained the ability to shiver, humans began to lay down greater volumes of WAT and dispense of the BAT (Lee et al., 2013). However, it appears the ambient temperatures at which we have been imaging patients during MRI or CT scans do not pick up these tissues and when temperatures have been dropped to 20 and even 10 degrees Celsius, BAT is observed in adults (Blondin et al., 2014). BAT is primarily located in specific

regions, including the interscapular area (between the shoulder blades), around the neck, and along the spinal cord and its role in metabolism and cancer cachexia progression is discussed later in ***1.3 Zinc Alpha 2-Glycoprotein***.

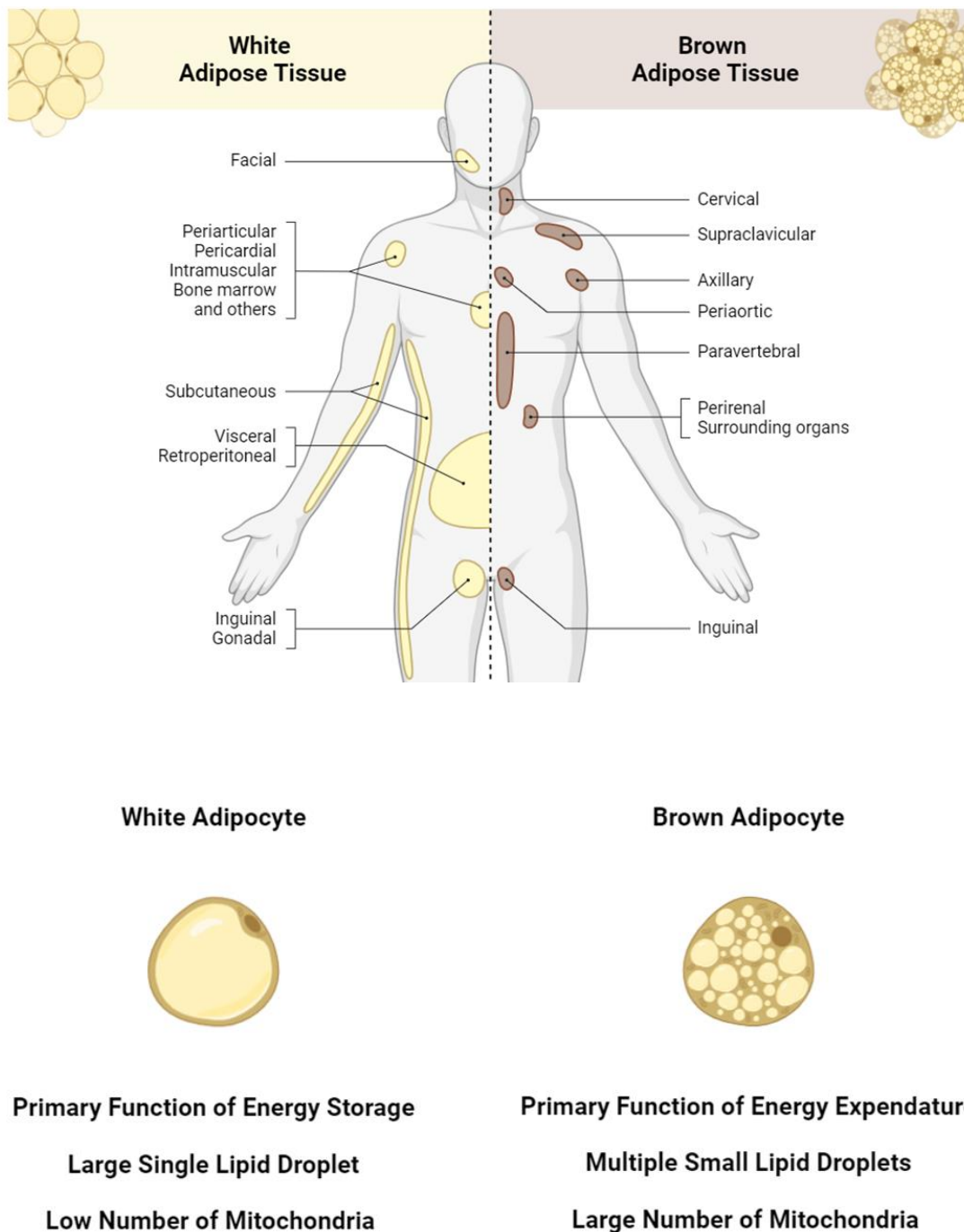


Figure 1. 2. Overview of Adipose Distribution and Function

Adipose tissue has many depots in the body and can be broadly categorised into two classes; White Adipose Tissue (WAT) and Brown Adipose Tissue (BAT). WAT is comprised of white adipocytes and their primary function is for lipid storage as energy reserves. They reside as depots under the skin (subcutaneous) and in the abdominal regions around organs (visceral). BAT is comprised of brown

adipocytes and their primary function is for energy expenditure by thermogenesis. These depots are found closer to the nervous system at the head, neck and spine. Figures are adapted from BioRender.

Traditionally, adipose tissue was thought to only function as storage for energy reserves. However, this complex tissue is now classified as an organ due to its metabolic, endocrinological and immunological functions (Kershaw & Flier, 2004). Despite being classed as an organ, adipose tissue exhibits a great deal of plasticity in its phenotype and metabolic activity. Adipose tissue is primarily composed of adipocytes, specialized cells that store excess fatty acids and lipids through esterification and storing them as triacylglycerides in lipid droplets. However, like all organs, the function of this tissue can become dysregulated in disease and it can be influenced by environmental factors. The optics surrounding fat are negative, with the focus on it contributing to diseases such as obesity and diabetes. However, adipose tissue is essential and its importance is demonstrated by the mutation in a gene called *CIDEA* (Ganeva et al., 2023; Rubio-Cabezas et al., 2009). Individuals with this mutation are unable to generate adipocytes that can expand their storage capacity for the intake of fatty acids and lipids in the diet. Therefore, these circulating fatty acids and lipids deposit in other tissues and organs such as skeletal muscle and liver in the form of lipid droplets that in turn lead to disease such as hepatic steatosis (Borén et al., 2013; Byrne & Targher, 2014). This exemplifies the critical role adipocytes play. This of course is an exaggerated phenotype, however, is mirrored when we look at diseases such as obesity (Borén et al., 2013; Byrne & Targher, 2014) and diabetes (Cusi, 2010; Fryk et al., 2021). Primary adipocytes in humans can expand to upwards of ~300 µm. At this point, adipocyte storage is 'at capacity' and the same mechanisms of disposal of circulating fatty acids and lipids are observed with obese subjects (Cusi, 2010) that have been observed in the mutated *CideA* patients (Rubio-Cabezas et al., 2009). Thus, adipose tissue is essential, but the expansion of its lipid droplets beyond capacity leads to disease (Verboven et al., 2018). There are two methods of expansion for adipocytes; hyperplasia (Horwitz & Birk, 2023), where adipogenesis results in larger numbers of smaller adipocytes for lipid storage, and hypertrophy (Horwitz & Birk, 2023) where already existing

adipocytes expand. The latter is observed in obesity and is associated with inflammation, reduced glucose uptake and reduced insulin sensitivity as seen with obesity progressing to type 2 diabetes (Gustafson et al., 2009; Kim et al., 2015). As well as the variation of droplet size and number, the location of excess adipose tissue is important in health (Tchkonia et al., 2013). Subcutaneous fat is stored under the skin whilst visceral is stored around the organs and it is this adipose depot that has a negative impact on health (Tchkonia et al., 2013). Furthermore, the species of lipid stored in adipose tissue also effects metabolic health (Phillips et al., 2012). Unsaturated fats are considered ‘healthy fats’ by helping regulate cholesterol with high density lipoproteins (Mensink & Katan, 1989). In contrast, saturated fats have negative correlations in health by upregulating low density lipoproteins that can lead to atherosclerosis, increasing the risk of stroke and heart disease (Maki et al., 2021; Phillips et al., 2012). Thus, despite adipose tissue being comprised primarily of adipocytes, the overall function of adipose depots are varied (Tchkonia et al., 2013). This is exemplified further from observations that individual adipocytes within the tissue exhibit heterogeneity in both morphology and metabolic activity (Dewal & Wolfrum, 2023; Duerre & Galmozzi, 2022; Kwok et al., 2016).

Dietary Factors Regulating Metabolic Health

Diet plays a pivotal role in shaping metabolic health, with poor dietary choices being a key driver of obesity, diabetes, and related metabolic disorders (Askari et al., 2020; Poti et al., 2017). Diets high in ultra-processed foods are especially harmful, as they are rich in energy-dense but nutrient-poor ingredients, particularly saturated fats (Phillips et al., 2012). Saturated fats are strongly implicated in the pathogenesis of obesity and diabetes, primarily due to their effects on energy balance and metabolic regulation. The high caloric density of saturated fats promotes excessive caloric intake, leading to positive energy balance and weight gain. Additionally, diets rich in saturated fats enhance lipogenesis, increasing triacylglycerol storage in adipocytes, which further accelerates the accumulation of adipose tissue. Moreover,

saturated fats may have a weaker influence on satiety signalling (Maljaars et al., 2009) compared to other macronutrients, often resulting in overeating and heightened energy consumption.

Saturated fats are also closely linked to the development of insulin resistance, a hallmark of metabolic dysfunction (Riccardi et al., 2004). This occurs when cells become less responsive to insulin, impairing glucose uptake in tissues and contributing to elevated blood sugar levels (hyperglycemia). Furthermore, high saturated fat intake is associated with systemic inflammation (Fritsche, 2015), characterized by increased levels of pro-inflammatory cytokines. These inflammatory mediators disrupt insulin signalling pathways, intensifying insulin resistance. Hyperplasia and hypertrophy describe two distinct processes that adipocytes can undergo to manage the increased calories observed in the high processed diet. Hyperplasia refers to an increase in the number of adipocytes, while hypertrophy describes the enlargement of existing adipocytes (Santoro & Kahn, 2023; Santoro et al., 2021). Adipocyte hyperplasia is driven by the differentiation of precursor cells, or preadipocytes, into mature fat cells. This process is regulated by hormonal signals such as insulin and glucocorticoids, as well as the body's nutritional status. During periods of growth, such as childhood and adolescence, or when energy intake exceeds energy expenditure, hyperplasia allows the adipose tissue to accommodate increased energy storage. Hypertrophy in adipocytes occurs when individual fat cells enlarge due to lipid droplet accumulation, primarily composed of triacylglycerols. Nutritional factors, including excess dietary fat, and hormones such as insulin stimulate this lipid accumulation. Physiologically, hypertrophy is a normal response to short-term energy surpluses, such as after meals, when adipocytes expand to store additional energy. However, in the context of prolonged energy excess, as in obesity, adipocyte hypertrophy becomes pathological. Overloaded fat cells can become dysfunctional, leading to impaired lipid metabolism, systemic inflammation, and insulin resistance. It is this hypertrophy process that

has been observed in contributing to insulin resistance and obesity (Santoro & Kahn, 2023; Santoro et al., 2021).

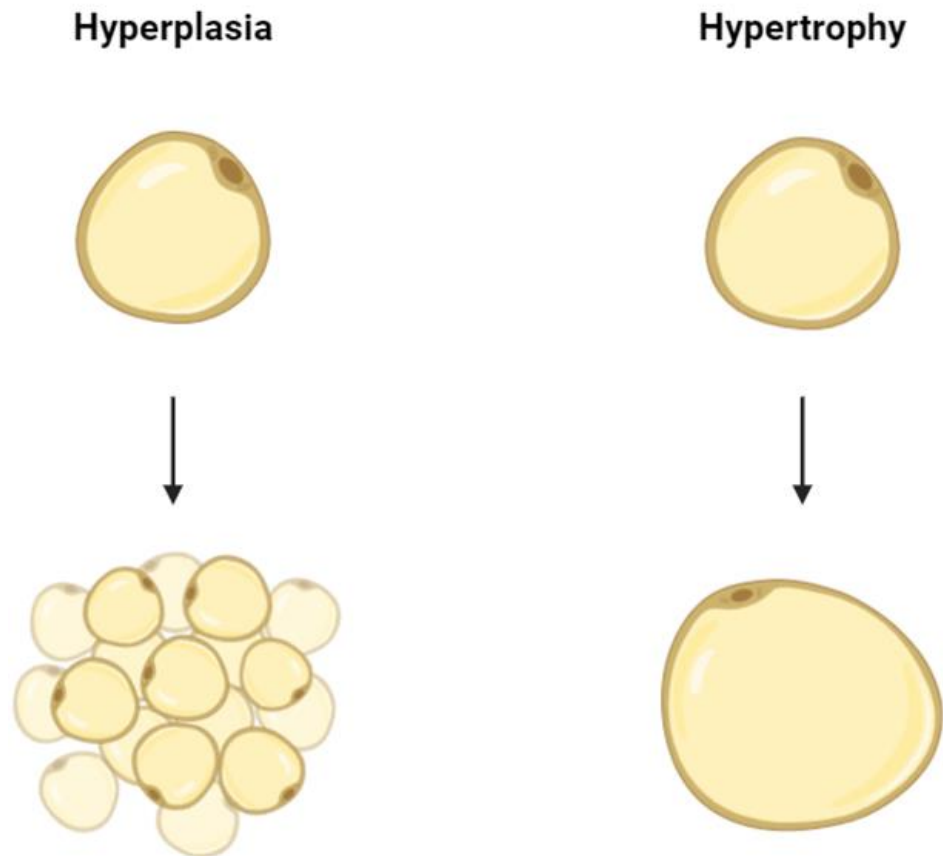


Figure 1. 3. Two Mechanisms to Accommodate for Increased Lipid Storage

When a surplus of fatty acids are available, increased lipid storage can be facilitated by the adipose tissue utilising two systems. Hyperplasia is the generation of new adipocytes (adipogenesis) by directing precursor cells to differentiate into mature adipocytes. This results in numerous but smaller adipocytes to share the lipid storage burden. Hypertrophy is the expansion of previously residing adipocytes within the tissue and results in large white adipocytes. Figures are adapted from BioRender.

Enlargement Affecting Insulin Action

Increased fat mass in the visceral adipose tissue compared to the subcutaneous adipose tissue is an indicator of increased cardiovascular disease risk, but it is the process of hypertrophy that has been observed in having a negative impact in obesity and insulin resistance progression in comparison to hyperplasia (Santoro & Kahn, 2023; Santoro et al., 2021). With hypertrophic adipocytes, an enhanced inflammatory response is observed. These enlarged cells secrete elevated levels of pro-inflammatory cytokines, such as tumour necrosis factor-alpha (TNF- α), interleukin-6 (IL-6), and monocyte chemoattractant protein-1 (MCP-1) also known as CCL2. This secretion establishes a state of chronic low-grade inflammation within adipose tissue, which has been shown to disrupt insulin signalling pathways (Saltiel, 2021; Santoro & Kahn, 2023; Santoro et al., 2021). The inflammatory milieu is further intensified by the recruitment of immune cells, particularly macrophages, which infiltrate hypertrophic adipose tissue and release additional pro-inflammatory mediators (Verboven et al., 2018; Zatterale et al., 2020). This synergistic effect exacerbates insulin resistance not only in adipocytes but also in peripheral tissues such as muscle and liver, leading to a systemic impairment of metabolic function. However, insulin resistance has also been observed in absence of inflammation. The expansion of the lipid droplet results in less cytosolic space in the adipocyte, and this is thought to be significant in itself to impact metabolic activity negatively (Kim et al., 2015). This expansion results in a disorganisation in the cytosol and as a consequence, extracellular matrix (ECM) remodelling and fibrosis are observed in the adipose tissue. The expansion of adipocytes results in disrupted cortical actin structures, resulting in adipocytes having reduced tissue compliance and flexibility, whilst changes in cytosolic space impact GLUT4 translocation and resulting in decreased glucose uptake due to insufficient glucose transporters reaching the plasma membrane (Saltiel, 2021; Santoro & Kahn, 2023; Santoro et al., 2021). The expansion of adipocytes also induces endoplasmic reticulum (ER) stress, a condition

characterized by the accumulation of misfolded or unfolded proteins within the ER lumen (Gregor & Hotamisligil, 2007). The increased metabolic demands associated with hypertrophy exacerbates ER stress, activating the unfolded protein response (UPR) (Gregor & Hotamisligil, 2007). While the UPR aims to restore cellular homeostasis, prolonged ER stress can lead to cellular dysfunction and impair insulin signalling pathways, contributing to the development of insulin resistance (Gregor & Hotamisligil, 2007).

Adipokine dysregulation is another critical consequence of adipocyte hypertrophy (Unamuno et al., 2018). Hypertrophic adipocytes produce significantly lower levels of adiponectin, an adipokine known for its insulin-sensitizing properties (Pham et al., 2023). Reduced adiponectin levels impair insulin signalling and glucose uptake in peripheral tissues, contributing to decreased insulin sensitivity (Pham et al., 2023). Conversely, hypertrophic adipocytes secrete higher levels of leptin, which normally functions to regulate appetite and energy balance (Pham et al., 2023). However, chronic overproduction of leptin can lead to leptin resistance, thereby disrupting metabolic homeostasis and further exacerbating insulin resistance (Pham et al., 2023).

Further Consequences of Adipocyte Hypertrophy

A further consequence of adipocyte hypertrophy is that an adipocyte will become ‘at capacity’, and no longer able to store lipids. Enlarged adipocytes will no longer store lipids and become leaky releasing elevated concentrations of non-esterified fatty acids (NEFAs) into circulation (Fryk et al., 2021(Carpentier, 2021). These NEFAs will then deposit into other organs known as ectopic lipid deposits and due to these cells being non-specialised for storing lipids, results in lipotoxicity of the tissue and form lipid droplets (Borén et al., 2013).

Lipid droplets are dynamic organelles essential for safe lipid storage and metabolism, and are formed when glucose enters the cell (Gao et al., 2019; Olzmann & Carvalho, 2019). In this

pathway, glucose is converted to fatty acids, which are esterified into triacylglycerols (TAGs) or cholesterol esters. Fatty acids may also be directly transported into adipocytes. In adipocytes, glucose uptake, like in muscle, is mediated by insulin-dependent GLUT4 transporters. Once inside, glucose is converted to pyruvate via glycolysis, then enters the tricarboxylic acid (TCA) cycle, where it provides precursors for fatty acid synthesis. The fatty acids are then esterified with glycerol to form TAGs, which are stored in lipid droplets. Much of the glucose transported into adipocytes in culture is used as a source of glycerol. Lipid droplet formation occurs within the ER (Gao et al., 2019; Olzmann & Carvalho, 2019) , where neutral lipids accumulate between the phospholipid bilayer, forming a lens structure that gradually expands, resulting in a core of neutral lipids consisting primarily of TAGs, and cholesteryl esters. Surrounding this neutral lipid core is a phospholipid monolayer, distinct from the bilayer of most cellular membranes. This monolayer is primarily composed of various phospholipids such as phosphatidylcholine, phosphatidylethanolamine, phosphatidylinositol and phosphatidylserine. The droplet then begins to bud away from the bilayer forming an independent lipid droplet. This budding process is regulated by proteins such as perilipins, CIDE proteins, and seipin, which facilitate the proper formation and stabilization of lipid droplets (Gao et al., 2019; Olzmann & Carvalho, 2019). This storage of neutral lipids within adipocytes is a metabolically healthy way to handle excess glucose, allowing for energy reserves to be accumulated without disrupting cellular function.

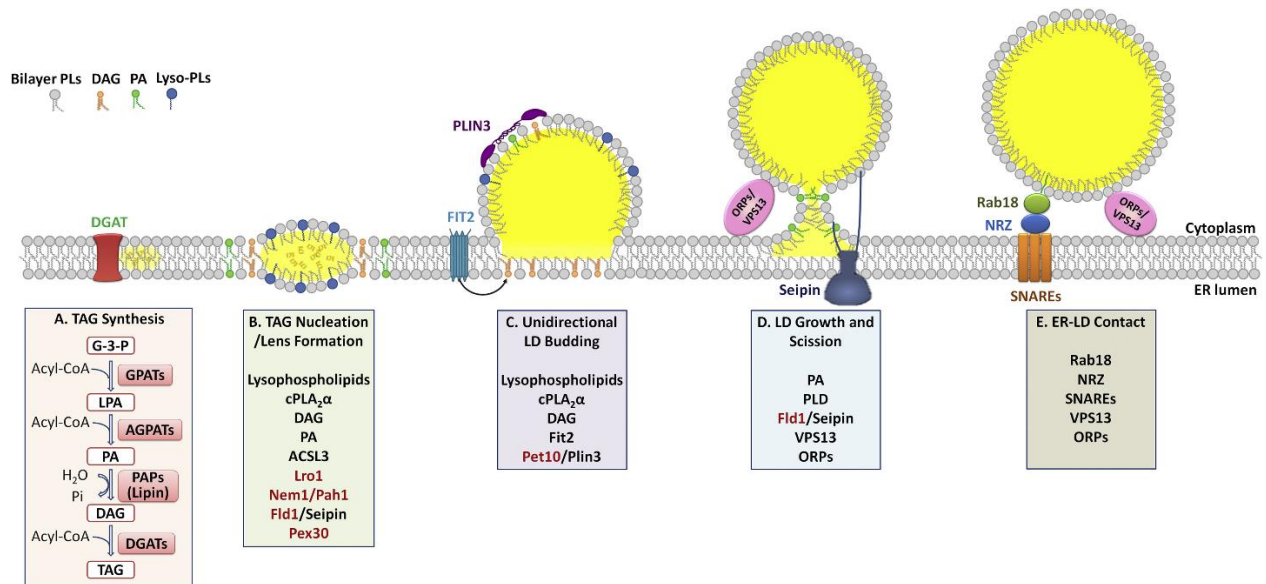
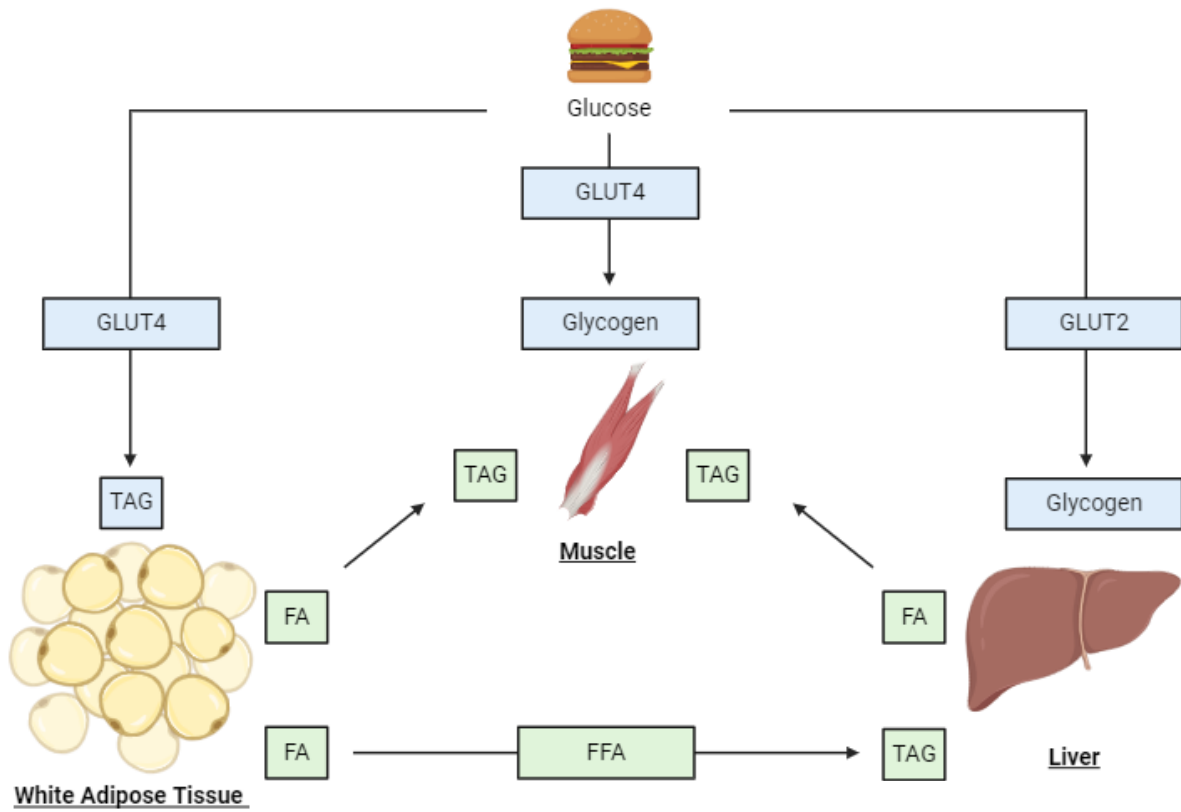


Figure 1. 4. A Conserved Mechanism to Store Lipids in Lipid Droplet Organelles

Neutral lipid synthesis such as triacylglycerol (TAG) and sterol esters take place in between the bilayer of the plasma membrane of the Endoplasmic Reticulum (ER) and is facilitated through diacylglycerol acyltransferases (DGAT) for TAG (Box A). This process results in the accumulation of lipids and results in an oil lens formation, decreasing surface tension in the outer leaflet and protrusion is observed (Box B). Further accumulation and surface tension decrease results in budding of the membrane and is facilitated through the recruitment of transmembrane proteins such as fat storage-inducing transmembrane (FIT) and seipin whilst surface tension is managed through surface proteins like perilipins (PLIN) (Box C). Droplets begin to bud away from the plasma membrane of the ER due to the size and surface tension restrictions of the droplet (Box D) and when released as droplets can form contact sites with other organelles. The example shown here is contact with the ER being facilitated by the Ras-related protein 18 (Rab18) – NAG-RINT1-ZW10 (NRZ) – Syntaxin 18, Use1, BNIP1 (SNARE) complex (Box E). Figure adapted from (Gao et al., 2019)

However, this same process packaging the excess circulating fatty acids due to hypertrophic adipocytes results in the unhealthy ectopic fat deposition in non-adipose tissues such as the liver (Byrne & Targher, 2014). Over time, this can lead to the development of non-alcoholic fatty liver disease (NAFLD) (Byrne & Targher, 2014), where fat accumulates in the liver in the absence of significant alcohol consumption. NAFLD is considered a reversible condition in its early stages, but if left unchecked, it can progress to non-alcoholic steatohepatitis (NASH) (McPherson et al., 2015), which is characterized by hepatic inflammation, oxidative stress, and cellular damage (Sheka et al., 2020). NASH significantly increases the risk of liver fibrosis, cirrhosis, and hepatocellular carcinoma, as chronic inflammation and lipid toxicity cause irreversible scarring and damage to liver tissue (Thomas et al., 2024). Thus, while glycogenesis and *de novo* lipogenesis are essential processes for managing glucose and lipid homeostasis (Han et al., 2016) (Hargreaves & Spriet, 2020) (Ameer et al., 2014), their dysregulation in the context of excessive nutrient intake and insulin resistance can lead to severe metabolic consequences (Nagarajan et al., 2022). The body's capacity to store glucose as glycogen in the liver and muscle or as fat in adipocytes is crucial for energy balance, but once this capacity is exceeded in adipocytes, overflow of lipids into non-adipose tissues sets the stage for metabolic diseases such as NAFLD, type 2 diabetes, and cardiovascular disease.

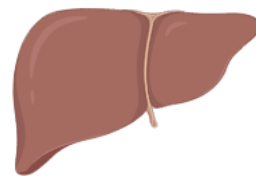


B

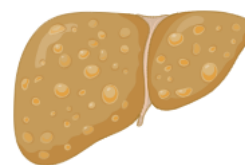


D

Hepatic Steatosis



Healthy Liver



Fatty Liver

C

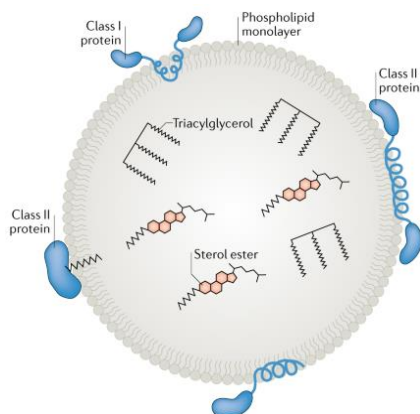


Figure 1. 5. Whole Body Glucose Homeostasis and Dysfunction

Glucose derived from our food after digestion is distributed to different tissues around the body. Glucose is up taken into the liver through an insulin independent GLUT2 transporter where it is stored as glycogen. Insulin facilitated glucose uptake via GLUT4 occurs in both white adipose tissue (WAT) where it is stored as triacylglycerol (TAG) and in muscle where it is stored as glycogen (demonstrated in blue). Chronic continuation of this process results in increased lipid storage in WAT and can result in leaking of free fatty acids (FFA) where it is up taken by other tissues such as the liver and muscle and stored as TAG (demonstrated in green) (A). This leaking from WAT (B) results in unhealthy lipid storage in these non-specialised tissues as lipid droplets (C). Lipid droplets are organelles comprised of a phospholipid monolayer with integrated proteins from the Endoplasmic Reticulum (ER) (Class I proteins) and recruited proteins from the cytosol (Class II proteins) to aid in maintaining tension to safely contain neutral lipids. Continued overflow into these tissues results in disease progression such as Hepatic Steatosis (D) where fat accumulation results in inflammation and consequently fibrosis and scarring of the tissue occurs leading to irreversible damage. Glucose homeostasis diagram was created in BioRender whilst lipid droplet composition (C) was adapted from (Olzmann & Carvalho, 2019).

The Interplay of Adipocytes and Mitochondria in Metabolism

Adipogenesis store glucose as lipids for times in which energy reserves are required. Lipolysis in adipocytes is the process by which these stored triacylglycerols (TAGs) are broken down into free fatty acids (FFAs) and glycerol (Duncan et al., 2007; Grabner et al., 2021; Lass et al., 2011; Yang & Mottillo, 2020), which are then utilised by mitochondria in the adipocyte for ATP production (Houten et al., 2016) or are released from the adipocyte into the bloodstream to be used by other tissues (Jensen, 2006). Lipolysis is facilitated by enzymes known as lipases which catalyse the hydrolysis of the stored TAG (Lass et al., 2011). Firstly, TAG is hydrolysed into diacylglycerols (DAGs) by adipose triglyceride lipase (ATGL) and then monoacylglycerols via hormone-sensitive lipase (HSL) and finally into glycerol and FFA through monoglyceride lipase (MGL) (Lass et al., 2011) (Figure 1. 6). Mitochondria use these now readily available FFAs to generate ATP for energy through β -oxidation (Bartlett & Eaton, 2004). Due to their size, FFAs transportation across the mitochondrial membrane is facilitated by the carnitine palmitoyltransferase I (CPT1A), the rate-limiting enzyme for fatty acid oxidation (Bartlett & Eaton, 2004). Once across the membrane, FFAs are degraded into Acetyl-CoA, which feeds into The Citric Acid Cycle (TCA) where the production of reducing equivalents NADH and FADH_2 facilitate electron transfer in the electron transport chain (ETC) (Martínez-Reyes & Chandel, 2020). The ETC generates a proton gradient across the mitochondrial membrane and produces ATP for energy use by the cell and body (Martínez-Reyes & Chandel, 2020) (Figure 1. 6).

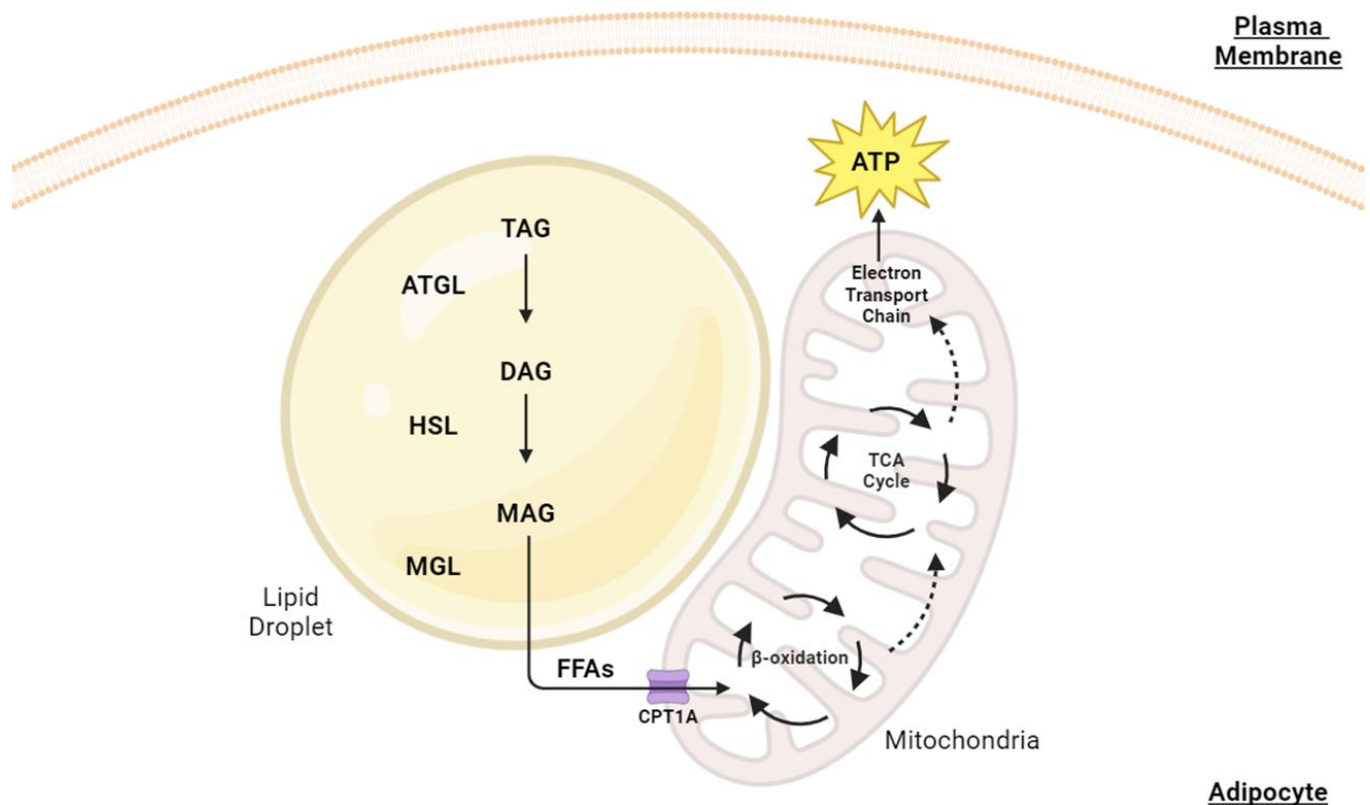


Figure 1. 6. The Interplay Between Lipid and Mitochondria for Energy Production

To provide energy for the body, lipids stored as triacylglycerols (TAG) are broken down into free fatty acids (FFAs) and glycerol, which FFAs are then utilised by mitochondria in the adipocyte for ATP production. TAG is hydrolysed into diacylglycerols (DAG) by adipose triglyceride lipase (ATGL) and then monacylglycerols (MAG) via hormone-sensitive lipase (HSL) and finally into glycerol and FFA through monoglyceride lipase (MGL). FFAs transport into the mitochondria is facilitated by carnitine palmitoyltransferase I (CPT1A) where they undergo a series of β -oxidation cycles and resulting Acetyl-CoA feeds into The Citric Acid Cycle (TCA). The resulting reducing equivalents of NADH and FADH₂ facilitate the transfer of electrons for the Electron Transport Train and ATP is produced by the mitochondria. Figure was made using BioRender.

The striking phenotypes of cachexia are muscle atrophy and weight loss (Porporato, 2016). Our focus is on weight loss that occurs during this disease and specifically the fate of the adipose tissue. We have introduced WAT and BAT and their different metabolic capacities and functions in **1.2 Adipocyte Biology and Their Role in Metabolism** and introduced the process of beiging of WAT in **1.3 Zinc Alpha 2-Glycoprotein**. Adipose browning has gained significant attention in metabolic research with its potential in being a therapeutic strategy for obesity (McNeill et al., 2021; Peres Valgas Da Silva et al., 2019; Xu et al., 2019). This has been prominently studied within the context of cold exposure therapy where the use of approaches such as ice baths have been popularized for their positive effects on body and even mental health (Peres Valgas Da Silva et al., 2019).

Cold Exposure and Sympathetic Nervous System Activation

Cold exposure triggers a decrease in the body's basal temperature, activating the sympathetic nervous system (SNS) to initiate thermogenic processes to maintain core temperature (Tabuchi & Sul, 2021). The SNS releases norepinephrine (NE) from sympathetic nerve endings onto adipose tissues, where it binds to β_3 -adrenergic receptors on the surface of white and brown adipocytes (Tabuchi & Sul, 2021). Upon activation of β_3 -adrenergic receptors, adenylyl cyclase is stimulated, resulting in increased production of cyclic adenosine monophosphate (cAMP) which in turn activates protein kinase A (PKA) and initiates the activation of thermogenic gene regulators and metabolic processes within adipocytes (Tabuchi & Sul, 2021). PPAR γ Coactivator 1-alpha (PGC-1 α) is a transcriptional coactivator that enhances the expression of genes responsible for mitochondrial biogenesis and oxidative metabolism and is prominently induced through cold exposure (Liang & Ward, 2006). PGC-1 α activates nuclear respiratory factors 1 and 2 (NRF1, NRF2) and mitochondrial transcription factor A (TFAM) alongside the co-factor PR domain-containing 16 (PRDM16) leading to gene expression of critical

thermogenesis genes such as the peroxisome proliferator-activated receptor (PPAR γ) (Liang & Ward, 2006). The translational changes initiated through cold exposure promote the transition of white adipocytes into beige adipocytes through browning resulting in a key shift of adipose metabolic activity (Rosell et al., 2014) (Figure 1. 7). These beige adipocytes now resemble brown adipocytes in their energy demands, steering away from energy storage of white adipocytes. A key component of this translation change is the expression of a mitochondrial carrier protein called uncoupling protein 1 (UCP-1) (Nedergaard et al., 2001). As covered in ***1.2 Adipocyte Biology and Their Role in Metabolism***, brown adipocytes produce heat through thermogenesis and UCP-1 is a hallmark protein in this process. As shown in Figure 1. 6, mitochondria use FFAs for energy production. However, the expression of UCP-1 disrupts the proton gradient created during oxidative phosphorylation, and instead of mitochondria utilising FFAs available for ATP production, it results in heat production through non-shivering thermogenesis (Tabuchi & Sul, 2021) (Figure 1. 7). This is a key distinction between white and brown adipose tissue (Rosell et al., 2014). To maintain core temperature, mitochondrial biogenesis occurs to provide increased numbers of mitochondria to generate more heat (Tabuchi & Sul, 2021). This results in greater levels of lipolysis to provide mitochondria with FFAs and to match these energy demands, beige adipocytes uptake greater concentrations of glucose and fatty acids to accommodate this (Tabuchi & Sul, 2021). This transformation in the bodies metabolic activity to burn lipid storage has enticed researchers to advocate this as a weight loss therapy (Maassen et al., 2007; McNeill et al., 2021; Peres Valgas Da Silva et al., 2019).

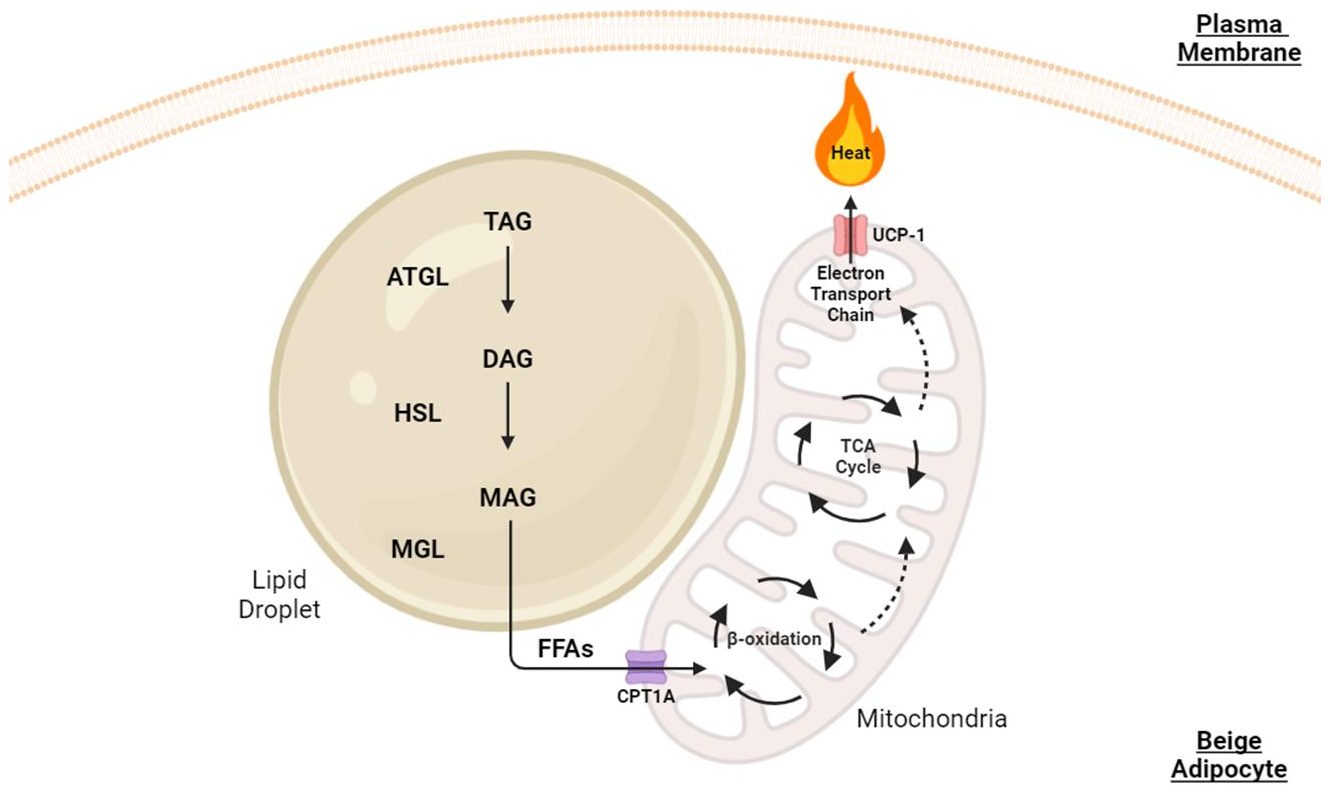
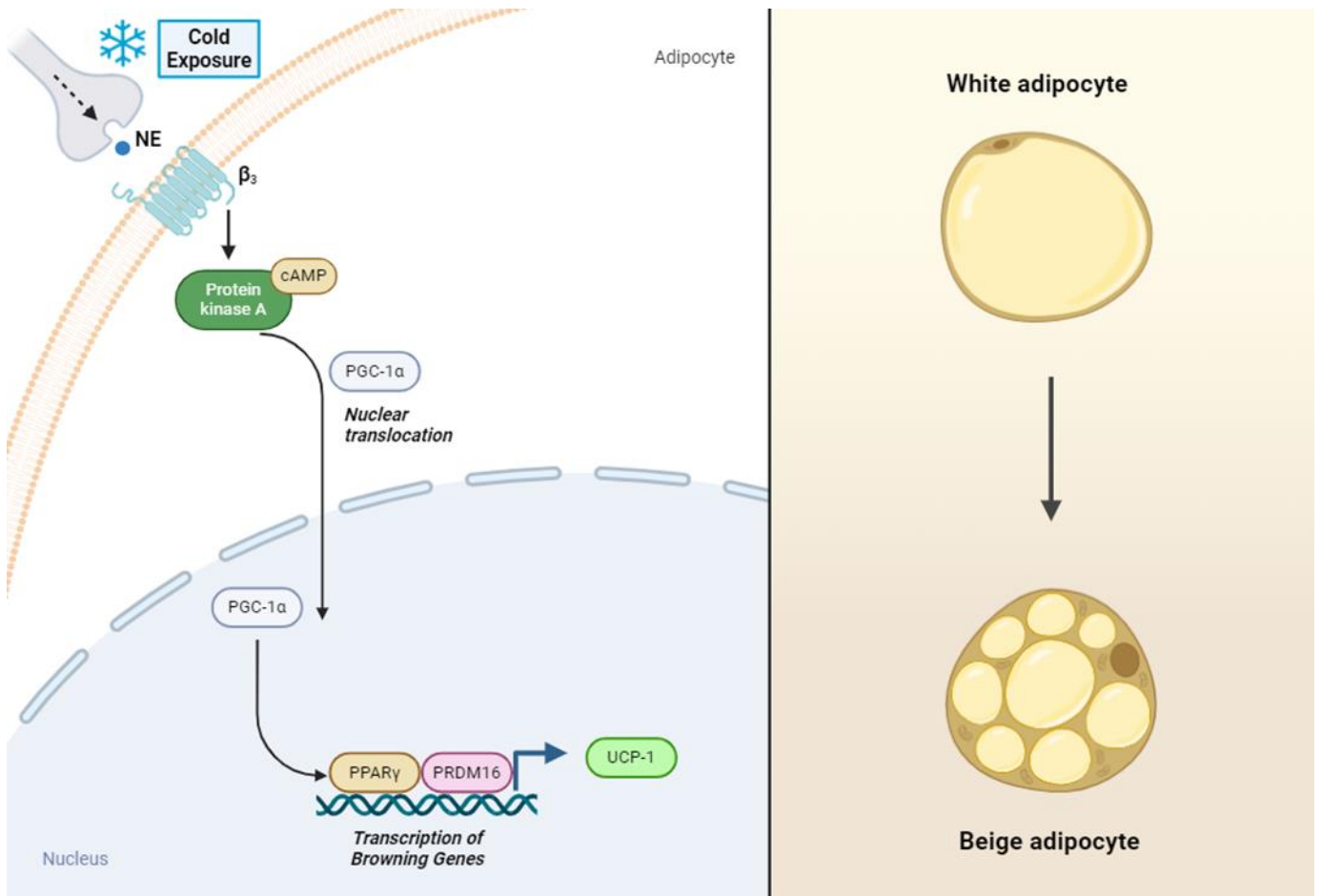


Figure 1. 7. Exposure to Cold Results in Adipocyte and Mitochondria Remodelling

When temperatures drop, the sympathetic nervous system (SNS) initiates a thermogenic response to maintain core temperatures. The SNS releases norepinephrine (NE) from sympathetic nerve endings where it binds to β_3 -adrenergic receptors on the surface of white adipocytes. A downstream signalling cascade is initiated with adenylyl cyclase resulting in increased production of cyclic adenosine monophosphate (cAMP), which in turn activates protein kinase A (PKA) and initiates the activation of adipose browning gene expression peroxisome proliferator-activated receptor (PPAR γ). This is regulated through PPAR γ Coactivator 1-alpha (PGC-1 α), nuclear respiratory factors 1 and 2 (NRF1, NRF2), mitochondrial transcription factor A (TFAM) and PR domain-containing 16 (PRDM16), resulting in the expression of uncoupling protein 1 (UCP-1) and starts adipose browning (top panel). The expression of UCP-1 results in the metabolic change of the mitochondria with them now producing heat via thermogenesis instead of ATP production (bottom panel). Figures were made using BioRender.

1.3 Zinc Alpha 2-Glycoprotein

Introduction to ZAG Biology

Zinc α 2-glycoprotein (ZAG) - previously called Lipid Mobilizing Factor (LMF) - is a ~40-kDa single-chain polypeptide that was originally isolated from human plasma (Burgi and Schmid, 1961) and is the product of the *AZGP1* (Gene ID: 563). Previous studies have shown that ZAG is synthesised by epithelial cells of the liver and prostate, as well as WAT and BAT (Bundred et al., 1987). ZAG is secreted from these cells and ZAG protein is found in blood and other body fluids such as cerebrospinal fluid, milk and sweat (Bundred et al., 1987). ZAG contributes to the regulation of weight and body fat through lipid and glucose metabolism (M. Liu et al., 2018). In healthy individuals, ZAG is involved in lipolysis of adipose tissue, resulting in reduced fat storage and overall weight (Hirai et al., 1998). However, in obese individuals ZAG levels are decreased, and therefore the rate of lipolysis is decreased (Mracek et al., 2010). The decline in expression of ZAG has also been viewed to contribute to insulin resistance, implying that reduced ZAG levels could contribute to obesity and Type 2 Diabetes or these diseases downregulate ZAG production (Mracek et al., 2010). These claims are supported by studies overexpressing ZAG and as a result, an increase in insulin sensitivity and glucose tolerance was observed together with decreased fasting glucose levels.

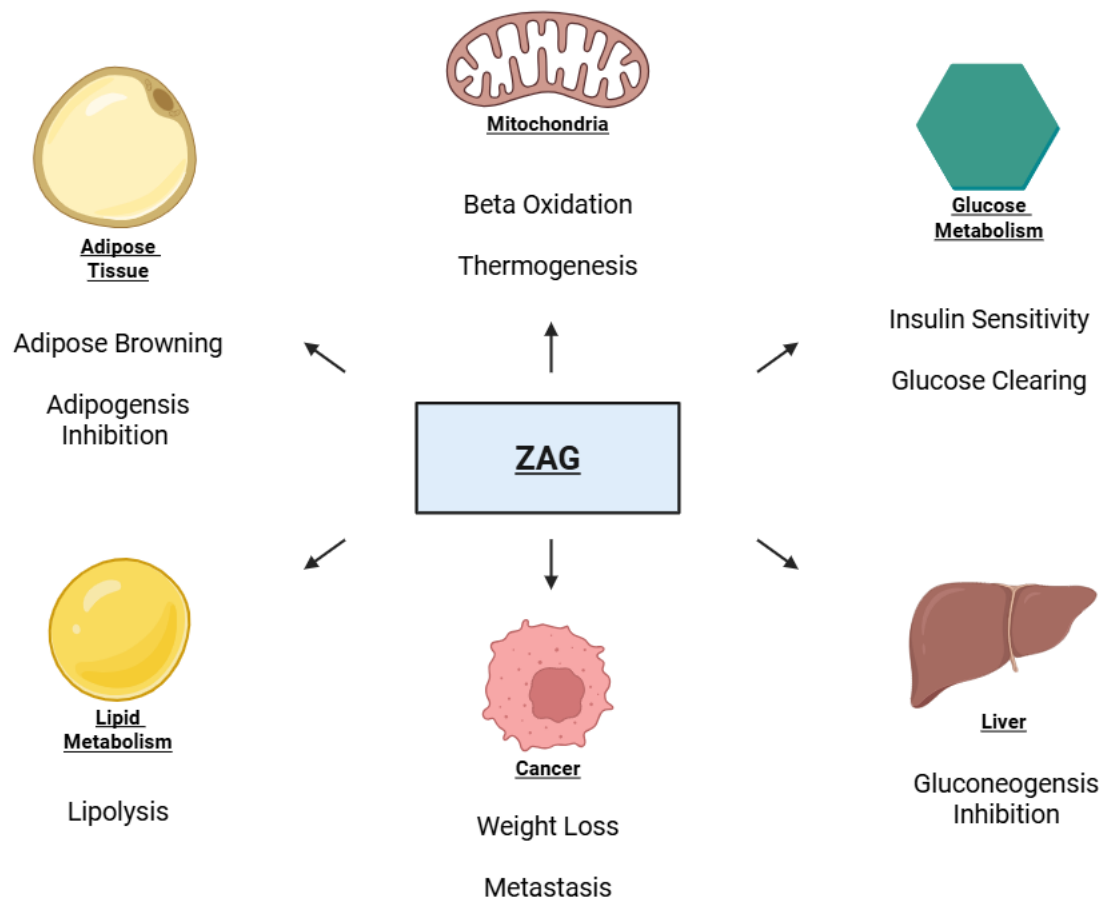


Figure 1. 8. An Overview of ZAGs Metabolic Activity

ZAG has a myriad of metabolic effects throughout the body. It is involved in driving beta oxidation in mitochondria for catabolism of free fatty acids, using these as a source for heat generation through thermogenesis. It plays a role in glucose homeostasis by driving insulin dependent glucose clearing from the blood. It dysregulates glucose production in the liver from non-carbohydrate sources. ZAG is seen to drive weight loss in cancer patients - known as cachexia - and its role in cell adhesion promotes cell migration and invasion in tumours. It is involved in lipid metabolism by stimulating lipolysis in lipid droplets. It has a prominent role in driving adipose browning to divert adipose tissue from storage to energy production and it inhibits the generation of new adipocytes. Figure was made using BioRender.

ZAG in Lipid Metabolism

It is reported that ZAG mediates its lipolytic effect of adipose tissue through the same mechanisms as described above in Figure 1. 6 by initiating β_3 -adrenergic receptor activation and downstream signalling events of cAMP and PKA activation (Hirai et al., 1998) (Bing et al., 2010). This results in the translocation of HSL to lipid droplets by phosphorylation (Russell & Tisdale, 2011b). The same metabolic pathway to break down triacylglycerides into FFA through enzymatic steps of ATGL, HSL and MGL are observed and results in an upregulated FFA and glycerol into the blood circulation to serve as fuel for the body (Banaszak et al., 2021; Mracek et al., 2011). ZAG drives the oxidation of these FFA by increasing mitochondrial β -oxidation, further enhancing energy expenditure (Russell & Tisdale, 2011a). By upregulating CPT1A, these fatty acids can be transported across the mitochondrial membrane into the cytoplasm and undergo catabolism as shown in Figure 1. 7. Furthermore, ZAG stimulates the expression of UCP-1 in adipose tissue and results in catabolised FFA to be ultimately released for heat expenditure instead of ATP production and again results in increased energy expenditure (Elattar et al., 2018; Sanders & Tisdale, 2004).

As well as promoting lipolysis, ZAG is seen impeding the differentiation steps of progenitor adipocyte cells into mature adipocytes (Gong et al., 2009; Mracek et al., 2010). This is achieved in part by downregulating the adipogenesis regulator PPAR γ and lipogenic enzyme fatty acid synthase (FAS), preventing lipid droplet formation (Gong et al., 2009). This inhibits the body to lay down new adipose tissue and further prevents storage capacity for incoming glucose in the diet and therefore stopping weight gain.

ZAG in Glucose Metabolism

ZAG expression correlates with increased insulin sensitivity in adipose tissue (Gao et al., 2018). In adipocytes, ZAG regulates steps in the phosphoinositide 3-kinase/protein kinase B

(PI3K/Akt) pathway which facilitates the translocation of GLUT4 to the plasma membrane for insulin mediated glucose internalisation into the adipocyte (Figure 1. 1) (Russell & Tisdale, 2012). ZAG enhances insulin sensitivity by upregulating insulin receptor substrate 1 (IRS1) expression and increasing Akt phosphorylation, stimulating this glucose intake mechanism and enhancing glucose metabolism (Faulconnier et al., 2019). In turn, GLUT4 expression is also upregulated and further stimulating glucose uptake. To support this, overexpression of ZAG in mouse models has been observed to improve glucose tolerance with clearing of glucose from the blood and improving results in the Homeostatic Model Assessment of Insulin Resistance (HOMA-IR) (Gong et al., 2009). A method used to assess insulin resistance from fasting blood glucose levels.

In the liver, ZAG interferes with gluconeogenesis by downregulating gluconeogenic enzymes such as phosphoenolpyruvate carboxykinase (PEPCK) and glucose-6-phosphatase (G6Pase) (M. Liu et al., 2018). These enzymes are involved in the *de novo* production of glucose which help regulate glucose blood levels and the decreased availability results in fewer energy sources present for organs such as brain and kidneys impairing function (Wang & Dong, 2019).

Its role in metabolism has also been investigating in the brain by overexpression in proopiomelanocortin (POMC) neurons (Qiu et al., 2024). These neurons are involved in regulating metabolism by suppressing food intake and body weight gain and disruption in function of these neurons lead to dysregulation in energy metabolism (Sohn, 2015). Overexpression of ZAG in these neurons promoted leptin-mediated neuron excitation and increased energy expenditure in obese mice. ZAG knock out models are observed to inhibit leptin signalling with the absence of ZAG allowing the ubiquitination degradation of acylglycerol kinase (AGK) and preventing leptin to initiate satiety (Qiu et al., 2024).

ZAG and Diabetes/Insulin Resistance

With ZAGs metabolic involvement outlined above, the dysregulation of this protein has been observed to contribute to disease progression. In particular, its involvement in glucose homeostasis has brought focus to its involvement in Diabetes and insulin resistance. Absence of ZAG results in observed upregulated glucose blood levels and susceptibility in weight gain in mice fed high fat diets (Gao et al., 2018). Furthermore, decreased ZAG levels increase insulin resistance with treatment of ZAG stimulating glucose utilization and lipolysis of adipose tissue (Gao et al., 2018). The HOMA-IR results with ZAG treatment mention above also support this glucose clearing affect (Gong et al., 2009). As obesity is common with Diabetes, it has been observed that ZAG is downregulated with adipose expansion, specifically hypertrophy (Mracek et al., 2010). As discussed above and illustrated in Figure 1. 3, hypertrophy of existing adipocytes results in metabolic disease and ZAG downregulation could contribute to this.

Taking this together, ZAGs involvement in a myriad of metabolic mechanisms has identified it as a potential biomarker in T2D prognosis. Its involvement in lipolysis, inhibition of lipid storage production, catabolism of FFA, blood glucose homeostasis and gluconeogenesis supports this. The downregulation of ZAG contributes to factors that drive insulin resistance and T2D.

ZAG in Cancer and Cachexia

ZAG is upregulated in various carcinomas (Fan et al., 2020). Cancer patients with upregulated ZAG are observed to lose weight rapidly and unable to attenuate this weight loss through diet (Mracek et al., 2011). This suggests a complex relationship between ZAG, body adipose levels and muscle cachexia, this thesis attempts to unravel elements of this relationship.

Cachexia is a metabolic disease that results in drastic weight loss and muscle wasting and is tightly associated with cancer (Porporato, 2016). The incidence of cachexia is different depending on the tumour type. Eighty percent of patients who suffer from pancreatic or gastric cancer will have some degree of cachexia whilst 40% of breast cancer patients will suffer (Fearon et al., 2012). Twenty percent of total cancer patients will die due to cachexia-related complications (Porporato, 2016). Cachexia results in the patient becoming weak and frail. Unlike a disease such as anorexia, cachexia cannot be directly regulated through diet alone (Melstrom et al., 2007). The inclusion of a balanced diet is imperative, but it does not attenuate the lean skeletal muscle protein that is lost during cachexia. The underlying complication is excess lipolysis and decreased levels of fat storage. Cachexia affects numerous areas around the body. It results in muscle atrophy and dysfunction in the heart (Johns et al., 2013) which ultimately leads to reduced contraction and decreased heart rate, fibrosis of the heart and ultimately death (Houten and Reilley, 1980; Kalantar-Zadeh et al., 2013). Due to the nature of the disease, patients are also less likely to have successful treatment for cancer. The frailties that are a result of cachexia limit the levels of chemotherapy and radiotherapy due to the toxic nature of the treatments and the weakness of the patient (Fearon and Baracos, 2010; Vaughan et al., 2013). So, it is not only a debilitating disease resulting in poor health, it is also interfering with the appropriate types of treatments that can be used.

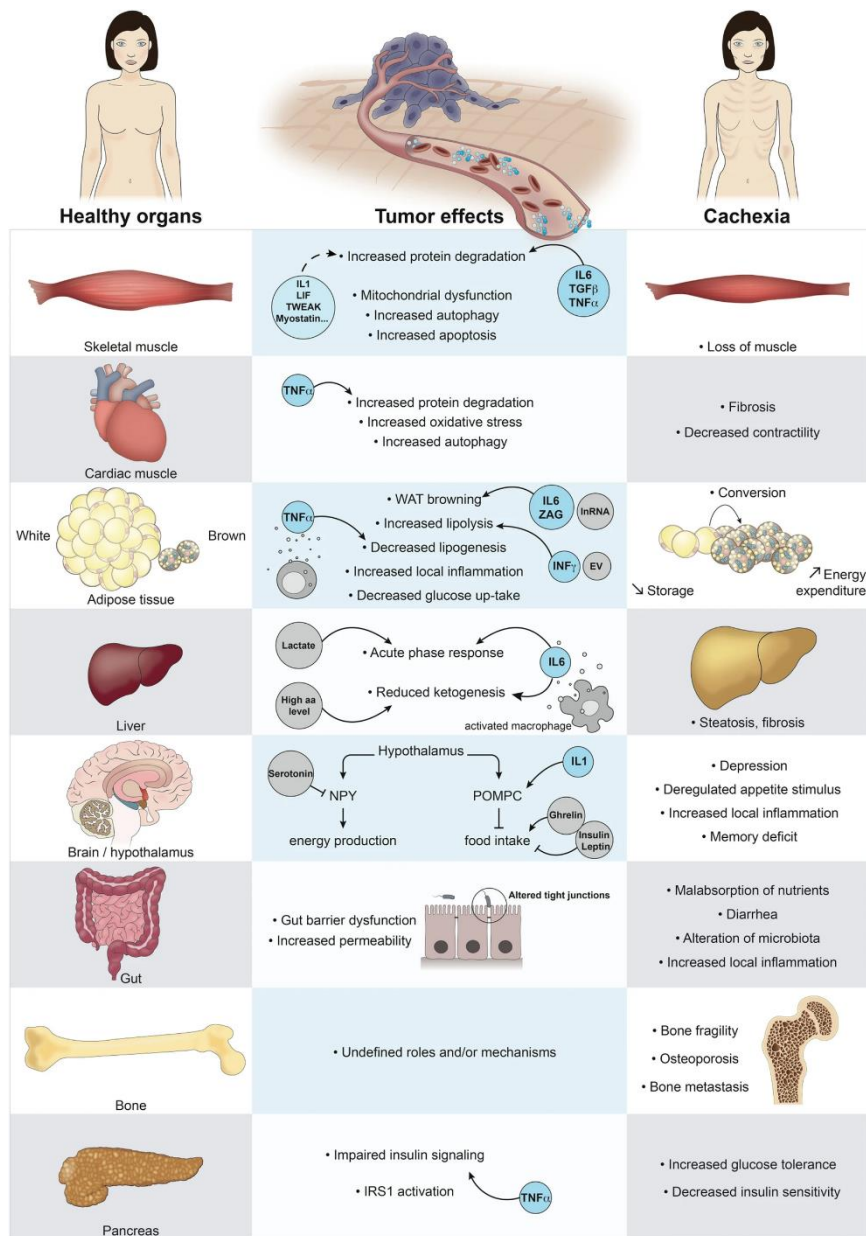


Figure 1. 9. A Whole Body Cachexia Overview

Cachexia within a patient results in a myriad of organ and tissue dysfunctions which accumulate in patients undergoing significant weight loss that cannot be attenuated by diet alone. Skeletal muscle atrophy occurs due to increased protein degradation from Interleukin-1 (IL1), Leukaemia Inhibitory Factor (LIF) and TNF-like weak inducer of apoptosis (TWEAK) overexpression. Cardiac muscle fibrosis is observed due to Tumour Necrosis Factor-alpha (TNFα). Liver steatosis is associated with overexpression of Interleukin-6 (IL6), resulting in fat accumulation. IL1 is also involved in satiation by suppressing the hunger hormone Ghrelin, resulting in decreased nutrient intake. TNFα also impairs

insulin signalling by impacting Insulin Receptor Substrate 1 (IRS1), resulting in insulin resistance and improper glucose clearing in the blood. The focus of this study is the symptom of white adipose tissue (WAT) browning. Continued tumour release of an adipokine such as Zinc α 2-glycoprotein (ZAG) results in a conversion of WAT to brown adipose tissue (BAT) which increases energy expenditure. This results in a net loss of energy for the patient leading to an unregulated weight loss associated with this disease. This image has been taken from (Di Girolamo & Tajbakhsh, 2022).

ZAG levels are elevated in patients with epidermal carcinomas such as breast (Sánchez et al., 1992), prostate (Henshall et al., 2006), and cervical (Abdul-Rahman et al., 2007). The role in which ZAG contributes to regulating weight is shifted. ZAG is secreted as a cytokine from tumours and the elevated levels now contribute to increased weight loss (Bing et al., 2004).

Mouse models that were implanted with ZAG expressing HEK239 cells resulted in no overall weight change; lean muscle mass did not decrease but ZAG-expressing mice exhibit a loss of both epidermal WAT and total body fat mass in comparison with control mice (Elattar et al., 2018). The adipose loss observed was a result of WAT atrophy which led to elevated levels of circulating free fatty acids (FFA) (Elattar et al., 2018). Furthermore, WAT presented with a BAT-like morphology, suggesting that ZAG influenced WAT progenitors into BAT (Fan et al., 2020). Therefore, it was postulated that elevated levels of ZAG resulted in increased WAT lipolysis and browning of WAT. BAT have a smaller capacity to store lipids and have increased levels of mitochondria (Fenzl & Kiefer, 2014). BAT have an energy expending phenotype where they upregulate lipolysis. This results in increased levels of free fatty acids (FFA). Browning of WAT has been shown to be an effect of β_3 AR agonist treatments (Collins and Surwit, 2001). Browning works through β_3 AR (Russell et al., 2002) acting via the Protein Kinase A (PKA) pathway (Hirai et al., 1998).

The increased levels of mitochondria in BAT drive thermogenesis, where the mitochondria generate heat (Collins and Surwit, 2001) generating further energy expenditure. BAT mitochondria express uncoupling proteins (UCP) which result in oxidation of the FFA that have become available via ZAG treatment. This contributes to decreased levels of FFA available for storage and results in further energy expenditure and weight loss (Petruzzelli et al., 2014). WAT atrophy resulting in decreased energy storage, browning of WAT resulting in decreased numbers of lipid storing fat and increasing energy releasing fat, elevated levels of

BAT resulting in upregulated thermogenesis, and elevated UCP all contribute to severe weight loss in afflicted individuals.

Mice inoculated with MAC16 tumours (cachexia tumour model) exhibited elevated ZAG gene expression in WAT, BAT and liver in comparison to control models (Bing et al., 2004). In relation to weight, ZAG protein levels increased in adipose tissue (WAT and BAT) when mice lost weight.

Mouse models expressing elevated levels of ZAG expressed elevated levels of mRNA expression of genes related to cachexia, UCP-1 for thermogenesis activity, Cox8 for identifying mitochondrial respiration and Tbx1 for beige adipose tissue detection (Fan et al., 2020). Elevated ZAG levels also upregulated β_3 AR stimulation which also resulted in increased mRNA expression of the same cachexia related genes.

In C57BL/6J mice models ZAG protein levels are low in WAT but strongly expressed in BAT (Elattar et al., 2018), providing further evidence of increased ZAG expression in mice models. A hallmark of cachexia is the shift of white adipose tissue (WAT) to brown adipose tissue (BAT) (Evans et al., 2008). In healthy individuals, adipose tissue is used for the storage of excess energy whilst brown adipose tissue is to generate heat and to generate energy through lipolysis (Luo & Liu, 2016). In cachexia, patients are seen with disproportionate levels of BAT in comparison to WAT (Costa and Holland, 1962; Tisdale, 1999). The white 'beiges' and now no longer stores energy but releases it contributing to the struggle of weight gain seen in patients (Das et al., 2011; Kir et al., 2014). BAT also undergoes thermogenesis and this excess heat loss also results in greater energy expenditure due to the upregulated levels of BAT. A characteristic of BAT is they have a greater number of mitochondria in comparison to white (Petruzzelli et al., 2014). These mitochondria use the free fatty acids generated by lipolysis from BAT via oxidation resulting in further energy expenditure (Petruzzelli et al., 2014). The beiging of the WAT transitions the host into a state of energy expending mechanisms that are

chronically increased due to the nature of the disease and seem difficult to attenuate due to the progressive nature (Petruzzelli et al., 2014).

Other Actions of ZAG

The focus of this work is steered towards ZAGs metabolic involvements revolving around glucose homeostasis, lipolysis and adipose browning. Although not in the scope of this work, other effects of ZAG deserve a brief mention. For example, downregulation of ZAG expression has shown to destabilise cell adhesion and enhance migration and invasion of cells observed in soft tissue sarcoma samples worsening disease progression and prognosis (J. Liu et al., 2018). In another study, ZAG downregulation results in an increased angiogenesis capacity of prostate cancer, increasing its ability to proliferate (Wen et al., 2024).

Other studies have detected increased levels of ZAG in infant's saliva with MALDI-TOF mass spectrometry, with increased concentrations resulting in susceptibility to a bitter taste (Morzel et al., 2014). Lastly it appears to have a role in epilepsy, with overexpression suppressing seizures induced by inflammatory factors such as $\text{TNF}\alpha$ (X. Wei et al., 2019).

ZAG Structural Biology

ZAG is synthesised as a 295-amino acid-long immature polypeptide (Araki et al., 1988). Mature ZAG is comprised of three alpha helical domains (α_1 , α_2 and α_3) and two beta sheet domains (β_1 and β_2) (Sánchez et al., 1997). ZAG was initially crystallised in 1999 (Sánchez et al., 1999) and the structure is shown in Figure 1. 10. . This similarity with MHC class proteins has focussed attention on the α_1 and α_2 helices which form a groove, which in MHC-I proteins has been identified as a peptide binding site (Delker et al., 2004). This peptide binding site in MHC-I results in the restricted recognition by T-cell receptors (TCR) and therefore, the binding of this ligand is imperative to the interaction between MHC-I and TCR (Adams & Luoma,

2013). By analogy with MHC-1, the ligand binding in MHC-1-like groove may be crucial in ZAG function; presently, the identity of the ligand is unknown and therefore identifying this ligand could provide significant therapeutic benefit. This is one of the aims of this thesis.

The crystallised ZAG (Protein Data Bank ID – 1t7v) contains an exogenous ligand bound in this pocket; Hexaethylene Glycol (P6G). P6G is a hydrophobic ligand and is encompassed by hydrophobic residues within the groove (Figure 1. 11). This hydrophobic groove is a key characteristic to ZAG and provides evidence of ZAG's capacity to bind peptides or hydrophobic ligand which could affect activity. In particular fatty acids have been posited to bind within this groove (Lau et al., 2019).

More recent work (Kennedy et al., 2001) has examined the structure of ZAG in complex with the fluorescent ligand 11-(dansylamino)undecanoic acid (DAUDA) which is thought to bind to the groove between the $\alpha 1$ and $\alpha 2$ domains. DAUDA was constructed using a fatty acid backbone to provide evidence of the proposed fatty acid binding. DAUDA was shown to emit a fluorescence signal when incorporated with ZAG, providing evidence for binding. Other fatty acids were also incorporated in the assays which resulted in decreased fluorescence due to the displacement of DAUDA. These include arachidonic, linoleic and linolenic acids, which exhibit competitive binding with DAUDA and provided evidence for the binding of multiple fatty acids in the groove of ZAG (Kennedy et al., 2001) In these experiments they identified a 192 kDa crystallographic assembly unit with six ZAG molecules and 8 fatty acid molecules, and identified a key residue, Arg⁷³ hydrogen bonding to the fatty acid in the groove. Importantly, their work using recombinant purified ZAG suggests that ZAG is a monomer in the absence of DAUDA but forms a tetramer in the presence of the ligand (Kennedy et al., 2001).

Mutation of the Arg⁷³ results in various effects on the ability of ligand binding in the pocket. One effect was the closing of the groove (McDermott et al., 2006). The same closing is

observed in the groove of the MHC-I class protein with a homologous mutation (Bennett et al., 2000; Burmeister et al., 1994), providing compelling evidence for similar binding mechanisms between the two proteins. Arg⁷³Lys appeared to disrupt ligand binding, affecting anchoring of the ligand into the groove residue (McDermott et al., 2006). The P6G ligand exhibits strong interactions with the Arg⁷³ residue and supports this hypothesis (Figure 1. 11) .

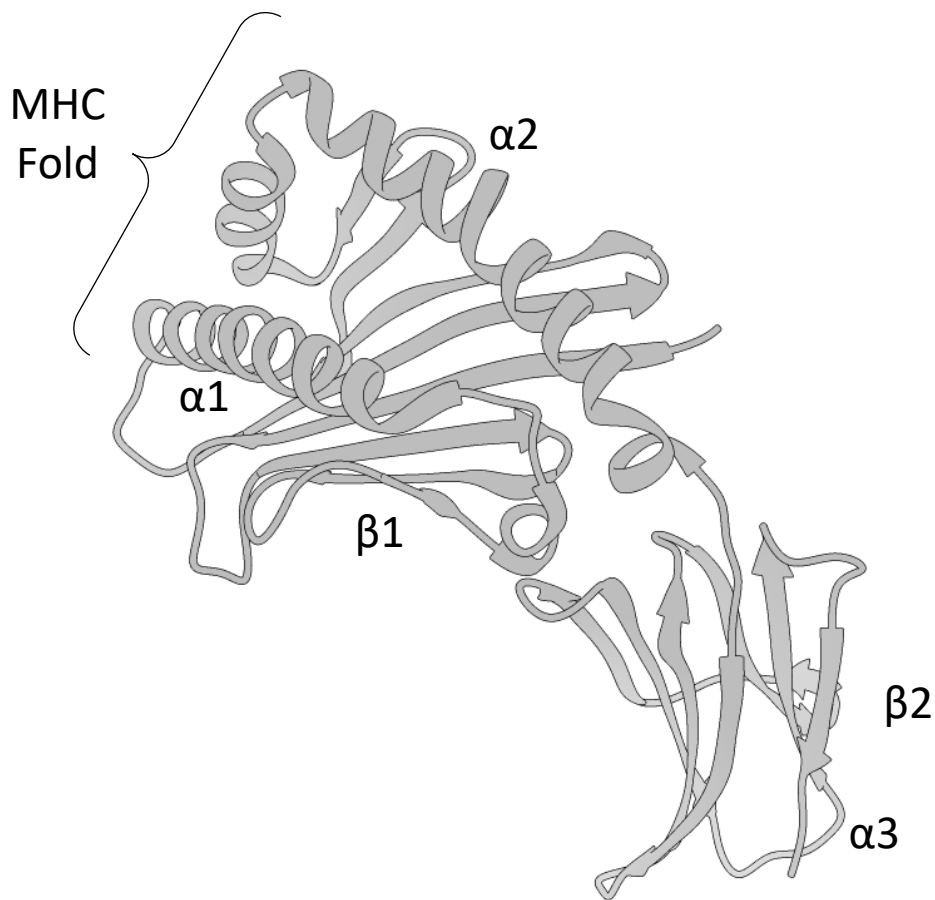


Figure 1. 10. Crystal Structure of Zinc Alpha-2 Glycoprotein (ZAG)

Shown is the structure of human ZAG purified from serum and crystallised as outlined (Burgi and Schmid, 1961). The protein is comprised of three alpha subunits ($\alpha 1$, $\alpha 2$ and $\alpha 3$) and two beta subunits ($\beta 1$ and $\beta 2$) with the protein presenting a Major Histocompatibility Complex (MHC) fold between the $\alpha 1$ and $\alpha 2$ subunits. The structure was solved to 1.95 Angstrom resolution and shown is the ribbon structure obtained from the PDB database at <https://www.rcsb.org/structure/1T7V>.

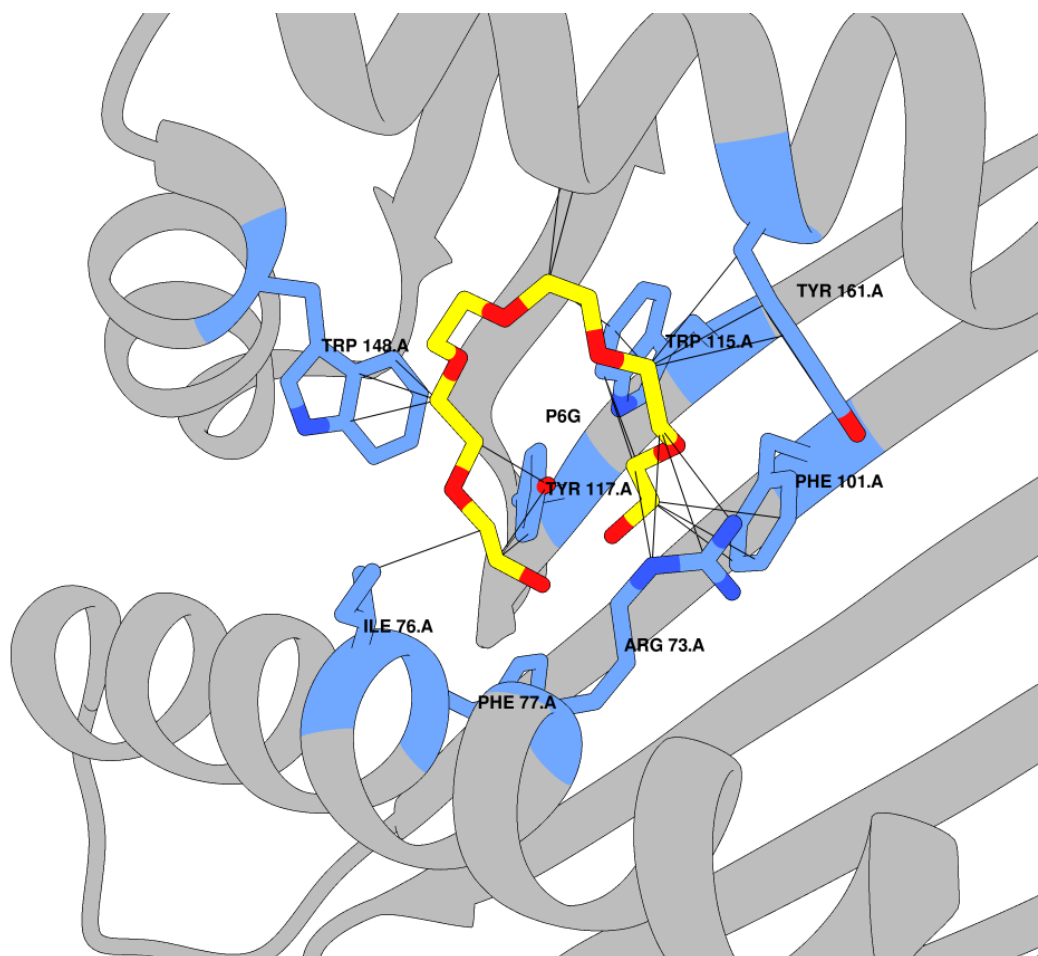


Figure 1. 11. Crystal Structure of Zinc Alpha-2 Glycoprotein (ZAG) with native ligand Hexaethylene Glycol (P6G)

Shown is the structure of human ZAG purified from serum and crystallised as outlined (Burgi and Schmid, 1961). The structure was solved to 1.95 Angstrom resolution and is in the PDB database at <https://www.rcsb.org/structure/1T7V>. Residue and ligand interactions were visualised using UCSF Chimera.

But What is the True Ligand?

A predicament arises however with the unknown identity of the ligand. MHC-I proteins have shown to bind various ligands that alter the biological function (Germain, 1994). With ZAG's close relation to MHC-I, it is possible that ZAG could bind an unknown number of ligands, which like MHC-I would then result in different biological function depending on which ligand is bound. Previous studies mentioned above (Kennedy et al., 2001) show the binding of these fatty acids. With this additional evidence, some focus can be shifted to other residues within the groove. There is a cluster of aromatic residues that also show strong interactions between the crystallised P6G ligand. Tryptophan¹⁴⁸, Tyrosine¹¹⁷ and Phenylalanine¹⁰¹ residues are on the inside of the groove and at the opposite end of the Arg⁷³. With the idea of the Arg⁷³ being the anchor, these other residues could be involved in holding the ligand in the required conformation for ZAG activity.

What does ZAG bind to?

The binding of this ligand could result in conformational change that would allow binding to a putative ZAG receptor. It is unclear through what receptor ZAG exhibits its effect in cachexia, but it has been proposed to function through β -adrenergic receptors in adipocytes (Russell et al., 2002; Russell and Tisdale, 2012). ZAG is a protein that is released from tumours and contributes to the high degree of adipose tissue loss in cachexia (Hirai et al., 1998). ZAG's lipolytic effect is thought to be mediated through the cAMP pathway by β_3 -adrenergic activation. There are 3 isoforms of β -adrenergics (1, 2 and 3). They are G-protein coupled receptors known to be important in thermogenesis and lipolysis in adipocytes (Collins & Surwit, 2001). All three receptor subtypes are found in both WAT and BAT. By binding to the β_3 -adrenergic receptor, lipolysis is promoted by activation of adenylate cyclase (Russell et al., 2002).

ZAG has recently been shown to be a novel binding partner to amine oxidase copper-containing 3 (AOC3) (Romauch, 2020). By utilising cross-linking and co-immunoprecipitation experiments, it was identified that ZAG binds to AOC3 allosterically, resulting in conformational change of the enzyme and inhibits its activity. AOC3 is an enzyme located on the cell surface and is strongly expressed in adipocytes (Romauch, 2020). AOC3 is known to catalyse the oxidative deamination of primary amines resulting in production of hydrogen peroxide, ammonia and aldehydes. The inhibition of AOC3 via ZAG prevents it catalysing the removal of amino groups from lipolytic hormones, and therefore promotes lipolysis. AOC3 inhibition also results in fibrosis and ZAG deficiency leads to fibrosis (Romauch, 2020). This study provides insight to another method of action in which ZAG stimulates lipolysis.

In MHC-I, different ligand pairings result in specific T cell receptor interactions (Germain, 1994). With increasing evidence in the literature that there is a possibility of ZAG interacting with different receptors and proteins such as enzymes, specific ligand-ZAG pairings could result in distinct pairings. This meaning a specific ligand may have to bind for ZAG to pair with AOC3 and another for β -adrenergics, possibly resulting in a complex and variable mechanism in which ZAG exerts its biological effects in cachexia. Such studies exemplify the need to understand the nature of the ligand and to attempt to identify how this could modulate biological activity. We will be attempting to identify these ligands with the aid of *in silico* work using UCSF Chimera with collaborators Moleculomics in Swansea.

3.0 Investigating Zinc Alpha 2-Glycoprotein Ligand Binding Through Computational Techniques.

1.4 Aims of the Project

We hypothesise that ZAG plays major roles in regulating adipocyte function and metabolic health. With incidence of obesity at a high rate and the risk of diabetes and cancer increasing with increased weight (Pati et al., 2023), obesity can lead to various conditions of adverse health (Zatterale et al., 2020). Obesity results in increased adipose tissue size, and cancers that are derived from adipose tissues have elevated levels of ZAG which contribute to developing cachexia. These three appear to go hand in hand, and understanding the mechanisms in which ZAG induces cachexia could be of great clinical significance. Hence, our overarching hypothesis is that ZAG plays a major role in adipocyte function. To that end, investigations followed four inter-related avenues.

In Chapter 3, we set out to gain an understanding of the nature of ZAG's ligand binding pocket and to identify important residues which may interact with hydrophobic ligands in the MHC pocket using *in silico* techniques for protein visualization and ligand docking (work initiated during COVID). With these techniques we hoped to identify the endogenous ligand(s) that interact with ZAG and ultimately introduce these into *in vitro* models (**3.0 Investigating Zinc Alpha 2-Glycoprotein Ligand Binding Through Computational Techniques**)

In Chapter 4, we sought to produce recombinant ZAG using bacterial and mammalian expression systems, and to examine the functional properties of recombinant ZAG using cultured 3T3-L1 adipocytes.

Because a major action of ZAG is to influence adipocyte metabolism, we focussed on developing stimulated Raman spectroscopy as a tool to study glucose metabolism. Chapter 5 describes the development of this assay pipeline, and describes experimental work which compares control and hypertrophic adipocytes.

Chapter 6 explores the effect of recombinant ZAG on adipocytes *in vitro* and explores potential effects of ZAG on various signalling systems.

2.0 Materials and Methods

2.1 Materials

2.1.1 List of General Suppliers

General laboratory kits, reagents, and plasticware were obtained from the following suppliers:

- Beckman Coulter, High Wycombe, UK
- BioRad Laboratories, Watford, UK
- Cell Signalling Technology Europe B.V., Leiden, Netherlands
- Fisher Scientific UK, Loughborough, Leicestershire, UK
- Merck UK, Poole, UK
- New England Biolabs, Hitchin, UK
- Stratech Scientific, Ely, UK
- Thermo Fisher Scientific UK, Cheshire, UK

2.1.2 Solutions

The following solutions were made with pure sterile water unless otherwise stated:

2x Yeast Extract Tryptone media (2YT):

1.6% Tryptone (w/v), 1% Yeast extract (w/v) and 0.5% Sodium Chloride (NaCl) (w/v)

Media for Agar Plates:

1.6% Tryptone (w/v), 1% Yeast extract (w/v) 0.5% Sodium Chloride (NaCl) (w/v), 2% agar (w/v), dH₂O and ampicillin (100 µg/ml)

Tris-acetate-EDTA buffer (TAE):

40 mM Tris, 20 mM acetic acid, and 0.4 mM EDTA.

Agarose Gel:

0.8% agarose powder (w/v), TAE buffer

Lysis Buffer for Bacterial Cultures:

50 mM Tris-HCl, pH 8.0, 25% sucrose (w/v), 1 mM EDTA

Detergent Buffer:

0.2 M NaCl, 1% deoxycholic acid (w/v), 1% Nonidet P-40 (v/v), 20 mM Tris-HCl (pH 7.5), 2 mM EDTA

Refolding buffer:

0.1 M Tris-HCl, 2mM EDTA, 0.4 M L-arginine, 0.5 mM oxidised glutathione, 5 mM reduced glutathione

Phosphate buffered saline (PBS):

85 mM NaCl, 1.7 mM KCl, 5 mM Na₂HPO₄, 0.9 mM KH₂PO₄, pH 7.4

Phosphate buffered saline with Tween (PBST):

85 mM NaCl, 1.7 mM KCl, 5mM Na₂HPO₄, 0.9 mM KH₂PO₄, 0.1% (v/v) Tween, pH 7.

Tris buffered saline (TBS):

20 mM Tris, 150 mM NaCl, pH 7.4

Tris buffered saline with Tween (TBST):

20 mM Tris, 150 mM NaCl, 0.1% (v/v) Tween, pH 7.4

Cell lysis buffer:

50 mM Tris-HCl, 50 mM NaF, 1 mM Na₄P₂O₇, 1 mM EGTA, 1 mM EDTA, 1% (v/v) glycerol, 1% (v/v) Triton X-100, 0.5% (v/v) IGEPAL, 1 mM DTT, 1% (v/v) Sigma-Aldrich Phosphatase Inhibitor Cocktail Set II, plus Sigma-Aldrich complete mini EDTA-free protease inhibitor tablet, pH 7.4

SDS-PAGE sample buffer:

Trizma®base (125 mM, pH 6.7), sodium pyrophosphate ($\text{Na}_4\text{P}_2\text{O}_7$) (0.5 mM), EDTA (1.25 mM), sodium dodecyl sulphate (SDS) 0.5% (w/v), glycerol 12.5% (v/v), bromophenol blue sodium salt 0.06% (w/v), and dithiothreitol (DTT) 10 mM

RIPA buffer:

Sodium Chloride (NaCl) (150 mM), EDTA (5 mM), Tris (50 mM, pH 8.0) NP-40 1% (v/v), Sodium Deoxycholate 0.5% (w/v), sodium dodecyl sulphate (SDS) 0.1% (w/v) and dithiothreitol (DTT) 10 mM

Acrylamide resolving gel:

75 mM Tris-HCl pH 8.8, 0.1 % (w/v) SDS, 8 to 12% (v/v) acrylamide, 0.05 % (v/v) ammonium persulfate and 0.01 % (v/v) TEMED

Acrylamide stacking gel:

25 mM Tris-HCl pH 6.8, 0.1 % (w/v) SDS, 4 % (v/v) acrylamide, 0.05 % (v/v) ammonium persulfate and 0.01 % (v/v) TEMED

SDS running buffer:

25 mM Tris, 190 mM glycine, 0.1 % (w/v) SDS

Wet transfer buffer:

25 mM Tris, 190 mM glycine, 20% methanol (v/v)

Ponceau S:

0.2% (w/v) Ponceau S, 1% (v/v) acetic acid

Mitochondria Isolation Buffer:

250 mM sucrose, 5 mM HEPES, 2 mM EGTA, pH 7.2

Mitochondria Isolation Buffer + Bovine Serum Albumin:

250 mM sucrose, 5 mM HEPES, 2 mM EGTA, 1% fatty acid-free BSA, pH 7.2

Quenching buffer

85 mM NaCl, 1.7 mM KCl, 5 mM Na_2HPO_4 , 0.9 mM KH_2PO_4 , 50 mM NH_4Cl , pH 7.4

2.1.3 Bacterial Strains and Eukaryotic Cell Lines

DH5- α and BL21 *E. coli* cells were used for bacterial transformation studies.

3T3-L1 cells (Cat# CRL-173;RRID:CVCL_0123) used in this study are derived from mouse embryonic fibroblasts. HEK293 cells (Cat# CRL-3216 RRID:CVCL_0063) used in this study are derived from the kidney of a human embryo. Both were supplied by American Type Culture Collection (ATCC).

2.1.4 Primary Antibodies

Table 2.1. List of Primary Antibodies

List of primary antibodies used in this project, showing target protein, host species, supplier, supplier catalogue number, Research Resource Identifier (RRID) number where one was available, and dilution factor used for western blotting (WB).

Target	Species	Supplier	Catalogue Number	RRID	Dilution for WB
VDAC1/3	Mouse	Abcam	ab14734	AB_443084	1:1000
β_3 -AR	Rabbit	Abcam	ab94506	AB_10863818	1:1000
UCP1	Rabbit	Abcam	ab209483	AB_2722676	1:5000
PPAR γ	Rabbit	Abcam	ab209350	AB_2890099	1:500
FAS	Rabbit	Cell Signalling Technologies	3180	AB_2100796	1:1000
ACC	Rabbit	Cell Signalling Technologies	3676	AB_2219397	1:1000
GAPDH	Mouse	Ambion	4300	AB_437392	1:80,000

2.1.5 Secondary antibodies

Table 2.2. List of Secondary Antibodies

List of secondary antibodies used in this project, showing antibody name including host and target species, Research Resource Identifier (RRID) number, which technique the antibody was used for, and the dilution factor the antibody was routinely used at.

Antibody	Supplier	RRID	Dilution Factor
IRDye 800CW Goat anti- Mouse IgG	LI-COR Biosciences	AB_621842	1:10,000
IRDye 800CW Goat anti- Rabbit IgG	LI-COR Biosciences	AB_621843	1:10,000
IRDye 680RD Goat anti- Mouse IgG	LI-COR Biosciences	AB_10956588	1:10,000
IRDye® 680RD Goat anti- Rabbit IgG	LI-COR Biosciences	AB_10956166	1:10,000

2.1.6 Plasmids

The plasmids used in **4.0 ZAG Expression Methodology** of this study were pQE60 and pcDNA3.1 plasmids containing the AZGP1 gene for ZAG expression constructed by GeneScript as custom orders, designed by Gwyn Gould prior to initiation of the experimental work outlined here. Plasmid maps are provided in the supplement material.

2.1.7 Lentivirus Particles

Lentivirus for mammalian transduction used in **4.0 ZAG Expression Methodology** were purchased from ©Horizon Discovery Ltd. Vector sequence map is provided in the supplementary material.

Item name: Precision LentiORF AZGP1 w/o Stop Codon

Clone ID: PLOHS_ccsbBEn_05876

Catalogue ID: OHS5900-224628376

2.1.8 Commercial ZAG

Commercial ZAG used for fluorescence spectroscopy experiments in **4.0 ZAG Expression Methodology** was supplied by Malcolm Kennedy and purchased from R&D Systems®.

Commercial ZAG used for glucose uptake assays in **6.0 Investigating the Impact of Zinc Alpha 2-Glycoprotein in Adipose Browning Biology** and was purchased from BioBench ShiJiaZhuang Quan Jing Biotechnology co., ltd.

2.2 Methods

2.2.1 Cell Lines

HEK293 human embryonic kidney cells (Cat# CRL-3216 RRID:CVCL_0063) were purchased from the American Tissue Culture Collection facility,) and used for transfection and Lenti-virus transduction experiments. 3T3-L1 murine fibroblasts were purchased from American Tissue Culture Collection (Cat# CRL-173;RRID:CVCL_0123).

2.2.2 Bacterial Transformation

DH5- α and BL21 *E. coli* cells were used for transformation and protein expression. DH5- α and BL21 *E. coli* cells were mixed with pQE60 plasmid expressing ZAG and were incubated for 5 minutes in an Eppendorf tube on ice. Bacteria and plasmid transformation mixes were heatshocked at 42°C on a hot plate for 45 seconds and the transformation mix was placed back on ice for 2 minutes. 2YT media (1.6% Tryptone (w/v), 1% Yeast extract (w/v) and 0.5% Sodium Chloride (NaCl) (w/v)) was added to the transformation mix in a 20 ml falcon tube and incubated at 37°C in shaking incubator for 60 minutes. After the incubation, the transformation mix was then spread onto agar plates (1.6% Tryptone (w/v), 1% Yeast extract (w/v) 0.5% Sodium Chloride (NaCl) (w/v), 2% agar (w/v), dH₂O and ampicillin (100 μ g/ml)) using an ethanol-soaked spreader under sterile conditions using a Bunsen burner. The spreader was passed through the Bunsen after each plate to prevent cross contamination. Plates were then wrapped in parafilm and incubated at 37°C overnight for growth of single colonies. Colony growth results from a successful transformation as the pQE60 plasmid expresses ampicillin resistance.

2.2.3 Miniprep

Single colonies were taken from a transformed plate using a pipette tip and dispensed into 20 ml falcon tubes with 2YT media and ampicillin (100 µg/ml). Falcon tubes were placed in a shaking incubator and incubated overnight at 37°C. Cultures underwent the Wizard® Plus SV Minipreps DNA Purification System protocol as follows: After overnight incubation the cultures were then centrifuged at room temperature (23°C) for 5 minutes to form a pellet. The pellet was resuspended with 250 µl of Cell Resuspension Solution and 250 µl of Cell Lysis Solution was added and inverted 4 times to mix. 10 µl of Alkaline Protease Solution was added, inverted 4 times, and then incubated for 5 minutes at room temperature (23°C). 350 µl of Neutralization Solution was added, inverted 4 times, transferred to an Eppendorf tube and then centrifuged at top speed in the microfuge for 10 minutes at room temperature (23°C). A spin column was inserted into a collection tube and the resulting cell lysate from the previous step was decanted into the spin column and centrifuged at top speed in microfuge for 1 minute at room temperature (23°C). The collected flow through in the collection tube was discarded and the spin column was reinserted into the collection tube. 750 µl of Wash Solution with ethanol was added and previous spin step was repeated. The flow through was discarded again, and the wash step was repeated using 250 µl of Wash Solution. Wash solution was then centrifuged at top speed for 2 minutes at room temperature (23°C). The spin column was transferred to a sterile 1.5 ml microcentrifuge tube and 100µl of Nuclease-Free Water was added to the spin column. The centrifuge tube containing the spin column was then spun at top speed in the microfuge for 1 minute at room temperature (23°C) and resulting in pQE60 DNA being eluted and stored at -20°C.

2.2.4 Restriction Digest

Agarose gel (0.8% agarose powder (w/v), Trichloroacetic acid (TAE buffer)) was heated in the microwave to liquify agarose and the agarose was poured into gel mould and ethidium bromide was added and mixed until clear. The comb was then added and left until set. 5 µl of 1 kb DNA ladder and 10 µl of each sample was pipetted into the wells and gel was run at 75 volts for 30 minutes. After samples had finished running, the gel was placed under U.V. light to image the bands.

2.2.5 Protein Purification

Transformed BL21-pQE60 ZAG expressing single colonies were taken from transformed plate using a pipette tip and dispensed into 20 ml falcon tubes with 2YT media and ampicillin (100 µg/ml). Falcon tubes were placed in shaking incubator and incubated at 37°C overnight until OD₆₀₀ optical density was achieved. The resulting culture was then transferred to a 1 litre conical flask containing 400 ml of 2YT and ampicillin (100 µg/ml) and grown for 2-3 hours until OD₆₀₀ is achieved. The culture was transferred to 500 ml drums and weighed, before spinning at 3500xg for 20 minutes at room temperature (23°C) in worktop centrifuge to create a pellet. The sample pellet (~0.5 g) was suspended in lysis buffer (50 mM Tris-HCl, pH 8.0, 25% sucrose (w/v), 1 mM EDTA) and cells were lysed with the addition of lysozyme (1 mg) dissolved in lysis buffer and then incubated on ice for 30 minutes. The solution became viscous because of the lysozyme treatment. MgCl₂ (10 mM), MnCl₂ (1 mM) and DNase I (10 µg/ml) were then added and incubated on ice for 30 minutes. Detergent buffer (0.2 M NaCl, 1% deoxycholic acid (w/v), 1% Nonidet P-40 (v/v), 20 mM Tris-HCl (pH 7.5), 2 mM EDTA) was added to the cell lysate, incubated for 20 minutes on ice and then centrifuged at top speed in microfuge for 10 minutes at 4°C. After centrifugation, the resulting supernatant was removed

and the pellet was re-suspended in 0.5% Triton X-100, 1 mM EDTA solution and centrifuged at top speed in microfuge for 10 minutes at 4°C. This process was repeated 5 times to produce a tight pellet containing the recombinant protein.

The tight pellet was resuspended in 1 ml of 8 M UREA to remove recombinant protein from inclusion bodies and 3 ml of Refolding buffer (0.1 M Tris-HCl, 2 mM EDTA, 0.4 M L-arginine, 0.5 mM oxidised glutathione, 5 mM reduced glutathione) was added and incubated overnight at 4°C. After the refolding step, two different approaches were taken. The first was taking 1 ml of the overnight incubation and placing it in vivaspin 20 centrifugal concentrator. Refolding buffer was gradually added to a total of 20 ml. The sample was then spun at 3500xg until 5 ml of concentrated ZAG solution was left in the top part of the vivaspin tube. The second approach injected 1 ml of refolded ZAG using a 23-gauge needle into a dialysis slide (3.5-7 kDa) and dialysed in 1 litre of refolding buffer at 4°C overnight.

2.2.6 Cell Culture

2.2.6.1 Cell Culture of HEK293 Cells

HEK293 cells were maintained in a humidified incubator at 37°C, with 5% (v/v) CO₂ in 75 cm² flasks and accompanied by 12 ml of Dulbecco's Modified Eagle's Medium (DMEM) full medium consisting of 10% (v/v) Foetal Bovine Serum (FBS), penicillin (50 µg/ml) and streptomycin (50 µg/ml) (DMEM full media). When cells approached confluence, they were split by rinsing the mono-layer of cells with 5 ml of sterilised Phosphate Buffered Saline (PBS) and incubated with 1 ml trypsin-EDTA (0.25%) at 37°C for 5 mins to detach the cells from the flask surface. The cells were then resuspended with 11 ml of DMEM full medium and passaged for continued culture. Additionally, cells were transferred to 6 well plates for cell transfection experiments and placed in an incubator for 24 hours. When the cells became approximately

60% confluent, cells underwent transfection treatment as detailed below. Cells were harvested for SDS-PAGE and western blotting.

2.2.6.2 *Cell Culture of 3T3-L1 Fibroblasts*

3T3-L1 murine fibroblasts were maintained in a humidified incubator at 37°C, with 10% (v/v) CO₂ in 75 cm² flasks and accompanied by 12 ml of DMEM full medium consisting of 10% (v/v) Newborn Calf Serum (NCS), penicillin (50 µg/ml) and streptomycin (50 µg/ml). Cells were fed every second day and passaged as described in **2.2.6.1 *Cell Culture of HEK293 Cells***. 3T3 -L1 murine fibroblasts were also grown in 12 well plates in preparation for differentiation described in **2.2.6.3 *3T3-L1 Adipocyte Differentiation***.

2.2.6.3 *3T3-L1 Adipocyte Differentiation*

3T3 -L1 murine fibroblasts were grown to confluence in 12 well plates incubated at 37°C, with 10% (v/v) CO₂. Differentiation into adipocytes was initiated 2 days post confluence and the differentiation process lasted 10 days. Day 0 medium consisted of DMEM supplemented with 10% (v/v) FBS, 0.5 mM 3-isobutyl-1-methylxanthine (IBMX), 1 µM insulin, 0.25 µM dexamethasone, and 1 nM troglitazone. 3 days after differentiation media was changed to Day 3 medium containing DMEM supplemented with 10% (v/v) FBS, 1 µM insulin and 1 nM troglitazone. On day 6 and day 8, media was replaced with medium containing DMEM supplemented with 10% (v/v) FBS. Cells were fully differentiated after Day 10 and ready for treatments described in **2.2.6.4 *3T3-L1 Adipocyte Treatments***. For aging studies - after differentiation maturity was reached after day 10 – cells were fed with medium containing DMEM supplemented with 10% (v/v) FBS and cells were used between day 10 and day 66.

2.2.6.4 *3T3-L1 Adipocyte Treatments*

Cells were typically used on day 10 after induction of differentiation to investigate adipocyte browning biology as follows:

[A] For mitochondria analysis, cells were treated with recombinant and mammalian ZAG (27 μ M) alongside their respective vehicle controls (Refolding Buffer and Serum Free Media collected from Wild Type HEK293 cells) for 4 hours and mitochondria were isolated as described in **2.2.11 Mitochondrial Isolation**. Mitochondria samples were then blotted for voltage-dependent-anion-channel 1/3 (VDAC 1/3) and uncoupling protein 1 (UCP-1).

[B] For browning associated cell signalling, cells were treated with mammalian ZAG (27 μ M) for 2, 24 and 48 hours and samples were blotted for peroxisome proliferator-activated receptor gamma (PPAR γ), acetyl-CoA carboxylase (ACC), fatty acid synthase (FAS) and β 3-adrenergic receptor (β 3 AR).

[C] Cells were treated to measure lipolysis as outlined in **2.2.6.5 Measuring Lipolysis of 3T3-L1 Cells** below.

[D] Cells were treated with bacterial and mammalian ZAG (27 μ M) and commercial ZAG (5 μ g/ml) to measure glucose uptake as outlined in **2.2.6.6 Measuring Glucose Uptake in 3T3-L1 Cells**.

2.2.6.5 *Measuring Lipolysis of 3T3-L1 Cells*

3T3 cells were grown and differentiated as stated in **2.2.6.2 Cell Culture of 3T3-L1 Fibroblasts** and **2.2.6.3 3T3-L1 Adipocyte Differentiation**. Once cells had reached day 10 of differentiation, fresh media was given to cells and were treated with bacterial expressed ZAG (50 μ M) and respective control of refolding buffer for 1 and 4 hours. Cells were also treated with mammalian expressed ZAG (27 μ M) and respective control of Serum Free Media collected from Wild Type HEK293 cells for 2 hours. After appropriate incubation period,

media was collected from cells and were subject to the Lipolysis Colorimetric Assay Kit from Sigma Aldrich. Samples were measured on a 96-well plate at 570 nm using the BioTek EPOCH Microplate Spectrophotometer.

2.2.6.6 *Measuring Glucose Uptake in 3T3-L1 Cells.*

3T3 cells were grown and differentiated as stated in **2.2.6.2 *Cell Culture of 3T3-L1 Fibroblasts*** and **2.2.6.3 *3T3-L1 Adipocyte Differentiation***. Glucose uptake was measured by the uptake of 2-[3H]-deoxy-glucose as previously described (Gould et al, 1988). 3T3-L1 adipocytes grown in 24 well plates and were incubated for 2 hours in serum-free DMEM prior to the start of this experiment. Cells were then transferred to a hot plate at 37°C and washed 3 times with 0.5 mL of Krebs-Ringer phosphate (KRP; 130 mM NaCl, 4.8 mM KCl, 5 mM NaH₂PO₄, 1.25 mM MgSO₄, 1.25 mM CaCl₂, pH 7.4) solution before being incubated in 475 µL of KRP. The cells were then stimulated with 100 nM insulin for 20 minutes. Glucose transport was initiated by the addition of 25 µL of 2-deoxy-glucose and 2-[3H]-deoxyglucose (final concentration of 50 µM and 0.5 µCi respectively) for 5 minutes. The assay was terminated by removing the assay mixture from the cells and immersing the plates in 2 litres of ice-cold PBS. After air-drying the plates for 1 hour, 0.25 mL of 1% (v/v) Triton-X100 was added to the wells and incubated at room temperature for up to 24 hours. The samples were added to 5 ml of scintillation fluid and radioactivity levels were measured using a Beckman Multi-Purpose scintillation counter.

2.2.7 *HEK Transfection*

Cells were plated on 6 well plates and incubated at 37°C, with 5% (v/v) CO₂. Once cells reached approximately 60% confluence, treatments of a vehicle control of Opti-Mem only, Opti-Mem and Lipofectamine (2% (v/v) final), Opti-Mem and Xfect reaction buffer and Xfect polymer (25% (v/v) and 0.3% (v/v) final), Opti-Mem and pCDNA3.1 plasmid expressing ZAG

(2.5 µg/ml per well), Opti-Mem, Lipofectamine and pCDNA3.1 expressing ZAG (2% (v/v) final and 2.5 µg/ml per well) and Opti-Mem, Xfect reaction buffer, Xfect polymer and pCDNA3.1 expressing ZAG (25% (v/v), 0.3% (v/v) final and 2.5 µg/ml per well) were prepared, vortexed and spun in microfuge at top speed for 30 seconds. Treatments were then incubated for 20 minutes. Media in 6 well plate was aspirated and replaced with 1 ml of Opti-Mem, swirled and then aspirated. Incubated treatments were then added to the centre of each desired well in a dropwise manner and incubated for 4-6 hours. After incubation, media was aspirated and replaced with DMEM and plates were incubated at 37°C, with 5% (v/v) CO₂ for 48 hours.

2.2.7.1 *Lentivirus Transduction of HEK293 Cells*

HEK293 cells were plated on a 24 well plate at a density of 5×10^4 per well and incubated overnight at 37°C, with 5% (v/v) CO₂. The next day, DMEM growth media was aspirated and replaced with DMEM supplemented with Blasticidin S containing the appropriate concentrations for kill curve (0-20 µg/ml) and incubated at 37°C, with 5% (v/v) CO₂. Media was replaced approximately every 2-3 days with the same concentration of Blasticidin S supplemented DMEM. Cell survival was monitored and optimum effectiveness was observed between 3-6 days. Optimum effectiveness is classed as the minimum concentration of antibiotic that kills 100% of cells within 3-6 days. Once the appropriate concentration of Blasticidin S was determined, HEK 293 cells were seeded onto a 24 well plate at a density of 5×10^4 cells per well in DMEM and incubated for one day at 37°C, with 5% (v/v) CO₂. DMEM media was aspirated and replaced with serum-free medium and Precision LentiORF™ 10^8 TU/ml was added to each well. Cells were incubated at 37°C, with 5% (v/v) CO₂ for 4 hours, transduction mixture was aspirated and replaced with DMEM and incubated at 37°C, with 5% (v/v) CO₂ for 48 hours. Successful transduced colonies expressing TurboGFP were then imaged using the

EVOS™ FL Auto Imaging System at x10 magnification.

2.2.8 Harvesting Cells and Supernatants for SDS-PAGE

After HEK 293 cell transfection and 3T3-L1 adipocyte treatments, plates were removed from incubator and placed on ice. Cell conditioned media was collected into labelled Eppendorf tubes. 15 µl of Trichloroacetic acid (TCA) was added to each Eppendorf and inverted 3 times to mix TCA and media, vortexed and then incubated on ice for 15 minutes. After incubation, samples were spun at top speed at 4°C in microfuge for 20 minutes. Samples were then placed on ice and incubated for 10 minutes with occasional mixing. Samples were then transferred back to microfuge and spun for 10 minutes at top speed at 4°C. Resulting supernatant was carefully removed using a 200 µl pipette tip and discarded. The remaining pellet was resuspended in sample buffer (SDS-PAGE buffer) (Trizma®base (125 mM, pH 6.7), sodium pyrophosphate ($\text{Na}_4\text{P}_2\text{O}_7$) (0.5 mM), EDTA (1.25 mM), sodium dodecyl sulphate (SDS) 0.5% (w/v), glycerol 12.5% (v/v), bromophenol blue sodium salt 0.06% (w/v), and dithiothreitol (DTT) 10 mM) and was vortexed to mix. 2 M Tris buffer was then added to neutralise the TCA. SDS-PAGE buffer was then added to reach the desired final volume to run samples on gel. Samples were stored at -20°C if not used immediately.

To harvest cells, each well was washed with Phosphate Buffered Saline (PBS) twice and discarded. RIPA buffer (Sodium Chloride (NaCl) (150 mM), EDTA (5 mM), Tris (50 mM, pH 8.0) NP-40 1% (v/v), Sodium Deoxycholate 0.5% (w/v), sodium dodecyl sulphate (SDS) 0.1% (w/v) and dithiothreitol (DTT) 10 mM) was added to each well and cells were removed using a cell scraper. Cells were collected using a 1 ml pipette tip and placed in labelled Eppendorf tubes. Each cell lysate was sheared 10 times through a 23-gauge needle to break released DNA and samples were spun in microfuge at 4°C at top speed for 10 minutes to pellet insoluble

debris. Supernatant was removed and can be stored at -20°C if not used immediately. If using that day, samples are mixed in 2x SDS-PAGE buffer and heated at 95°C for 10 minutes before western blotting.

2.2.9 Western Blotting

3 µl of pre-stained molecular weight marker and 15 µl of each sample was loaded into 15 well polyacrylamide gels 10% (w/v) using a 20 µl pipette. Gels were secured in clamp stands and submerged with running buffer comprising of glycine (0.19 M), SDS 0.1% (w/v) and Trizma®base (25 mM). The gel apparatus was then attached to a power source and was set at 150 V for 60 minutes and then increased to 200 V when samples had run halfway down the gel. Once the separation was complete, the gel was placed into a transfer cassette against nitrocellulose paper, supported with sponge and card. The assembled transfer cassette was submerged in transfer buffer consisting of glycine (0.19 M), Trizma®base (25 mM) and methanol 20% (v/v). Protein transfer from the gel to the nitrocellulose was at 100 V for 120 minutes. The nitrocellulose paper was incubated in blocking buffer comprising of Bovine Serum Albumin (BSA) 3% (w/v) in Tris buffered saline with Tween 20 (TBST) (NaCl (100 mM), Trizma®base (10 mM, pH 7.5) and Tween®20 0.1% (v/v)) for 1 hour at room temperature (23°C). The membrane was then placed in appropriate primary antibody (1:1000) diluted in BSA 1% (w/v), TBST and rotated overnight at 4°C. After primary incubation, blots underwent three 7-minute washes with TBST whilst rocking. They were then incubated with the corresponding LI-COR IRDye-conjugated anti-mouse/rabbit secondary antibody (1:10,000) diluted in BSA 3% (w/v) and TBST for 1 hour at room temperature (23°C). Subsequently, blots underwent another three 7-minute wash steps in TBST. Proteins were visualised using the LI-COR imaging system.

2.2.10 Fluorescence Spectroscopy

The fluorescent fatty acid 11-((5-dimethylaminonaphthalene-1-sulfonyl)amino)undecanoic acid (DAUDA) was stored as a stock solution of 3 mg/ml in ethanol, in the dark at -20 °C, and freshly diluted in Phosphate Buffered Saline (PBS; 171 mM NaCl, 3.35 mM KCl, 10 mM Na₂HPO₄, 1.8 mM KH₂PO₄, pH 7.2) to a final concentration of 1 µM before use in the fluorescence experiments. Commercial ZAG was bought from R&D Systems® and was made to stocks of 1 µg/ml in PBS and our ZAG was at a stock concentration of 0.95 mg/ml. Spectrofluorimetry and Fluorescence-based Ligand Binding—Fluorescence binding emission spectra (uncorrected) were recorded at 20 °C with a SPEX Fluo-Max spectrofluorimeter (Spex Industries, Edison, NJ) using 2 ml samples in a silica cuvette. Raman scattering by solvent water was subtracted where necessary. The excitation wavelengths used for DAUDA was 345 nm, respectively. Fluorescence data were corrected for dilution where necessary and fitted by standard nonlinear regression techniques (using Microcal ORIGIN software) to a single site binding model to give estimates of the dissociation constant (K_d) and maximal fluorescence intensities (F_{max}).

2.2.11 Mitochondrial Isolation

Five 10 cm plates of fully differentiated 3T3-L1 adipocytes were placed on ice and washed with ice cold Phosphate Buffered Saline pH 7.0 (PBS) twice. Cells were then coated in 1.5 ml ice cold Mitochondria Isolation Buffer (250 mM sucrose, 5 mM HEPES, 2 mM EGTA, pH 7.2) and removed from dish with a cell scraper and adipocytes were collated together. Cells were then homogenised with a glass dounce by descending and ascending the pestle with rotation ten times. Cell homogenate was transferred to 1.5 ml Eppendorfs and spun at 900 x g in microfuge at 4°C for 10 minutes. The homogenate should now be separated with a layer of

fat at the top of the Eppendorf containing peridroplet mitochondria (PDM) and the supernatant containing the cytosolic mitochondria (CM). The fat cake was removed by cutting the top of a tip off and pipetting and placed into a new Eppendorf and the supernatant was also transferred into a fresh Eppendorf. The supernatant fraction containing the CM was resuspended thoroughly with Mitochondria Isolation Buffer and spun again at 900 x g in microfuge at 4°C for 10 minutes and any further fat layer was removed. Keeping both fragments separate, the fat cake and supernatant were mixed thoroughly with Mitochondria Isolation Buffer + BSA and spun at 9000 x g at 4°C to pellet the mitochondria. The supernatant was removed from both isolates and resuspended in Mitochondria Isolation Buffer + BSA and re spun at 9000 x g at 4°C to pellet the mitochondria again. These final pellets were resuspended with Mitochondria Isolation Buffer absent of BSA and aliquoted at 50 µl. PDM and CM mitochondria populations were aliquoted and stored separately at -80°C.

2.2.12.1 *Fixing Cells for Imaging*

3T3-L1 cells were grown to the desired differentiated state in a 12 well plate with glass coverslips and placed on ice and washed with ice cold Phosphate Buffered Saline pH 7.0 (PBS) once. Cells were then incubated with 4% Paraformaldehyde (PFA) for 20 minutes at room temperature on benchtop with no rocking. PFA was removed and cells were washed with ice cold PBS x3. Cells were then incubated in quenching buffer (85 mM NaCl, 1.7 mM KCl, 5 mM Na₂HPO₄, 0.9 mM KH₂PO₄, 50 mM NH₄Cl, pH 7.4) for 40 mins at room temperature with slight rocking. Quenching buffer was removed and washed in ice cold PBS once. Fixed cells can be stored in PBS and covered at 4°C until needed for Stimulated Raman Scattering (SRS).

2.2.12.2 *Stimulated Raman Scattering Microscopy (SRS)*

An integrated laser system (picoEmerald S, Applied Physics & Electronics, Inc.) was used to

produce two synchronized laser beams at 80 MHz repetition rate. A fundamental Stokes beam (1031.4 nm, 2 ps pulse width) was intensity modulated by an electro-optic-modulator (EoM) with >90% modulation depth, and a tunable pump beam (700–960 nm, 2 ps pulse width, < 1 nm (<10 cm⁻¹) spectral bandwidth) was produced by a built-in optical parametric oscillator. The pump and Stokes beams were spatially and temporally overlapped using two dichroic mirrors and a delay stage inside the laser system and coupled into an inverted laser-scanning microscope (Leica TCS SP8, Leica Microsystems) with optimized near-IR throughput. SRS images were acquired using a 40× objective (HC PL IRAPO 40×, N.A. 1.10 water immersion lens) with a 9.75–48 μs pixel dwell time over a 512 × 512 or a 1024 × 1024 frame. The Stokes beam was modulated with a 20 MHz EoM. Forward scattered light was collected by a S1 N.A. 1.4 condenser lens (Leica Micro-systems). Images were acquired at 12-bit image depth. The laser powers measured after the objective lens were in the range of 10–30 mW for the pump beam only, 10–50 mW for the Stokes beam only, and 20–70 mW (pump and Stokesbeams). The spatial resolution of the system is ~450 nm (pump wavelength = 792 nm).

2.2.12.3 *Hyperspectral SRS Imaging.*

10 ul of PBS was pipetted on 0.8-1 mm glass slides and fixed cells on coverslips were placed on top and sealed with nail varnish to prevent cells drying out. Hyperspectral SRS images were acquired across the range 2800–3050 cm⁻¹ using a 0.4nm retune in the pump beam and 9.75 μs pixel dwell time across a 512 × 512 frame.

2.2.12.4 *Spectral Phasor Analysis.*

The SRS image data set across the range 2800–3050 cm⁻¹ was imported into ImageJ, and an average intensity projection was created. The spectral phasor analysis was performed as described by Fu et al., 2018, using a plug-in for ImageJ.²¹ The background areas were

removed from the image using a threshold intensity mask. Segmentation of the phasor plot was performed manually using regions-of-interest to create images of discrete cellular locations. The corresponding average spectra for each ROI were plotted using Excel.

2.2.13 Data Analysis of Lipid Droplets

Images of 3T3-L1 adipocytes were uploaded in FIJI and the following steps were performed to analyse characteristics of area, perimeter and diameter of lipid droplets in adipocytes:

- Image > Adjust > Threshold > B&W > Dark Background
- Analyse > Set Measurements:

Area

Perimeter

Diameter

Limit to Threshold

Send to the threshold image

- Analyse > Analyse Particles

Size: 5-Infinity

Circularity: 0.5-1.0

Show: Mask

Display Results

Exclude on Edges

Overlay

- Display of results were then transferred and analysed in PRISM

2.2.14 In Silico Ligand Docking

ZAG and candidate ligand crystallised structures were obtained from the protein data bank (PDB) and visualised in UCSF Chimera. All ZAG mutations were performed using the 'Rotamers' function in UCSF Chimera.

Docking method.

All docking was performed using the online server at Swansea University in conjunction with Moleculomics and all files containing ZAG (wild type and mutants), candidate ligands and subsequent docking files are all stored on this server. The following steps were carried out to perform ligand docking:

- Logged onto the server of Swansea University to access the virtual machine containing the PLANTS docking program. The docking simulations need the following files:
- A denuded receptor saved as a .pdb file. This receptor is wild type or mutant ZAG
- An example binding saved as a .pdb file. This is ZAG that already has a ligand bound so the program has a reference.
- A ligand structure derived from PubChem saved as a .sdf file. These are our candidate ligands that are to be docked.

These files have to be prepared for them to be accepted to run in the PLANTS program by performing the following:

- Receptor is prepared for docking: 'felix prepare-rec rec.pdb prep/'
- Prepare example: 'obabel ex.pdb -O ex.sdf'
- Prepare ligand: 'felix prepare_lig --method=eem lig.sdf prep/'

Lastly are the files needed to run the docking simulation:

- call.plants and plants.cfg

Plants docking run using:

- `./call.plants prep/rec.mol2 ex.sdf prep/lig.mol2 out/`

Files are then viewed using 'less bestfeatures.csv' where ligand docking scores are accessed.

All files are exported and viewed and edited using Chimera and Excel.

2.2.15 Data and Statistical Analysis

All ligand docking work has been performed using the PLANTS docking software (Korb et al., 2007) and docking simulations have been ran with my PC but remotely using the computers at Moleculomics in Swansea University. All analysis of ligand docking work has been performed with UCSF Chimera (Pettersen et al., 2014).

All Stimulated Raman Scattering image analysis was performed using FIJI (Schindelin et al., 2012) and spectral phasor analysis and cell segmentation images were generated using the Spectral Phasor plugin for FIJI (Fu & Xie, 2014).

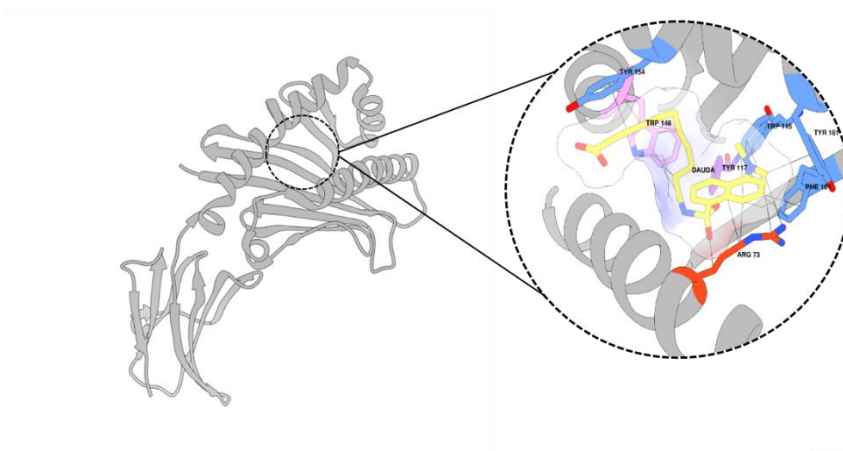
Western Blot images were generated using FIJI (Schindelin et al., 2012) and all quantification and statistical analysis was performed in GraphPad PRISM.

Fluorescence Spectroscopy data obtained from ZAG and DAUDA binding studies were analysed and generated using Microcal ORIGIN software.

No power calculations have been performed in this thesis.

Chapter 3

Investigating Zinc Alpha 2-Glycoprotein Ligand Binding Through Computational Techniques



UCSF CHIMERA
an Extensible Molecular Modeling System



3.0 Investigating Zinc Alpha 2-Glycoprotein Ligand Binding Through Computational Techniques

3.1.1 Introduction

One direction taken to fight disease progression is for pharmaceutical companies to develop therapeutics for diseases such as cancer by developing a drug discovery program (Takebe et al., 2018). For example, a protein -such as a receptor- that has been identified to drive disease progression will be extensively studied and the ligand that binds to this protein resulting in downstream signaling will be identified (Perola, 2010). This ligand and its interaction with the protein are then mapped and a screening program is initiated. The identification of the key residues in the protein and the key groups in the ligand allow for the development of a synthetic compound that can bind to the protein irreversibly and prevent function stemming disease progression. This approach is one that can be applied to our efforts in identification of the ligand binding partner in the ZAG protein.

This drug development work can be undertaken using chemical assays designed to modify potential structures based on an identified pharmacophore to identify more efficacious or soluble drug targets using simple *in vitro* or *in vivo* assays. However, here we sought to initiate this work through computational means. AlphaFold 3 has revolutionized our ability to study protein structural biology by using *in silico* approaches to model protein structures (Jumper et al., 2021). Utilizing additional computational programs allows for visualization of protein-ligand binding sites and assessment of the key residues, and bonds that are involved in these interactions (Pettersen et al., 2004). This approach aims to reduce chemical reagent use, time and cost by exploring candidate ligands virtually with a library of selected ligands, by-passing the heavy leg work *in vitro/in vivo* assays with a high virtual throughput system that we can use as a screening process to narrow the number of ligands used in our studies.

For this work we have utilized the protein visualization software UCSF Chimera (Pettersen et al., 2004). Chimera is a multi-functional, interactive program with good rendering quality whilst allowing for customization of visuals using direct interface without the need for coding, providing a somewhat user friendly experience without compromise in quality. Like other molecular programs such as PyMOL (Rigsby & Parker, 2016), UCSF Chimera allows for imports from the protein data bank (PDB) that takes an established protein structure and generates a computer model which can be manipulated through orientation, residue selection, naming and coloring to allow for visualization and molecular analysis.

Considering structural analysis, there are different approaches when it comes to computational predictions. One example is AlphaFold, that has been developed to accurately predict protein structures that have not been resolved through conventional means as mentioned. Our method however requires a known structure for these docking studies. Another route is through molecular dynamics (Durrant & McCammon, 2011) that simulates the orientation of protein-protein and protein-ligand interactions but is significantly computationally intensive and requires a particular skill set. Therefore, we employed software that specializes in ligand-protein interactions that can be incorporated with the UCSF Chimera program.

As models of protein-ligand interactions have developed, so has understanding of the molecular chemistry. For example, the lock and key developed by Fisher (Lichtenthaler, 1995) presents a rigid system with the ligand (key) having to precisely fit the protein (lock). This was further developed by Koshland (Koshland, 1995) with the induced fit model where the protein can undergo conformational change as well as the ligand. It is this flexibility in both the ligand and protein that has been the focus when developing ligand docking programs such as PLANTS.

PLANTS

Protein-Ligand ANT System (PLANTS) is a docking software tool that allows for computational experiments to represent chemical reactions *in silico* (Korb et al., 2007). This

system in particular is named after how ants navigate by using pheromones to hone their direction to their destination and this is loosely translated to the how the docking system performs. The PLANTS software allows for the ligand and protein to exhibit degrees of freedom and flexibility, allowing various iterations of orientation between the two. The software loads the ligand into an indiscriminate area around the protein of interest and the program begins to dock the ligand by taking incremental steps towards the protein binding pocket whilst allowing flexibility in the ligand. This is determined by the ligands atom spatial arrangements that are resolved through the rotation about single bonds and is searching for what orientation of the ligand exhibits the least degrees of freedom. With this first run of simulations complete, the program selects that orientation of ligand presenting the least degrees of freedom and uses this as the new starting point for the next set of docking simulations. The simulation is complete when the ligand exhibits the least degrees of freedom in the docked model showing it has reached an end point and the ligand no longer wants to change orientation. This final docked ligand is then assigned a binding affinity score that can be compared with subsequent docking simulations. All of the docked files can then be visualized in UCSF Chimera to investigate the molecular chemistry of the binding site and elucidate the residues which are providing the strongest interactions with the ligand such as identifying hydrogen bonds. Another beneficial feature is that mutations can also be made computationally using UCSF Chimera allowing for conformational changes in the binding site of the protein. As with the wild type, these mutated models can be used for docking simulations and through structure based sequence alignment can be superimposed on top of one another and the mutations effect on ligand docking orientation can be visualized. In conjunction with Moleculomics -a protein computational team based in Swansea University- there are expertise in this line of *in silico* drug discovery. One example being that Moleculomics were awarded funding to find a drug treatment for the mutating SARS-CoV-2 using their technology platforms and are well placed

for this work. Collating all these features together, allows for a comprehensive *in silico* screening study to be performed, providing insight in ZAG's ligand preferences and binding motifs. A workflow has been included here to demonstrate the thinking and steps taken in performing this *in silico* ligand docking study (Figure 3. 1).

Ligand Docking Workflow

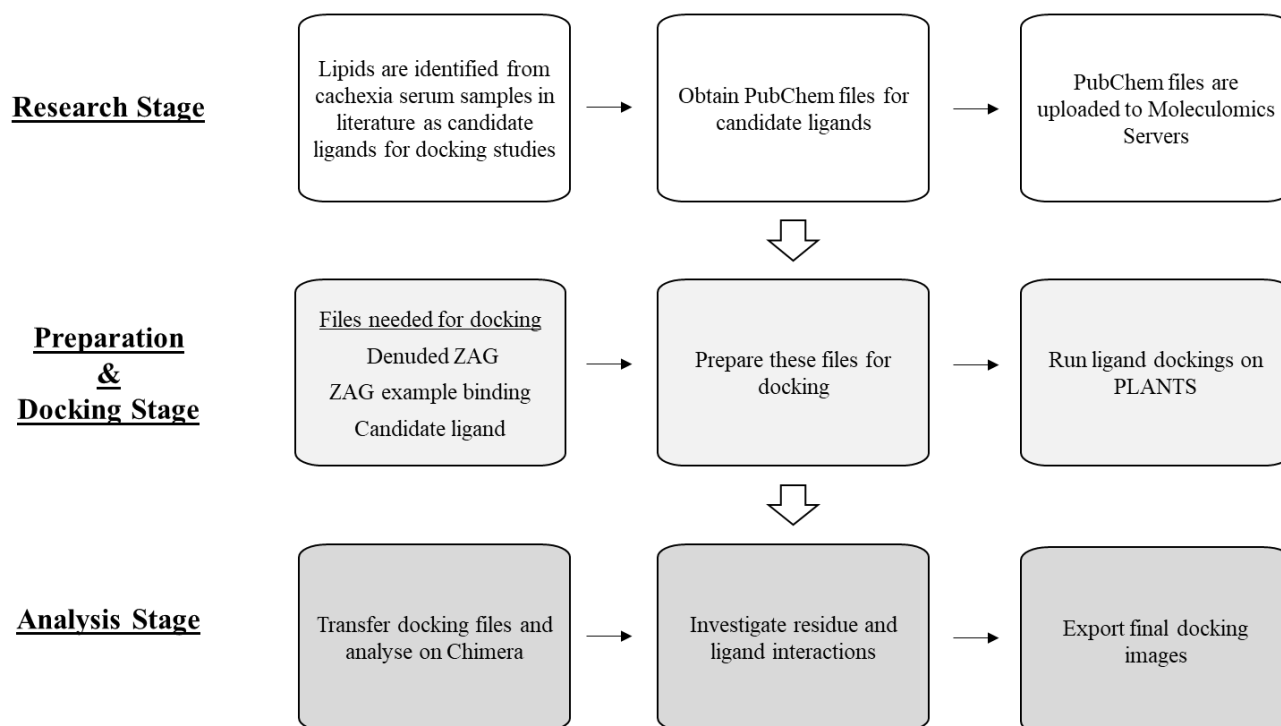


Figure 3. 1. Research and Experimental Design for *in silico* Ligand Docking

Computational ligand docking studies performed in this thesis followed the outlined steps. A research stage to investigate the literature and identify our candidate ligands. A preparation and docking stage to prepare the ZAG and candidate ligand files to use in the PLANTS docking program. Finally, all docking results were transferred and analysed using UCSF Chimera to identify interactions between the residues in the ZAG pocket and the candidate ligands.

3.1.2 Validation of Ligand Docking Programme PLANTS

It has been hypothesised that ZAG's biological activity is determined by the binding of a possible selection of ligands in a groove between the $\alpha 1$ and $\alpha 2$ helices (Delker et al., 2004). Crystallised models of ZAG have shown two ligands bound in this pocket, P6G (Sánchez et al., 1999) and DAUDA (Kennedy et al., 2001). Part of this project is to determine how these ligands interact within the groove through protein modelling and ligand docking analyses. To determine the validity of the docking simulations that were going to be undertaken, control docking simulations of the crystallised ligands P6G and DAUDA were performed to determine if this approach was appropriate in identifying possible novel ligands. The crystallised DAUDA in the ZAG pocket was initially transferred into the protein modelling programme UCSF Chimera (Figure 3. 2 A) and showed interactions between a Tryptophan ¹⁴⁸ residue, a Tyrosine ¹¹⁷ and an Arginine ⁷³ residue. The same DAUDA and ZAG .pdb files were then uploaded to the Molculomics server and ligand docking simulations were performed using a programme called PLANTS. This docking was then observed using UCSF Chimera (Figure 3 .2 B) and the ligand has docked in a similar orientation with shared residue interaction with the crystallised DAUDA with Tryptophan ¹⁴⁸, Tyrosine ¹¹⁷ and Arginine ⁷³. The P6G ligand was analysed using the same process but docking did not result in the same orientation (data not shown). However, with a strong match between the crystallised and PLANTS docked DAUDA, there was now a comparative result going forward.

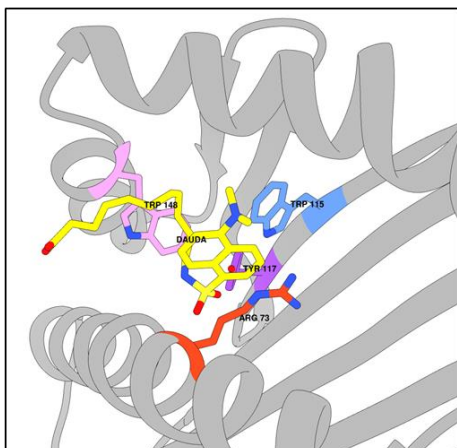
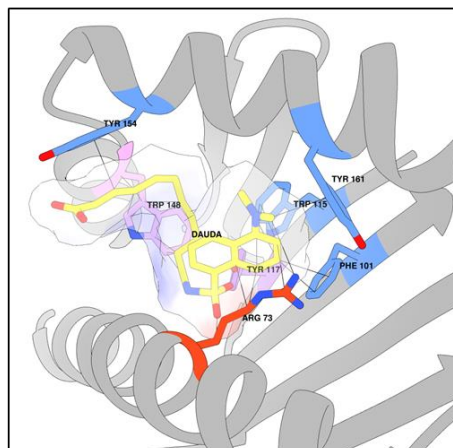
A**B**

Figure 3. 2. Initial Ligand Docking Simulation in ZAG Alpha Helix Groove

Crystallised structure of ZAG and DAUDA ligand was obtained through Protein Data Bank (PDB) and was initially analysed using the UCSF Chimera protein imaging software (A). The ligand DAUDA was uploaded to the MolScribe server and a simulation of ligand docking was run using PLANTS software to compare with the crystallised DAUDA orientation in native ZAG (B).

3.1.3 Ligand Screening to Identify Suitable Ligand Candidates for ZAG

With a control established to start the ligand docking work, suitable candidate ligands were identified using the literature with lipid serum analyses of cachexia patients seeing an upregulation of Palmitic acid and Stearic acid (Miller et al., 2019; Riccardi et al., 2020). With it being hypothesised that a hydrophobic molecule could be the potential ligand binding partner to ZAG and that ZAG is upregulated in cachexia patients, it seemed reasonable to use these two ligands as a starting point. 20 molecules closely related to these acids were selected as candidate ligands (Table 3.1) and docking simulations were performed as previous (**3.1.2 Validation of Ligand Docking Program PLANTS**). The PLANTS docking programme assigns a scoring system for each docking (Table 3.1) based on its number of interactions between the ligand and the protein. Our control for these docking experiments is the docked DAUDA ligand and it has a ligand score of -111.062. Anything equal to this score or numerically lower would be a desirable ligand candidate to further investigate. 8,11-Eicosadiynoic acid has a ligand score of -115.276 (Table 3.1) and exhibits hydrogen bonding between the residues of Tryptophan ¹⁴⁸, Glutamic acid ⁷⁹, and Threonine ⁸⁰ whilst also interacting with the residues Arginine ⁷³, Phenylalanine ¹⁰¹, Tryptophan ¹¹⁵, Tyrosine ¹¹⁷, Isoleucine ⁷⁶ and Aspartic acid ⁸³ (Figure 3.3 A). Another ligand candidate, 9,12-Octadecadiynoic acid has a ligand score of -110.062 (Table 3.1). It also exhibits hydrogen bonding between the residues of Tryptophan ¹⁴⁸, Glutamic acid ⁷⁹, and Threonine ⁸⁰. It shows further interactions with Phenylalanine ¹⁰¹, Isoleucine ⁷⁶, Tyrosine ¹⁴ and Tyrosine ¹⁵⁴ but does not appear to interact with Arginine ⁷³ (Figure 3.3 B). A 3rd desirable candidate ligand, Arachidic acid, has a ligand score of -112.568 (Table 3.1). Arachidic acid shows hydrogen bonding between Tryptophan ¹⁴⁸ and Tryptophan ¹³⁴ residues whilst interacting with Arginine ⁷³, Phenylalanine ¹⁰¹, Tryptophan ¹¹⁵, Tyrosine ¹¹⁷ and Tyrosine ¹⁶¹ (Figure 3.3 C). Hexadecanedioic acid is another ligand to investigate with a ligand score of -104.965 (Table 3.1). As with 8,11-Eicosadiynoic acid and 9,12-

Octadecadiynoic acid it exhibits hydrogen bonding between Tryptophan ¹⁴⁸ and Threonine ⁸⁰ but also with Isoleucine ⁷⁶ and other interactions with Tyrosine ¹¹⁷ and Lysine ¹⁴⁷ (Figure 3.3 D). The last candidate is Stearic acid itself. It is given a ligand score of -106.141 (Table 3.1). Its orientation is mirrored in comparison with 8,11-Eicosadiynoic acid and 9,12-Octadecadiynoic acid and as a result it interacts with Tryptophan ¹⁴⁸ and Threonine ⁸⁰ as they do but exhibits hydrogen bonding between Arginine ⁷³ and Tyrosine ¹¹⁷. There are also interactions Threonine ¹⁴⁴ and Aspartic acid ⁸³ (Figure 3.3 E). These top 5 ligand candidates share common residues that they interact with varying degrees (Table 3.2). All candidates 8,11-Eicosadiynoic acid, 9,12-Octadecadiynoic, Arachidic acid, Hexadecanedioic acid and Stearic acid interact with Tryptophan ¹⁴⁸. 8,11-Eicosadiynoic acid, 9,12-Octadecadiynoic acid, Hexadecanedioic acid and Stearic acid interact with Threonine ⁸⁰. 8,11-Eicosadiynoic acid, Arachidic acid and Stearic acid have a common residue in Arginine ⁷³. 8,11-Eicosadiynoic acid, Arachidic acid, Hexadecanedioic acid and Stearic acid interact with Tyrosine ¹¹⁷. Phenylalanine ¹⁰¹ is a common residue between 8,11-Eicosadiynoic acid 9,12-Octadecadiynoic acid and Arachidic acid. 8,11-Eicosadiynoic acid, 9,12-Octadecadiynoic acid and Hexadecanedioic acid share a common residue in Isoleucine ⁷⁶. Finally, Glutamic acid ⁷⁹ is a common residue between 8,11-Eicosadiynoic acid and 9,12-Octadecadiynoic acid. With this small screening of ligands undertaken to determine suitable candidates for the ligand binding partner, it has resulted in the identification of possible key residues in play. The significance each common residue plays in the ligand interaction with ZAG can be investigated by focusing on each residue individually.

Table 3.1. Candidate Ligands for Docking Simulations in ZAG

Candidate ligands were chosen based on their similarity to stearic and palmitic acid. Ligand .pdb files were obtained through the Protein Data Bank (PDB) and were initially analysed using the UCSF Chimera protein imaging software. The ligands were then uploaded to the Molculomics server and simulations of ligand docking were run using PLANTS software to compare with the crystallised DAUDA orientation in native ZAG. Total ligand score is an accumulation of the total interactions between ligand and ZAG.

Candidate	Ligand Score	Chemical Formula
8,11-Eicosadiynoic acid	-115.276	C ₂₀ H ₃₂ O ₂
Arachidic acid	-112.568	C ₂₀ H ₄₀ O ₂
DAUDA	-111.062	C ₂₃ H ₃₄ N ₂ O ₄ S
9,12-Octadecadiynoic acid	-110.941	C ₁₈ H ₂₈ O ₂
Stearic acid	-106.141	C ₁₈ H ₃₆ O ₂
Hexadecanedioic acid	-104.965	C ₁₆ H ₃₀ O ₄
P6G	-104.131	C ₁₂ H ₂₆ O ₇
Heptadecanoic acid	-101.3	C ₁₇ H ₃₄ O ₂
16-Hydroxyhexadecanoic acid	-101.142	C ₃₂ H ₆₄ O ₆
2-fluoropalmitic acid	-97.984	C ₁₆ H ₃₁ FO ₂
Palmitic acid	-97.9451	C ₁₆ H ₃₂ O ₂
Myristic acid	-89.9454	C ₁₄ H ₂₈ O ₂
Lauric acid	-83.4269	C ₁₂ H ₂₄ O ₂
Undecanoic acid	-80.9033	C ₁₁ H ₂₂ O ₂
Decanoic acid	-75.6844	C ₁₀ H ₂₀ O ₂
Nonanoic acid	-72.2906	C ₉ H ₁₈ O ₂
Octanoic acid	-68.1017	C ₈ H ₁₆ O ₂

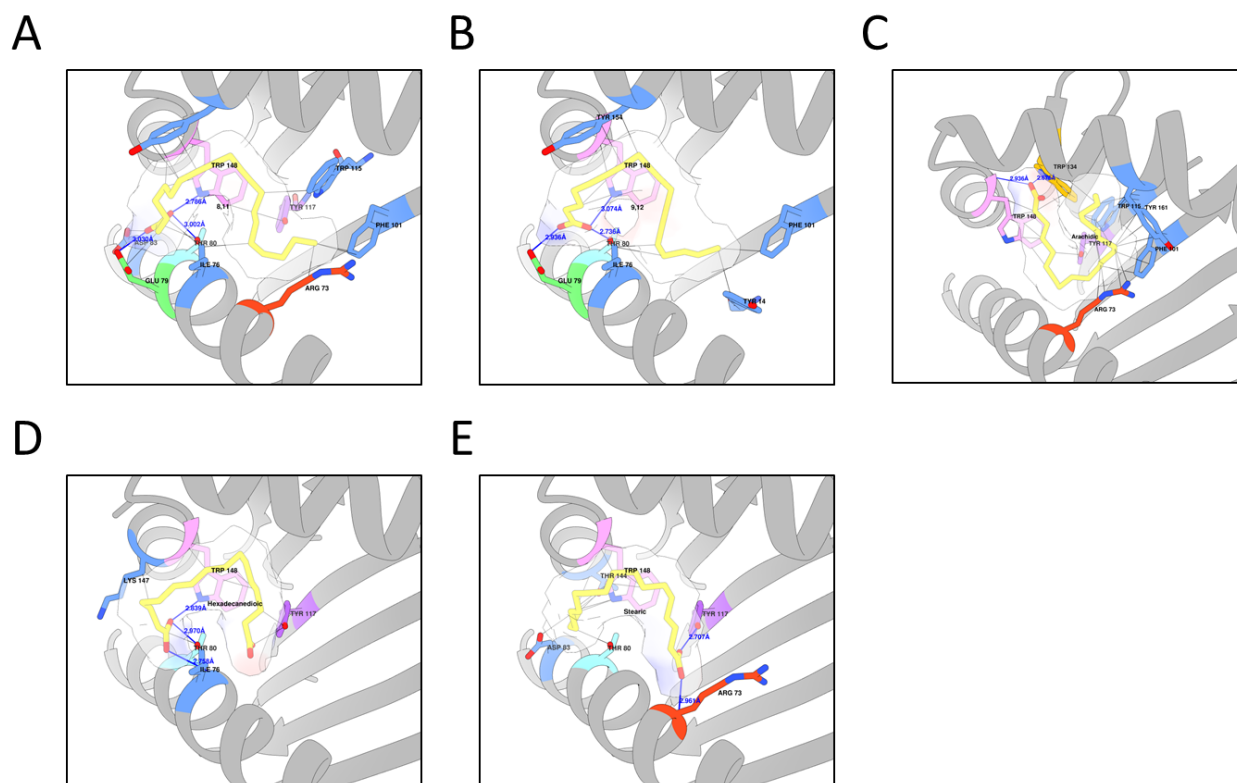


Figure 3. 3. Protein Modelling of Successful Candidate Ligand Dockings in ZAG

Candidate ligands were chosen based on their similarity to stearic and palmitic acid. Ligand .pdb files were obtained through the Protein Data Bank (PDB) and were initially analysed using the UCSF Chimera protein imaging software. The ligands were then uploaded to the Molculomics server and simulations of ligand docking were run using PLANTS software to compare with the crystallised DAUDA orientation in native ZAG. Successful ligands of 8,11-Eicosadiynoic acid (A), 9,12-Octadecadiynoic acid (B), Arachidic acid (C), Hexadecanedioic acid (D) and Stearic acid (E) were visualized using UCSF Chimera to identify the participating residues and the ligand interactions.

Table 3.2. Common Residues That are Interacting with Successful Ligand Candidates.

Successful ligands of 8,11-Eicosadiynoic acid, 9,12-Octadecadiynoic acid, Arachidic acid, Hexadecanedioic acid and Stearic acid were visualized using UCSF Chimera to identify the participating residues and the ligand interactions. Common residues were identified and collated to determine importance of the interacting residues.

Common Residues for Binding Ligand	Ligands That are Using These Residues
Tryptophan ¹⁴⁸	8,11-Eicosadiynoic acid 9,12-Octadecadiynoic acid Arachidic acid Hexadecanedioic acid Stearic acid
Threonine ⁸⁰	8,11-Eicosadiynoic acid 9,12-Octadecadiynoic acid Hexadecanedioic acid Stearic acid
Tyrosine ¹¹⁷	8,11-Eicosadiynoic acid 9,12-Octadecadiynoic acid Hexadecanedioic acid Stearic acid
Arginine ⁷³	8,11-Eicosadiynoic acid Arachidic acid Stearic acid
Phenylalanine ¹⁰¹	8,11-Eicosadiynoic acid 9,12-Octadecadiynoic acid Arachidic acid
Isoleucine ⁷⁶	8,11-Eicosadiynoic acid 9,12-Octadecadiynoic acid Hexadecanedioic acid
Glutamic acid ⁷⁹	8,11-Eicosadiynoic acid 9,12-Octadecadiynoic acid

3.1.4 Evaluating the Degree in which ZAG Residue Mutations Effect Lipid Binding

By analysing the top ligand candidates, common residues that these ligands interact with were identified. To gain an understanding if any of these residues are significant in the way these ligands could bind, each residue would be mutated to an alanine and the dockings would be repeated. Of note, the rotamers function in UCSF Chimera allows the mutation of these residues but keeps the protein in the same orientation as the wild-type. This allows consistency with the wild-type dockings to investigate the interactions with the residue, but does not consider the conformational change that could occur with structural residue changes. This type of work could be included with a molecular dynamics program that simulates these changes, however for our residue interaction investigations, this static approach is suitable. Tryptophan¹⁴⁸ and Arginine⁷³ were the first residues to be mutated using the rotamers function in UCSF Chimera. The candidate ligands 8,11-Eicosadiynoic acid, 9,12-Octadecadiynoic acid, Arachidic acid, Hexadecanedioic acid, Stearic acid and DAUDA were docked using the method as previously set out in ***3.1.2 Validation of Ligand Docking Program PLANTS***.

Tryptophan¹⁴⁸ Alanine

8,11-Eicosadiynoic acid (Figure 3.4 A) and 9,12-Octadecadiynoic acid (Figure 3.4 B) docked in a different orientation in relation to the wild-type. Both ligands are no longer exhibiting hydrogen bonds with Tryptophan¹⁴⁸ mutant and the ‘head’ of the ligands are now facing the Arginine⁷³ side. Arachidic acid (Figure 3.4 C) is in a similar orientation in both the wild-type and mutant, most likely due to the hydrogen bonding in the Tryptophan¹³⁴. Hexadecanedioic acid (Figure 3.4 D) exhibits a change in orientation with the left ‘head’ losing its hydrogen bond partner of Tryptophan¹⁴⁸ and instead, shifting upwards to the top of the groove and interacting with Threonine⁸⁰ and Isoleucine⁷⁶. Stearic acid (Figure 3.4 E) no longer interacts with Arginine⁷³ in the Tryptophan¹⁴⁸ mutant and is still in a similar orientation within the

groove. But, is not forming hydrogen bonds as seen in the wild-type. Finally, DAUDA (Figure 3.4 F) docked in the mutant results in a complete flip, with the oxygens located at the base of the rings now pointing towards the top of the pocket as opposed to the bottom seen in the wild-type's orientation.

Arginine⁷³ Alanine

Arginine⁷³ has been identified as a possible ligand anchor within the ZAG groove.

8,11-Eicosadiynoic acid, 9,12-Octadecadiynoic acid and Hexadecanedioic acid did not present a drastic shift in orientation when docked in the mutant in comparison to the wild-type (data not shown). In the wild-type, the Arginine⁷³ does not appear to play as a significant role in ligand binding in these candidates and could therefore be the reason for the lack of ligand orientation shift. However, Arachidic acid (Figure 3.5 A), Stearic acid (Figure 3.5 B) and DAUDA (Figure 3.5 C) have all presented radical changes in their docking position within the groove. Despite not showing hydrogen bonding with Arginine⁷³, Arachidic acid has become outstretched and not fitting in the proposed ZAG-ligand binding pocket (Figure 3.5 A). Stearic acid has reversed without its capacity to exhibit hydrogen bonding with the Arginine⁷³ residue (Figure 3.5 B). And finally, as seen with the Tryptophan¹⁴⁸ residue mutation (Figure 3.5 F) DAUDAs' position has shifted drastically with the rings now orientated towards the Tryptophan¹⁴⁸ end as opposed to the Arginine⁷³ side.

Threonine⁸⁰ Alanine

8,11-Eicosadiynoic acid (Figure 3. 6 A) and Hexadecanedioic acid (Figure 3. 6 C) maintained a similar orientation in relation to the wild-type. Both ligands are still able to interact with the Tryptophan¹⁴⁸ residue which help maintain the ligand's orientation within the pocket. 9,12-Octadecadiynoic acid (Figure 3. 6 B) as a result of the mutation now presents the 'head'

upwards as opposed to pointing downwards. Stearic acid (Figure 3. 6 D) also has a similar orientation to 9,12-Octadecadiynoic acid in the mutant. However, stearic acid has flipped horizontally due to Threonine 80 no longer being able to exhibit Van der Waals forces on the tail end of the ligand and hold it in place. Lastly DAUDAs (Figure 3. 6 E) orientation has also changed. Despite Threonine ⁸⁰ not appearing to interact with DAUDA as Arginine ⁷³ does, the mutation appears to affect the way the rings cannot align in the groove made by Arginine ⁷³, Phenylalanine ¹⁰¹, Tryptophan ¹¹⁵ and Tyrosine ¹⁶¹.

Phenylalanine ¹⁰¹ Alanine

8,11-Eicosadiynoic acid (Figure 3. 7 A) and 9,12-Octadecadiynoic acids (Figure 3. 7 B) head are no longer fixed down towards the important residue cluster of Isoleucine ⁷⁶, Glutamic acid ⁷⁹, Threonine ⁸⁰ and Tryptophan ¹⁴⁸. Instead they now face upwards due to the absent interaction with Phenylalanine ¹⁰¹ holding the tail end of the ligands in place. The mutation of Phenylalanine ¹⁰¹ means it can no longer assist in helping the tail of Arachidic acid (Figure 3. 7 C) fit in the groove made by Arginine ⁷³, Phenylalanine ¹⁰¹, Tryptophan ¹¹⁵ and Tyrosine ¹⁶¹. Instead, the tail now resides towards the center and in consequence the head of the ligand now sits similarly to 8,11-Eicosadiynoic acid (Figure 3. 7 A) and 9,12-Octadecadiynoic acid (Figure 3. 7 B) in the wild-type. The rings of DAUDA (Figure 3. 7 D) do not fit in the groove as they do in the wild-type. As seen with Arachidic acid (Figure 3. 7 C), Phenylalanine ¹⁰¹ participates in holding DAUDA in this groove.

Tyrosine ¹¹⁷ Alanine

Both 8,11-Eicosadiynoic acid (Figure 3. 9 A) and DAUDA (Figure 3. 9 E) present similar orientations to their wild-type counterparts, indicating Tyrosine ¹¹⁷ does not play a major role in the interactions between ZAG and these ligands. 9,12-Octadecadiynoic acid (Figure 3. 9 B),

Hexadecanedioic acid (Figure 3. 9 C) and Stearic acid (Figure 3. 9 D) on the other hand are affected. The head of 9,12-Octadecadiynoic acid (Figure 3. 9 B) is now pointing upwards despite the minimal role Tyrosine ¹¹⁷ appears to have in the interactions. The absence of the oxygen from the Tyrosine ¹¹⁷ Alanine mutation means it is no longer exhibiting Van der Waals forces on Hexadecanedioic acid (Figure 3. 9 C) or hydrogen bonding with Stearic acid (Figure 3. 9 D). This results in the ligands flipping vertically and horizontally respectively.

Glutamic Acid ⁸⁰ Alanine

8,11-Eicosadiynoic acid (Figure 3. 10 A) and 9,12-Octadecadiynoic acid (Figure 3. 10 B) can no longer exhibit hydrogen bonding with Glutamic acid and therefore the head of the ligand is protruding out of the pocket. The mutation appears to not interact directly with DAUDA (Figure 3. 10 C) and results in minimal change to the ligand orientation.

Each single mutation has affected the ligand binding to various degrees, all of which have been quantified using a root mean square deviation test (RMSD). A RMSD takes the coordinates of all the atoms of the ligand in the wild type dockings and then compares them to the atom coordinates in the mutant dockings. If a score is below 2.5 Angstroms (Å), then the change in ligand orientation is deemed negligible and the mutations have had minimal effect on the docking simulations. If the RMSD score is above 2.5 Angstroms, then it is a significant result with the greater the value representing a greater ligand orientation change. The significant changes seen in the docking simulations are represented in **Table 3.3**, with the Tryptophan ¹⁴⁸ Alanine mutations affecting all of its ligand dockings whilst Isoleucine ⁷⁶ Alanine mutations (Figure 3. 8) had negligible effect in the docking of the candidate ligands.

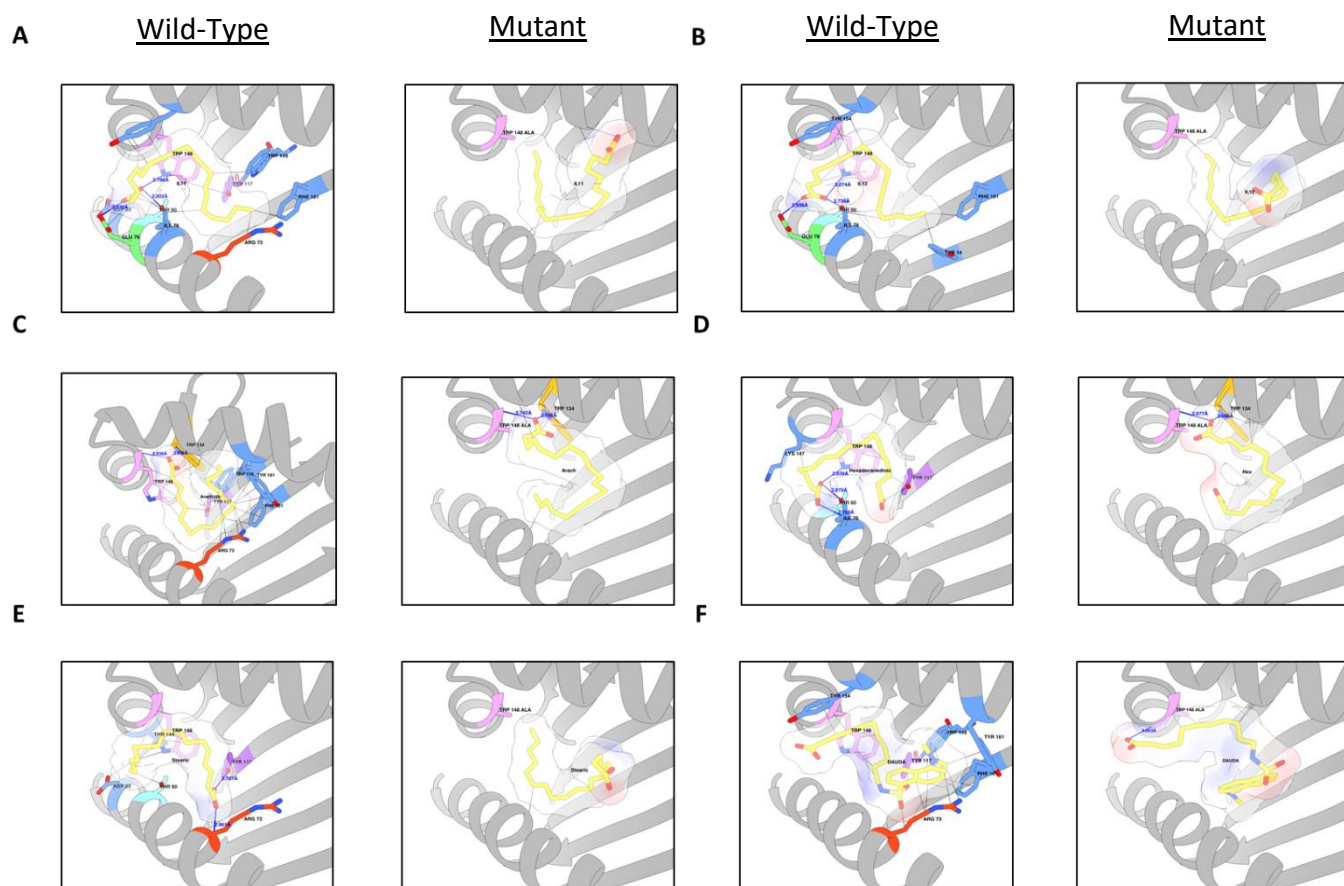


Figure 3. 4. Protein Modelling of Successful Candidate Ligand Dockings in Mutated Tryptophan¹⁴⁸

ZAG

Tryptophan¹⁴⁸, identified as a common residue, was mutated to an Alanine residue using UCSF Chimera. Mutated ZAG .pdb file was then uploaded to the Moleculomics server and simulations of ligand dockings using 8,11-Eicosadiynoic acid (A), 9,12-Octadecadiynoic acid (B), Arachidic acid (C), Hexadecanedioic acid (D), Stearic acid (E) and DAUDA (F) were run using PLANTS software to compare with native ZAG simulations. Ligand dockings were visualized using UCSF Chimera to identify the participating residues and the ligand interactions.

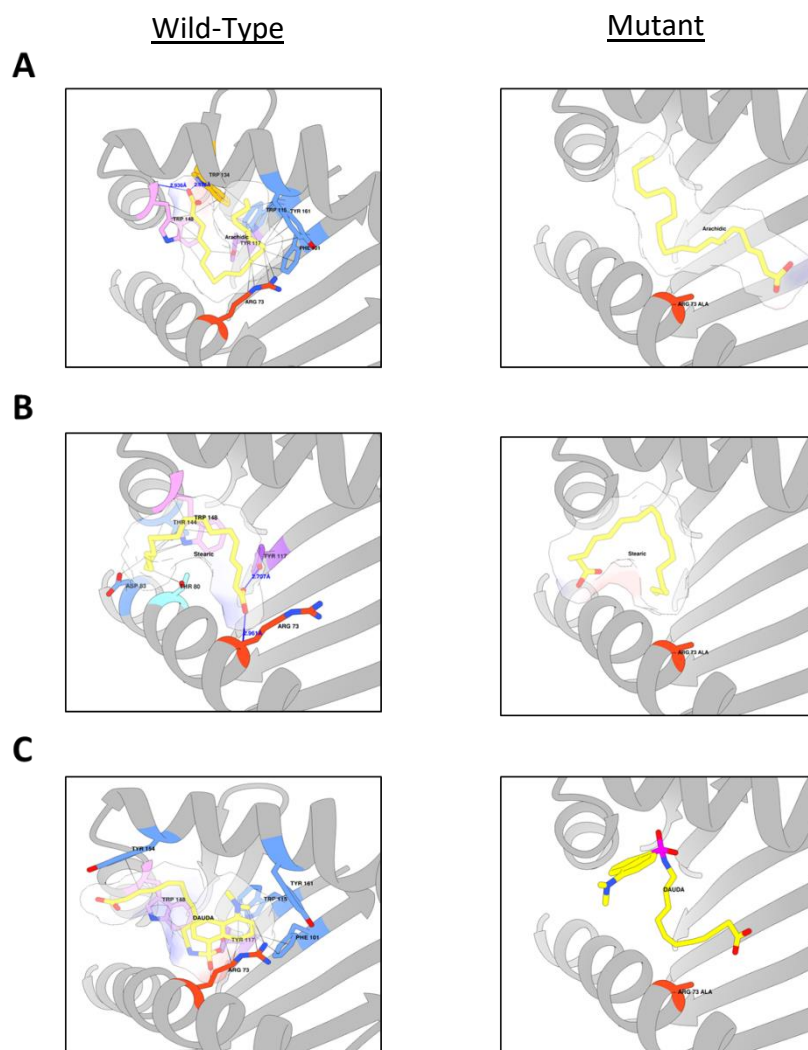


Figure 3. 5. Protein Modelling of Successful Candidate Ligand Dockings in Mutated Arginine⁷³ ZAG

Arginine⁷³, identified as a common residue, was mutated to an Alanine residue using UCSF Chimera. Mutated ZAG .pdb file was then uploaded to the Moleculomics server and simulations of ligand dockings using 8,11-Eicosadiynoic acid, 9,12-Octadecadiynoic acid, Arachidic acid (A), Hexadecanedioic acid, Stearic acid (B) and DAUDA (C) were run using PLANTS software to compare with native ZAG simulations. Ligand dockings were visualized using UCSF Chimera to identify the participating residues and the ligand interactions.

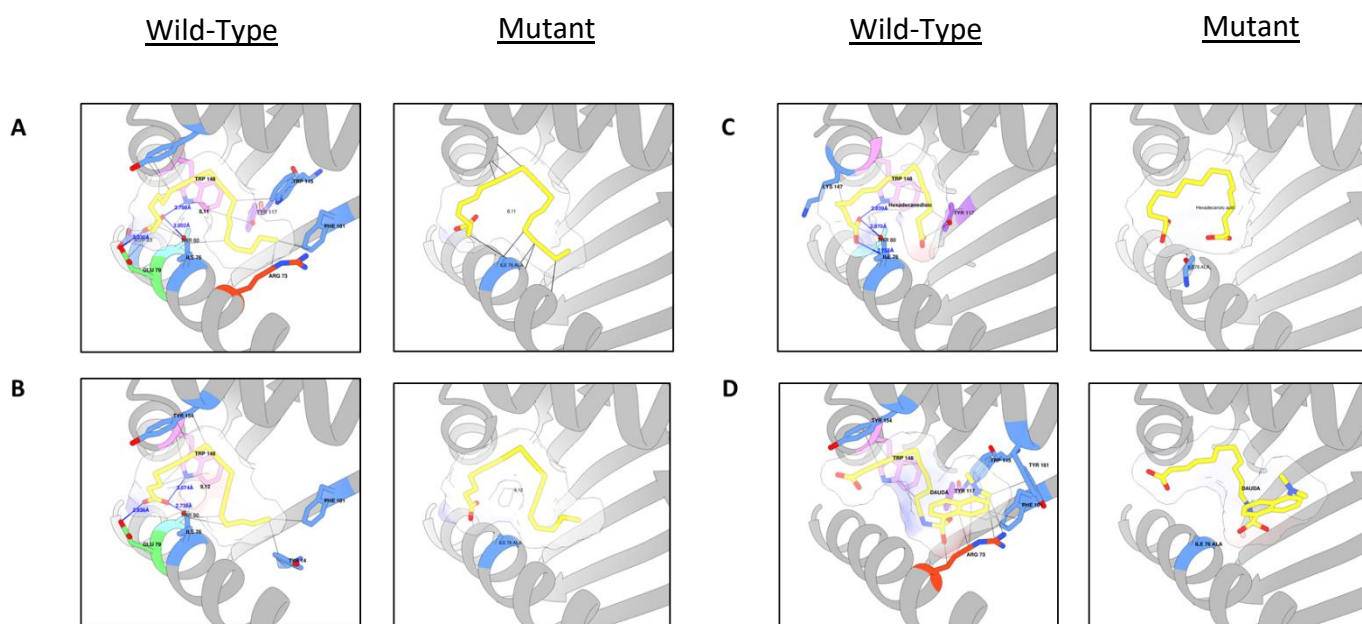


Figure 3. 8. Protein Modelling of Successful Candidate Ligand Dockings in Mutated Isoleucine ⁷⁶

ZAG

Isoleucine ⁷⁶, identified as a common residue, was mutated to an Alanine residue using UCSF Chimera. Mutated ZAG .pdb file was then uploaded to the Moleculomics server and simulations of ligand dockings using 8,11-Eicosadiynoic acid (A), 9,12-Octadecadiynoic acid (B), Hexadecanedioic acid (C) and DAUDA (D) were run using PLANTS software to compare with native ZAG simulations. Ligand dockings were visualized using UCSF Chimera to identify the participating residues and the ligand interactions.

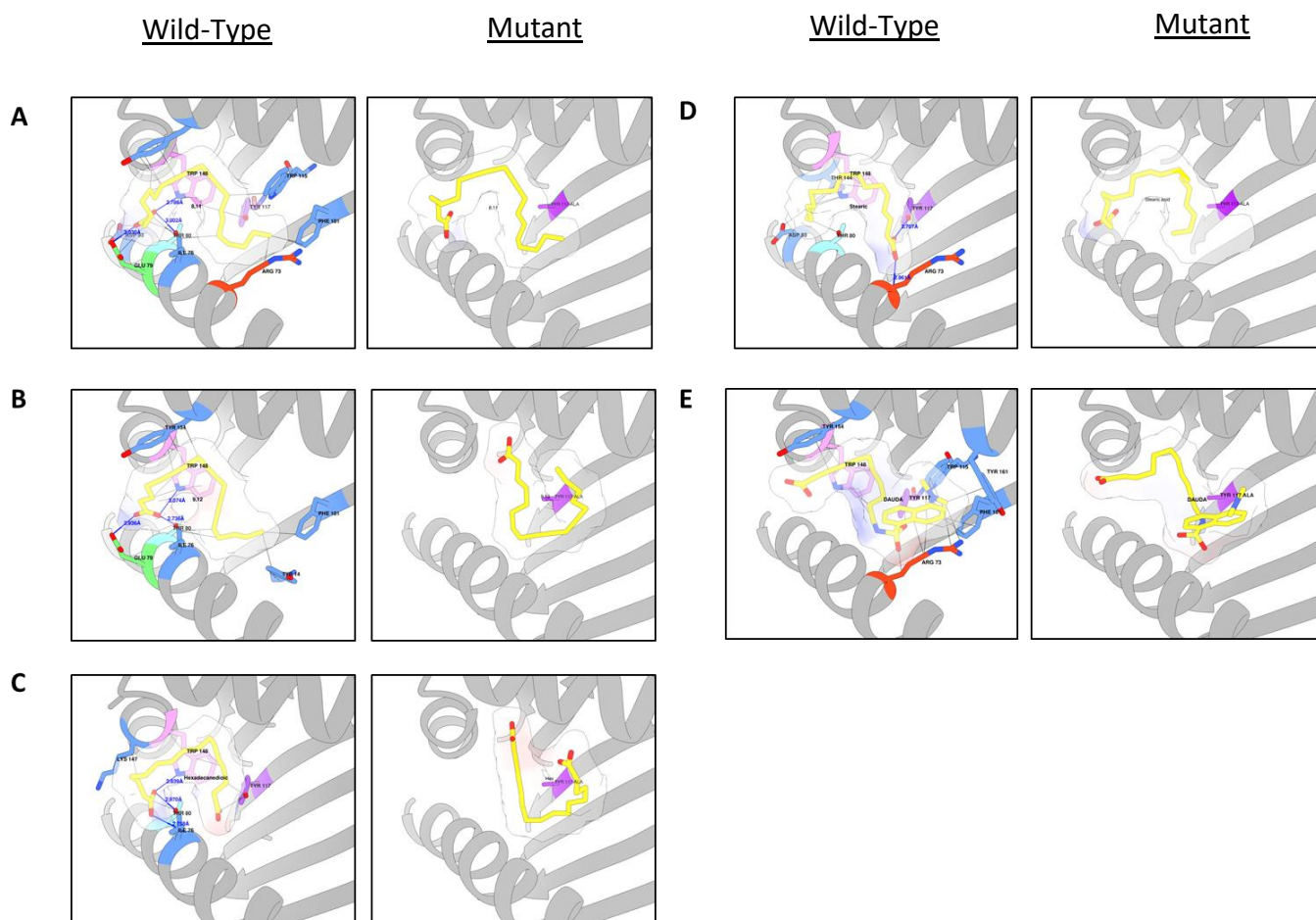


Figure 3. 9. Protein Modelling of Successful Candidate Ligand Dockings in Mutated Tyrosine ¹¹⁷ ZAG

Tyrosine ¹¹⁷, identified as a common residue, was mutated to an Alanine residue using UCSF Chimera. Mutated ZAG .pdb file was then uploaded to the Moleculomics server and simulations of ligand dockings using 8,11-Eicosadiynoic acid (A), 9,12-Octadecadiynoic acid (B), Hexadecanedioic acid (C), Stearic acid (D) and DAUDA (E) were run using PLANTS software to compare with native ZAG simulations. Ligand dockings were visualized using UCSF Chimera to identify the participating residues and the ligand interactions.

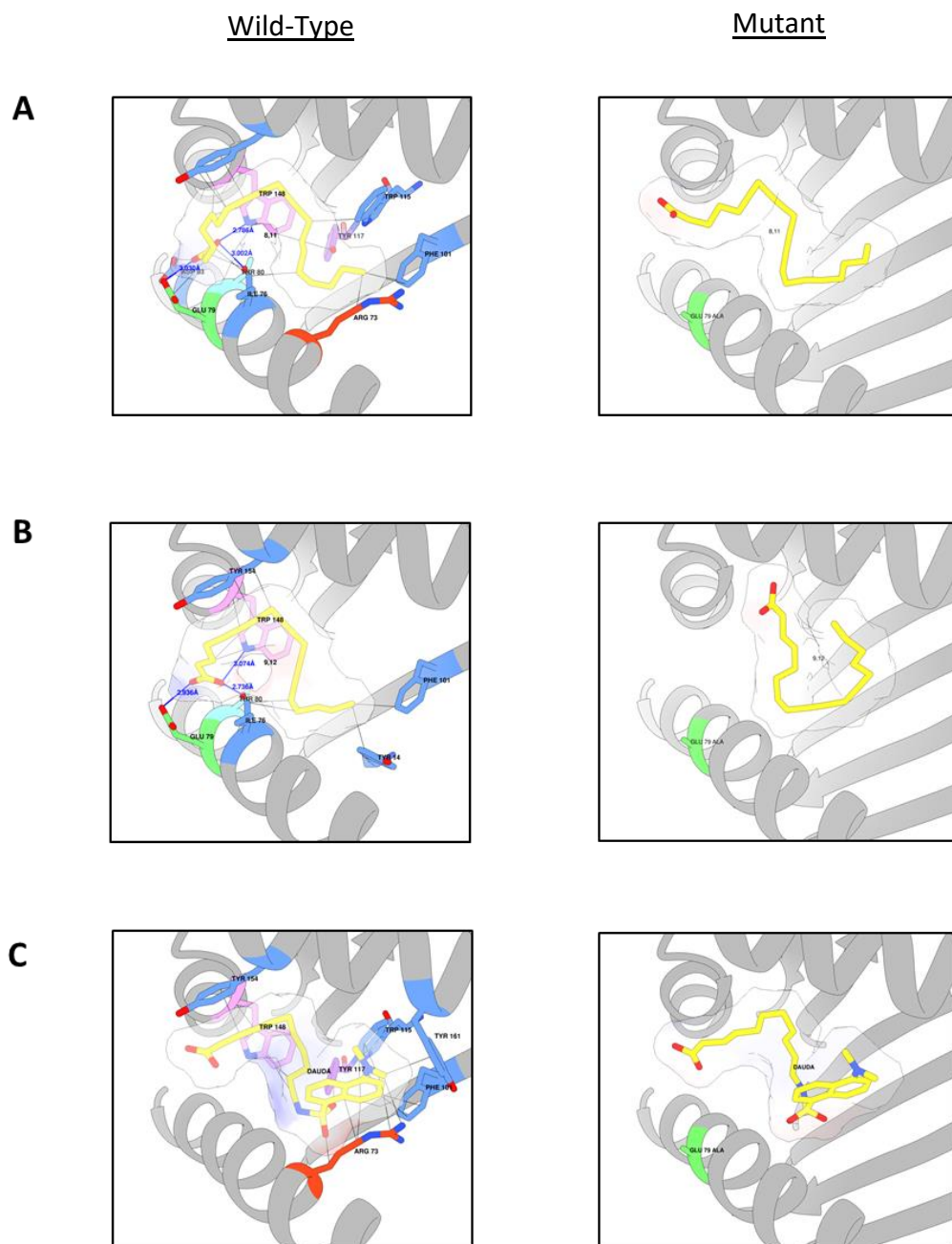


Figure 3. 10. Protein Modelling of Successful Candidate Ligand Dockings in Mutated Glutamic Acid

⁸⁰ ZAG

Glutamic Acid ⁸⁰, identified as a common residue, was mutated to an Alanine residue using UCSF Chimera. Mutated ZAG .pdb file was then uploaded to the Moleculomics server and simulations of ligand dockings using 8,11-Eicosadiynoic acid (A), 9,12-Octadecadiynoic acid (B) and DAUDA (C) were run using PLANTS software to compare with native ZAG simulations. Ligand dockings were visualized using UCSF Chimera to identify the participating residues and the ligand interactions.

Table 3.3. RMSD Scores of Candidate Ligands Docked in Native and Mutated ZAG

Candidate ligands that had been docked into mutant variants of ZAG were subjected to a Root Mean Square Deviation (RMSD) test to identify the difference in atom positions between the wild type and mutant dockings. Results were then organised based on the significant change in ligand orientation.

*indicates the RMSD test is not effective for these ligands.

Common Residues Mutated to Alanine	Ligands That are Affected by Residue Mutations	RMSD score compared to native docking (Å)
Tryptophan ¹⁴⁸	8,11-Eicosadiynoic acid 9,12-Octadecadiynoic acid Hexadecanedioic acid Stearic acid Arachidic acid DAUDA	9.933 9.614 7.92 7.548 7.92 5.547
Threonine ⁸⁰	Stearic acid 9,12-Octadecadiynoic acid Hexadecanedioic acid DAUDA	10.110 7.325 6.539* 7.234
Tyrosine ¹¹⁷	Hexadecanedioic acid 9,12-Octadecadiynoic acid Stearic acid	8.070 7.436 6.876
Arginine ⁷³	Arachidic acid Stearic acid	8.121 6.56
Phenylalanine ¹⁰¹	Arachidic acid 9,12-Octadecadiynoic acid 8,11-Eicosadiynoic acid DAUDA	8.779 7.152 4.085 3.742
Isoleucine ⁷⁶	Hexadecanedioic acid	6.253*
Glutamic acid ⁷⁹	9,12-Octadecadiynoic acid 8,11-Eicosadiynoic acid	7.398 3.876

3.1.5 Expanding Ligand Binding Simulations with Other ZAG Mutants

When the identified important residues have been mutated to alanine they lose their side chain, and as a result have been seen in some cases to have a significant effect in the way the ligands are binding in the pocket. As well as the mutations to alanine, Tryptophan ¹⁴⁸ and Arginine ⁷³ were mutated to all of the other amino acids to see what influence they had in the ligand docking simulations. The fatty acids of 8,11-Eicosadiynoic acid and Arachidic acid were chosen as they were impacted the most by the alanine mutation of the Tryptophan ¹⁴⁸ and Arginine ⁷³ residues respectively. A selection of mutations are depicted in Figure 3. 11 and Figure 3. 12 with all of the RMSD scores for Tryptophan ¹⁴⁸ and Arginine ⁷³ presented in **Table 3.4** and **Table 3.5** respectively.

Tryptophan ¹⁴⁸ Mutations

These further mutations performed on Tryptophan ¹⁴⁸ effect the docking of 8,11-Eicosadiynoic acid negatively as reflected in the RMSD scores in **Table 3.4**. All of the scores exceed the 2.5 Å cut off with no mutations presenting a score close to that mark. Despite the Tryptophan ¹⁴⁸ Glutamine mutation having a nitrogen to facilitate hydrogen bonding in the same way the wild type Tryptophan ¹⁴⁸ does, it is not the case. The ligand, as is the case with the other mutations depicted, no longer interacts with the cluster of Isoleucine ⁷⁶, Glutamic acid ⁷⁹ and Threonine ⁸⁰ residues, but now points upwards. The Serine residue has the greatest effect on the ligand orientation with a RMSD scoring of 10.065 Å and whilst still a vast change in orientation, Phenylalanine presents the lowest scoring of 7.032 Å.

Arginine ⁷³ Mutations

These further mutations performed on Arginine ⁷³ effect the docking of Arachidic acid negatively as reflected in the RMSD scores in **Table 3.5**. Again, all of the scores exceed the

2.5 Å cut off. The Tyrosine mutation results in the greatest change in Arachidic acid orientation with a score of 9.367 Å, whilst the change to Glutamine results in the lowest score of 5.534 Å.

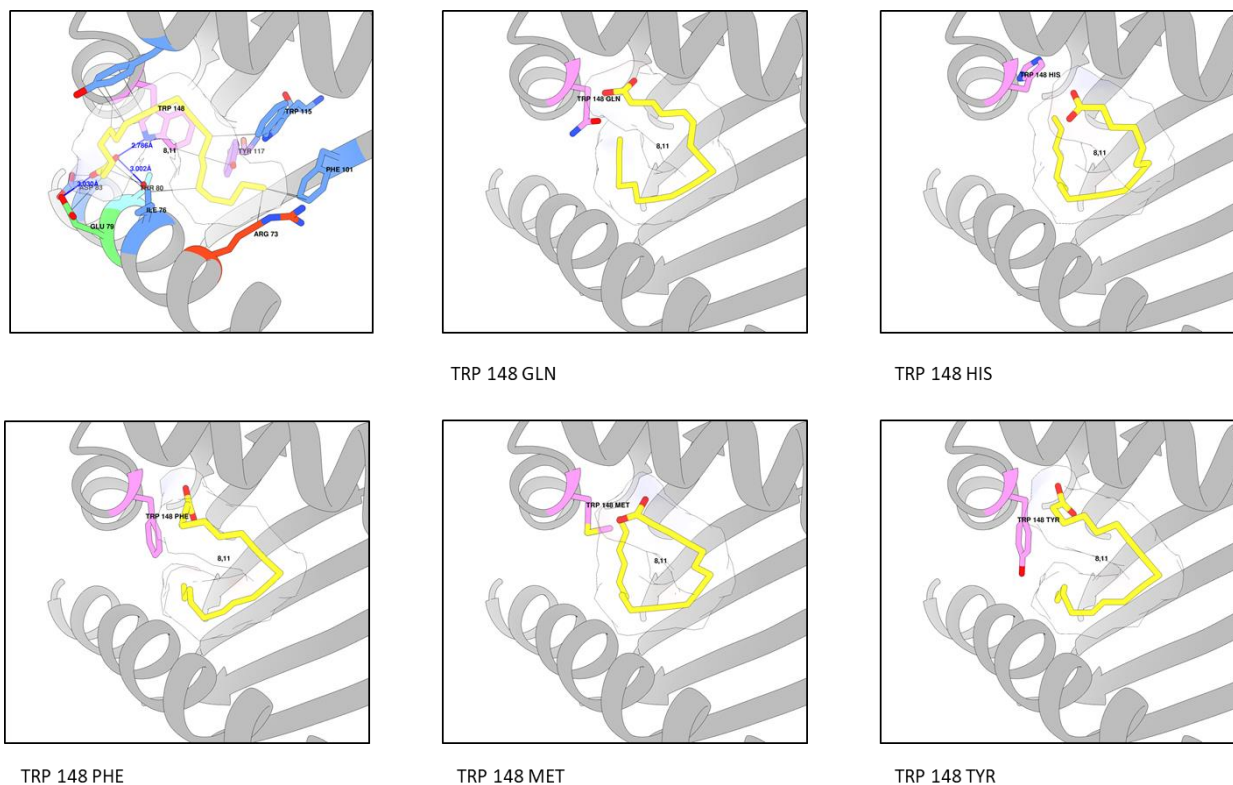


Figure 3. 11. Selection of Protein Docking Models in Tryptophan¹⁴⁸ Mutation Simulations

Tryptophan¹⁴⁸, identified as a common residue, was mutated to all other amino acid residues using UCSF Chimera. Mutated ZAG .pdb file was then uploaded to the Molculomics server and simulations of ligand dockings using 8,11-Eicosadiynoic acid were run using PLANTS software to compare with native ZAG simulations. Ligand dockings were visualized using UCSF Chimera to identify the participating residues and the ligand interactions.

Table 3.4. RMSD Scores of 8,11-Eicosadiynoic acid Docked in Mutant ZAG Variants in Comparison to Native ZAG

8,11-Eicosadiynoic acid docked into mutant variants of ZAG were subjected to a Root Mean Square Deviation test to identify the difference in atom positions between the wild type and mutant dockings. Results were then organised based on the significant change in ligand orientation.

Tryptophan ¹⁴⁸ Residue Mutation	RMSD score of 8,11-Eicosadiynoic acid in mutated ZAG in comparison to Tryptophan ¹⁴⁸ binding (Å)
Serine	10.065
Alanine	9.933
Histidine	8.950
Methionine	8.903
Glutamic Acid	8.378
Lysine	8.278
Leucine	8.187
Valine	8.171
Proline	8.148
Glycine	8.115
Cysteine	8.093
Aspartic Acid	8.083
Threonine	8.080
Isoleucine	7.931
Asparagine	7.900

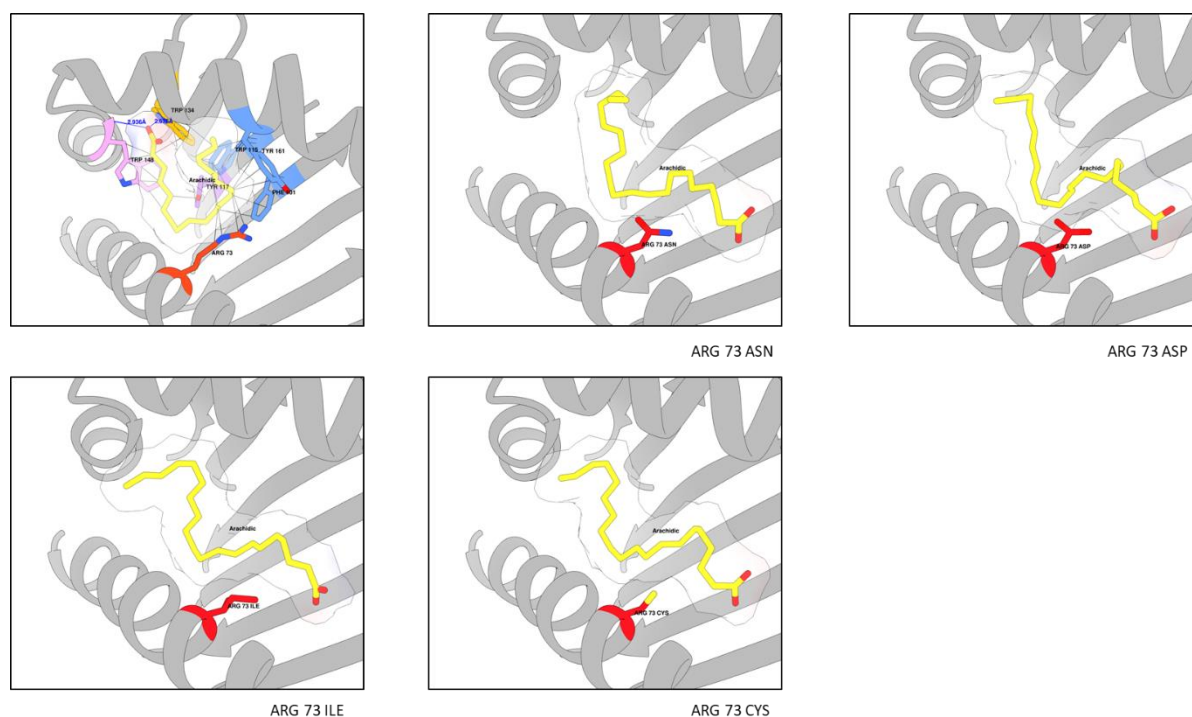


Figure 3. 12. Selection of Protein Docking Models in Arginine ⁷³ Mutation Simulations

Arginine ⁷³, identified as a common residue, was mutated to all other amino acid residues using UCSF Chimera. Mutated ZAG .pdb file was then uploaded to the Molculomics server and simulations of ligand dockings using Arachidic acid were run using PLANTS software to compare with native ZAG simulations. Ligand dockings were visualized using UCSF Chimera to identify the participating residues and the ligand interactions.

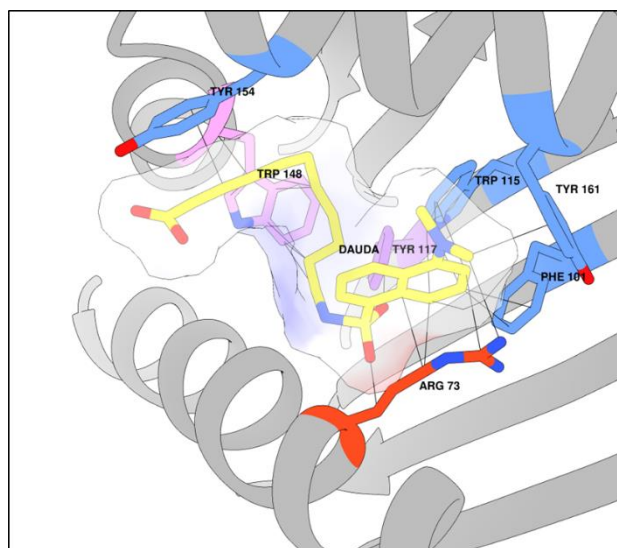
Table 3.5. RMSD Scores of Arachidic acid Docked in Mutant ZAG Variants in Comparison to Native ZAG

Arachidic acid docked into mutant variants of ZAG were subjected to a Root Mean Square Deviation test to identify the difference in atom positions between the wild type and mutant dockings. Results were then organised based on the significant change in ligand orientation.

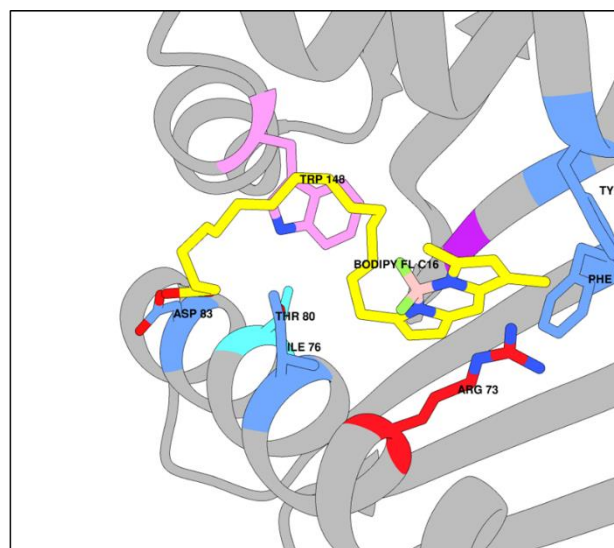
Arginine ⁷³ Residue Mutation	RMSD score of arachidic in mutated ZAG in comparison to Arginine ⁷³ binding (Å)
Tyrosine	9.367
Phenylalanine	9.203
Tryptophan	8.832
Histidine	8.762
Glycine	8.605
Lysine	8.506
Glutamic Acid	8.350
Threonine	8.303
Methionine	8.187
Leucine	8.178
Proline	8.140
Cysteine	8.127
Alanine	8.121
Isoleucine	8.111
Serine	7.900
Aspartic Acid	7.844
Asparagine	7.731
Valine	7.374
Glutamine	5.534

3.1.6 Investigating A Reported Second Binding Site Within ZAG's Groove

Our *in silico* data has provided preliminary investigatory evidence of the importance that each residue plays in the binding of ligands in the pocket and altering them to other residues results in poor ligand binding as shown by the docking images and RMSD scores. Interestingly, a study was recently published that has introduced the idea of ZAG having two independent binding sites within the same pocket (Zahid et al. 2021). The study had used two fluorescent probes, DAUDA and C16 BODIPY alongside a number of ligands to demonstrate their hypothesis. Their findings suggested that ZAG could accommodate two ligands independently and C16 BODIPY's binding site was separate from DAUDA. If these findings are true, then all docking work up to this point could be scrutinized and the significance of having a secondary binding site going forward would present further complications in finding a therapeutic relating to ZAG. Curiously, *in silico* docking experiments had been performed but there were no docking images in the paper and no docking of C16 BODIPY itself (Zahid et al. 2021). We had decided then to dock C16 BODIPY into ZAG ourselves and see where it resided within the pocket. C16 BODIPY was docked using the same coordinates provided in the McDermott paper. With our docking techniques, it appears C16 BODPIY resides in the same area as DAUDA and with the same important residues identified with our previous dockings (Figure 3. 13).



DAUDA



BODIPY C16

Figure 3. 13. Proposed Binding Site of BODIPY C16

Crystallised structure of ZAG and DAUDA ligand was obtained through Protein Data Bank (PDB) and was initially analysed using the UCSF Chimera protein imaging software (A). The ligand C16 BODIPY was obtained as a SMILES code and converted to mol.2 file. This file was uploaded to the Molculomics server and a simulation of ligand docking was run using PLANTS software to compare with the crystallised DAUDA orientation in native ZAG (B).

3.2 Discussion

3.2.1 Establishing ZAGs Biochemistry with *in silico* Docking Work

Although initial docking simulations with P6G did not match the crystalized orientation, this does not conflict with subsequent results. Due to the size and flexibility of the P6G ligand, it will have many orientations within the pocket and therefore a ligand with a well-defined structure was required. DAUDA had also been crystalized in the pocket of ZAG and due to its dansyl head group, provided a structure with less flexibility in docking orientation and therefore a good base comparison to validate the *in silico* method of docking. The DAUDA simulation match (Figure 3.2) then gives confidence to screen the candidate ligands (Table 3.1). The PLANTS docking program compiles a score for each ligand docking simulation based on the interactions the ligand has with the surrounding residues such as van der Waals forces and hydrogen bonds. The DAUDA that was docked (Figure 3. 2) is our known ligand example and therefore our control to compare the candidate ligands against. These screened ligands that then produced a similar score have merit that they could be a ligand and binding partner for ZAG. From the 20 candidate ligands screened, the 5 of 8,11-Eicosadiynoic acid, 9,12-Octadecadiynoic acid, Arachidic acid, Hexadecanedioic acid and Stearic acid were the closest match to our control of DAUDA (Table 3.1). The molecular models obtained from the docking simulations show key common residues that were interacting with the ligands (Table 3.2). Although these residues have been observed (Kennedy et al., 2001; McDermott et al., 2006), these common residues have been identified independently from the dockings with no bias input and further validate the docking simulations work. Tryptophan¹⁴⁸ was chosen for mutation first as it was identified to interact with all the successful ligand candidates in the docking simulations. With the residue mutated to an alanine, there was no longer the nitrogen on the tryptophan available to exhibit hydrogen bonding with the oxygen on the ligands. It

appears that Tryptophan ¹⁴⁸ plays a significant role in the binding of these ligands based on the shift of orientation in the mutant compared to the wild type presented in the ligand dockings (Figure 3. 4).

As with Tryptophan ¹⁴⁸, the Arginine ⁷³ was also identified as a potential important residue in the ZAG-ligand interaction. Although it was not identified to interact with as many ligands as the tryptophan residue, its position at the end of the binding pocket presented it as a potential target. By mutating the Arginine ⁷³ to an alanine it does appear to play a significant role in the binding of Arachidic acid, Stearic acid and DAUDA due to drastic change in binding within the pocket. Previous studies have shown that Arginine side chains bind fatty acids such as arachidonic in the adipocyte lipid-binding protein (ALBP) (LaLonde et al., 1994). With Arachidic acid also being a 20-carbon chain fatty acid, it was chosen via the screening process and the arginine to alanine mutation resulting in the ligand orientation adds further validation to the Arginine ⁷³ being important in the ligand binding site of ZAG. These simulations then have to be translated into *in vitro* experiments. The Gould lab has pQE60 plasmids expressing these mutant variants of ZAG. BL21 cell lines have been transformed and the mutant ZAG is now ready to be produced using the protocol that has been produced from the work carried out in steps 4.1.3 – 4.1.7. Time prevented further work on this element of the project.

3.2.2 Further Investigation into the ZAG Ligand Binding Pocket

The *in silico* data presented in **3.1.3 Evaluating the Degree in which ZAG Residue Mutations Effect Lipid Binding** and **3.1.4 Expanding Ligand Binding Simulations with Other ZAG Mutants** provide preliminary investigatory evidence on the importance of the identified residues in the ZAG ligand binding groove. Alongside the conformational changes and interactions identified from the docking of the candidate ligands, the mutation of these residues and RMSD scores collected, further emphasize the role the native residues play in ligand binding within the groove. As discussed in **3.1.3 Evaluating the Degree in which ZAG Residue Mutations Effect Lipid Binding** a RMSD score above 2.5 is a representation that the ligands position has significantly changed as a result of the mutations. By introducing further mutant models, it provides further evidence of the importance of the original residues and helps consolidate our *in silico* work. As observed in Table 3.2 and Table 3.3, mutation to another amino acid does not improve the docking of the ligands under the conditions selected. The RMSD score is evaluated by comparing the selected ligand docking coordinates in the mutated ZAG in comparison to our original ligand dockings in native ZAG. However, as observed for fatty acids like Hexadecanedioic acid, the symmetry of the molecule highlights a limitation in the scoring system. Hexadecanedioic acid is residing in the same place as the wild type in Isoleucine⁷⁶ ALA and Threonine⁸⁰ ALA, but the score of 6.253 and 6.539 respectively would suggest otherwise. The ligand has flipped horizontally, meaning the oxygen atoms now reside on the opposite side. The coordinates given for these atoms are therefore different and the scoring is a result of this. However, due to the symmetry of the molecule, Hexadecanedioic acid can have the same orientation, but the scoring cannot reflect this. However, taking these two outliers aside, the mutations, dockings and RMSD scoring provide further simulated evidence in the importance of the native residues.

As described in **3.1.4 Evaluating the Degree in which ZAG Residue Mutations Effect Lipid Binding**, a limitation in this *in silico* study is the use of a static docking simulation as opposed to a dynamic docking program. A further limitation of this study would be scale. 20 candidate ligands were docked in ZAG and mutant variants of ZAG, however implementing a ... would allow for a larger scale screening to be performed. This would mean a greater quantity of candidates analysed and possible identification of more ligands.

3.2.3 New Insights or Conflicting Information?

As discussed previously, it has been hypothesized that ligand interactions in ZAG's groove would be imperative to give ZAG its biological function. The groove identified between the $\alpha 1$ and $\alpha 2$ domains has been shown to have an electron density residing in a pocket formed by the designated important amino acid residues. Only in this position has it been discussed that the ligand would reside. However, two recent studies by (Zahid et al. 2016) and (Zahid et al. 2021) have suggested otherwise. This group hypothesised that ZAG has two independent binding sites adjacent to one another in the same groove and that these can accommodate two ligands simultaneously. If this were to be the case, all of our in silico work would need to be reevaluated. Their hypothesis is based on spectrofluorimetric data. As discussed in 4.1.7 Validating the Refolding Procedure of ZAG, fluorophores like DAUDA and BODIPY will emit a different wavelength of fluorescence depending on their environment. The first case put forward is that as ZAG oligomerises with the addition of increasing concentration of zinc, the binding site is obstructed and effects BODIPY binding but not DAUDA, concluding that BODIPY utilizes a different binding site in the groove of ZAG to DAUDA (Zahid et al. 2016). The second paper expands this further by suggesting that DAUDA and BODIPY compete for the same pocket as the two separate binding sites overlap with one another (Zahid et al. 2021). The supplementary data provided in (Zahid et al. 2021) shows the same shifts in fluorescence as observed previously, however, these shifts are observed with BODIPY and ligands in the absence of ZAG. The papers reasoning behind this is "Oxidative photo-induced electron transfer from the singlet excited state of the BODIPY fluorophore to an electron-poor chelator on the BODIPY probe causes an increase in BODIPY fluorescence emission intensity". The notion is that BODIPY and ligands are creating a complex with one another, which the ZAG groove can accommodate side by side as opposed to the ligand competing with the BODIPY fluorophore. However, we believe that the explanation of this arises from the formation of micelles. Micelles

are a cluster of amphiphilic molecules that will form when fatty acids in solution aggregate to provide protection for their hydrophobic tails (Figure 3. 14). In these instances, the fluorescent probe -which is also a fatty acid derivative- can integrate into these micelles and result in artificial fluorescence spikes due to the probe transitioning from the aqueous state to an apolar state. Each fatty acid chain length has a critical micelle formation index (CMC) that measures when micelle formation will occur (Table 3.6). There isn't a 'tipping point' for micelle formation, instead it is an accumulation process based on the fatty acids available. If this is the case, then it would be critical to verify this with our own experiments as the current findings are superficial. With this reasoning, the idea would be to repeat these BODIPY and ligand experiments to generate data to show that the fluorescence peaks are from micelle formation and not the BODIPY and ligands binding side by side in the ZAG pocket as suggested.

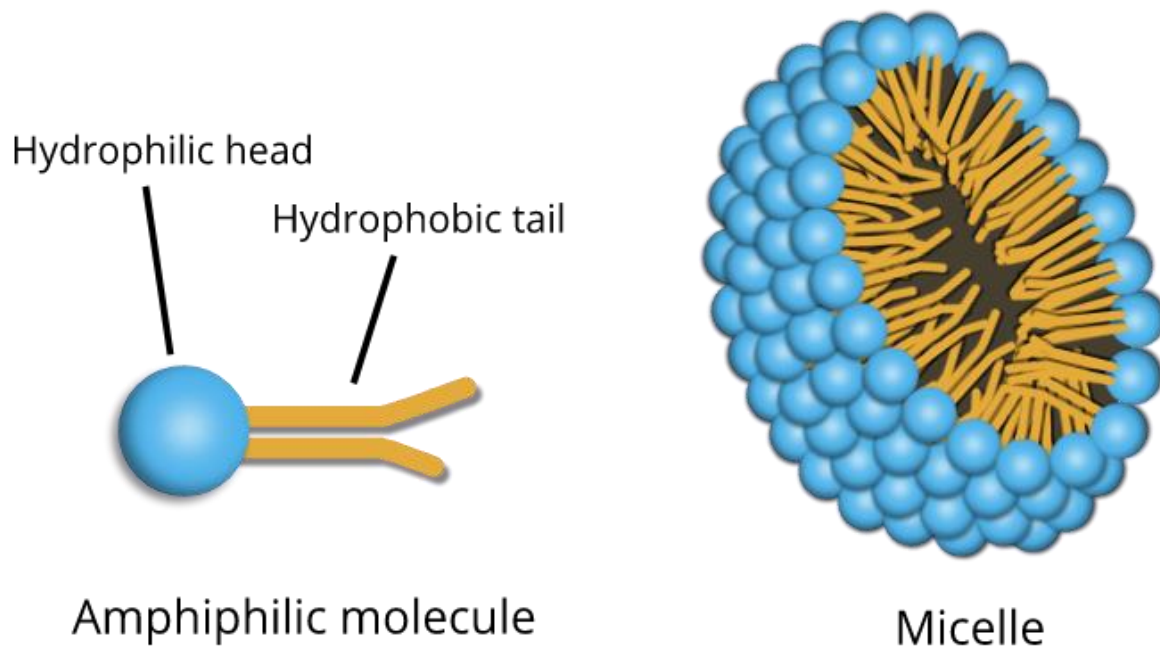


Figure 3. 14. Representation of Micelle Formation

Amphiphilic molecules like fatty acids consist of a hydrophilic head and a hydrophobic tail (left). When these molecules are in solution, they aggregate together to protect the hydrophobic tail and form a micelle (right).

Table 3.6. Critical Micelle Formation Index

When lipids accumulate to a certain concentration, they reach their critical micelle formation concentration (CMC). Micelle formation can interfere with experiments such as the Spectro-fluorimetry work with fluorophores and result in false positives.

Lipid	CMC (mM)
5:0 PC	90
6:0 PC	15
7:0 PC	1.4
8:0 PC	0.27
9:0 PC	0.029
10:0 PC	0.005
12:0 PC	90 nM
14:0 PC	6 nM
16:0 PC	0.46 nM
8:0 PG	1.21
10:0 PG	0.42
12:0 PG	0.13
14:0 PG	0.011

Lipid	CMC (mM)
4:0 PS (5mM Ca ²⁺)†	4
5:0 PS (5mM Ca ²⁺)†	2
6:0 PS (5mM Ca ²⁺)†	1.2
7:0 PS (5mM Ca ²⁺)†	0.8
8:0 PS (5mM Ca ²⁺)†	0.4
8:0 PS	2.282
10:0 PS	0.096
8:0 Lyso PC	60
10:0 Lyso PC	6-8
12:0 Lyso PC	0.4-0.9
14:0 Lyso PC	0.043-0.090
16:0 Lyso PC	4-8.3 µM
18:0 Lyso PC	0.4 µM

Lipid Acronyms Key

PC = phosphatidylcholine

PG = phosphatidylglycerol

PS = phosphatidylserine

Preliminary investigatory work has begun on this two site hypothesis with the docking simulation shown in Figure 3. 13. This is the same BODIPY fluorophore that was used in the spectrofluorimetric experiments and the same coordinates have been used to dock BODIPY as the paper used for their own docking experiments. The proposed new binding site is formed with the residues of Tyrosine¹², Glutamate⁶¹, Leucine⁶⁹, Arginine¹⁵⁷, Alanine¹⁵⁸, Glutamate¹⁶⁵ and Threonine¹⁶⁹, and from our docking, BODIPY does not dock in the newly proposed second binding site shown in Figure 3. 15, but resides in the same pocket as the original site. This provides us with preliminary data to support the micelle formation hypothesis and gives reason to question the two binding site findings. To further build on from this work, we can perform docking simulations that will dock the BODIPY and selected ligands simultaneously and observe if they are indeed accommodated side by side in ZAG's pocket.

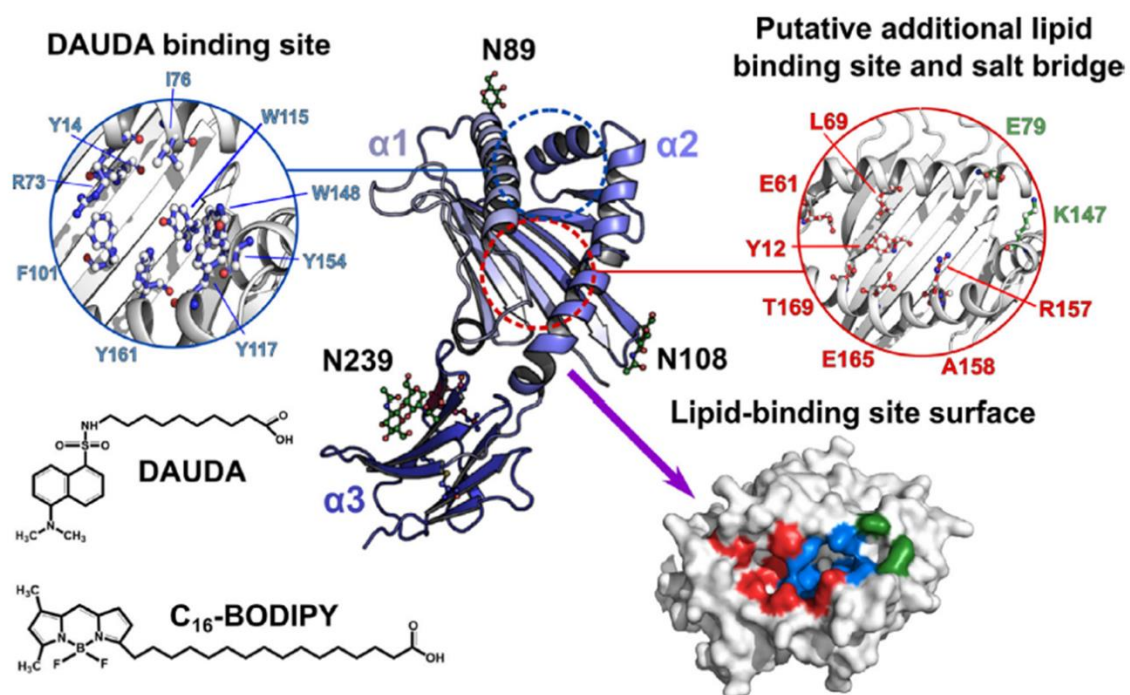
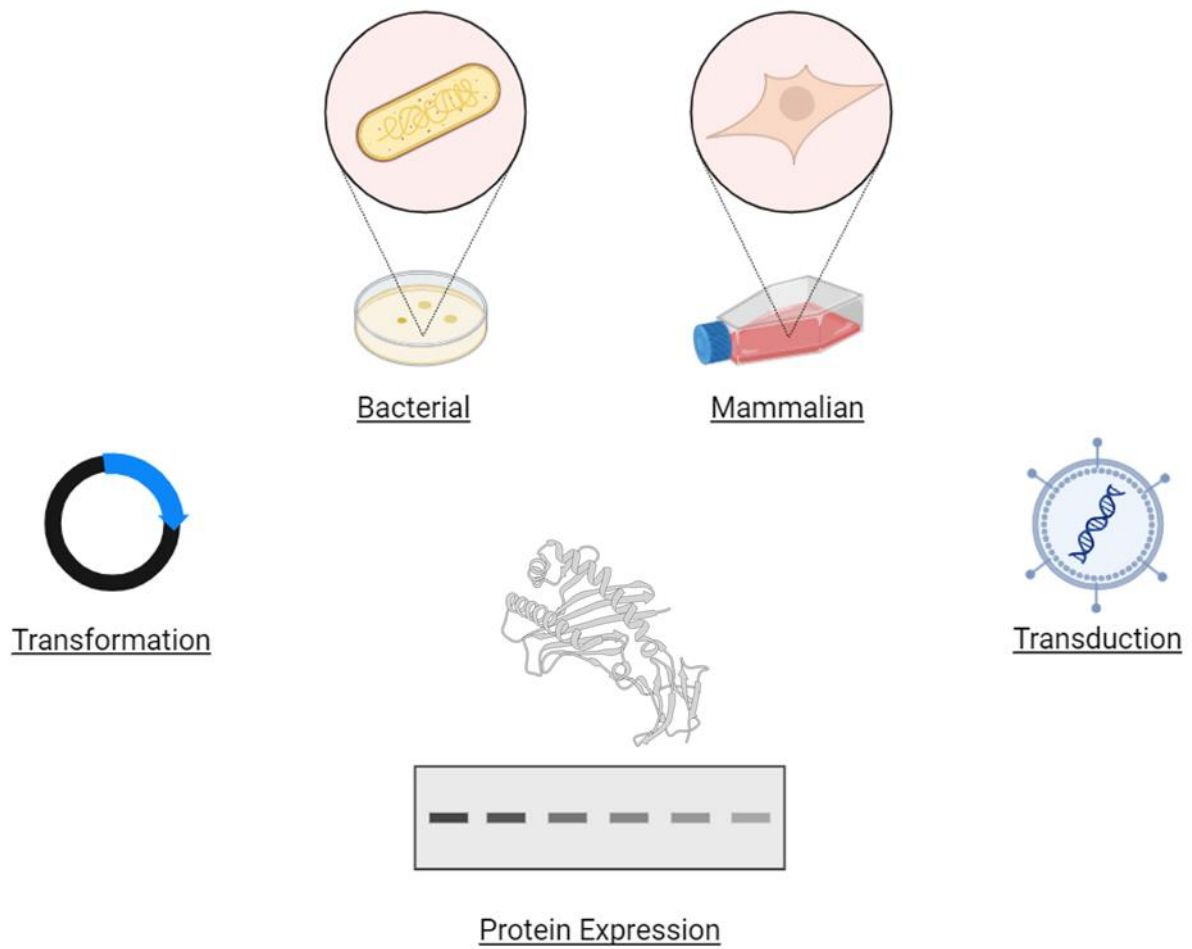


Figure 3. 15. Proposed Secondary Binding Site in ZAG

Original ligand binding site is represented in blue whilst the new site is represented in red. Figure has been taken from (Zahid et al. 2021)

Chapter 4

ZAG Expression Methodology



4.0 ZAG Expression Methodology

4.1.1 Introduction

The original intention was to visit Oxford Expression Systems to perform expression tests for protein production. Unfortunately, due to COVID restrictions the facility closed to external visitors and did not reopen in time for the visit to take place. The intention of this visit was to test various expression systems (bacterial, yeast, baculovirus, mammalian cells) and determine which suited best for our protein production. With the expertise and guidance available, this process was anticipated to have taken around 3 months. Without this, we proceeded to express our protein and looked at various expression systems to make our protein in house. Protein expression systems are essential tools for the production of recombinant proteins, playing a critical role in molecular biology, biopharmaceuticals, and industrial applications. The choice of expression system is guided by factors such as protein complexity, requirement for post-translational modifications (PTMs), yield, scalability, and cost. Examples of systems used include bacterial, insect, and mammalian cell cultures, each with specific advantages and limitations for heterologous protein expression (Rivera-De-Torre et al., 2022).

Bacterial Expression Systems, in particularly *Escherichia coli* (*E. coli*) are a favoured vector for protein production as they can be readily transformed with an engineered plasmid. The plasmid is engineered to express a protein of interest and can be grown under selection pressure with a resistant gene present such as G418 or Blasticidin S. *E. coli* are capable of rapid growth of high density cultures in short time frames which result in large scale protein production accounting to mg/ml of final product. Due to their easy handling, they are widely used and are therefore cultured through robust methods using well defined medias such as a Terrific Broth or 2YT resulting in a cost effective method.

One drawback however are bacteria's lack of organelles such as the Golgi and Endoplasmic Reticulum resulting in protein production lacking post translation modifications (PTMs) such as glycosylation, phosphorylation and acetylation (Bhatwa et al., 2021). These PTMs can be crucial to a protein's function and therefore opens questions to proteins synthesised via bacteria in their effect in mammalian cells. Another crucial complication is that proteins expressed in bacteria cells can be packaged in inclusion bodies (Bhatwa et al., 2021). When produced in high quantities, the proteins are misfolded and are contained in these inclusion bodies and therefore the cells have to be treated harshly with UREA or Guanidinium to release the protein and denature it. This protein then has to be refolded and these extra steps can add further steps in protein production. However, they are a strong model for structural enzymes and basic proteins and with their forgiving handling, high yields and cheap costs are an effective model. Another consideration is insect cell expression systems using *Spodoptera frugiperda* (Sf9, Sf21) with the Baculovirus Expression Vector System (BEVS). This system is primarily used in the production of recombinant proteins including vaccines, viral coat proteins, and eukaryotic proteins used in functional assays and structural biology (Felberbaum, 2015). Although these are a more specialised system of protein production, this is the system the group in Oxford specialise in. Compared to bacterial systems, the insect cell culture requires large bioreactors and the ability to transfer the genes via transduction (Schütz et al., 2023). It is also a more complicated system with a greater number of steps resulting in greater time consumption. However, unlike the bacterial cells, protein production in insect cells undergo the PTMs mentioned above with proper protein folding and therefore can be used to 'map' post translational effects on protein activity (Schütz et al., 2023). With the large bioreactors in place protein production can be at a larger scale. Protein production can be excreted from the media making for easier collection and purification with no need for denaturing and refolding steps as seen in some bacterial systems (Schütz et al., 2023).

The last system introduced here is mammalian cell expression systems which utilise cells such as Chinese Hamster Ovary (CHO) cells and Human Embryonic Kidney (HEK293) cells (Fliedl et al., 2015). These are immortal cells lines that can be cultured and passaged for extended periods making them a desired candidate for protein production (Fliedl et al., 2015). These systems are preferred over insect cells for producing therapeutic proteins, such as monoclonal antibodies, cytokines, and hormones, as well as viral vectors for gene therapy due to their closeness to human cell protein production (McKenzie & Abbott, 2018). Mammalian cells are also burdened with a greater price point with specialised media such as DMEM and bovine serum, heated incubators and extensive cell culture periods in air flow cabinets to generate stable cell lines. However, despite these requirements, lab groups that include cell culture in their practice have these facilities in place and with personnel well versed in cell culture techniques. As these cells are mammalian, proteins undergo the PTMs like the insect cells but are related closer to human PTMs which is desirable when studying a protein for its effects in a human system like our ZAG is in cachexia (McKenzie & Abbott, 2018). Again, these proteins are secreted with correct folding due to disulphide bond formation (Darby & Creighton) and with being secreted into the surrounding media of cells, can be collected and concentrated for treatments or even used to supplement media to form a conditioned media (Dowling & Clynes, 2011). Stable cell lines can be generated through various means such as transfection with DNA and a transfection reagent such as Lipofectamine or Xfect and then selected with a selection pressure such as G418 and Blasticidin S (Fus-Kujawa et al., 2021). Another method, transduction, uses a virus such as an adenovirus or lentivirus which leads to stable integration into the host cell and a higher rate of introduced gene expression (Fus-Kujawa et al., 2021).

With these multiple options on offer, the selection of a protein expression system depends on the endpoint for the user. Bacterial systems offer the highest yields and are highly scalable for simpler proteins, whilst insect and mammalian systems produce lower yields but result in

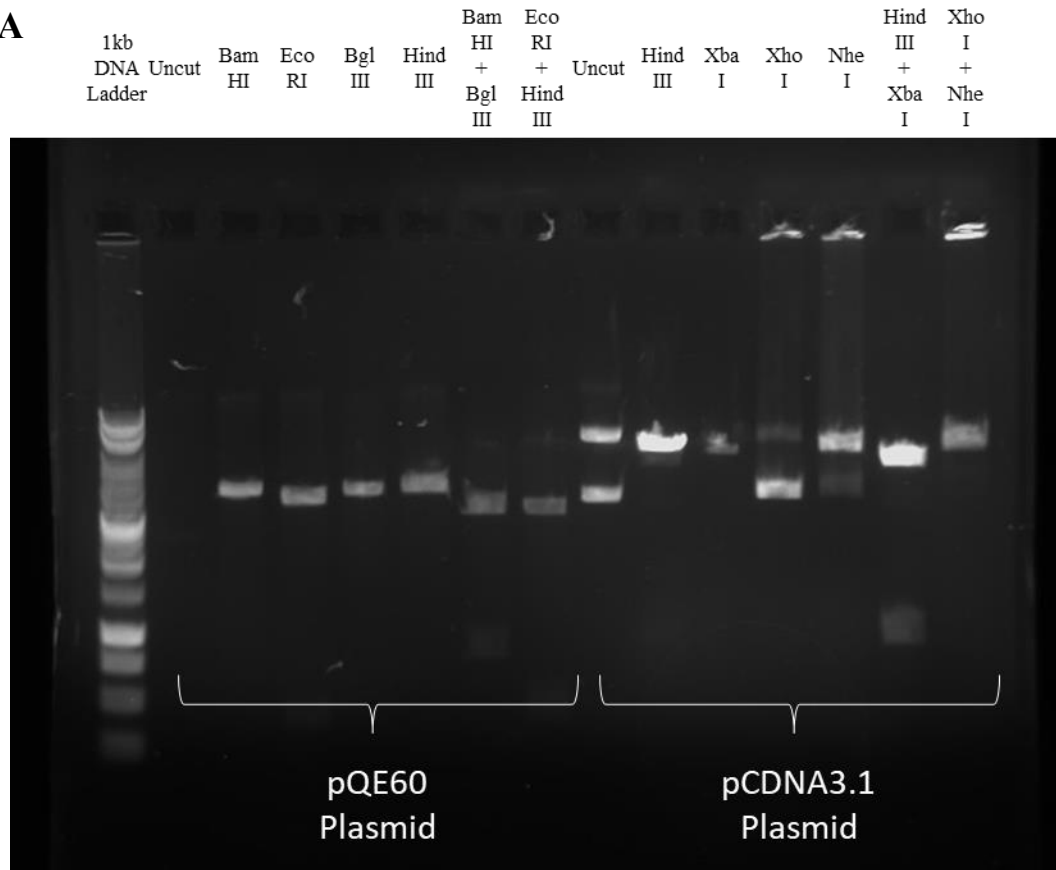
functionally relevant proteins with the required PTMs like glycosylation or phosphorylation (Duan & Walther, 2015; Ramazi & Zahiri, 2021).

In this chapter are outlined approaches for expression of ZAG using both bacterial and mammalian cell lines for subsequent functional analysis.

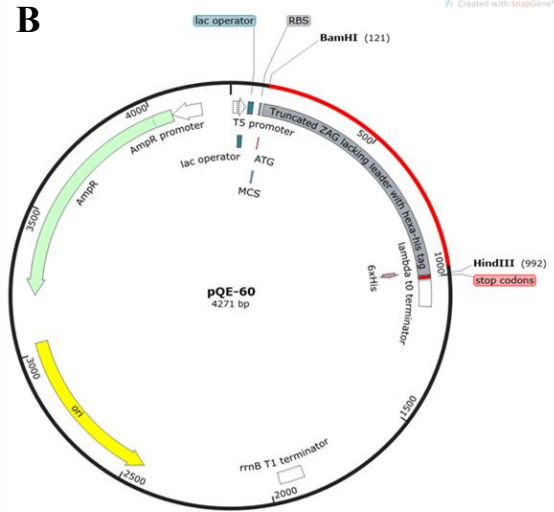
4.1.2 Conformation of pQE60 and pCDNA3.1 Plasmid Construction

A pQE60 plasmid with a ZAG expressing region was constructed to produce ZAG with no translational modifications in *E. coli* cells whilst a pCDNA3.1 plasmid expressing ZAG was constructed to express ZAG in mammalian cells with post-translation modifications that naturally occur. Both plasmids were manufactured by Genescript for the Gould Lab before my arrival (plasmid maps provided in Supplementary material). DH5- α cells were chosen for transformation as they are engineered to maximise transformation efficiency with a recA1 mutation that results in high plasmid insert stability (Kostylev et al., 2015). This recA1 mutation results in reduced recombinase activity and inhibits homologous recombination, therefore producing a greater transformation success rate. Each plasmid also contains an ampicillin resistance gene which allows the transformed cells to grow in presence of ampicillin whilst the wild type cells will not grow. Restriction digest assays were then performed to ensure the bacteria growing were expressing the correct plasmids and the restriction enzymes were cutting at the correct size (Figure 4. 1). pQE60 digest experiments resulted in single cuts with single digests using Bam HI, Eco RI, Bgl III and Hind III whilst a double digest of Bam HI + Bgl III resulted in two cuts producing two bands as predicted, one of which contains the ZAG coding sequence. The pCDNA3.1 double digest of Hind III + Xba I produced two bands as predicted, one of which encodes the ZAG insert.

A



B



C

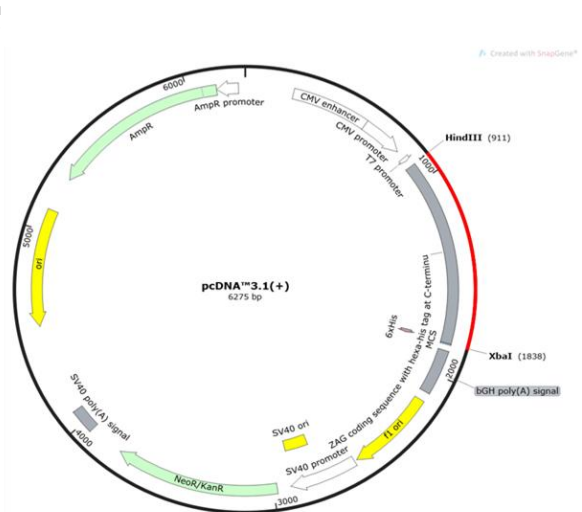


Figure 4. 1. Restriction Digest of pQE60 and pCDNA3.1 Plasmids

Minipreps of plasmids underwent single digests or double restriction digests as indicated before separation on agarose gels (A). Expected band sizes indicative of the presence of the ZAG insert were Bam/Bgl (for pQE60) and HindIII/XbaI (pCDNA3.1) which in both cases liberate the insert at the expected size. The small size of some of the released fragments mean they are not clearly visible on

this image. Both pQE-60 (B) and pcDNA3.1 (C) plasmids were designed and ordered by Gould lab from Genescript. Red line shows the addition of the ZAG insert cDNA. This included ZAG tagged with a hexa-his sequence at the C-terminus and lacking a leader sequence for the bacterial expression vector pQE60 as indicated (B). Plasmid maps were generated using SnapGene.

4.1.3 Optimising the Conditions for ZAG Expression in E. coli.

Now that plasmid transformations were shown to be successful, optimising growth conditions was the next step. Although DH5- α cells are optimal for plasmid transformation they are not be suitable for protein expression. BL21 *E. coli* competent cells are deficient in a cytoplasmic protease Lon and an outer membrane protease OmpT resulting in decreased protein breakdown and thus increased protein accumulation. Therefore, both DH5- α and BL21 cells were transformed and grown under various conditions to compare ZAG protein expression. DH5- α cells grown for 5 hours showed weak expression of ZAG in comparison with a 5-hour growth period of BL21, which showed a substantially greater expression of ZAG. The same was observed between the two strains for 24-hour growth – ZAG expression was consistently higher in BL21. Both plasmids were constructed with a lac operon gene to promote the expression of ZAG when in the presence of IPTG. However, IPTG induction appears to have a negligible effect in increasing ZAG production in both DH5- α and BL21 cells; this likely reflects a leaky promoter. Having established that BL21 cells grown for 24 hours expressed significant levels of ZAG, the next step was to optimise a method to extract ZAG from the transformed bacteria.

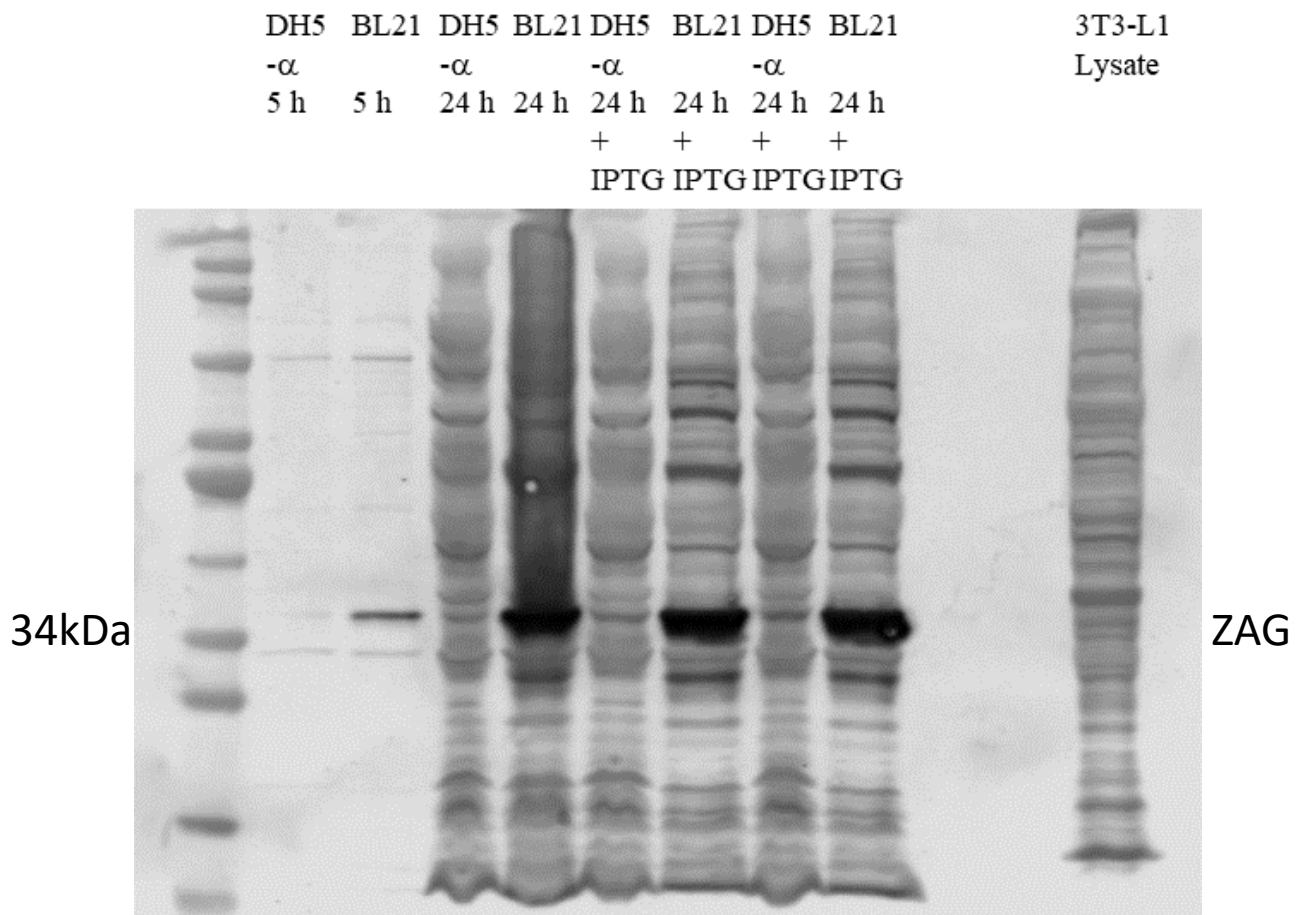


Figure 4. 2. Effects of Time and IPTG Induction on ZAG Expression in Transformed DH5-α and BL21 Competent Cells

DH5-α and BL21-pQE60 cells were grown at 37°C for 5 or 24 hours with or without induction using 1 mM IPTG. Cell lysates were analysed by Western Blotting for ZAG (34 kDa). Shown is a representative immunoblot using SIGMA anti-ZAG in which equal volumes of culture were loaded at each condition; similar data was also obtained using an Origene. Loaded in each lane are:

1. DH5 alpha 5 hour timepoint;
2. BL21 5 hour timepoint;
3. DH5 alpha 24 hour timepoint;
4. BL21 24 hour timepoint;
5. DH5 alpha 24 hour timepoint w/ IPTG induction;
6. BL21 24 hour timepoint w/ IPTG induction;
7. DH5 alpha 24 hour timepoint w/ IPTG induction (2);
8. BL21 24 hour timepoint w/ IPTG induction (2);

IPTG induction (2); 9. 3T3-L1 lysate sample. The positions of molecular weight markers are shown.

ZAG predicted size is 34.1 kDa.

4.1.4 Releasing ZAG from Inclusion Bodies in BL21 Cells.

When recombinant protein is expressed at high quantities in bacteria, it results in insoluble and misfolded protein being packaged in inclusion bodies. This is due to the foreign nature of the protein, with cysteine residues forming disulphide bonds which the bacteria systems do not support (Kennedy et al., 2001). Including the recombinant protein, inclusion bodies can also be heavily contaminated with other parts of the cell such as membrane and cell wall proteins. We considered it likely that ZAG may be in inclusion bodies and first tested this notion. BL21 bacteria expressing ZAG were grown overnight to achieve an OD_{600} of 1.0 and a cell pellet was collected. The pellet was lysed in 0.5% Triton X-100, 1 mM EDTA, followed by a centrifugation step, and a sample collected from the supernatant to determine the effectiveness of this step in releasing ZAG into a soluble fraction. The data in Figure 4.3 clearly reveal that even after two further extractions in detergent, the majority of ZAG remains in the pellet, representing inclusion bodies. Therefore, the next stage was to extract ZAG from the inclusion bodies and decontaminate it from other cellular proteins.

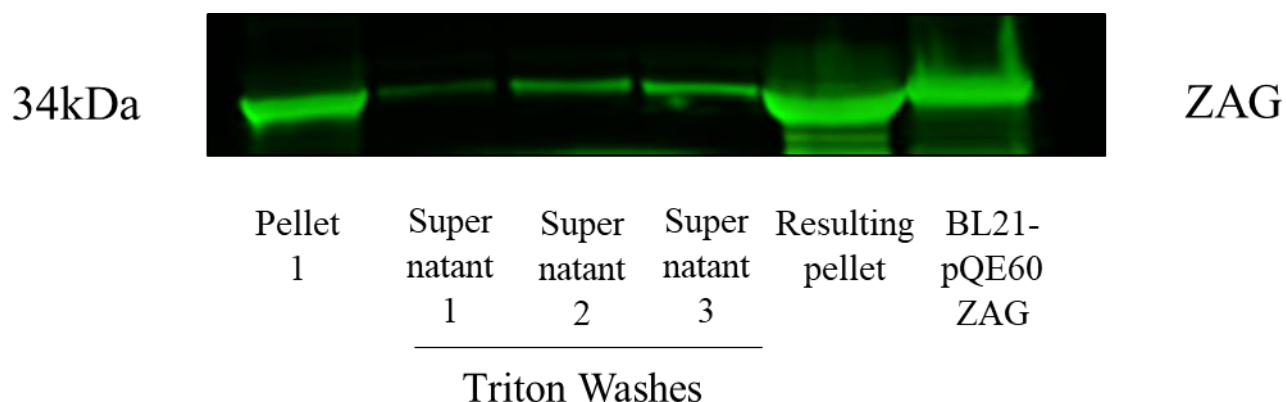


Figure 4. 3. Effects of Subsequent Triton-x-100 Wash Steps on the Cleanliness of ZAG Expression

BL21 expressing ZAG were grown to an OD₆₀₀ and centrifuged to harvest the bacteria. The cells were extracted using Triton X-100 to attempt to liberate soluble ZAG. The pellet from this first extraction is labelled Pellet 1 and the supernatant is labelled Supernatant 1. A further two extractions were performed (Supernatant 2 and 3) which liberated only modest amounts of proteins, with the majority of ZAG remaining in the Resulting pellet, indicating expression in inclusion bodies. The sample was centrifuged and a sample of supernatant collected and pellet washed in the same fashion. A positive control sample of BL21-pQE60 expressing ZAG was used for comparison of ZAG expression. Cell lysates and final pellet were analysed for ZAG (34 kDa) by Western blotting.

4.1.5 Denaturing and Refolding ZAG

The next process was to extract ZAG from the inclusion bodies by denaturing them and refolding the released protein (Garboczi et al., 1992). As shown in Figure 4. 3, the resulting pellet after Triton washes shows strong ZAG expression and we reasoned this was a good start-point as the detergent wash likely removes an element of contaminating proteins (although this was not formally examined). Urea extraction was used as outlined in section ***Method 2.2.5 Protein Purification*** and a representative result is shown in figure 4 .4. After the denaturing and refolding step, both supernatant and cell lysate samples were recovered. The pellet after Urea extraction contained a lower amount ZAG in comparison to the pellet before the denaturing and refolding steps. The supernatant however, resulted in a significantly increased ZAG concentration in comparison to the pellet. BL21 expressing ZAG was used a positive control. These results imply that ZAG has been released from the inclusion bodies and the next procedure would now be to isolate the ZAG protein to produce a homologous sample for experiments. Because of time limitations, we did not optimise this process as sufficient material was obtained from this method to allow further work. Hence, we focussed on the next stages.

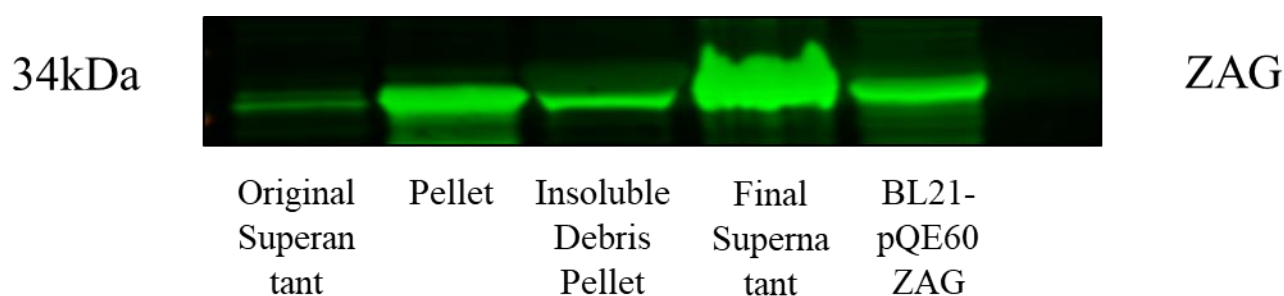


Figure 4. 4. Effects on ZAG Expression After Denaturing and Refolding Treatment of Resultant Triton X-100 Wash Step Pellet

After forming a tight pellet (Pellet), inclusion bodies were resuspended in 1ml of 8M urea to solubilise inclusion bodies. Thereafter 3ml of Refolding buffer (0.1 M Tris-HCl, 2 mM EDTA, 0.4 M L-arginine, 0.5 mM oxidised glutathione, 5 mM reduced glutathione) was added and incubated overnight at 4°C. Refolded sample was spun to pellet insoluble debris and final supernatant was collected. Original supernatant after triton wash steps (Original Supernatant) was included to confirm majority of ZAG resided in the pellet (Pellet) before denaturing steps. A positive control sample of BL21-pQE60 expressing ZAG was used for comparison of ZAG expression. Denatured sample was analysed for ZAG (34kDa) by Western blotting.

4.1.6 Evaluating Methods for Purifying ZAG

With the ZAG expressing in a large concentration in the resulting denatured-refolded supernatant mix, the next procedure was to purify the ZAG from the rest of the proteins in the mixture. The pQE60 plasmid was constructed so that the expressed ZAG has a His-Tag. This then allows the purification of ZAG through the application of Nickel beads or a Nickel column. Purification was attempted using Nickel beads, however a large quantity of ZAG was not attaching to the beads and furthermore, the ZAG that was attaching was not eluting off (data not shown). However, during this process, it became apparent that the majority of protein within the refolded fraction migrated with the molecular weight expected for ZAG (see below). Hence, we considered using this fraction 'neat' without subsequent purification as a first step in biological characterisation.

Two different approaches were then considered. The first, using a vivaspin 20 centrifugal concentrator and the second, dialysis. Both approaches were considered as they separate the desired target from the remaining contents they are in solution with. Figure 4. 5 shows the vivaspin experiment and a refolded ZAG sample obtained through the procedure described in ***Method 2.2.5 Protein Purification***. When processed in a vivaspin chamber, the refolded ZAG remains in the top compartment of the concentrator and everything else passes through the filter into the bottom of the tube. The concentrated ZAG solution produced a clean intense signal on both immunoblot and SDS-PAGE staining (Figure 4. 5). Similarly, the dialysis experiment also resulted in a clean intense ZAG expression (data not shown).

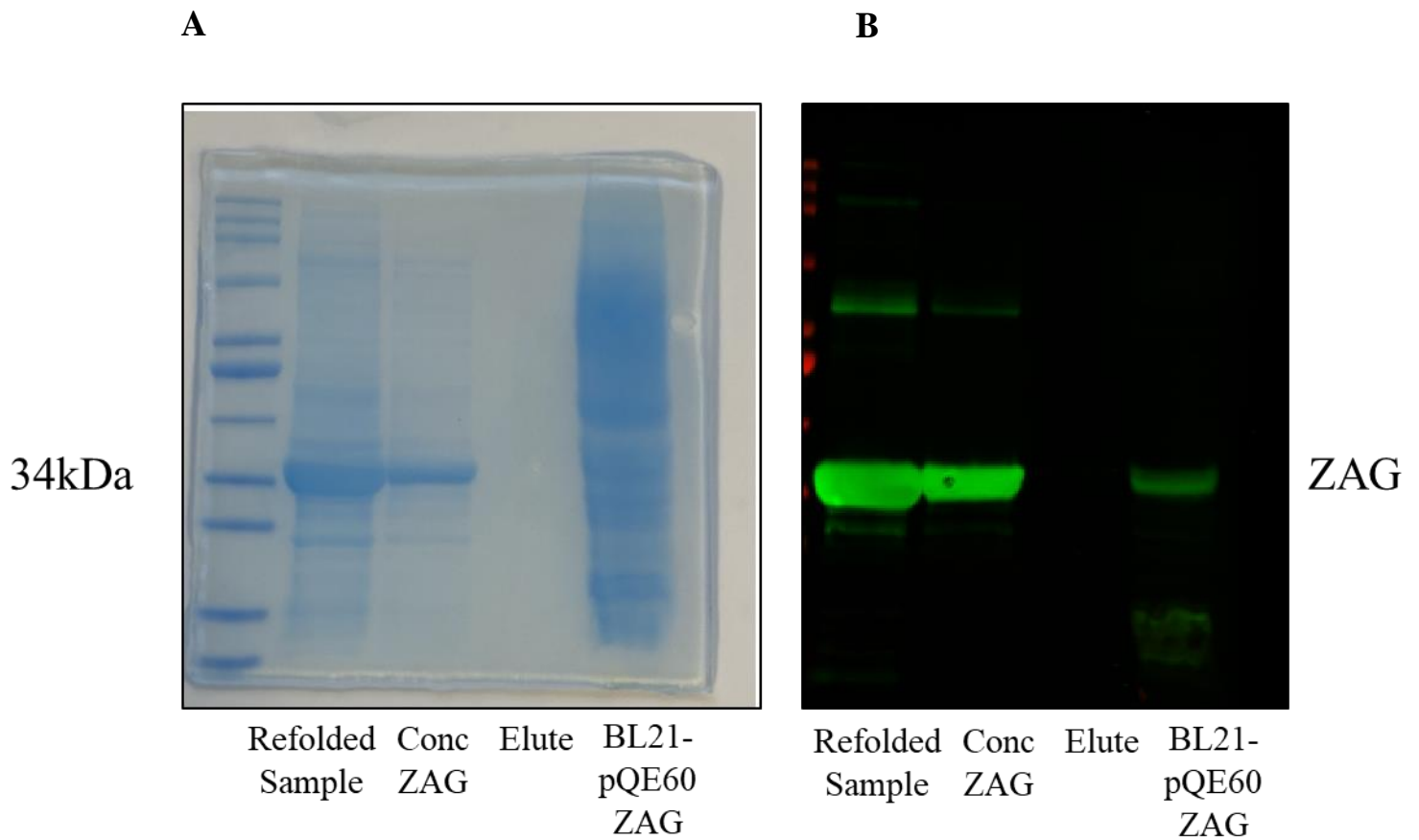


Figure 4. 5. ZAG Expression Cleanliness After Vivaspin Centrifugation

(A) Refolded ZAG sample was placed in a vivaspin 20 centrifugal concentrator and refolding buffer was gradually added to not precipitate the ZAG protein. Vivaspin was spun at 3500xg to concentrate ZAG (Conc ZAG) and elution was also collected (Elute). A positive control sample of BL21-pQE60 expressing ZAG was used for comparison of ZAG expression. (B) The same samples were analysed by immunoblotting.

4.1.7 Validating the Refolding Procedure of ZAG

With the *in silico* data giving us a strong investigatory base by providing us insights into the structure and residue roles, it was important to try and translate this into the lab work. Immunoblotting has shown that we can express and purify ZAG from BL21 cells and produce a clean blot after the wash, denaturing and refolding steps. The blots however provide no information on the structure or activity of the protein, only that it is present. To validate the refolding process of our ZAG protein, we have used fluorescence spectroscopy coupled to the binding of the fluorescent ligand DAUDA. As discussed in **3.0 Investigating Zinc Alpha 2-Glycoprotein Ligand Binding Through Computational Techniques**, DAUDA has been shown to bind in the groove of ZAG by crystallography (Lau et al., 2019), fluorescence spectroscopy (Kennedy et al., 2001) work and our own docking simulations (see **3.0 Investigating Zinc Alpha 2-Glycoprotein Ligand Binding Through Computational Techniques**). We used this well-characterised binding to validate our refolding process of ZAG. DAUDA's excitation wavelength is 345 nm and has an emission wavelength of 543 nm when alone in solution, as demonstrated in Figure 4. 6 A. DAUDA's emission wavelength alters when bound to protein. This transition from a solvent environment into an apolar protein binding site in ZAG is known to produce a blue shift in fluorescence (Kennedy et al., 2001). To further help us validate our refolding process, we used a commercially made ZAG as a positive control. Addition of 5 µl of commercial ZAG 1µg/ml to DAUDA resulted in a blue shift representing the DAUDA binding in the ZAG pocket. Addition of a second 5µl again emphasised this shift (Figure 4. 6 A).

With the commercial ZAG and DAUDA pairing providing a positive control, the same procedure was repeated for our ZAG. A blue shift was also observed with the increasing additions of our bacterial recombinant ZAG, shown by the shift from the DAUDA only peak represented by the black line (Figure 4. 6 B). This experiment is consistent with the notion that

bacterially expressed ZAG has refolded, validating our denaturing and refolding techniques and allowing us to proceed with using both our recombinant ZAG to investigate its effects in cell work.

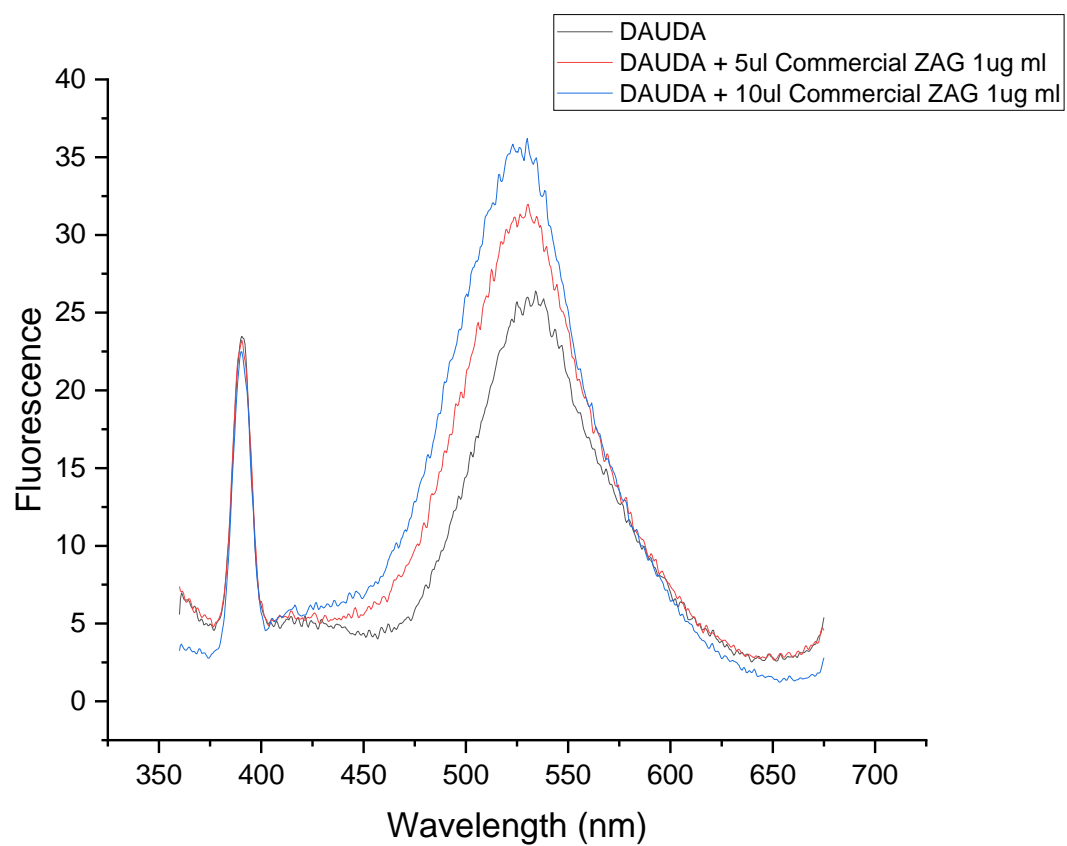
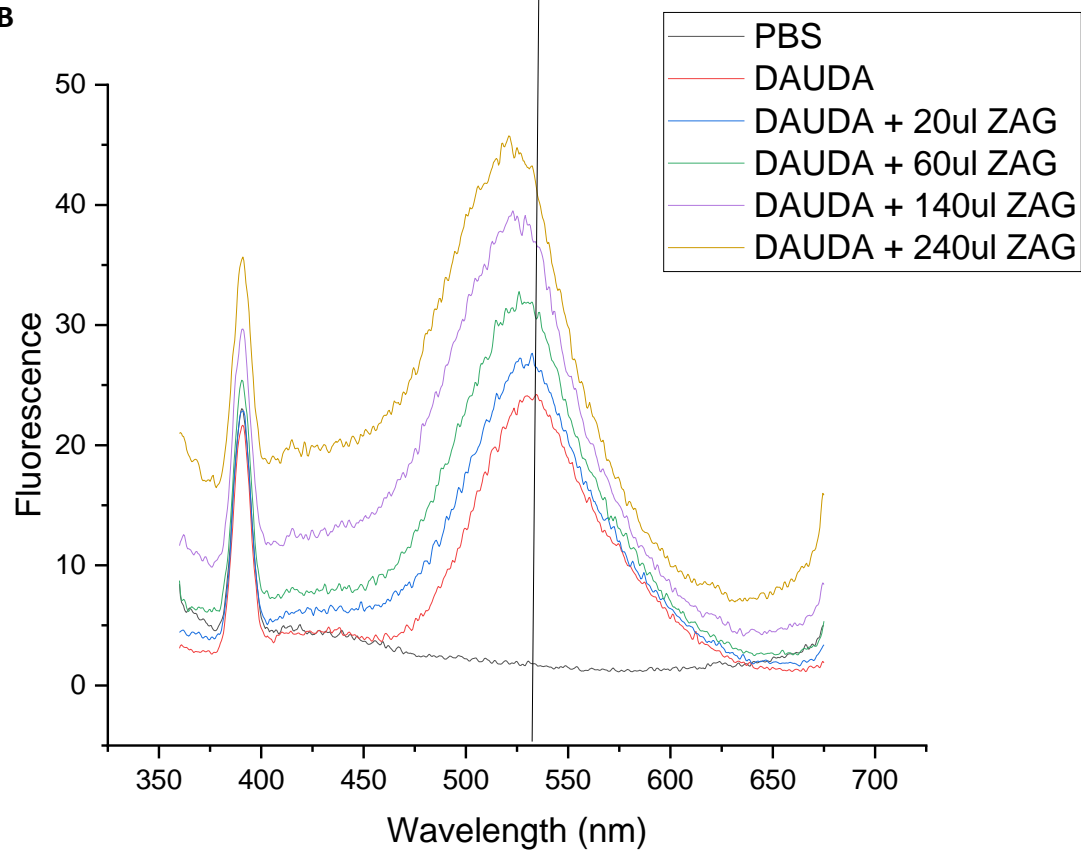
A**B**

Figure 4. 6. Fluorescence Spectroscopy Experiments Verify ZAG Refolding

A fluorescence emission spectrum ($\lambda_{\text{Exc}} = 345 \text{ nm}$) of $2 \mu\text{M}$ DAUDA alone in buffer or upon the addition of commercial ZAG ($1 \mu\text{g/ml}$) (A) or recombinant ZAG (0.95 mg/ml) produced from BL21 transformed cells (B). Fluorescence-based Ligand Binding—Fluorescence binding emission spectra (uncorrected) were recorded at 20°C with a SPEX Fluo-Max spectrofluorimeter (Spex Industries, Edison, NJ) using 2 ml samples in a silica cuvette. Raman scattering by solvent water was subtracted where necessary.

4.1.8 Testing the Biological Activity of ZAG

With our denaturing and refolding steps being validated by incorporating DAUDA and fluorescence spectroscopy, we sought to establish if our ZAG was biologically active. In the literature ZAG has been shown to stimulate lipolysis in 3T3-L1 adipocytes. We therefore incubated 3T3-L1 adipocytes with increasing concentrations of recombinant ZAG and assayed lipolysis using a colorimetric kit which allows the detection of glycerol from media samples by incorporating a glycerol probe into media after ZAG incubations have finished. As shown in Figure 4. 7, glycerol levels in the media increased with increasing concentrations of ZAG (0-40 μ l at 2 mg/ml) when assayed at either 1 hour or 4 hours. These results alongside the lack of glycerol in the control and refolding buffer samples demonstrate that our recombinant ZAG is indeed inducing lipolysis and therefore our ZAG has refolded and is active. Timepoints of 1 and 4 hours allow for an initial and then sustained lipolysis action to be captured. We recognize that these data do not inform on the concentration or fraction of the sample that is biologically active.

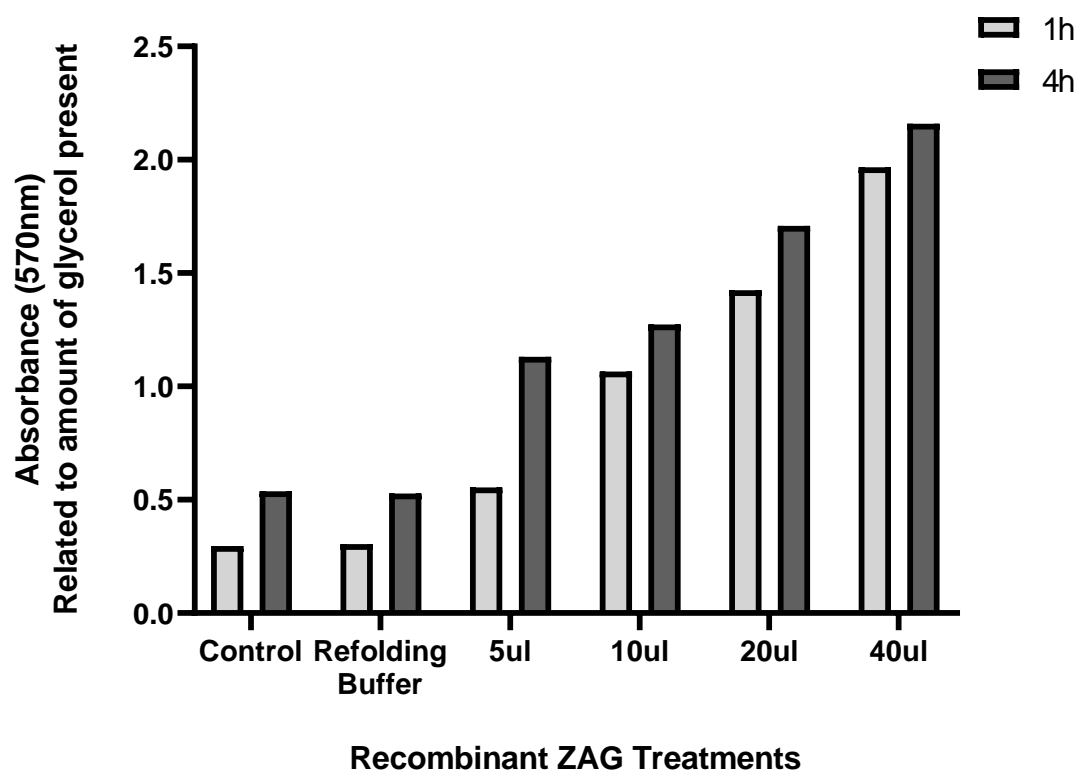


Figure 4. 7. Glycerol is Released from 3T3-L1 Adipocytes After ZAG Stimulation

3T3-L1 adipocytes at day 10 post-differentiation were incubated in fresh media and treated with increasing volumes of recombinant ZAG (50 μ M) for 1 and 4 hours. Media was then collected and probed for glycerol using Sigma Aldrich Lipolysis Colorimetric Assay Kit. Samples were measured at 570 nm using the BioTek EPOCH Microplate Spectrophotometer. n=1, Plotted using PRISM.

4.1.9 Transfection of HEK293 Cells to Establish a ZAG Expressing Cell Line

In addition to recombinant ZAG in bacteria, we reasoned that a ZAG with native post-translational modifications would also be of benefit to analyse if these modifications effect the biological activity of ZAG. Purely from a workload point of interest also, as ZAG is released from the cell, collecting the protein from the cell supernatants would be a more efficient process than from the bacteria. Therefore, transfection experiments were performed using HEK293 cells to express ZAG and to ascertain whether ZAG would be secreted; we also compared two different transfection agents (Xfect and Lipofectamine) (Figure 4. 8). The data shown in Figure 4. 8 reveal that ZAG is expressed and secreted from these cells, and that Xfect consistently gave high expression levels. Differences in band weight between recombinant ZAG and mammalian suggests that mammalian ZAG excreted from HEK293 cells has undergone PTMs resulting in a larger protein.

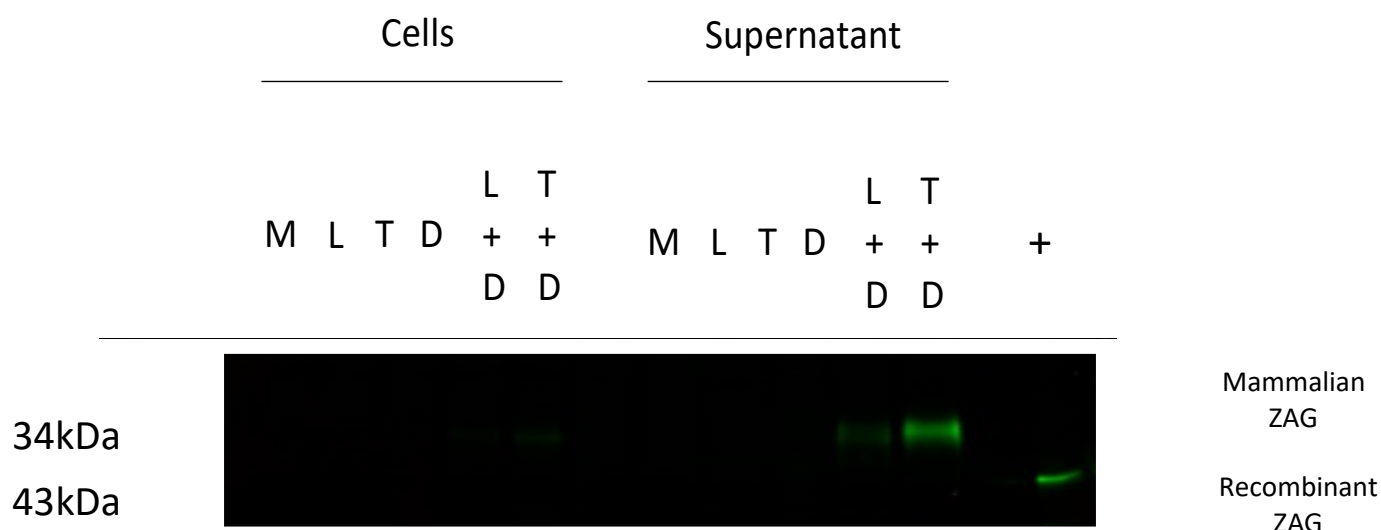


Figure 4. 8. ZAG Protein Expression in Cell and Supernatant Samples After pCDNA3.1 Transfection of HEK293 Cells

HEK293 cells were grown to approximately 60% confluence and treatments of a vehicle control of Opti-Mem only (M), Opti-Mem and Lipofectamine (2% (v/v) final) (L), Opti-Mem and Xfect reaction buffer and Xfect polymer (25% (v/v) and 0.3% (v/v) final) (T), Opti-Mem and pCDNA3.1 plasmid expressing ZAG (2.5 µg/ml per well) (D), Opti-Mem, Lipofectamine and pCDNA3.1 expressing ZAG (2% (v/v) final and 2.5 µg/ml per well) (L+D) and Opti-Mem, Xfect reaction buffer, Xfect polymer and pCDNA3.1 expressing ZAG (25% (v/v), 0.3% (v/v) final and 2.5 µg/ml per well) (T+D) were performed on individual wells for 4-6 hours. A positive control sample of BL21-pQE60 expressing ZAG (34kDa) was used for comparison (+). Both cell lysates and supernatants were collected and analysed for mammalian ZAG (43kDa) using Western blotting.

4.1.10 Transducing HEK293 Cells for ZAG Production

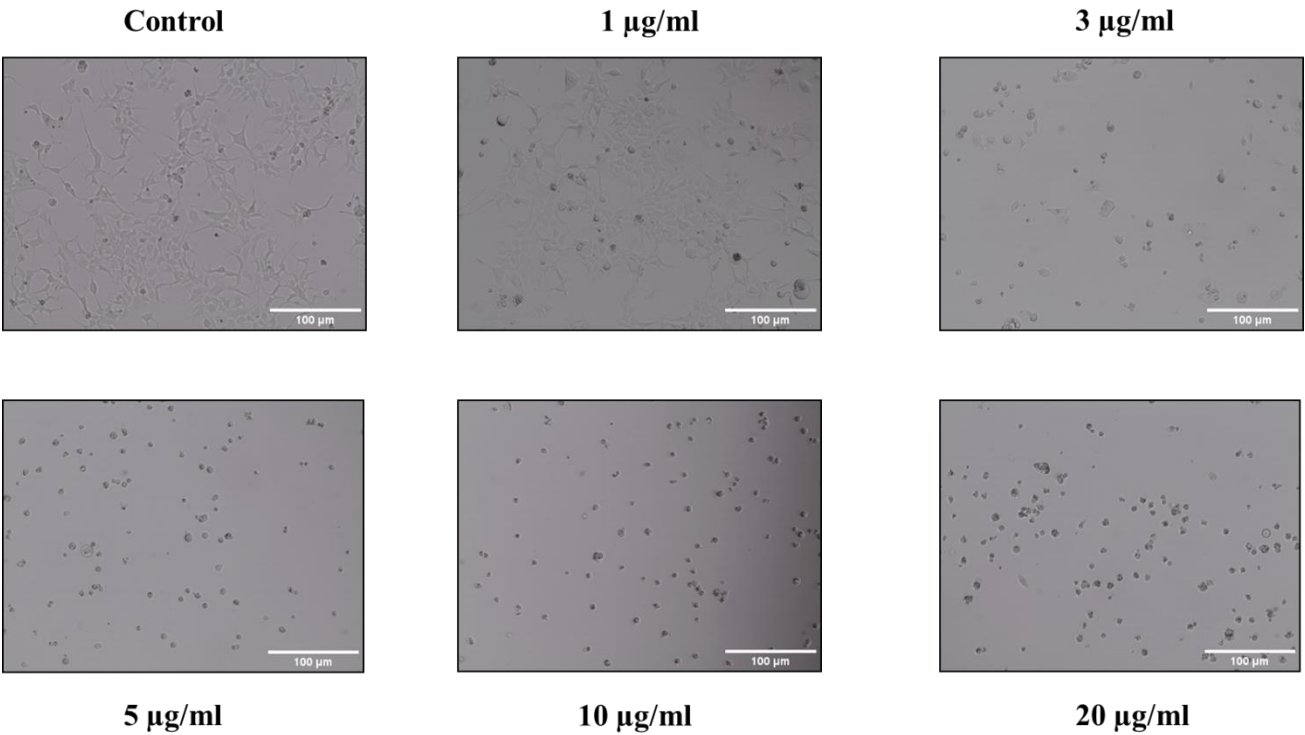
The advantage of expressing our protein using bacteria is the ease of transformation and the high expression rate using BL21 bacterium. However, the proteins being packaged in inclusion bodies result in a laborious and time consuming process in recovering the protein through the process of lysing, cleaning, denaturing and refolding. In mammalian cells, ZAG is secreted from the cell and, because the cells are eukaryotic, ZAG will be correctly folded and glycosylated, which will allow for easy collection and the protein being active.

Another method to express ZAG in mammalian cells is to create a stable HEK293 cell line using a Lentivirus construct from Lenti-ORF (©Horizon Discovery Ltd; Supplementary material) and employing an antibiotic selectable marker to identify ZAG-positive cell clones. The Lentivirus has been constructed with the AZGP1 gene to express ZAG, a Blasticidin S resistance gene to allow selection for our transient cells and a turboGFP gene that is expressed in the nucleus upon successful transduction allowing easy detection of ZAG expressing cells. The virus has a disabled viral genome and has been modified to contain only essential genetic elements necessary for packaging and integration. These include the 5' LTR, Psi sequences, polypurine tracts, Rev responsive elements and 3' LTR. The virus therefore can infect the host and pass the desired Blasticidin S resistance and AZGP1 gene into our HEK293 cells without replicating itself. Therefore, successful transduction would allow us to utilize the HEK293 cells as ZAG production lines.

We first had to establish what concentration of Blasticidin S was going to be used for our selection process. Wild type HEK293 cells were incubated with Blasticidin S (0-20 µg/ml) for 7 days. 5, 10 and 20 µg/ml had killed all cells when checked after 3 days, whilst 3 µg/ml had some viable cells and 1 µg/ml appeared to have negligible results (Figure 4. 9 A). The 1, 3 and 5 µg/ml Blasticidin S concentrations were continued for a total of 7 days where it was observed that 3 µg/ml resulted in total cell death (Figure 4. 9 B). Therefore, the selection concentration

for the Lentivirus transduction experiments was set at 3 $\mu\text{g/ml}$. HEK293 cells were grown to approximately 50% confluence and were infected with lentivirus particles with a titer of 10^8 TU/ml. Cells were imaged using EVOS imaging system to detect GFP signal in the nucleus (Figure 4. 10) A GFP signal was seen within the nucleus and therefore HEK293 cells had been successfully transduced. The next step was then to select these transduced cells with the 3 $\mu\text{g/ml}$ Blasticidin S supplemented DMEM to create stable cell lines. Initial transduction was performed at 10^8 TU/ml to test effectiveness of genome integration into our HEK293 cells. Since this was established, our desired outcome was to produce a stable cell line with the optimum genome integration, cell survival and protein production concentration. Too high a concentration of virus would result in poor cell survivability and too little would result in poor protein production. HEK293 cells were grown as above and exposed to lentivirus over a range of serial dilutions to transduce cells at decreasing concentrations of virus and afterwards subjected to the optimum 3 $\mu\text{g/ml}$ of Blasticidin S for stable cell line production. Titers (measurement of functional virus particles, with A1 having the greatest concentration of viral particles and decreasing incrementally to A7 with the lowest concentration of viral particles) of A1 resulted in greater cell death concentrations and titers of A5, A6 and A7 resulted in low quantities of virus integration (data not shown). However stable genome integration and cell selection was observed with A3, A4 and A5 titer concentrations and ZAG secretion was observed supernatants in a concentration dependent manner (Figure 4. 11). The band running at a larger weight also suggests ZAG is being secreted with PTMs compared to the bacterial ZAG from BL21 cells. These results indicate successful stable cell line production and mammalian ZAG secreted into the incubated media of cells.

A



B

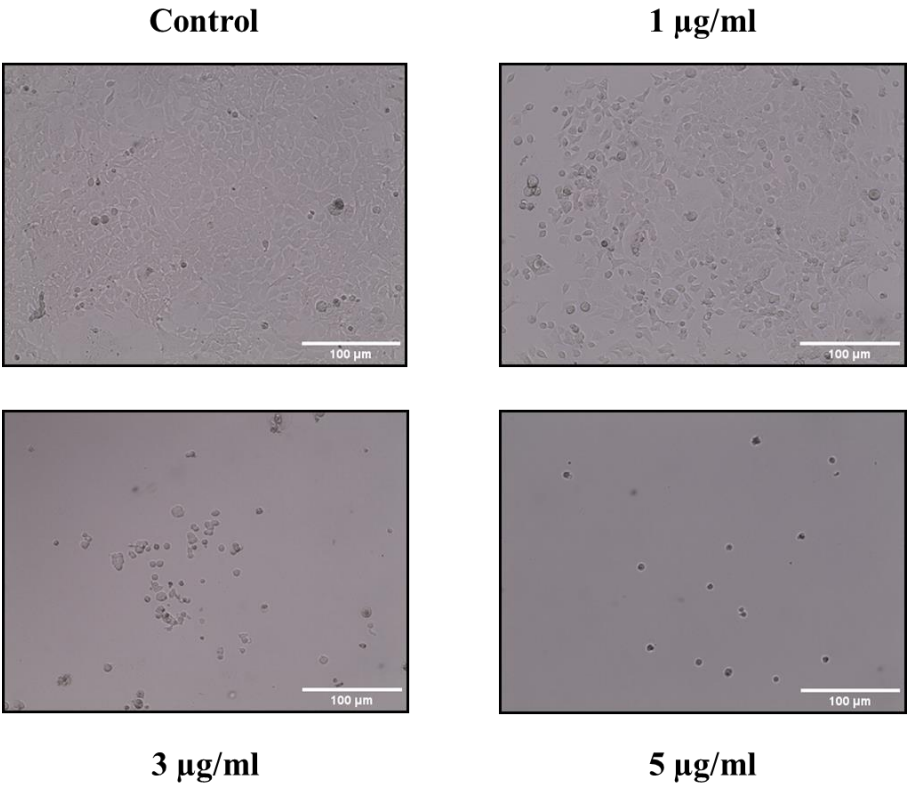


Figure 4. 9. Determining the Effective Dose of Blasticidin S for Transduced HEK293 Cell Selection

HEK293 cells were grown on a 24 well plate at a density of 5×10^4 per well and grown in DMEM supplemented with Blasticidin S containing the appropriate concentrations for kill curve (0-20 $\mu\text{g/ml}$). Cells were imaged after 3 days to check cell viability (A) and were imaged again after day 7 (B) to determine appropriate Blasticidin S selection concentration. Cells were imaged using the EVOS imaging system at x10 magnification.

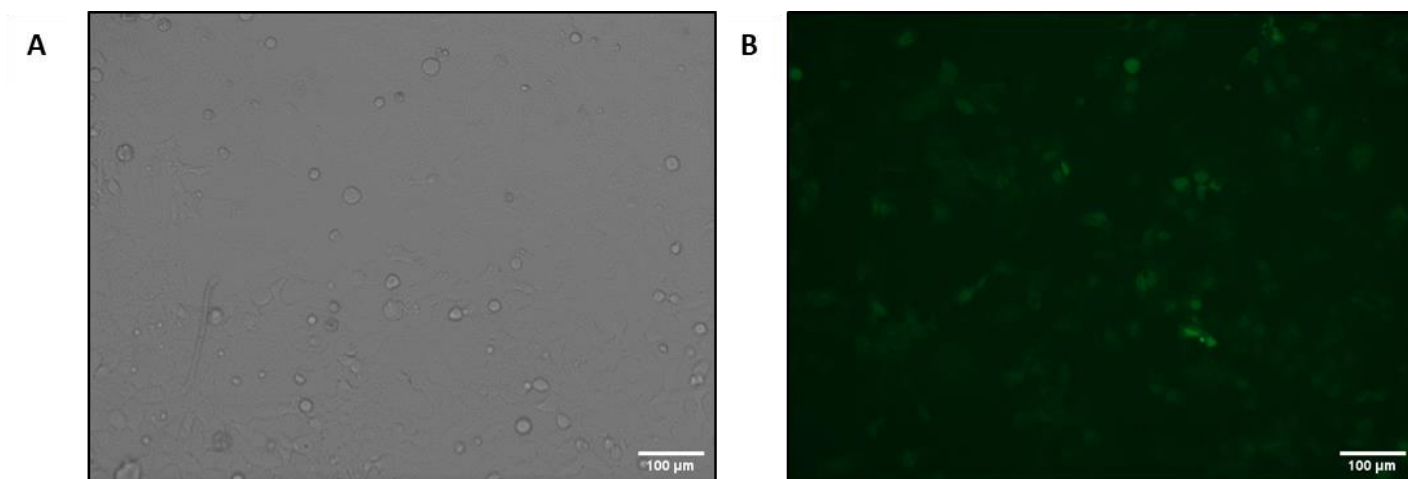


Figure 4. 10. Successful Lentivirus Transduction of HEK293 Cells to Express ZAG

HEK293 cells were grown on a 24 well plate at a density of 5×10^4 per well and incubated with Precision LentiORF™ for 72 hours. Cells were imaged using the EVOS imaging system at x10 magnification to detect TurboGFP signal in transduced cells. Brightfield (A) and GFP (B).

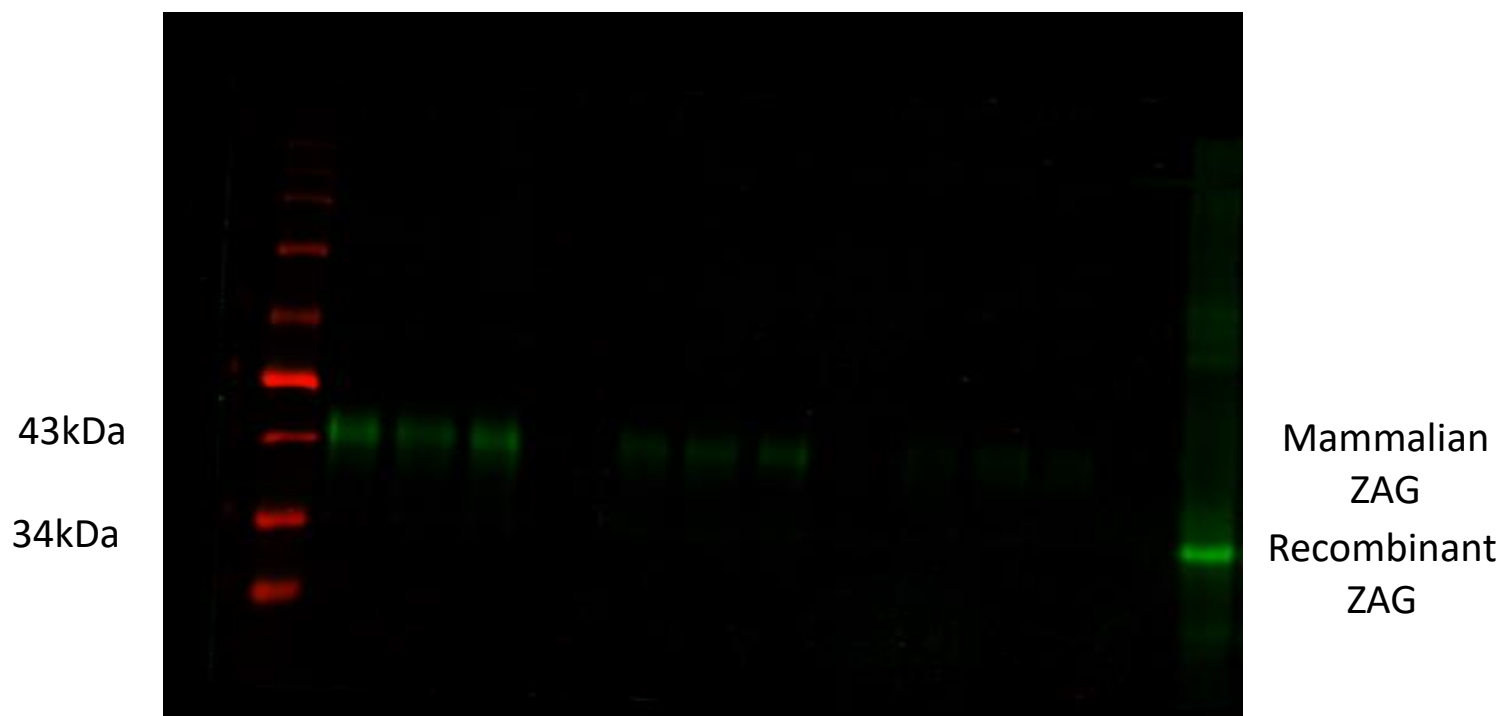
A2₁ A2₂ A2₃A3₁ A3₂ A3₃A4₁ A4₂ A4₃WT
ZAG

Figure 4. 11. Stable HEK293-ZAG Transduced Cell Lines Secrete ZAG in a Titer Dependent Manner

HEK293 cells were grown on a 24 well plate at a density of 5×10^4 per well and incubated with Precision LentiORF™ for 4-6 hours at various virus titer concentrations (A2 representing the greatest concentration of virus with greatest Multiplicity of Infection (MOI) and subsequent 5-fold dilutions for A3 and A4 resulting in lower viral content per well). Media was replenished with DMEM for 48 hours and afterwards transduced cells were then subjected to 7 days of selection medium (DMEM supplemented 3 μ g/ml Blasticidin S) and refreshed every 2-3 days to produce stable cell lines that express ZAG. Equal loading of cell supernatants at decreasing viral titer concentrations from three separate wells (A2₁ A2₂ A2₃ representing triplicate at the same viral concentration) and a positive control sample of BL21-pQE60 expressing ZAG was used for comparison. Samples were analysed for recombinant ZAG and mammalian ZAG (34kDa and 43kDa respectively) by western blotting.

4.1.11 Testing the Biological Activity of Mammalian ZAG

Our imaging and western blot data show our success in expressing mammalian ZAG. As with our recombinant ZAG, we performed the same lipolysis experiment laid out in ***4.1.8 Testing the Biological Activity of ZAG***. As shown in Figure 4.12, glycerol levels in the media increased with increasing concentrations of ZAG (0-40 μ l at 50 μ M) when assayed after 2 hour treatments. These results that our mammalian ZAG expressed from our HEK293 cells is indeed inducing lipolysis and therefore our ZAG secreted into the media is folded and is active. Again, we recognize that this data does not inform on the fraction of the sample that is biologically active.

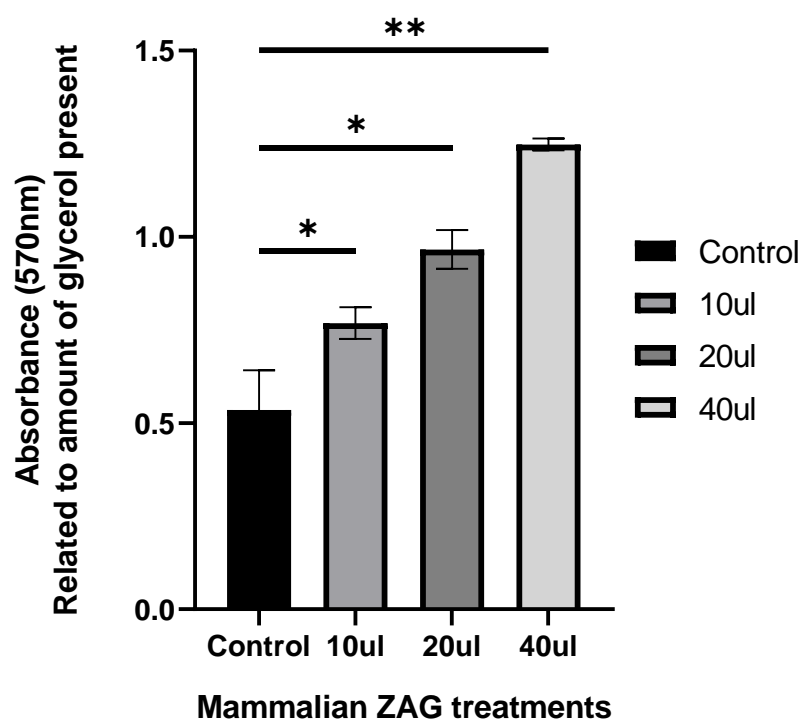


Figure 4. 12. Glycerol is Released from 3T3-L1 Adipocytes After Mammalian ZAG Stimulation

3T3-L1 adipocytes at day 10 post-differentiation were incubated in fresh media and treated with increasing volumes of mammalian ZAG (50 μ M) for 2 hours. Media was then collected and probed for glycerol using Sigma Aldrich Lipolysis Colorimetric Assay Kit. Samples were measured at 570 nm using the BioTek EPOCH Microplate Spectrophotometer. Each bar is the mean of triplicate wells, and data from a representative experiment is shown. Plotted using PRISM.

4.2 Discussion

4.2.1 *Optimizing ZAG Expression and Purification*

As discussed previously, ZAG is a driver of lipolysis in adipose tissue. ZAG is chronically upregulated in carcinomas derived from adipose tissue (Bing et al., 2004). This upregulation results in a weight loss that cannot be attenuated through diet and results in a poor prognosis for stage 4 cancer patients (Kalantar-Zadeh et al., 2013). The production of this protein will therefore allow the study of its biological effects *in vitro* and its biochemistry via *in silico* work. As mentioned at the start of this chapter, the unfortunate circumstances in which we could not visit Oxford meant a considerable period of time was spent learning and troubleshooting protein expression methods. The difficulty in purifying this protein is the involvement of the inclusion bodies. As mentioned, protein production in bacteria can result in protein being misfolded and packaged in these vesicles (Kalantar-Zadeh et al., 2013). These inclusion bodies have to be extracted from the cells and the protein removed to isolate the desired protein. Each subsequent step in purifying ZAG has been refined on a small scale to identify the most suitable method in producing ZAG from bacteria (4.1.2.-4.1.6).

Although not homogenous, the ZAG concentration after vivaspin centrifugation results in a large fraction of the total protein (88%) (Figure 4. 5). As mentioned in **4.1.6 *Evaluating Methods for Purifying ZAG***, there had been difficulties in isolating the protein using Nickel beads. Isolating ZAG using the vivaspin columns and dialysis methods were initially being used as a detection method to observe how clean the sample could be. Both methods result in a cleaner expression for ZAG, but provided no information on the protein structure or its function and this was a concern with the denaturing step needed to extract the protein from the inclusion bodies. As discussed in **4.1.7 *Validating the Refolding Procedure of ZAG***, we have means to test our proteins structure with the fluorescent spectroscopy and indeed with

DAUDA, we observe a blue shift in fluorescence in both our commercial ZAG and recombinant ZAG, showing we have successfully expressed and refolded our protein. However, this method is limited in approach. Due to the purity of the commercial ZAG (<95%) minuscule amounts are needed for these experiments. In contrast to this, our recombinant ZAG is having to be added in larger quantities to produce a detectable similar blue shift in fluorescence. This highlights that although refolding has taken place with our refined procedures, we do not know at what the extent of successful refolding is occurring – the increased concentrations needed might suggest a low refolding rate. To address this, circular dichroism (CD) would be a useful approach. CD provides information on the chemical structure of a protein by measuring the difference in absorption of polarised light. Differences in the structure results in polarity in opposite directions (left and right) and uses this to account for the secondary structures of alpha helices and beta sheets and then determines the structure of the protein. Our ZAG sample could then be referenced to a fully folded protein like our commercial ZAG and the CD spectrum would allow us to determine the percentage of how much recombinant ZAG is folded correctly in our sample. This was our initial approach (data not shown), but the formulation of the refolding buffer (0.1 M Tris-HCl, 2 mM EDTA, 0.4 M L-arginine, 0.5 mM oxidised glutathione, 5 mM reduced glutathione) interfered with CD spectral analysis. Attempts were made to perform salt exchanges with dialysis and vivaspin columns but resulted in our protein falling out of solution and therefore we could not ‘package’ our recombinant ZAG in an appropriate buffer; this resulted in reliance on the fluorescence spectroscopy experiments for structure data.

Although at what capacity was unclear, data from the fluorescence spectroscopy experiments showed that our refined protein production and refolding methods resulted in expressed and at least some folded ZAG. The lipolysis experiments in **4.1.8 Testing the Biological Activity of ZAG** show that this recombinant ZAG is functionally active and provides further support of

correct refolding. Alongside establishing a bacterial expression system, the generation of a mammalian system for ZAG was of equal importance and success of this is outlined in both **4.1.9 Transfection of HEK293 Cells to Establish a ZAG Expressing Cell Line** and **4.1.10 Transducing HEK293 Cells for ZAG Production** and biological activity of the expressed ZAG is recorded in Figure 4. 12.

Both HEK293 and CHO cells have been used for the production of stable cell line production due to their amenable nature towards transfection and transduction techniques paired with their robustness for cell culture. HEK293 cells also have a rapid growth rate and allow for protein collection from confluent cells regularly without the need to re-transfect. Additionally, as HEK293 cells are derived from human cells, they can express proteins with native PTMs which would mean expressed ZAG protein would perhaps better mimic human ZAG glycosylation patterns. Collating PTMs using a database (Ramazi & Zahiri, 2021) show that PTMs are involved in disease progression with neurodegenerative diseases and cancer being highly driven by these modifications on proteins. Furthermore, it is shown that even the expression system results in different activity with the ZAG secreted in triple negative breast cancer being functionally different than ZAG expressed in ER-positive breast cancer (Verma et al., 2024). Therefore, the expression system is an important consideration for protein production. In future, fluorescence spectroscopy and CD experiments should be performed with mammalian ZAG to support the biological activity observed.

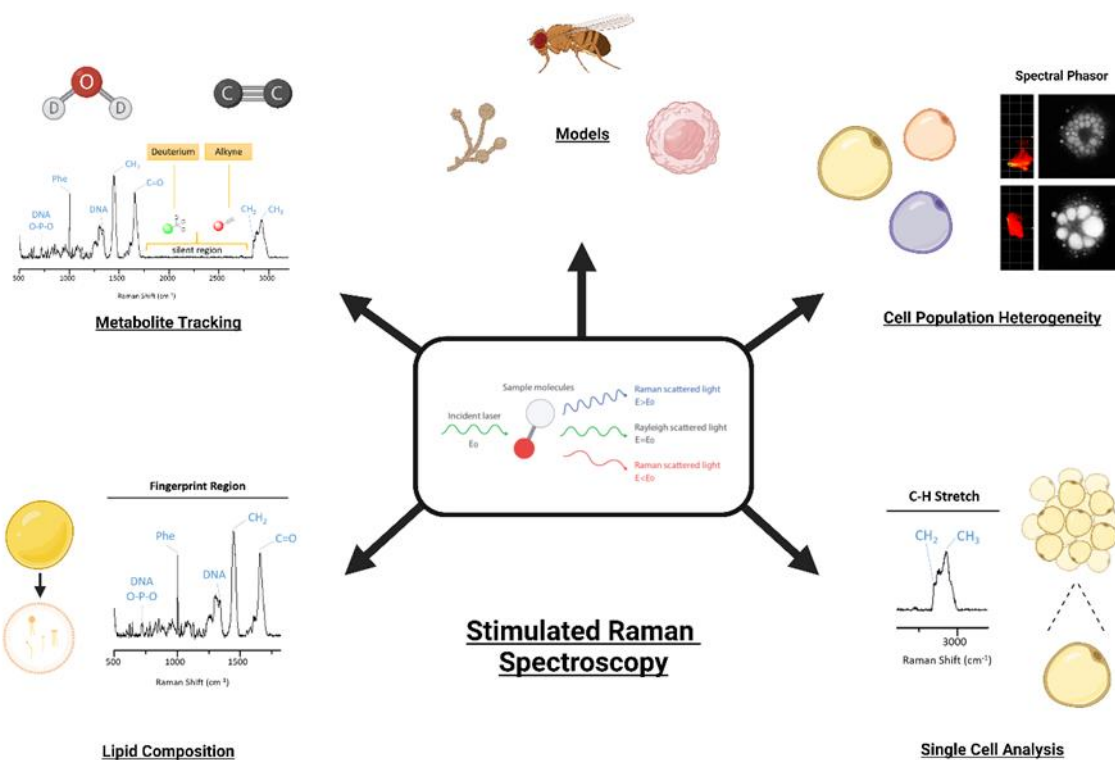
Limitations in this chapter are the lipolysis assays in **4.1.8 Testing the Biological Activity of ZAG** having only one experiment. Furthermore, lipolysis assay robustness could be improved by having a denatured ZAG to run as a negative control and positive control of isoproterenol would allow for clarity in ZAGs lipolytic effect.

Chapter 5

Developing a Workflow to Study Adipocyte

Heterogeneity Using Stimulated Raman

Spectroscopy



5.0 Developing a Workflow to Study Adipocyte Heterogeneity Using Stimulated Raman Spectroscopy

5.1.1 Introduction

Fat Cells are Heterogeneous

White adipose tissue (WAT) stores energy as triacylglycerols under conditions of energy surplus and efficiently mobilises this energy as fatty acids when required (Morigny et al., 2021). Changes in adipocyte metabolism are regulated by hormones, nutrients, and circadian rhythms (Santoro et al., 2021). In humans WAT is largely found in subcutaneous regions (scWAT) and around vital organs (visceral WAT; vWAT) which differ in physiological roles (Yang Loureiro et al., 2022) and are differentially associated with metabolic disease and disease risk (Santoro et al., 2021; Yang Loureiro et al., 2022).

Recent studies have used lineage tracing and transcriptomics to identify different populations of adipocytes within a single tissue (Backdahl et al., 2021; Langin, 2021). Interestingly, these different adipocyte populations are associated with different insulin sensitivity at both whole cell and whole-body levels, suggesting that these different adipocyte populations have a significant impact on disease development (Backdahl et al., 2021; Langin, 2021; Lee et al., 2019). However, how these populations differ metabolically is completely unknown, but this is likely to be of key importance.

Assigning functional properties such as metabolic activity to specific subsets of cells is difficult, as cells/tissues are usually studied as populations, and effects on specific subsets of cells are masked by population averaging. Therefore, although we know (e.g. from scRNAseq) that there are different populations of adipocytes within a depot, and that these relate to metabolic disease risk, we understand little about metabolism at a single cell level. Numerous population-based studies have correlated insulin sensitivity, nutrient uptake, lipogenesis and

lipolysis and release of adipokines with (for example) adipose cell size or cell-type (Santoro et al., 2021; Stenkula & Erlanson-Albertsson, 2018; Yang Loureiro et al., 2022). However, none have provided any insight into single-cell metabolic activity – a significant gap in our understanding of tissue function.

The study of adipocyte metabolic activity down to the individual cell level and how this may negatively impact the total adipose tissue function is a significant factor that must be considered when looking at metabolic health. Are the contents of these expanding droplets contributing to disease progression? Imaging techniques, most commonly the application of immunofluorescence imaging is widespread to study all cell types. However, this method requires the use of fluorescent tags that integrate with the chemistry of the cells and lipid stains such as Oil Red O (Mehlem et al., 2013), LipidTOX™ (Liu et al., 2009) and BODIPY (Spangenburg et al., 2011) are neutral lipid stains that cannot extract specific information on the lipid species within the adipocyte droplets. Therefore, an imaging technique that can elucidate this information on lipid species is of importance. This type of work has been previously demonstrated by applying Raman Spectroscopy techniques (Greig et al., 2024), as will be discussed below.

3T3-L1 Adipocytes as a Model System

3T3-L1 adipocytes are a widely used model to study adipocyte functions (Ruiz-Ojeda et al., 2016; Zebisch et al., 2012). Primary adipocyte isolation from animal and human models comes with difficulties in acquiring, handling and culturing longevity (Villanueva-Carmona et al., 2023). 3T3-L1 cells are fibroblast derived from mice and are directed to adipocytes through differentiation, resulting in a robust *in vitro* working model that translates to *in vivo* work (Zebisch et al., 2012). These adipocytes can be cultured for extended periods in plates and have been deployed in studying adipose biology with a range of techniques such as; investigating

GLUT4 trafficking cell signaling through protein expression changes by western blotting (Bremner et al., 2022) (Bremner et al., 2023), analyzing their metabolic activity by examining the cultured media contents for the release of free fatty acids and glycerol from the breakdown of triacylglycerols using lipolysis colorimetric kits (Merrett et al., 2020) and they can be grown on coverslips to be deployed for imaging by immunofluorescence (Neuhaus et al., 2023), super resolution (Geiser et al., 2023) and dSTORM (Anna et al., 2022) (Koester et al., 2022). They are widely used and exhibit robust insulin responses.

The Principles of Raman Spectroscopy

Raman scattering is an optical technique that investigates the vibrational modes of molecules through inelastic scattering of the incident light source. Most Raman scattering experiments make use of a confocal Raman microscope coupled to a monochromatic light source, typically a laser at 405, 532, 633, 785 or 1064 nm. A laser is focused on the sample with an objective lens such that both elastic (referred to as Rayleigh scattering) and inelastic scattered photons (referred to as Raman scattering) are produced following the interaction with the molecules at the sample focus. Raman scattering of photons can result in photons with lower energy and longer wavelength (red shifted) relative to the incident photons or with higher energy and shorter wavelength than the incident photons (blue shifted). These are known as Stokes and anti-Stokes respectively. At room temperature, most molecules will occupy the ground vibrational state, and therefore, Stokes Raman scattering is predominant, and the incident laser results in vibrational excitation. Rayleigh scattering photons have the same energy (and hence frequency) as the incident photons. Most commercial Raman systems use an upright microscope configuration whereby the objective lens focuses the laser onto the sample and collects the scattered (both Rayleigh and Raman scattered) photons. The Raman scattered photons are separated from the Rayleigh scattered photons using a dichroic mirror and a notch

or edge filter. By employing a spectrograph, the Stokes (or anti-Stokes) Raman scattered photons can be separated based on wavelength. By determining the wavelength shift in nm, which is usually expressed as a Raman shift, (ν , wavenumber cm^{-1}), the resulting Raman spectra can be used to identify molecular vibrations for molecular characterisation. As such, a Raman spectrum plots the wavelength shift (cm^{-1} , x-axis) against the relative number of photon counts (usually counts/s, or equivalent, y-axis).

Coherent Raman (CARS) scattering techniques require the use of two incident laser beams, termed the pump and Stokes laser. In most cases, the pump laser is a tuneable laser across the range 700 - 990 nm generated by an optical parametric oscillator, whilst the Stokes beam is a fixed wavelength laser, usually 1031, 1040 or 1064 nm. The two beams are spatially and temporally overlapped and focussed onto the sample. When the frequency difference between the two lasers is tuned to match a vibrational mode within the sample, coherent Raman scattering processes can occur. CARS was first described in 1965 (Maker & Terhune, 1965) and generates an anti-Stokes scattering signal through four-wave mixing of the incident pump and Stokes lasers. The CARS signal is technically simple to detect using a photomultiplier tube because the signal is blue-shifted relative to the incident laser wavelengths, with the use of bandpass filters enabling the detection of the CARS signal. However, non-resonant background and resultant spectral distortions can occur during image acquisition. Stimulated Raman Scattering (SRS) was first reported in 1962 (Woodbury & Ng, 1962) although it was not until 2008 that the first demonstration of SRS microscopy for biological samples was realised (Freudiger et al., 2008). When the frequency difference between the pump and Stokes photons is matched to a vibrational frequency in the sample, stimulated Raman loss (SRL) and stimulated Raman gain (SRG) result. The detection of SRS is achieved by detecting the SRL signal or SRG signal which is typically small (of the order $10^{-7} - 10^{-4} \text{ cm}^{-1}$) in the pump or Stokes beam (Dunnington et al., 2024), respectively using a modulation transfer scheme via

lock-in amplifier. However, SRS is free from non-resonant background and SRS spectra are free from spectral distortion unlike CARS, which makes SRS an attractive method for hyperspectral imaging applications for material characterisation.

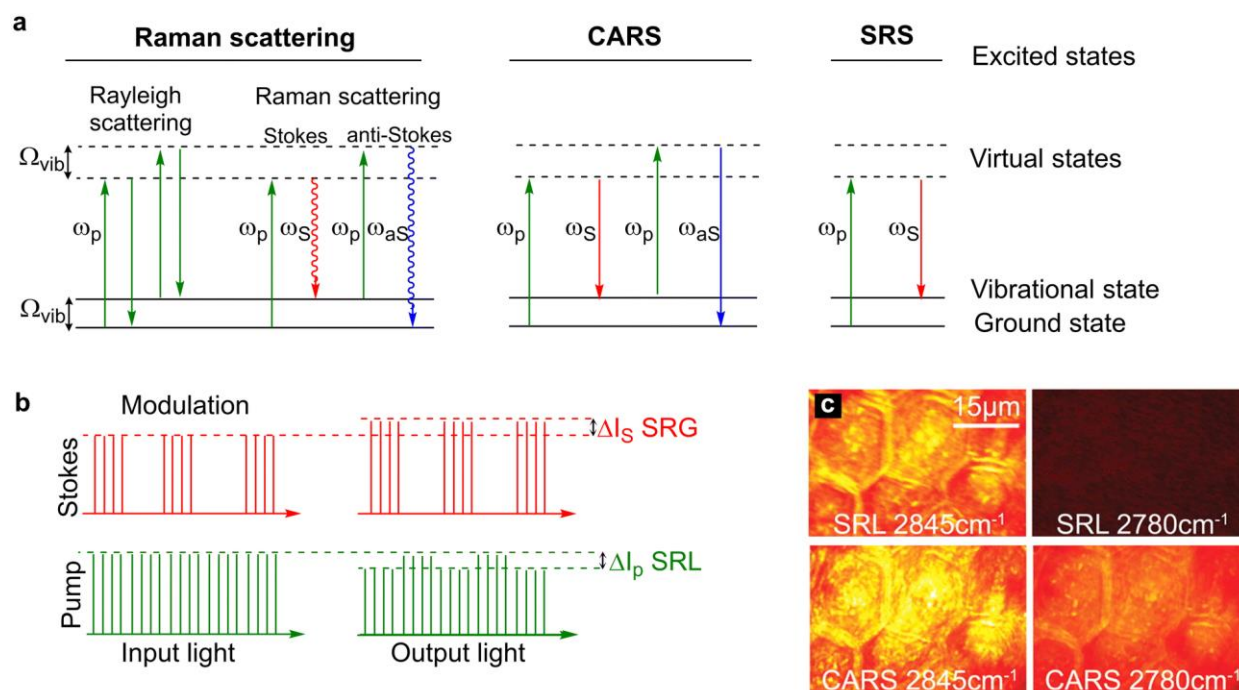


Figure 5. 1. Understanding the Key Differences in Raman Spectroscopy

Energy level diagrams for Rayleigh scattering, Raman scattering, CARS and SRS. (a) Rayleigh scattering is an elastic process whereby photons are scattered with the same energy as the incident photons. Raman scattering is an inelastic process where photons are scattered with a lower energy (Stokes scattering) or higher energy (anti-Stokes scattering) relative to the incident photons. In CARS, two incident photons at the pump (ω_p) and Stokes (ω_S) frequencies simultaneously interact with the chemical bond which has a vibrational frequency that is equal to the difference frequency of the two beams. In doing so, the chemical bond is stimulated to a vibrational excited state. Upon interaction of the coherently excited chemical bond with a second pump photon results in the generation of an anti-Stokes photon (ω_{aS}) which is blue shifted (higher energy than the incident photons). In SRS, two photons interact with a chemical bond such that the frequency difference between the pump and Stokes beams matches the energy of the chemical bond. In doing so, the energy of the pump photon is transferred to the chemical bond resulting in the generation of a Stokes photon with a lower energy. (b) Modulation transfer detection scheme. The Stokes beam is modulated at a high frequency which results in a SRL signal that is modulated in the pump beam and a SRG signal that is detected at the modulation frequency in the Stokes beam. The SRL signal is usually extracted from the laser noise using a lock-in

amplifier. (c) A comparison of SRS and CARS imaging of mouse skin. The CH_2 vibration of skin lipids is detected at 2845 cm^{-1} , whilst the off-resonance image at 2780 cm^{-1} is free from signal in SRS imaging, non-resonant background is detected in the CARS image. Image adapted and reproduced from (Freudiger et al., 2008) with permission the American Association for the Advancement of Science (2008).

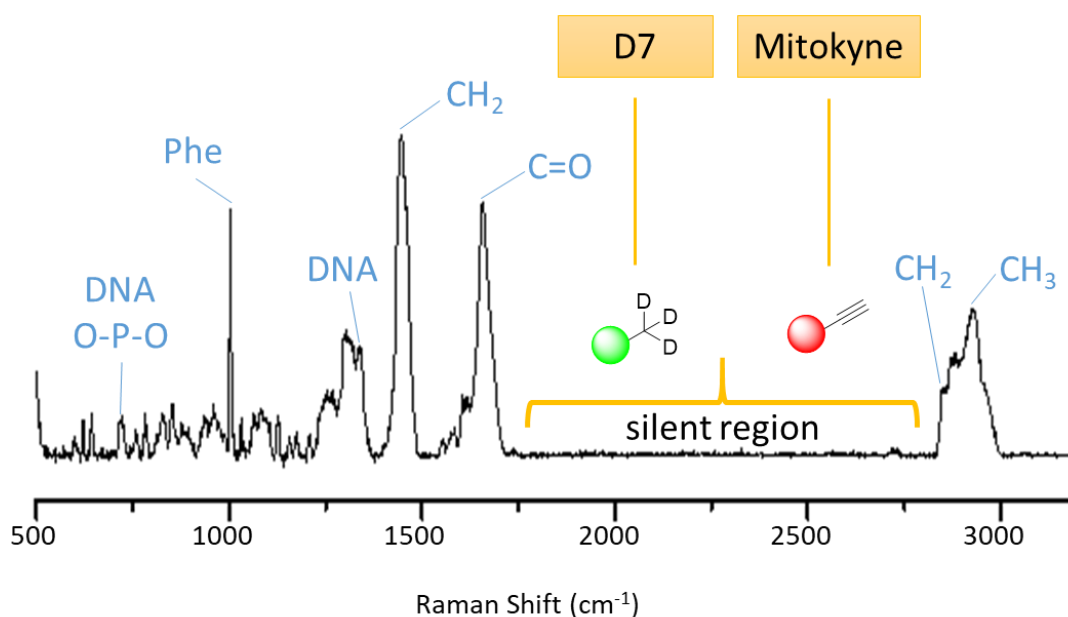


Figure 5. 2. Representative Raman Spectra of Biological Specimens

Biological samples stimulated with monochromatic light results in vibrations in chemical bonds. Each chemical functional group has its own distinct peak and by tuning to the desired wavelength, desired chemical groups can be targeted in the high wavelength region (2800-3005 cm⁻¹) and fingerprint region (300-1900 cm⁻¹). Tools developed to aid in biological study have been developed for the innate silent region (1800-2800 cm⁻¹) with deuterium and alkyne tags.

5.1.2 Development of SRS Techniques to Investigate Adipocyte Heterogeneity

With the information collated in the Raman spectra shown above in Figure 5. 2, we can select wavelengths of light that will induce vibrations in desired areas of interest and generate images of 3T3-L1 adipocytes (Butler et al., 2016). By stimulating samples at single wavelengths such as 2930 cm^{-1} (Figure 5.3), it is possible to focus on the CH_3 stretch representing proteins in our sample, whereas if samples are stimulated at 2851 cm^{-1} , the symmetric CH_2 stretch found in lipids are stimulated and visualized (Rensonnet et al., 2024). This individual tuning allows for single image acquisition of different chemical characteristics of our adipocytes and shows we can acquire label-free images of our cells. This method of single image acquisition has been used for example to identify lipid droplet formation in prostate cells (Hislop et al., 2022) and liver cells following exposure to drugs such as cyclosporin A (Tipping et al., 2024). This method is therefore effective in showing phenotypic differences in samples before and after treatments if it is suspected that the chemistry of the sample has altered.

Although we and the field have demonstrated that label-free imaging is possible, this single image process is limited in its application. So, as well as single images, it is possible to acquire a lambda scan in the high wavelength region ($3050\text{-}2800\text{ cm}^{-1}$), an example of which is presented in Figure 5. 3 for illustration, taken from studies discussed in more detail below. The system will initiate vibrations in cells at 3050 cm^{-1} and will re-tune down in incremental steps towards 2800 cm^{-1} whilst acquiring images at each retuning step. This generates ~ 40 separate images of cells collated as a stack that represents the total chemical information of the high wavelength region that can relate to molecular composition information. This stacked data set therefore allows for the generation of a Raman spectra of individual adipocytes. These Raman data sets contain spectra at pixel locations from a pre-defined sample area of interest and the result is a three-dimensional dataset with coordinates of x and y for the spatial area and the

spectral information contained in the Z axis. This is referred to as hyperspectral imaging and is a popular method for SRS microscopy of biological samples (Hu et al., 2018)(Fu, 2014)

As with Raman scattering, several multivariate analysis methods have been reported to unmix overlapping in the hyperspectral SRS datasets mainly because the C-H stretching region is highly overlapping and many biomolecules have similar Raman spectra. Spectral unmixing using spectral phasor analysis, PCA, multivariate curve resolution, and least absolute shrinkage and selection operator (LASSO) are popular methods for unmixing hyperspectral SRS imaging datasets to enable the detection of discrete features within a sample. Our selected post image unmixing method, Spectral phasor analysis (see methods **2.2.12.4 Spectral Phasor Analysis.**) uses Fourier transformation to project every pixel from a 3D hyperspectral SRS dataset onto the 2D phasor plane (a schematic outlining this approach is shown in Figure 5. 3 from datasets discussed more fully below). Spectral phasor analysis is a convenient method because it requires no prior knowledge of the sample, and clustering of the phasors based on spectral similarity can be used to identify regions in the sample which have similar, or the same, Raman spectral profile. The first example of spectral phasor analysis applied to hyperspectral SRS imaging data was reported in 2014 for label-free detection of cellular organelles (Fu & Xie, 2014), and since then it has been applied widely to study cellular and tissue composition (Hislop et al., 2023; Huang et al., 2020; Murphy et al., 2023; Swiatlowska et al., 2024; M. Wei et al., 2019), bioorthogonal Raman probes (Braddick et al., 2023; Zhu et al., 2023) and protein aggregates (Wong et al., 2023). We therefore now can conceptualise a workflow to image adipocytes label-free, whilst acquiring the chemical information of these samples and a post unmixing method. Specific steps in this workflow are outlined below.

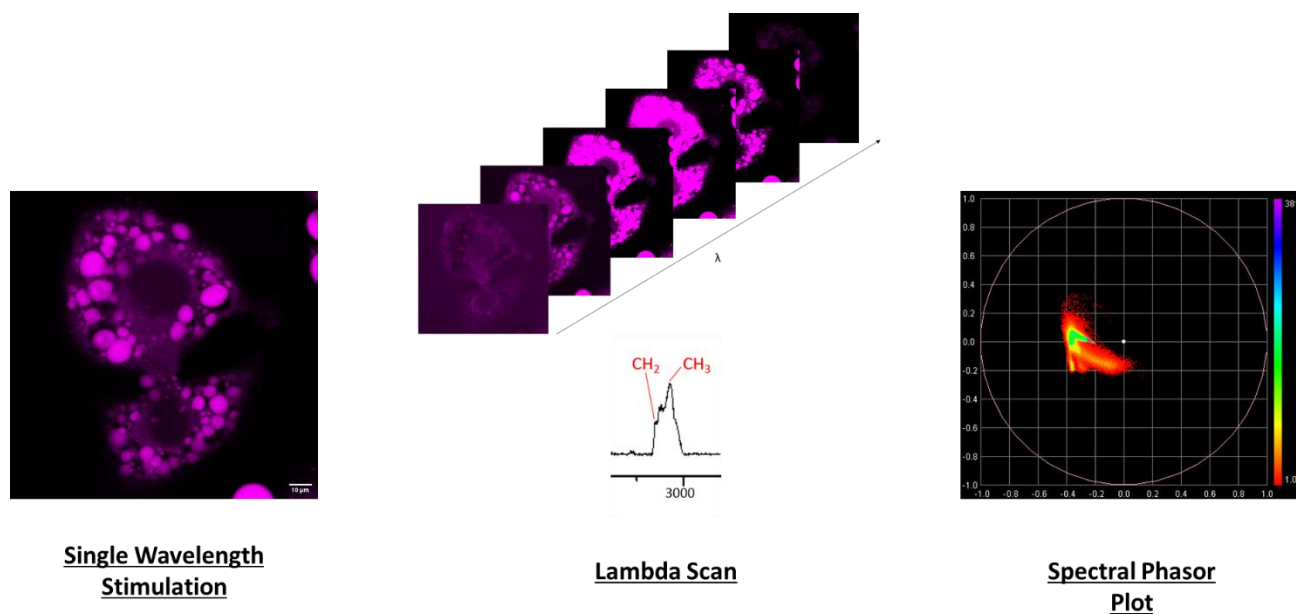


Figure 5. 3. Acquisition Capabilities of SRS

Single frame images of 3T3-L1 adipocytes can be acquired by stimulating cells at a single wavelength of light demonstrated here at 2930 cm^{-1} . A sweep of images can be taken as a stack (lambda scan) with incremental changes in wavelength ($3050\text{ cm}^{-1} - 2800\text{ cm}^{-1}$). These stacks can be given coordinates by post unmixing spectral phasor program which generates Raman spectra data as a heatmap representing biomolecule signals. Shown is representative data from studies outlined in detail below.

5.1.3 Raman Can be Exploited to Study Metabolic Readouts.

A key advantage of SRS for cellular imaging is the fact that detection of cellular biomolecules including proteins, lipids and DNA can be achieved based on the intrinsic Raman spectra and without any additional labelling. However, as shown in Figure 5. 2, Raman spectroscopy has a silent region ($1800\text{--}2800\text{ cm}^{-1}$) which has been exploited by the field for developing tools. In this region there are no stimulations of vibrations when biological samples are exposed to light and therefore no image can be generated. Due to this ‘silence’, a particularly attractive feature of developing Raman reporters is that they can be extremely small by design (down to a single chemical bond) which invokes a greatly reduced perturbation of the parent molecule. This has opened up opportunities for imaging drugs and small molecules using miniaturised Raman reporters based on alkynes and nitriles in a way that is not achievable using other optical imaging techniques (Benson et al., 2022). Furthermore, because the Raman stretching frequency is defined by the atoms which make up the molecular bond, the use of isotopic editing strategies for labelling and metabolic probing has been extremely fruitful. For example, the use of deuterium as a natural isotope of hydrogen results in a red shifting of the C–D stretching ($2000\text{--}2300\text{ cm}^{-1}$) compared to C–H stretching ($2800\text{--}3100\text{ cm}^{-1}$). As such, extremely minor modification of low-molecular weight metabolic precursors and drugs enables their visualisation in the cell-silent region of the Raman spectra using deuterium labelling.

For adipocyte metabolic studies, a key tool is deuterated labelled glucose (glucose- d_7) which can be used to study *de novo* lipogenesis by comparing newly synthesized lipid species after glucose- d_7 treatment by comparing the deuterium signal integrated into those lipids with the previous existing lipids (Du et al., 2020). Adipocytes store glucose, largely by conversion to glycerol and incorporation into TGAs and as a precursor for cholesterol esters in their droplets (Ameer et al., 2014). Further expansion of the isotopic colour palette for Raman microscopy has demonstrated the impact of ^{13}C labelling of alkynes and ^{15}N probing of nitrile groups to

increase the spectral colours available for imaging (Fujioka et al., 2020). The application of such tools could offer new insight into adipocyte heterogeneity.

Aims of this Chapter

A criticism of the 3T3-L1 adipocyte model is the multi-locular nature of the cells. Primary adipocytes isolated from mice and humans are unilocular and therefore a natural wariness has persisted that 3T3-L1 adipocytes are not an appropriate model for translational biology despite the back catalogue of studies performed in this cell line. They are generally used between days 7-12 post differentiation, however, a passing comment from Dr Robin Klemm (University of Oxford) at a conference suggested that upon prolonged incubation of these cells, they become uni-locular and more akin to primary cells isolated from rodent and human adipose tissue. To my knowledge, this increased incubation period has not been published and this could address the multi-locular criticism often made for this cell line. In this chapter, we set out to examine the biochemical and functional properties of 3T3-L1 adipocytes grown in culture for prolonged periods and to ascertain effects on lipid droplet size, number and chemical properties as a function of time post-differentiation.

Previous work to quantify glucose uptake in single cells has relied upon the expression of a fluorescent glucose biosensor within cells (Hu et al., 2018). While informative, this requires transfection and may be hampered by the expression of the bulky probe not accurately reflecting glucose levels. Moreover, this method cannot reliably report on subsequent glucose metabolism. Hence, we have turned to Raman imaging to study glucose metabolism, employing deuterated glucose (hereafter glucose-d₇). Here, we outline a novel analysis pipeline aimed at facilitating a molecular analysis of adipocyte metabolism using a suite of Raman imaging approaches, coupled to chemical probes and off-line image analysis tools and approaches which we believe will offer new insight into adipocyte (and other cell) lipid and glucose metabolism.

5.1.4 3T3-L1 Adipocytes Undergo Hypertrophy with Increased Incubation

3T3-L1 adipocytes were grown for prolonged periods to test how long these cells could be cultured, and the functional consequences of this period. Figure 5. 4A, shows 3T3-L1 adipocytes 14 days post differentiation (by convention, these cells are used in most experiments between day 10 and 14 after differentiation), and at 66 days post differentiation. Adipocytes were incubated for periods beyond 66 days but started to form sheets of cells and would detach during media replenishment (data not shown).

As can be observed, extended periods of culture did indeed result in the appearance of unilocular adipocytes (Figure 5. 4 A). There were less than half of the number of droplets in day 66 than day 14 (Figure 5. 4 B) with the larger droplets often completely occupying almost the entire adipocyte cytosol. Naturally, this results in droplets having greater diameter (Figure 5. 4 C) and perimeter measurements (Figure 5. 4 D) with the largest droplet of day 66 having an area of approximately $2600\ \mu\text{m}^2$, 6 times the size of the largest droplet at day 14 (which was approximately $400\ \mu\text{m}^2$) (Figure 5. 4 E). This presents an exciting opportunity of possible study of adipocyte expansion in cell culture as an alternative to the isolation from *in vivo* models. As well as 3T3-L1 adipocytes, studies have utilized HEK293 (Listenberger et al., 2007) and HEPG2 (Eynaudi et al., 2021) cell lines to investigate lipid droplet formation and/or fusion by treating with fatty acids like oleic acid (Eynaudi et al., 2021) - known as lipid loading - to study the mechanics of fusion and adverse effect on liver function. This expansion in droplet size however could allow for the 3T3-L1 model to be exploited to study the biochemical and functional consequences of lipid droplet expansion in future studies. Some preliminary data on this is presented in the discussion below from colleagues in the lab.

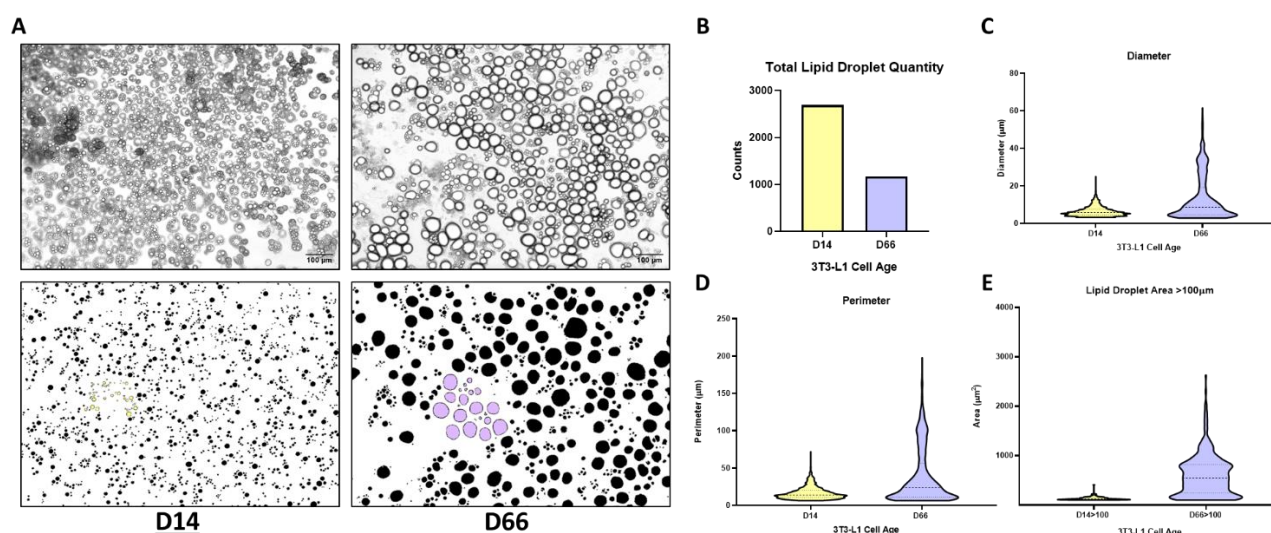


Figure 5.4. Lipid Droplet Expansion Observed in 3T3-L1 Adipocytes with Prolonged Incubation

3T3-L1 adipocytes were differentiated as outlined in 2.2.6.3 3T3-L1 Adipocyte Differentiation then grown in culture for either 14 or 66 days, (D14 and D66, respectively). Brightfield images of adipocytes were acquired with an EVOS imaging system at x10 magnification. 3T3-L1 image processing (A) and data acquisition were performed with FIJI and data analysis on droplet measurements (B) Lipid Droplet Quantity (C) Diameter (D) Perimeter and Area (E) was performed using PRISM as outlined in 2.2.13 Data Analysis of Lipid Droplets. A series of representative images is shown, with quantification of >100 cells under each condition presented in B-D.

5.1.5 *Demonstrating This Heterogeneity in Single Cells*

As the phasor plot is the coordinate data from the chemistry of the cells (Fu & Xie, 2014), a phasor plot could be described as a fingerprint for a cell as it will have unique chemical vibrations dependent on its chemical structure and therefore generate a different phasor plot for each cell (Figure 5. 5). As proof of concept, we imaged 3T3-L1 adipocytes and taken two representative images from the same coverslip to show how this workflow can be exploited. In Figure 5.5, two adipocytes are presented with notable phenotypical differences with smaller, numerous lipid droplets (Figure 5. 5 A) compared to Figure 5. 5 B which shows a cell with fewer, larger lipid droplet numbers.

This difference is then demonstrated further with the corresponding phasor plots of each cell differing in their spread of co-ordinate data that compliments the visual difference with this chemical difference. As the data collected to generate these images are a result of the stimulated chemical vibration within the adipocytes, the co-ordinate data in the phasor plot is a direct representation of chemistry within the adipocyte. Therefore, this workflow has demonstrated *chemically* and *phenotypically* the heterogeneity within our adipocyte samples without the use of lipid dyes and congruent with the ability to decompartmentalize those cell features. This is illustrated here using two clearly distinct cells, but quantification of many images of this type will facilitate deconvolution of harder to discern changes (see below).

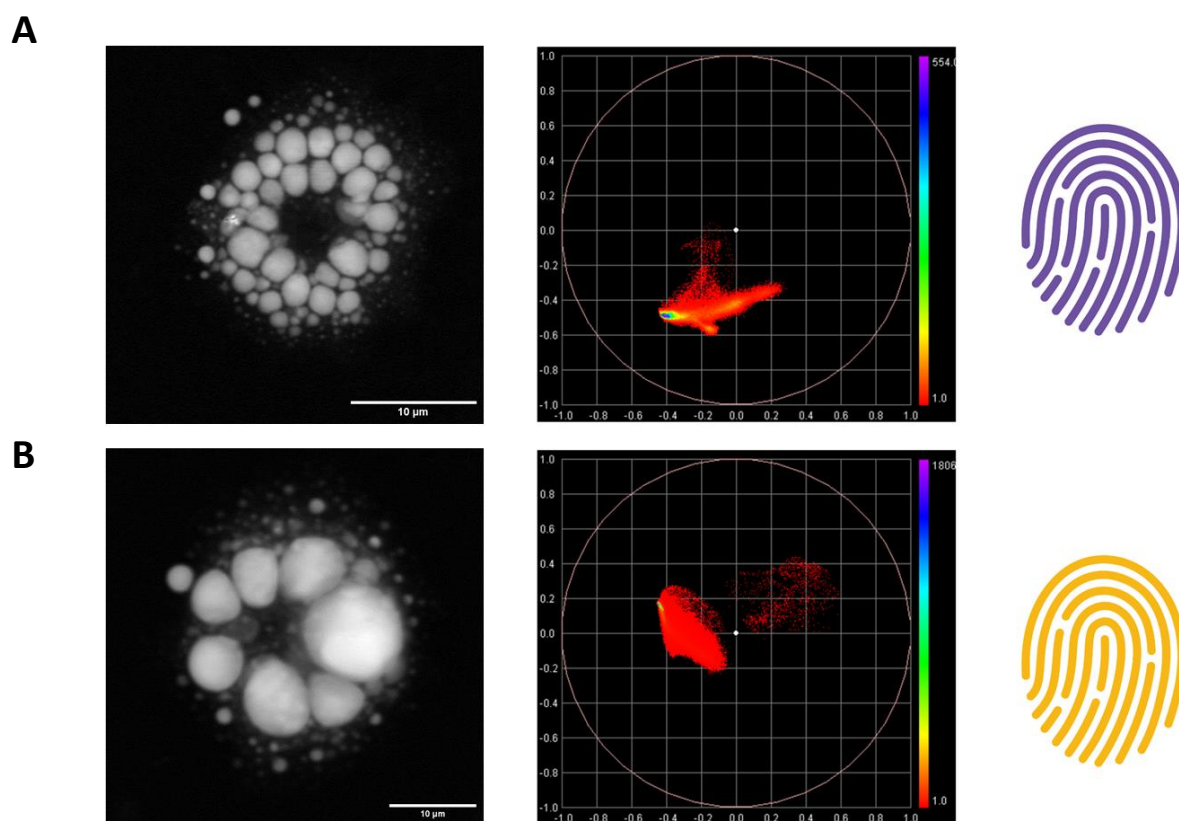


Figure 5.5. Heterogeneity in 3T3-L1 Adipocytes

3T3-L1 adipocytes at day 14 post-differentiation were imaged on SRS as outlined in **2.2.12.3 Hyperspectral SRS Imaging**. Despite fibroblasts being from the same passage, plated and differentiated under the same conditions, adipocyte heterogeneity is clearly evident here by the number of lipid droplets. Spectral phasor analysis from to quite visibly distinct cells are presented as image stacks to clearly demonstrate this, with the differences observed almost akin to a fingerprint.

5.1.6 SRS and Phasor Combination Allows for Cell Image Segmentation

The phasor plot contains molecular information of cells and has been demonstrated with lambda scans of individual adipocytes. Those plots have been applied to show whole cell heterogeneity (Figure 5. 5), however, the strength of the post unmixing phasor method allows for segmentation of the image itself and in doing so, provides a means to isolate desired regions of interest within the cells. We next applied this to study characteristic regions of the cell, as demonstrated in Figure 5. 6. Each characteristic of the cell has its own specific region within the plot: nucleus, plasma membrane and lipid droplets have been used here to visualize this. These regions can then be used to generate an image of isolated regions, as shown in figure 5. 7. Therefore, by utilizing SRS imaging, we can (i) take label-free images of cells, (ii) identify differences in the chemistry of the adipocytes and (iii) use post unmixing spectral phasor methods to segment desired regions of interest all within the same sample set and with minimum sample preparation, spatial and temporal visualization taking ~15 mins per lambda scan.

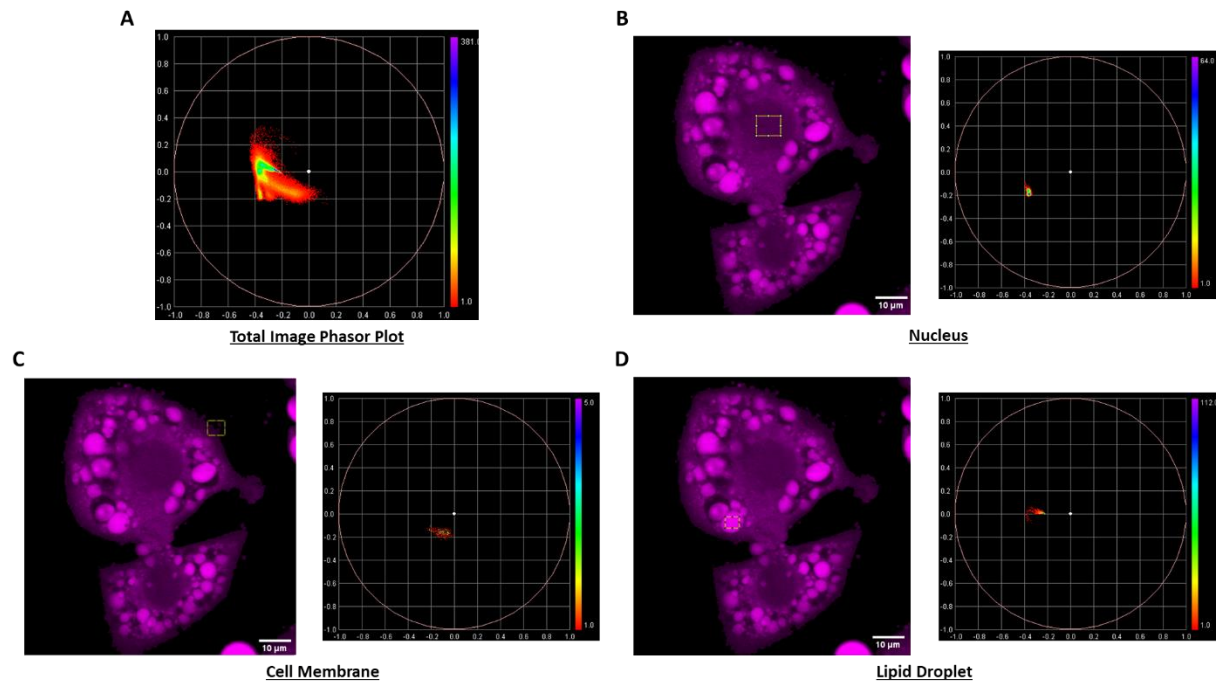


Figure 5. 6. Cellular Organelles Have Their Own Phasor Plots

3T3-L1 adipocytes were grown and used at day 14 after differentiation. Shown is data from a typical experiment. By selecting regions of interest in our cells, it is possible to dissect the coordinates for particular organelles. (A) represents the phasor plot for the entire image whilst organelles (B) nucleus, (C) cell membrane and (D) lipid droplet shown selected generate their own distinct region in the phasor plot. Hatched boxes indicate the regions used for phasor analysis in each panel.

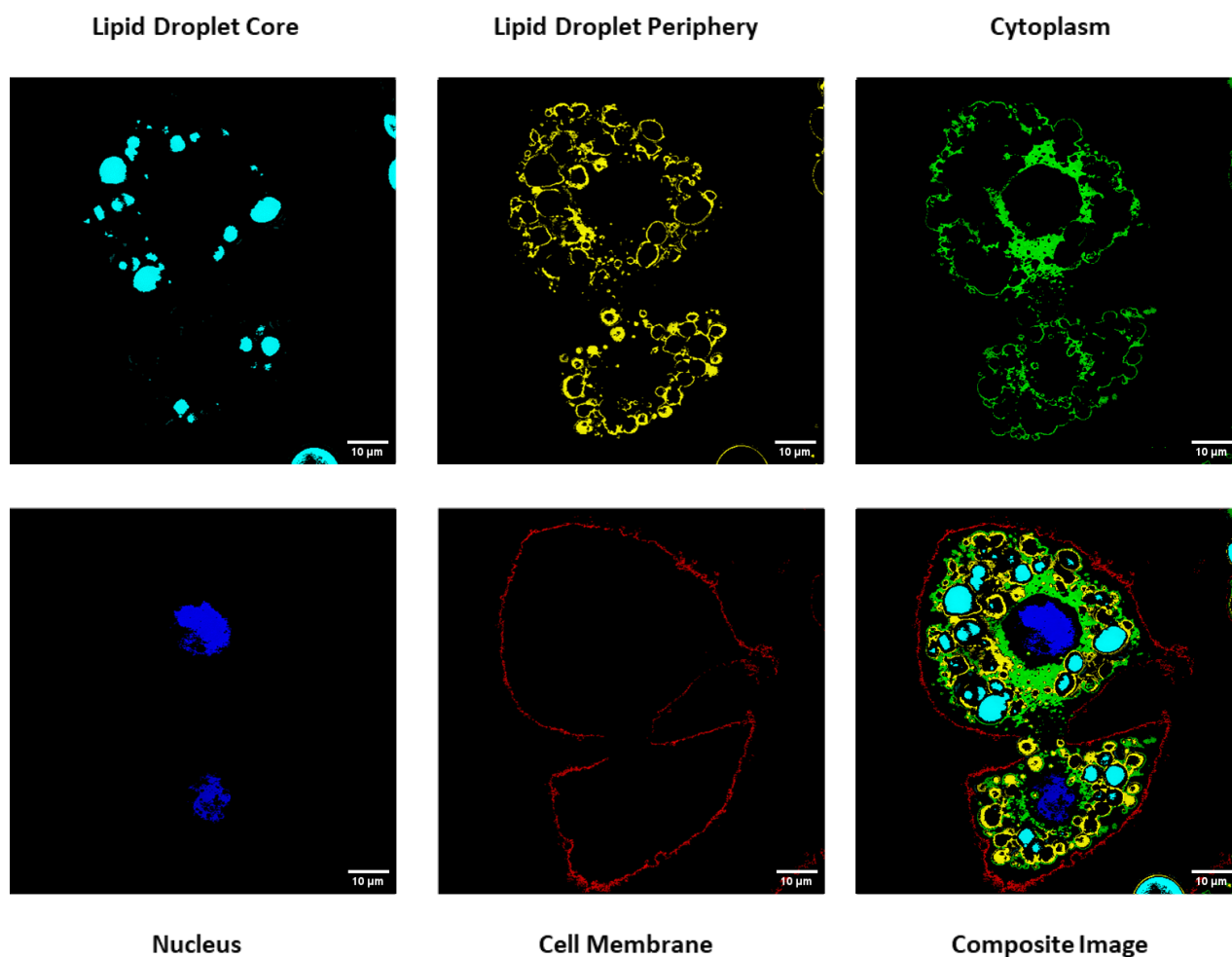


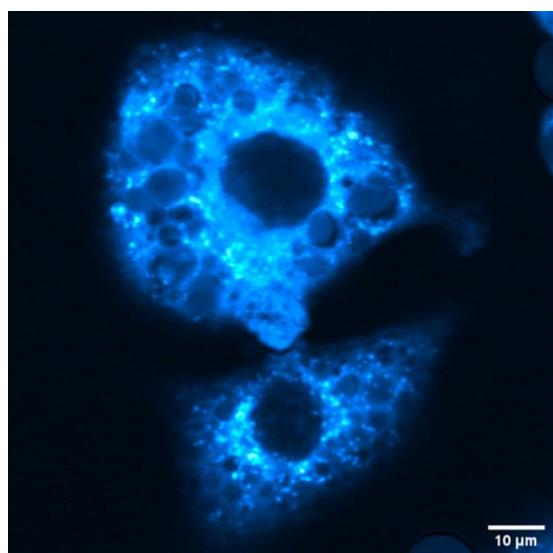
Figure 5. 7. Images of Particular Subcellular Compartments

These spectral phasor plots can then be used to generate segmented images of particular regions of interest by using the phasor to image plugin for Image J. Isolated regions are represented by central lipids (cyan), lipids around the periphery (yellow), cytoplasm (green), nucleus (blue), cell membrane (red) and a composite image of each selected region. Images were generated using the spectral phasor plugin downloaded for FIJI and using the Spectral phasor and Phasor to Image commands.

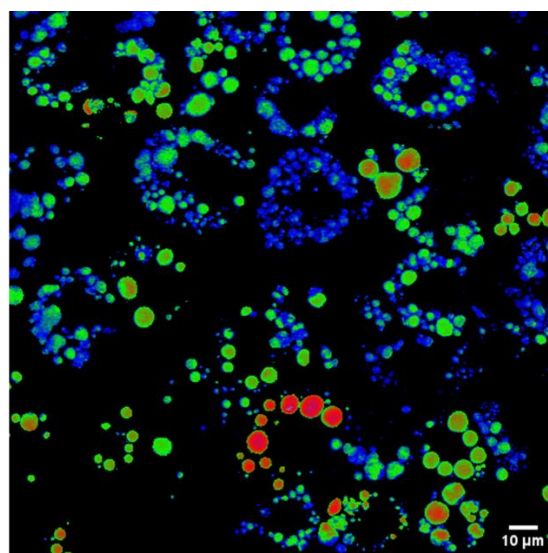
5.1.7 Using Chemical Probes to Study Adipocyte Biology.

Adipocytes store glucose, largely by conversion to glycerol and incorporation into TGAs and also as a precursor for cholesterol esters in their droplets (Ameer et al., 2014). Using glucose- d_7 for studies of metabolism has traditionally been viewed as problematic, due to the low signal intensity and time required for incorporation into cellular structures.

Using 3T3-L1 adipocytes, we labelled cells with glucose- d_7 treatments (10 mM for 24 hours) and first asked whether glucose incorporation into lipid droplets could be observed by stimulating at 2140 cm^{-1} . This can be compared with existing lipids already in droplets by stimulation at wavelength 2850 cm^{-1} . We reasoned that performing a ratiometric imaging analysis between the existing lipids and the newly synthesised lipid, would allow the visualization of the metabolic activity of the individual adipocytes within the population and also of the lipid droplets themselves. An example of this analysis is shown in figure 5.8 which includes a heat-map where blue represents low or limited incorporation of glucose- d_7 whilst red represents greater incorporation. This approach clearly reveals considerable heterogeneity both within cells, and within lipid droplets within a cell. Although this provides no insight into why individual adipocytes and droplets are incorporating glucose more than others, this demonstrates the heterogeneity within our sample set and provides proof of application to further study this.



Mitokyne



D7

Figure 5. 8. Utilising Tools in SRS

An alkyne tagged ratiometric mitochondria probe (mitokyne) can incorporate into 3T3-L1 adipocytes and enter mitochondria and visualised at 2225 cm^{-1} (left). Ratio metric analysis of deuterium labelled glucose (d7) allows visualization of the metabolic heterogeneity in glucose uptake and subsequent *de novo* lipogenesis within the same cell population (right). Increased *de novo* lipogenesis is observed through deuterium stimulation (2140 cm^{-1}) represented by the change of colour progressing from blue to green through to red.

A limitation often levelled at Raman imaging is sensitivity. Here, we have been able to detect glucose-d₇ incorporation after 1h incubation in culture and can observe a clear time-dependent increase in glucose-d₇ accumulation from 1 hour to 3 hours (Figure 5. 9 A); glucose-d₇ accumulation was also found to be insulin-dependent (Figure 5. 9 B), showing greater incorporation after 6 hours with 100 nM insulin treatment.

We next used spectral phasor analysis to identify the glucose-d₇ signal within lipid droplets in cells stimulated with insulin for 1, 3 and 6 hours compared to unstimulated controls (Figure 5. 10 A). Using this approach, a time-dependent increase in signal is evident (as would be expected for increasing exposure to glucose-d₇) but a clear insulin stimulation of incorporation into lipid droplets is only statistically significant at 6 hour incubation with insulin.

We next segmented the data obtained from each individual cell in this analysis based on cell area; the data are presented in Figure 5. 10 B. for insulin stimulated cells, and suggest that larger cells accumulate less glucose than smaller cells, in agreement with published work (Salans,et al., 1968)

Although preliminary, these data validate our assertion that SRS offers a powerful and exploitable pipeline to study single adipocytes within complex populations.

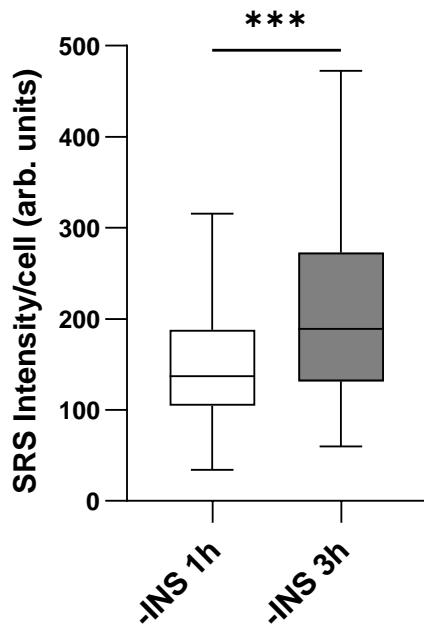
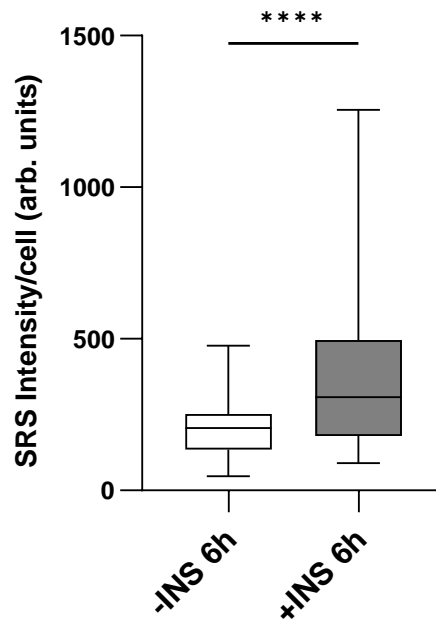
A**B**

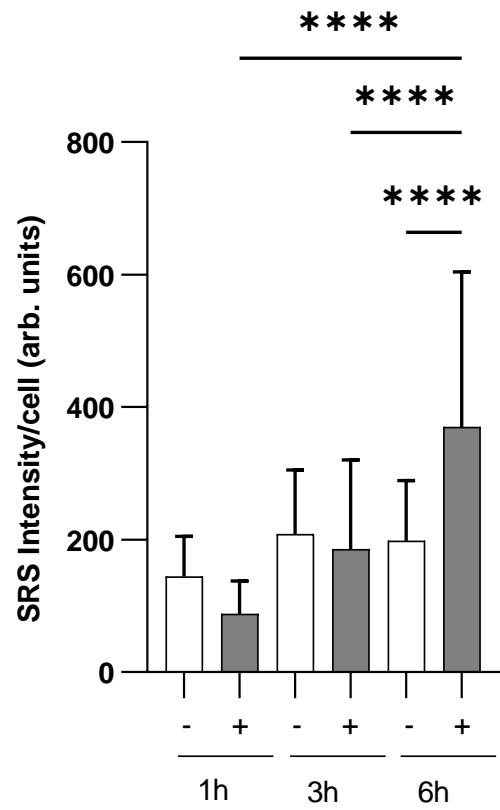
Figure 5. 9. Measuring Glucose-d7 Uptake in 3T3-L1 Adipocytes.

A. The time-dependent effect of glucose-d7 metabolism in cultured adipocytes - Adipocytes were cultured in Glucose-d7 (10 mM) for 1h and 3h prior to SRS images being acquired across the range 2100-2300 cm^{-1} . *** $P \leq 0.001$.

B. The insulin-dependent effect of glucose-d7 metabolism in cultured adipocytes - Adipocytes cultured in glucose-d7 (10 mM) in the presence and absence of insulin (100 nM) for 6 hours prior to SRS images acquired across the range 2100-2300 cm^{-1} . **** $P \leq 0.0001$.

Data in both figures represent the mean SRS signal per cell from >50 cells per condition. Statistical analysis of Mann-Whitney was performed for these experiments.

A



B

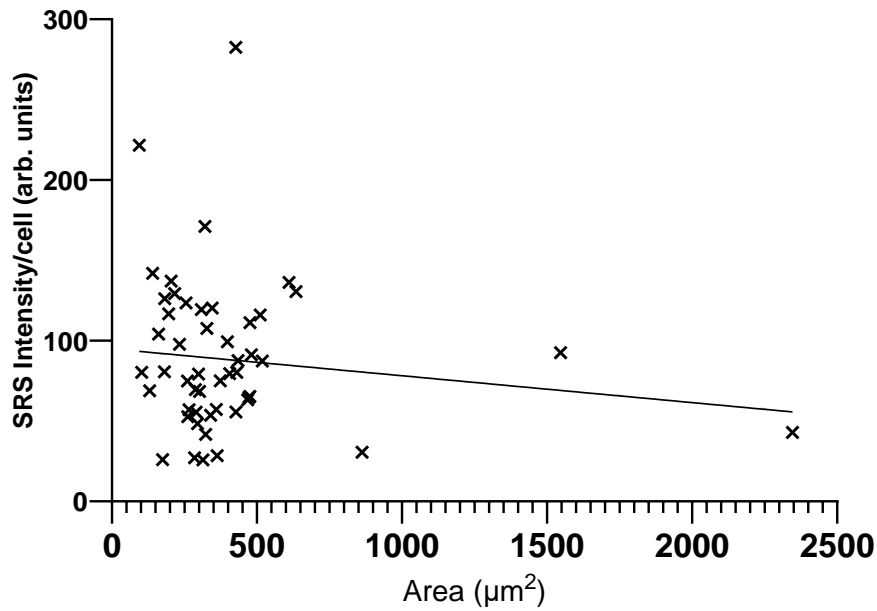


Figure 5. 10. Glucose Metabolism is Affected by Insulin and Adipocyte Size.

A. Time-dependent and insulin-dependent effect of glucose-d7 metabolism in cultured adipocytes at day 10 - Adipocytes cultured in glucose-d7 (10 mM) in the presence and absence of insulin (100 nM) for periods of 1, 3 and 6 hours prior to SRS images acquired across the range 2100-2300 cm^{-1} .

Data represent mean SRS signal per lipid droplet in >50 cells from three replicates. **** $P \leq 0.0001$.

B. Cell size effect of glucose-d7 metabolism in cultured adipocytes at day 10 - Adipocytes were cultured in Glucose-d7 (10 mM) for 1 hour in the presence of insulin (100 nM) prior to SRS images being acquired across the range 2100-2300 cm^{-1} . Glucose-d7 signal was extracted for each cell and then compared based on cell size.

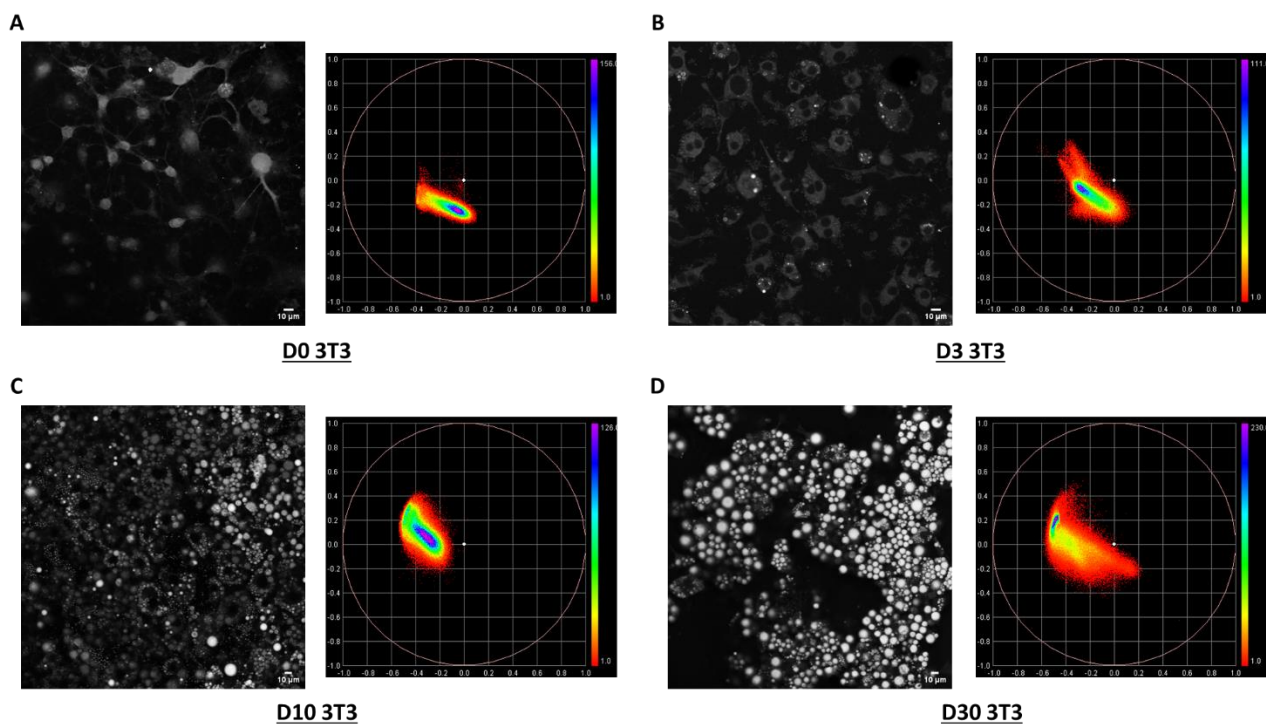
Data in both figures represent the mean SRS signal per cell from >50 cells per condition. Statistical analysis of One-way ANOVA was performed for (A).

5.1.8 Developing an Approach to Lipid Droplet Segmentation

Thus far, this chapter has demonstrated initial groundwork experiments to validate the use of SRS imaging to be implemented for investigation into adipocyte heterogeneity. An aim of this work was to apply this method to investigate lipid droplet content in 3T3-L1 adipocytes. As mentioned above, 3T3 cells start as fibroblasts and are differentiated into adipocytes. Lipids are stimulated and visualized effectively due to the abundance of CH₂ groups and the stages of 3T3-L1 differentiation are a suitable demonstration of both SRS imaging and phasor techniques (Figure 5. 11). As 3T3-L1 cells undergo differentiation into adipocytes, they lose their fibroblast characteristics and progress into spherical cells containing multiple lipid droplets. This change can be observed visually by the increased lipid droplet numbers in the Raman stacks and also in the corresponding phasor plots with the change in coordinate data distribution from Day 0-10 (Figure 5. 11 A-C). The increase in droplet number shows evidence of lipogenesis, however, as the cells incubation time is prolonged to the day 30 mark, the cells undergo hypertrophy-possibly through droplet fusion- with now less numerous, but larger droplets (Figure 5. 11 D) - also seen in Figure 5. 4. This lipid content increase is reflected in the change seen in the phasor plot where the region of interest selected becomes ‘fuller’ and a greater intensity of pixels are recorded as the days progress (Figure 5. 11 post unmixing A-D). This region of interest in the phasor plot has then been used to generate an image of the lipids (shown in yellow) and shows that lipid concentrations increase with time and has been represented by a percentage of total image coverage with Day 0 covering 0.03%, Day 3 2.33%, Day 10 7.01% and Day 30 23.74% (Figure 5. 12). As the signal recorded from SRS is due to the direct chemical vibrations of the sample, the signal is directly proportional to the concentration of lipids that are being stored as these adipocytes differentiate and are incubated over time. This analysis and quantification differ from the one performed in Figure 5. 4 using the threshold method, as instead of segmenting by eye and circularity for droplets, it is the CH₂

stretch vibrations of the lipid that allow for accurate and confident segmentation of these droplets. This then demonstrates SRS can be used in our models quantitatively to detect changes within our samples and not just as a qualitative method.

Pre Unmixing Whole Cell Images



Post Unmixing Segmented Lipid Images

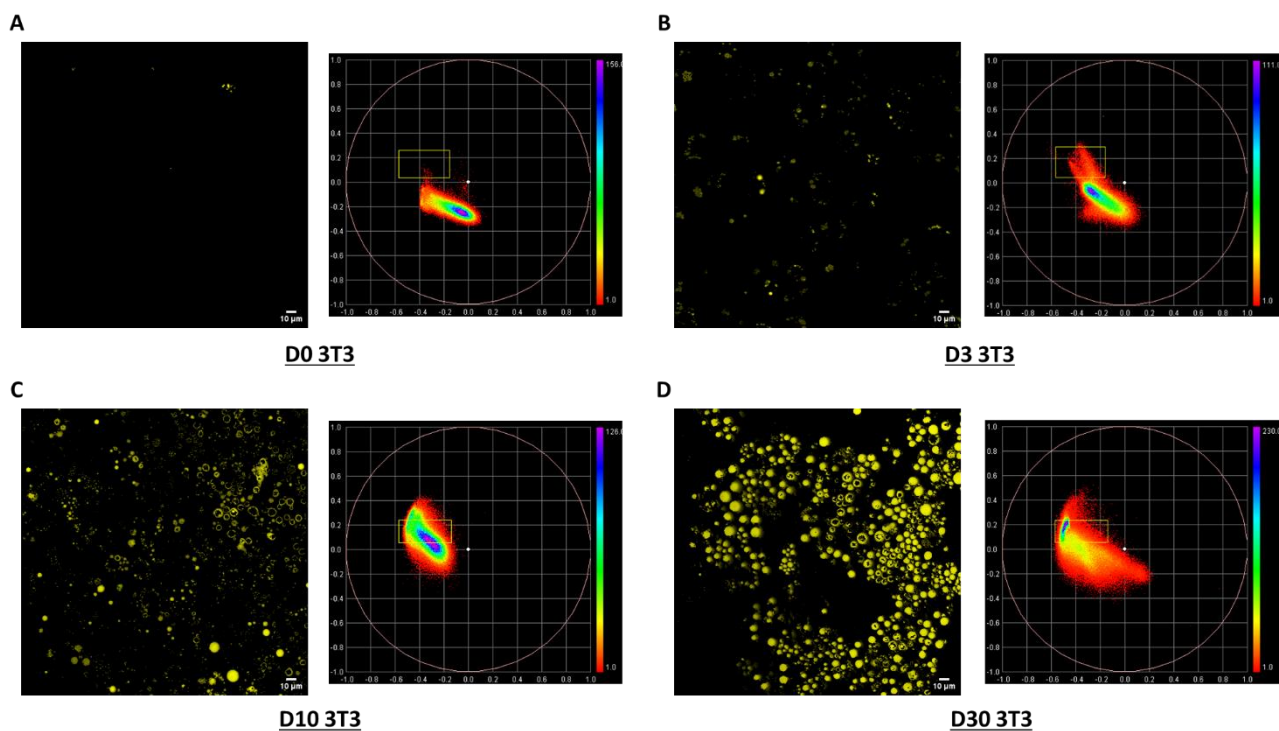


Figure 5. 11. Spectral Phasor Allows for Lipid Segmentation

Lambda scans in the high wavelength region ($3050\text{-}2800\text{ cm}^{-1}$) were taken of 3T3-L1 adipocytes at different points of differentiation Day 0 (A), Day 3 (B), Day 10 (C) and Day 30 (D). Respective phasor plots for each differentiation point allow for the segmentation of lipid droplets (shown in yellow). Lipid quantity can be measured by extracting percentage of image covered in yellow, tracking droplet formation. Analysis was performed in PRISM.

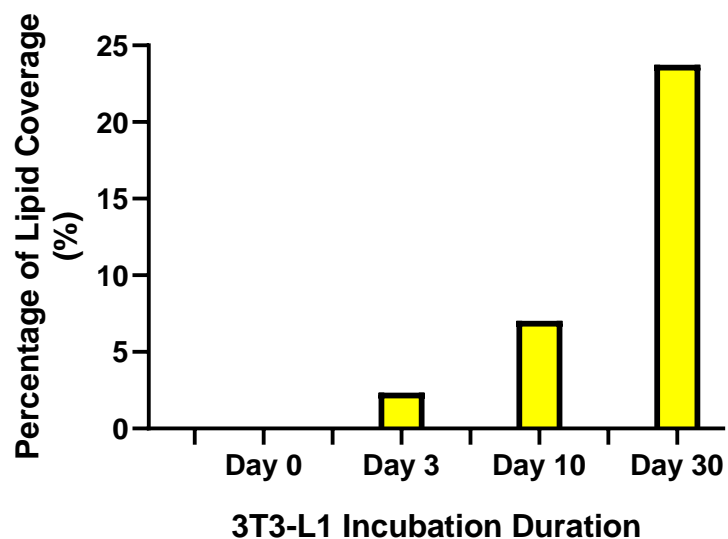


Figure 5. 12. Spectral Phasor Allows for Lipid Quantification

Lambda scans in the high wavelength region ($3050\text{-}2800\text{ cm}^{-1}$) were taken of 3T3-L1 adipocytes at different points of differentiation represented in ***Figure 5. 11. Spectral Phasor Allows for Lipid Segmentation and Quantification***. Lipid quantity can be measured by extracting percentage of image covered in yellow, tracking droplet formation. No statistical analysis was performed due to $n=1$. Graph was plotted in PRISM.

5.1.9 Investigating Differences in the Adipocyte Life Cycle

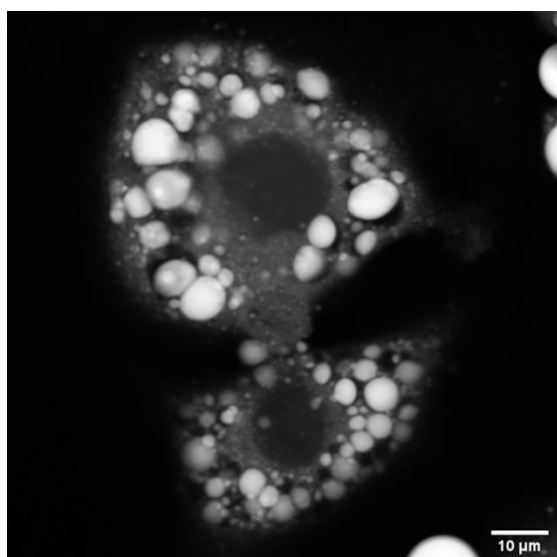
We next sought to apply these methods to different timepoints of 3T3-L1 differentiation – specifically to consider how multi-locular adipocytes may differ from unilocular cells. For this analysis, Day 10 and Day 35 were chosen. It is difficult to replicate the long timescale of Day 66 as shown in Figure 5. 4. as the expanding nature of the lipid droplets in the adipocytes results in cells readily detaching from the coverslips during washes etc. Day 35 allowed for imaging as cells stayed attached and lipid hypertrophy was evident in the samples (Figure 5.13).

Due to the method of acquiring lambda scan stacks for the high wavelength region, we captured images at incremental wavelengths between 3050 and 2800 cm^{-1} . By plotting a z-axis profile with this stack, we generate Raman spectra for the entire cell or desired points of interest by combining the SRS intensity from each frame. This z-axis profile contains all the information collected from the C-H stretches of our adipocyte samples and means when we select individual lipids from 3T3-L1 adipocytes, thereby allow molecularly-specific information on the content of these lipid droplets to be extracted. Figures 5. 14 and 5. 15 show representative examples of this analysis.

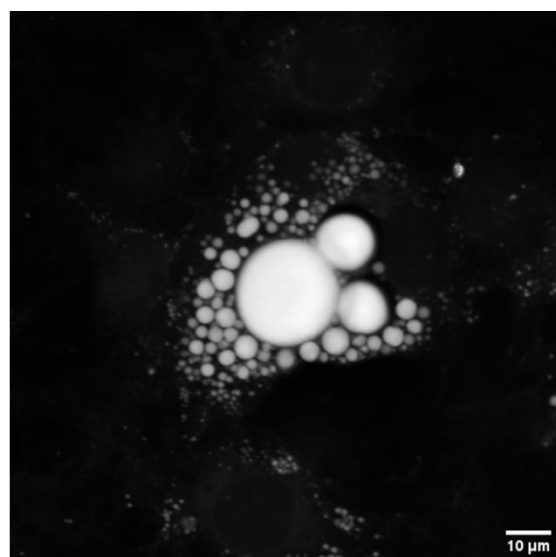
In Day 10 cells, lipid droplets of varying size have been selected to determine differences in droplet composition (Figure 5. 14). Droplet 7 has a diameter of approximately 8.5 μm and an area of approximately 53.2 μm^2 whilst droplet 10 has a diameter of approximately 3.2 μm and an area of approximately 7.7 μm^2 . This size difference is reflected in the intensity of the SRS signal with the larger droplet (droplet 7) having a greater intensity than the smaller droplet (droplet 10) (Figure 5. 14) representing a greater concentration of lipid with increased droplet size. Despite this 6.9x difference in area size and location, the contents of the lipid droplets are similar and when normalized to one another, their z-axis profiles show a similar spread of CH_R stretch stimulations for all droplets with maximum peak signals at $\sim 2935 \text{ cm}^{-1}$ representing the

CH₃ stretch and similar peaks at ~2866 cm⁻¹ (CH₂ unsaturated lipid) and ~3018 cm⁻¹ (C=C unsaturated lipids).

However, by analyzing Day 35 adipocyte in the same manner, we can identify differences in the droplet composition. Droplet 1 is approximately 22.6 μm in diameter with an area of approximately 393 μm² whilst Droplet 8 is approximately 5 μm in diameter and approximately 20.7 μm² in area. Again, lipid concentration is greater in the larger droplet (droplet 1) compared to the smaller droplet (droplet 8). Interestingly though, the z-axis profile presents the droplets with a different spread of data than the Day 10 droplets. This time, the maximum peak for SRS intensity is at the ~2866 cm⁻¹ (CH₂ unsaturated lipid) and not ~2935 cm⁻¹ showing greater accumulation of unsaturated lipids in these droplets. Despite the 19x difference in area size, the spread of peaks is similar between the two with a greater ratio of ~2886 cm⁻¹ signal to 2935 cm⁻¹ signal compared to the closer to equal ratio observed in the Day 10 droplets. Taking a smaller droplet (droplet 25) we can see the Raman spectra is similar to the spectra in the Day 10 droplets (Figure 5.15).



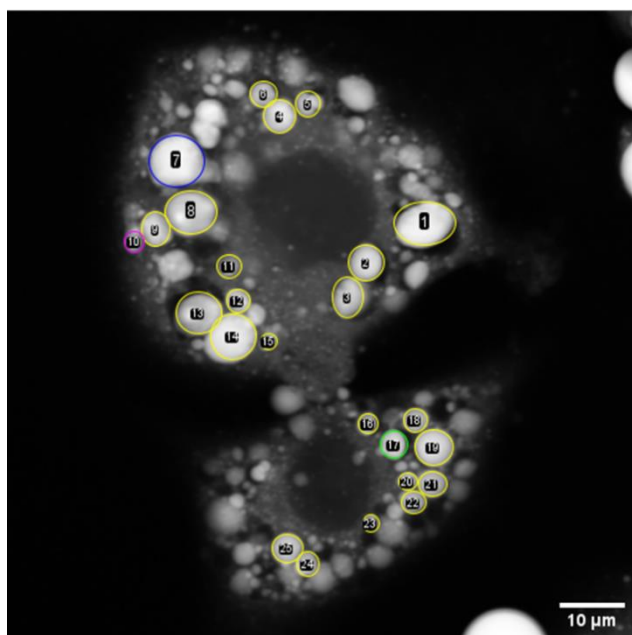
Day 10



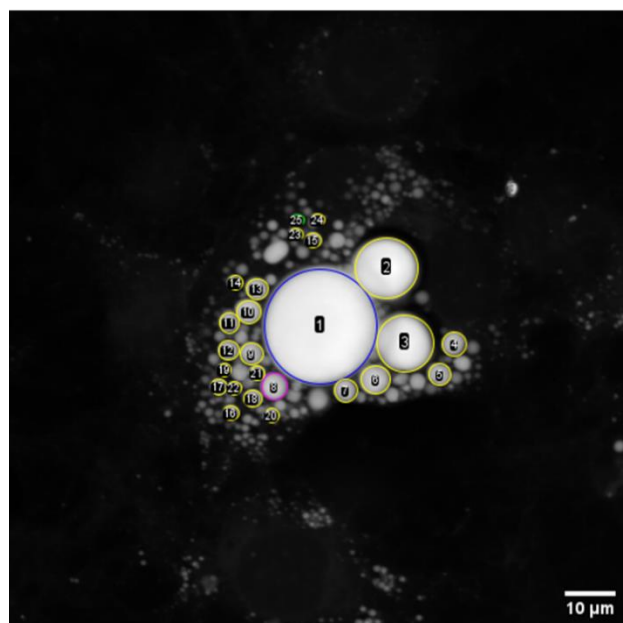
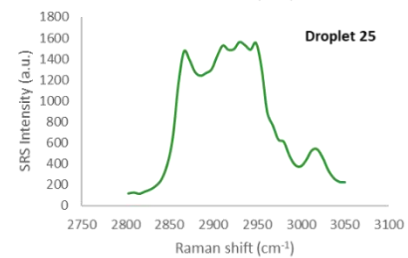
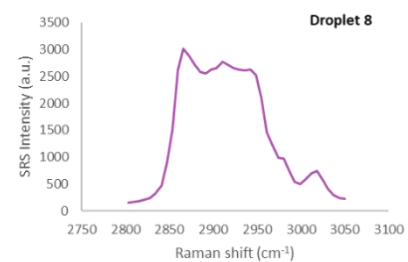
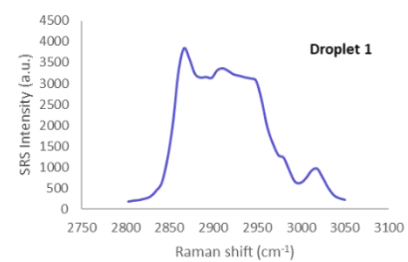
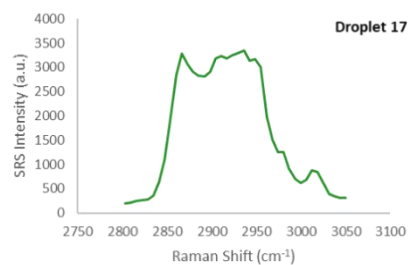
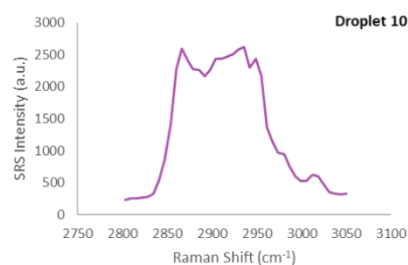
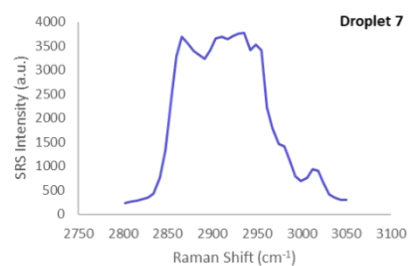
Day 35

Figure 5. 13. Evident Hypertrophy of Lipid Droplets in Lengthened Cultured 3T3-L1 Adipocytes

Label-free SRS imaging allows for the comparison of lipid droplet characterisation between cell culture incubation periods. Lambda scans in the high wavelength region ($3050\text{-}2800\text{ cm}^{-1}$) were taken of 3T3-L1 adipocytes at different points of differentiation Day 10 and Day 35.



Day 10



Day 35

Figure 5. 14. Lipid Droplet Content Characterization Possible Through SRS

Lambda scans in the high wavelength region ($3050\text{-}2800\text{ cm}^{-1}$) for 3T3-L1 adipocytes allow for Raman spectra to be generated for selected lipid droplets with each frame corresponding to a different wavelength. Droplets of various sizes were selected manually using a region of interest tool (ROI). Raman spectra generated in FIJI were plotted using Excel.

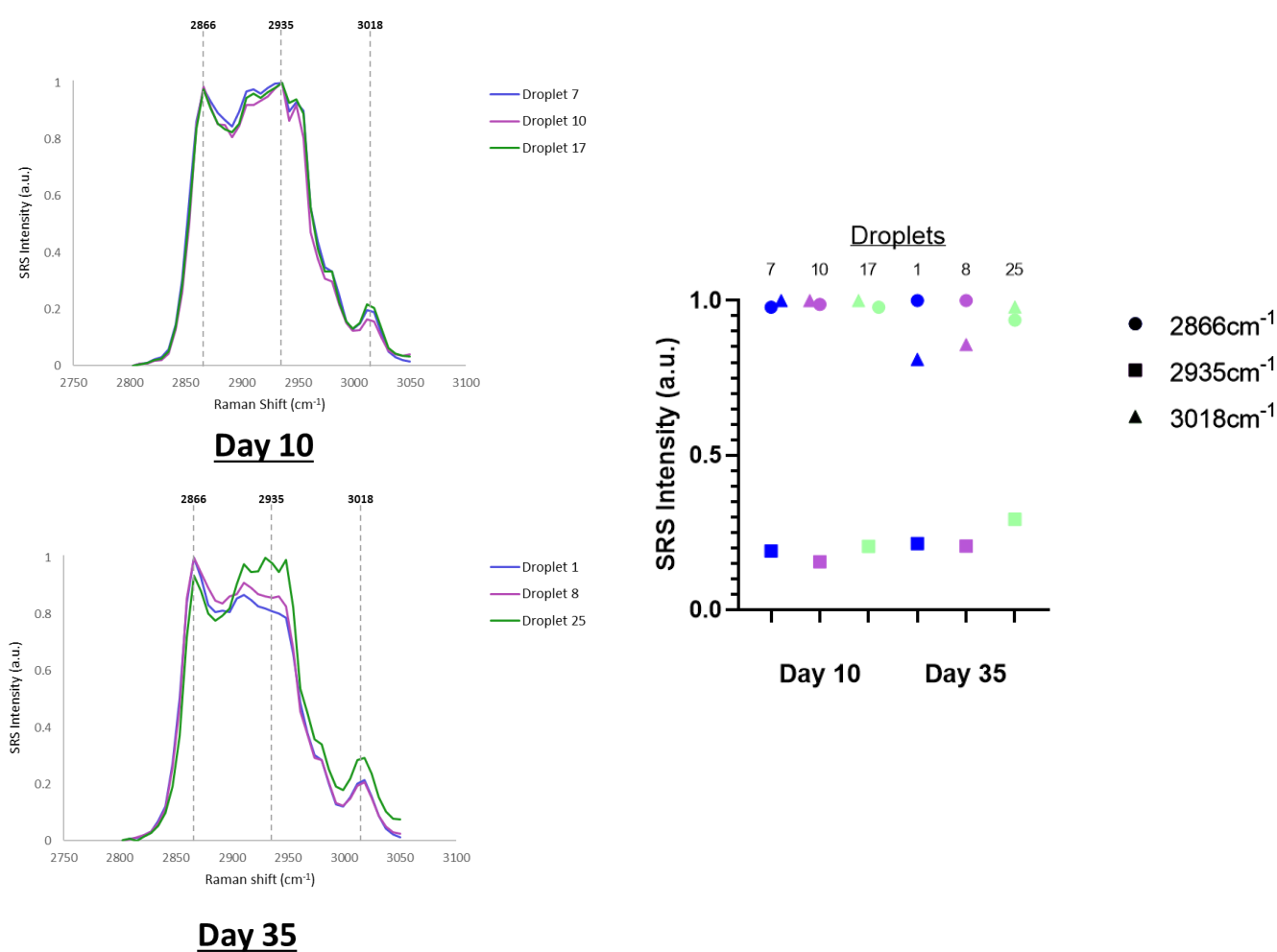


Figure 5. 15. Lipid Droplet Composition Changes Observed with Increased Incubation Periods

Lambda scans in the high wavelength region (3050-2800 cm⁻¹) for 3T3-L1 adipocytes allow for Raman spectra to be generated for selected lipid droplets with each frame corresponding to a different wavelength. Droplets of various sizes were selected manually using a region of interest tool (ROI). Raman spectra generated in FIJI were plotted using Excel and have been overlapped to compare the lipid content differences between size and incubation times.

5.1.10 Understanding Adipocyte Heterogeneity Further with Droplet and Whole Cell Segmentation

The lipid composition data acquired above was obtained by taking lambda scans in the high wavelength region ($3050\text{-}2800\text{ cm}^{-1}$). We have previously demonstrated the post image unmixing capabilities of the spectral phasor plugin. By using the spectral phasor plug in, we can perform the same segmentation techniques comparing lipid droplets from Day 10 and Day 35 adipocytes and use this to exemplify the kinds of information which may be obtained using this analysis pipeline.

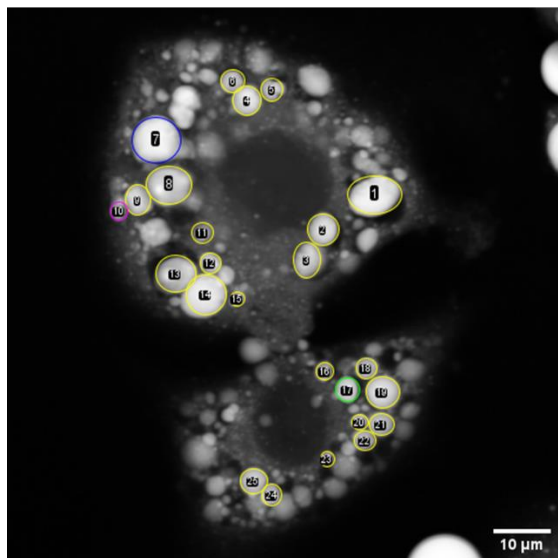
The phasor plugin has generated similar Raman spectra profiles for each lipid droplet (Figure 5. 16) as was shown in Figure 5. 14 for Day 10 and Day 35 adipocytes. The similarity in droplet composition in Day 10 cells is reflected in the respective phasor plots with the majority of pixels being in the $(-0.4, -0.0)$ quadrant of the plot for the three lipid droplets analyzed. The larger droplets (droplets 1 and 8) in the Day 35 cell have pixels in the above quadrant $(-0.4, 0.2)$, whilst droplet 25 -the smaller droplet- has a similar pixel spread as the Day 10 droplets. This difference in pixel spread for the larger droplets reflects the difference in Raman spectra with the larger droplets having a greater ratio of 2866 cm^{-1} to 3018 cm^{-1} signal.

The strength of the phasor is the segmentation demonstrated in Figures 5. 7 and 5. 11. With the plots for each lipid droplet obtained under different conditions -Day 10 and Day 35 incubations- each quadrant can be isolated to identify the location of the signal within our samples. By taking droplet 1 in our Day 35 adipocyte, the lower quadrant shows that the lipid signal is from the center of the droplet with a greater ratio of 2866 cm^{-1} signal and the upper quadrant represents signal from the periphery of the droplet with an even greater ratio of 2866 cm^{-1} signal. This has been repeated for droplet 7 in the Day 10 adipocytes and despite the same segmentation and locations as the Day 35 droplet, the peaks in the Raman spectra show a more even distribution of 2935 cm^{-1} and 2866 cm^{-1} signals.

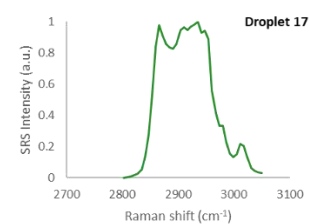
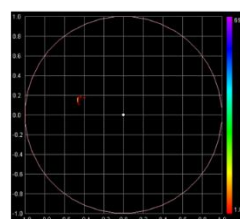
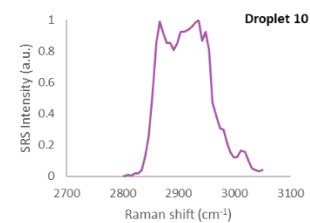
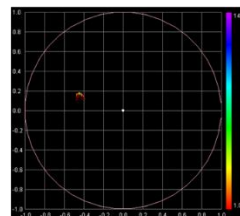
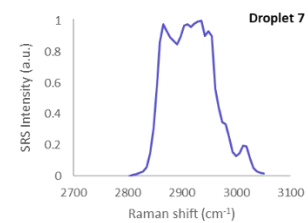
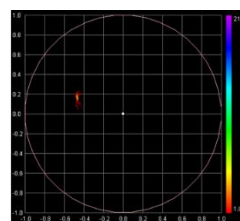
This segmenting was then applied to the entire cell to observe if the same trend would be observed across all lipids. By matching the co-ordinates of the quadrants on the phasor plot, you can segment the exact area in both cells, allowing for direct comparison between the two. By comparing two models of different incubation periods, we are comparing how adipocytes store their lipids and how this laying down changes as time progresses. This is observed to a greater extent in the whole cell analysis. To demonstrate the capabilities of the workflow, all lipid droplets were incorporated to demonstrate the differences in droplet size and contents. The adipocytes have more than enough droplets, but the contents of them differ. This is nicely shown with Figure 5. 18. The core of the droplets between the two incubation periods show similar resemblance represented by the yellow images and resulting Raman spectra, although the contents are different. However, with the blue and green segmentation images despite the Day 10 having abundant droplets, there is little signal compared to the Day 35 adipocytes. There is a considerable distribution around the periphery of the droplets in the Day 35 images. The key take-home from these data is the capacity of pairing the label-free approach, representing the true chemistry of the cell, with the segmentation capabilities of the phasor. Previous studies have used SRS to study metabolic ageing in *Drosophila* by evaluating lipid metabolism (Li et al., 2021), or cancer survival with changes in lipid metabolism (Tan et al., 2022) utilizing the Raman spectra to determine changes in lipid droplets. However, shown here is a method to display and quantify differences in spatial distribution of lipid species within either specific lipid droplets or on a whole cell basis. This is in stark contrast with work involving immunofluorescence which deploys fluorescent probes. These are limited due to the non-specific nature of the neutral lipids they stain and therefore extracting composition of the droplet is not possible (Kennedy et al., 2001; Liu et al., 2009; Mehlem et al., 2013; Spangenburg et al., 2011). Lipid profiling has been carried out with mass spectrometry techniques (Wang et al., 2015), but the samples are destroyed in the process, it is not high-

throughput and cannot be studied in real-time; further the approach is expensive in both experimental analysis and data analysis time-lines. By contrast, here we have shown a capacity to gather molecular insight and information on both lipid species and lipid distribution data in the same sample set as well as metabolic activity and cell phenotypic characteristics, e.g. by using specific probes such as glucose-d₇. Thus, we suggest that our analysis pipeline could be of wide use in the study of metabolic changes in adipocytes with disease, and provides a potential to study with single cell or even individual lipid droplet granularity how changes accompany cell function. Importantly, this approach does not rely on non-specific lipid probes or the use of protein biosensors. This is discussed further in our recent review (Greig et al., 2024).

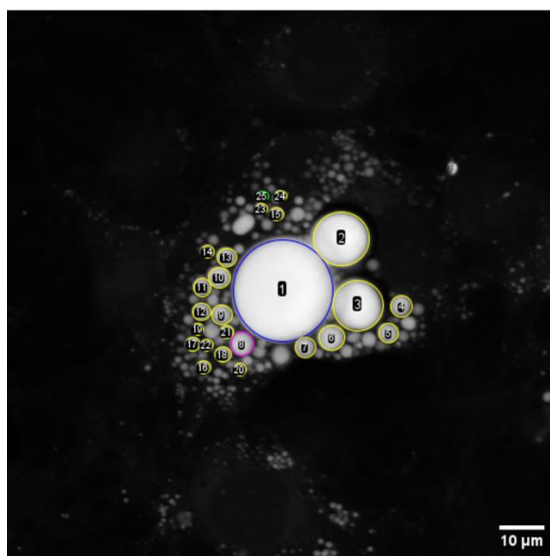
A



Day 10



B



Day 35

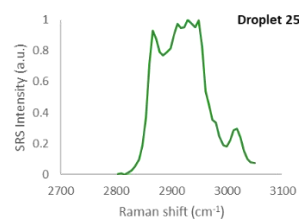
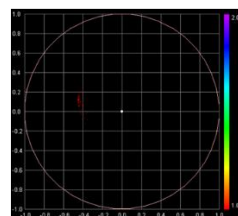
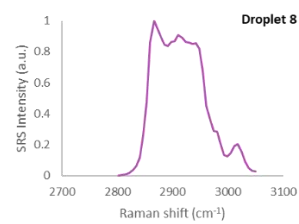
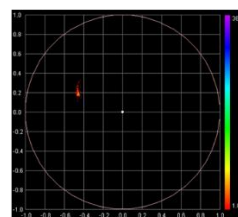
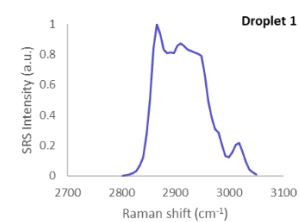
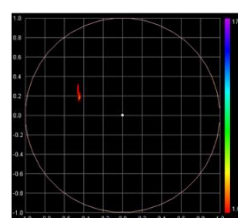


Figure 5. 16. Post Image Unmixing as an Alternative for Lipid Droplet Analysis

Lambda scans in the high wavelength region ($3050\text{-}2800\text{ cm}^{-1}$) for 3T3-L1 adipocytes allow for Raman spectra to be generated for selected lipid droplets with each frame corresponding to a different wavelength. 3T3-L1 adipocytes at timepoints Day 10 (A) and Day 35 (B) were imaged. Droplets of various sizes were selected manually using a region of interest tool (ROI) in FIJI. Post image unmixing phasor analysis generates phasor plots for each lipid droplet selected and Raman spectra generated in FIJI from these plots were plotted using Excel.

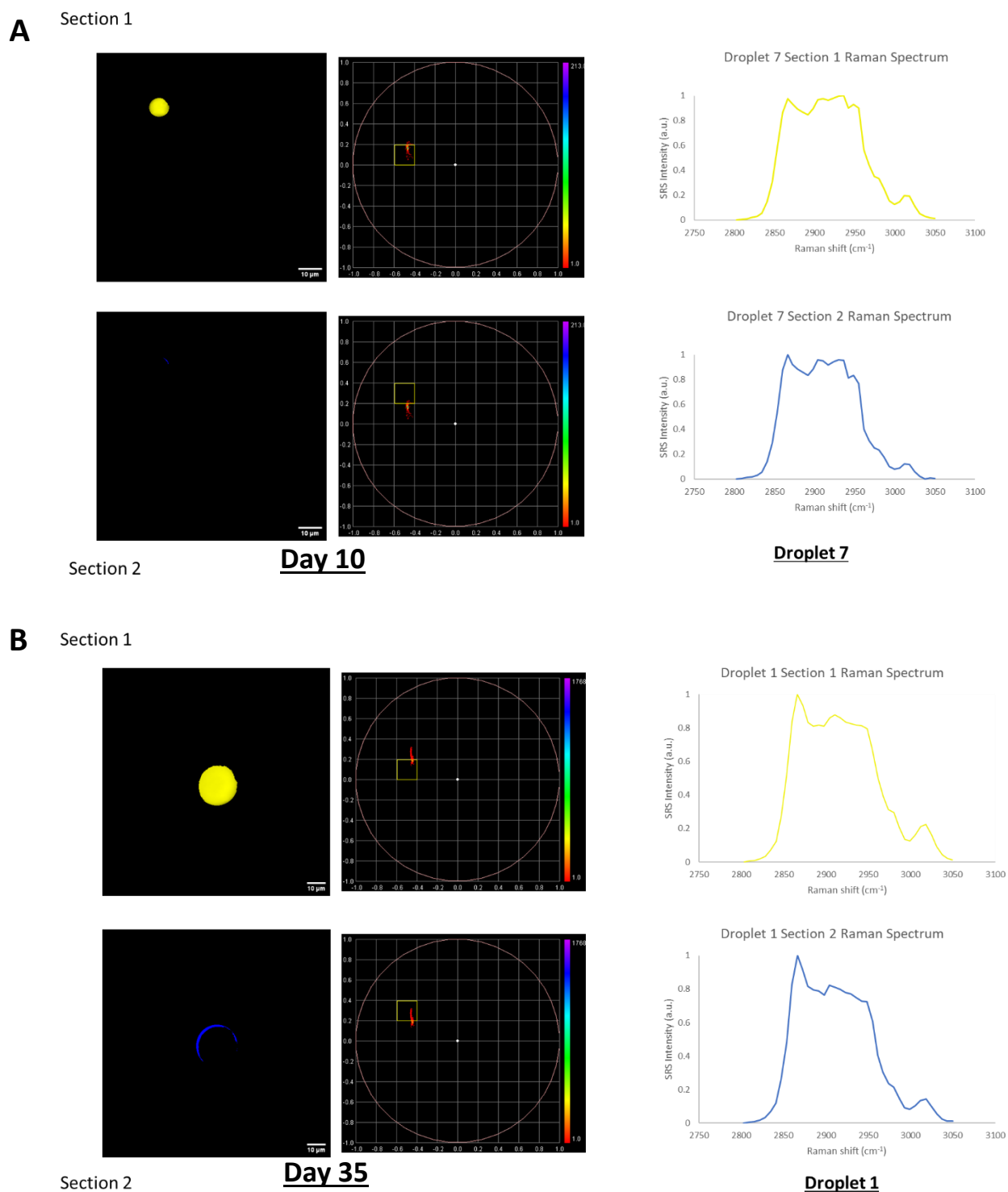
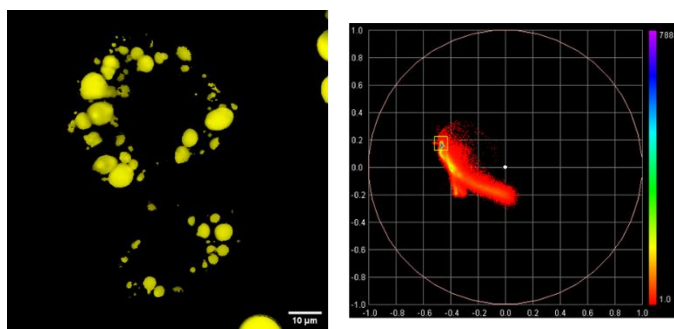


Figure 5. 17. Individual Lipid Droplet Interrogation Possible with Spectral Phasor

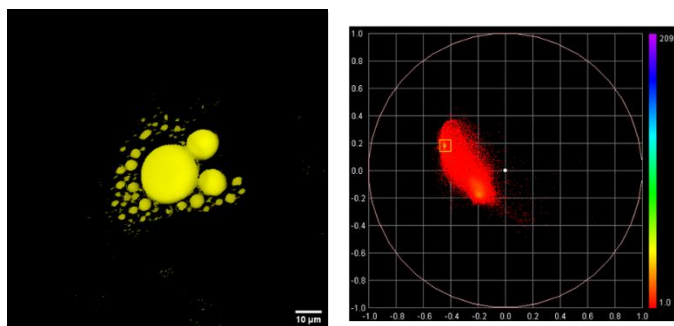
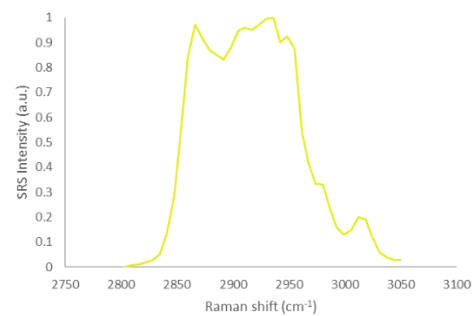
One droplet from each incubation period (Day 10 (A) and Day 35 (B)) were selected from lambda scans in the high wavelength region ($3050\text{-}2800\text{ cm}^{-1}$) using the ROI tool in FIJI. Post image unmixing phasor analysis generates phasor plots for each lipid droplet selected and separate quadrants selected in the

phasor plot allow for segmentation of the lipid droplet and Raman spectra generated for each selected quadrant in FIJI were plotted using Excel.

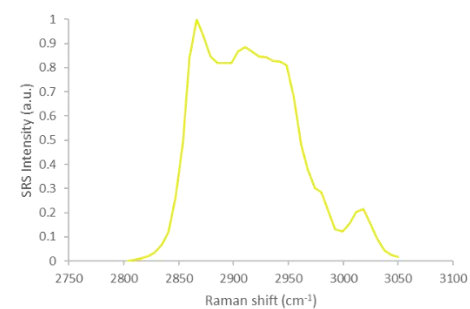
A



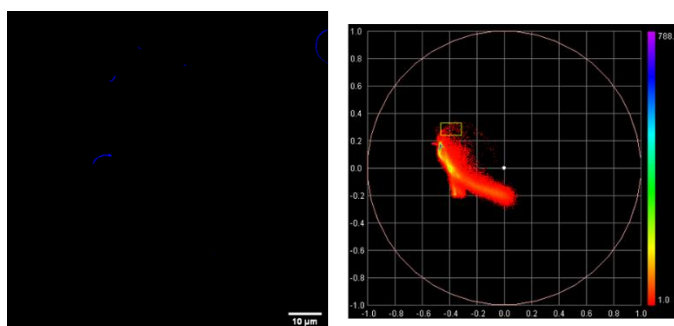
Day 10



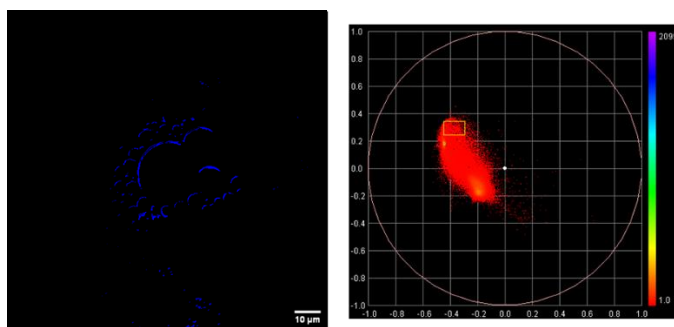
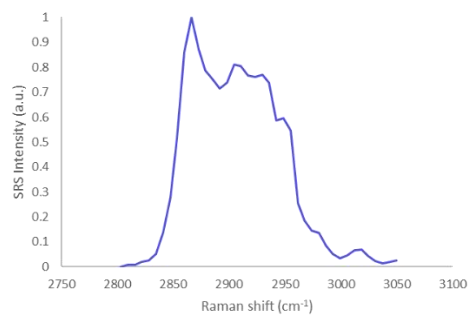
Day 35



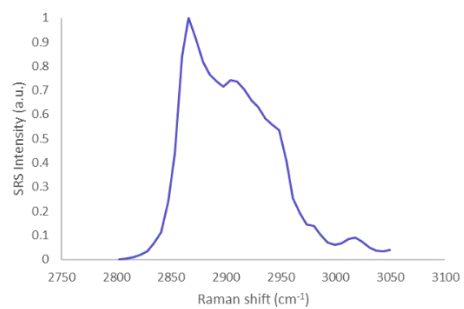
B



Day 10



Day 35



C

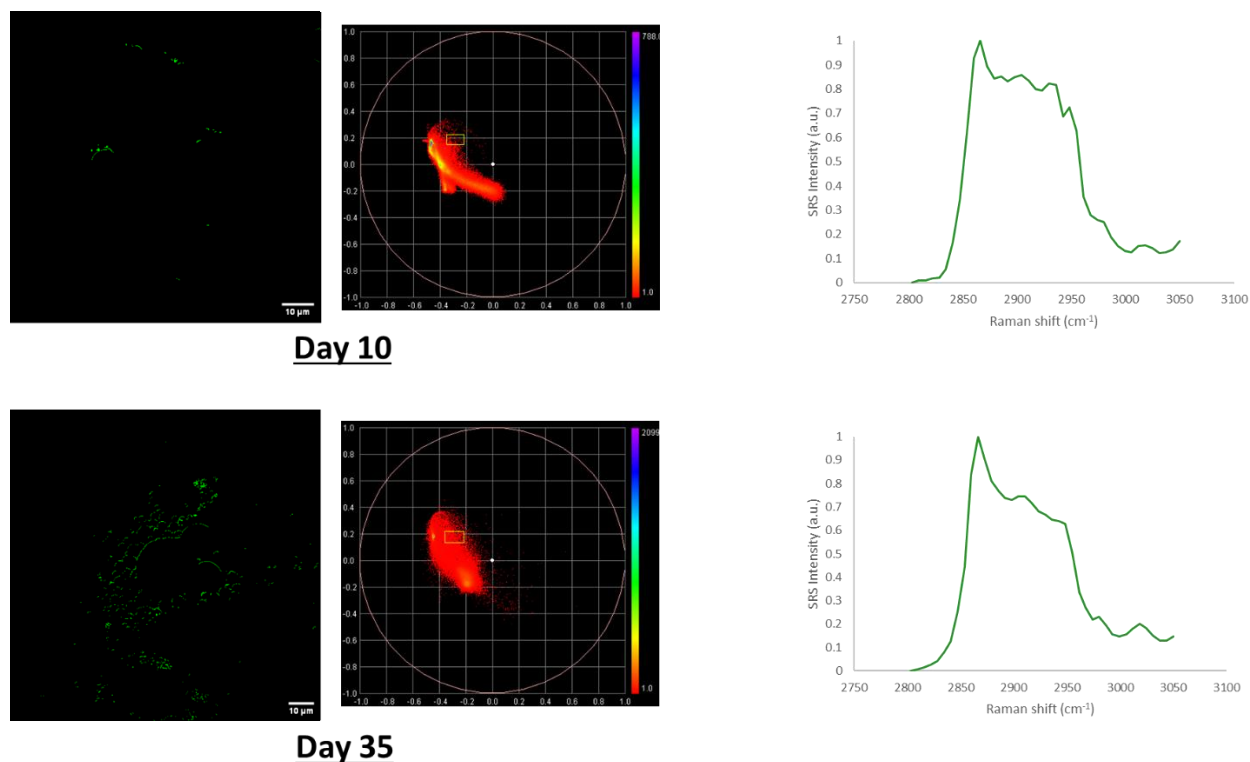


Figure 5. 18. Implementing Spectral Phasor for Total Cell Analysis

Total cell analysis of 3T3-L1 adipocytes (Day 10 and Day 35) was performed from lambda scans in the high wavelength region ($3050\text{-}2800\text{cm}^{-1}$). Post image unmixing phasor analysis generates phasor plots for entire cell. The same region was selected in Day 10 and Day 35 to extract images and compared the difference. This was performed for three separate regions of the cell and plotted separately (A, B and C. Raman spectra generated for each selected region in FIJI were plotted using Excel.

5.2 Discussion

5.2.1 A New Route for Adipocyte Metabolic Investigation

We have laid out a workflow and platform for non-invasive imaging and analyzing 3T3-L1 adipocytes. We have demonstrated we can successfully acquire label-free images in widefield for population images and of single cells in different conditions to analyze the heterogeneity in cells. This is not limited to qualitative research, due to the lambda scans these stacks are information rich with molecular information and can be analyzed quantitatively for cell numbers, droplet measurements and content and adipocyte metabolic activity. Time has prevented the further development of this element of the work.

Lipid droplet composition is important in metabolic health (Eynaudi et al., 2021; Onal et al., 2017). Enlarged adipocytes are associated with obesity and poor health (Santoro & Kahn, 2023; Santoro et al., 2021) and the incorporation of increased consumption of saturated lipids in the diet are drivers of this (Phillips et al., 2012). 3T3-L1 adipocytes are cultured in DMEM supplemented with L-Glutamine and with increased incubation times, the larger droplets are utilizing the glutamine in the TCA cycle and storing the resultant fatty acids as unsaturated lipids. Colleagues in the lab have shown that even with these increased droplet sizes, there is no change in either the basal or maximally stimulated rate of glucose transport, nor in insulin (*Figure 5. 19. Glucose Uptake with Increasing 3T3-L1 Adipocyte Incubation Periods*) in 3T3-L1 cells between day 10 and 40. Hence, this appears to represent healthy expansion in lipid droplet size (towards monocular) that is not affecting metabolic activity, at least as judged by glucose transport and insulin sensitivity. We have demonstrated two approaches in which we can extract the information from 3T3-L1 adipocytes and their lipid droplets through Raman imaging with z-axis projections and spectral phasor analysis with both methods complimenting/strengthening one another.

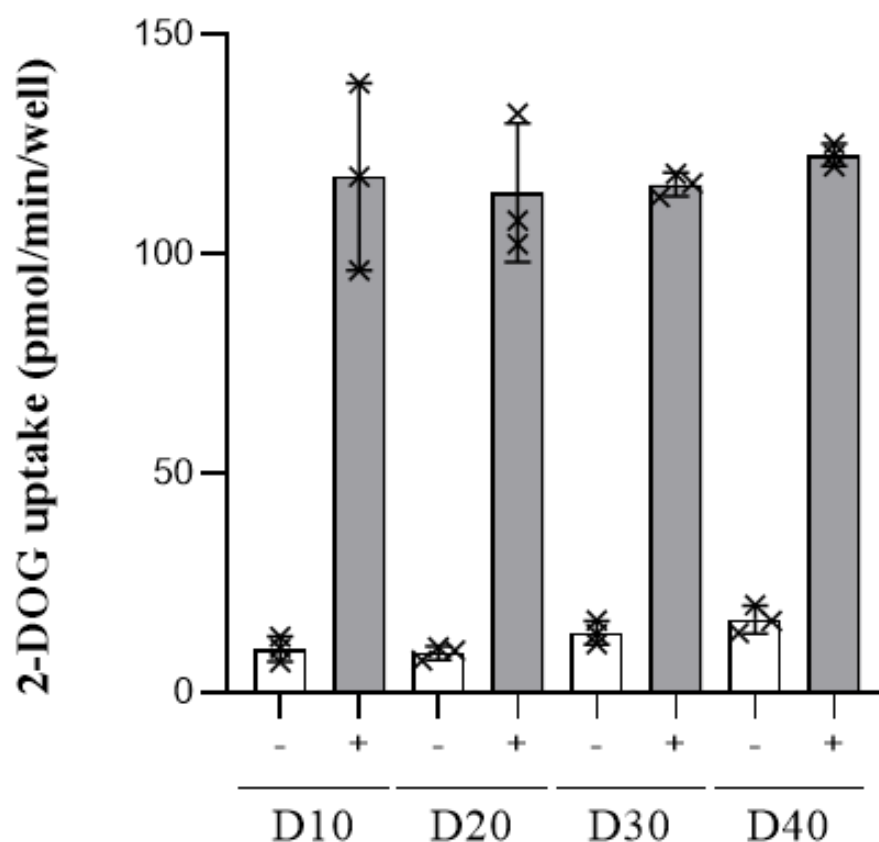


Figure 5. 19. Glucose Uptake with Increasing 3T3-L1 Adipocyte Incubation Periods

Glucose transport in basal (-) and insulin stimulated (+) 3T3-L1 adipocytes at increasing times after differentiation D10, D20, D30 and D40. Basal or 15 min stimulation with 100 nM insulin were used to assess uptake of 2-deoxy-D-glucose. Mean and SD of n = 3 independent experiments are shown, each 'x' on the graph is data from a sperate biological replicate and is the mean of triplicate technical replicates. Statistical analysis of two-way ANOVA was performed and no statistical significance was found between basal or insulin-stimulated 2-deoxy-D-glucose transport rates at any of the different days post-differentiation. Experiment and data performed and supplied by Rod Milligan.

5.2.2 Limitations of the Current Study

A strength of the SRS set up is its capacity to perform high throughput analysis on cell populations such as droplet measurements and observations in differences in Raman spectra that have been performed in Figure 5. 15 to show lipid concentration increases. However, I have been unable to perform Z profile projections for each individual lipid droplet to observe droplet differences in the entire frame taken on a large data set like the example shown of D35 adipocytes (Figure 5. 20). There may be a way of writing a macro to scroll through each identified lipid droplet and project a z profile. This way the capacity for the system to perform large high throughput analysis of both measurements and biological data could be performed together rather than the individual selection of droplets and analysis performed by myself.

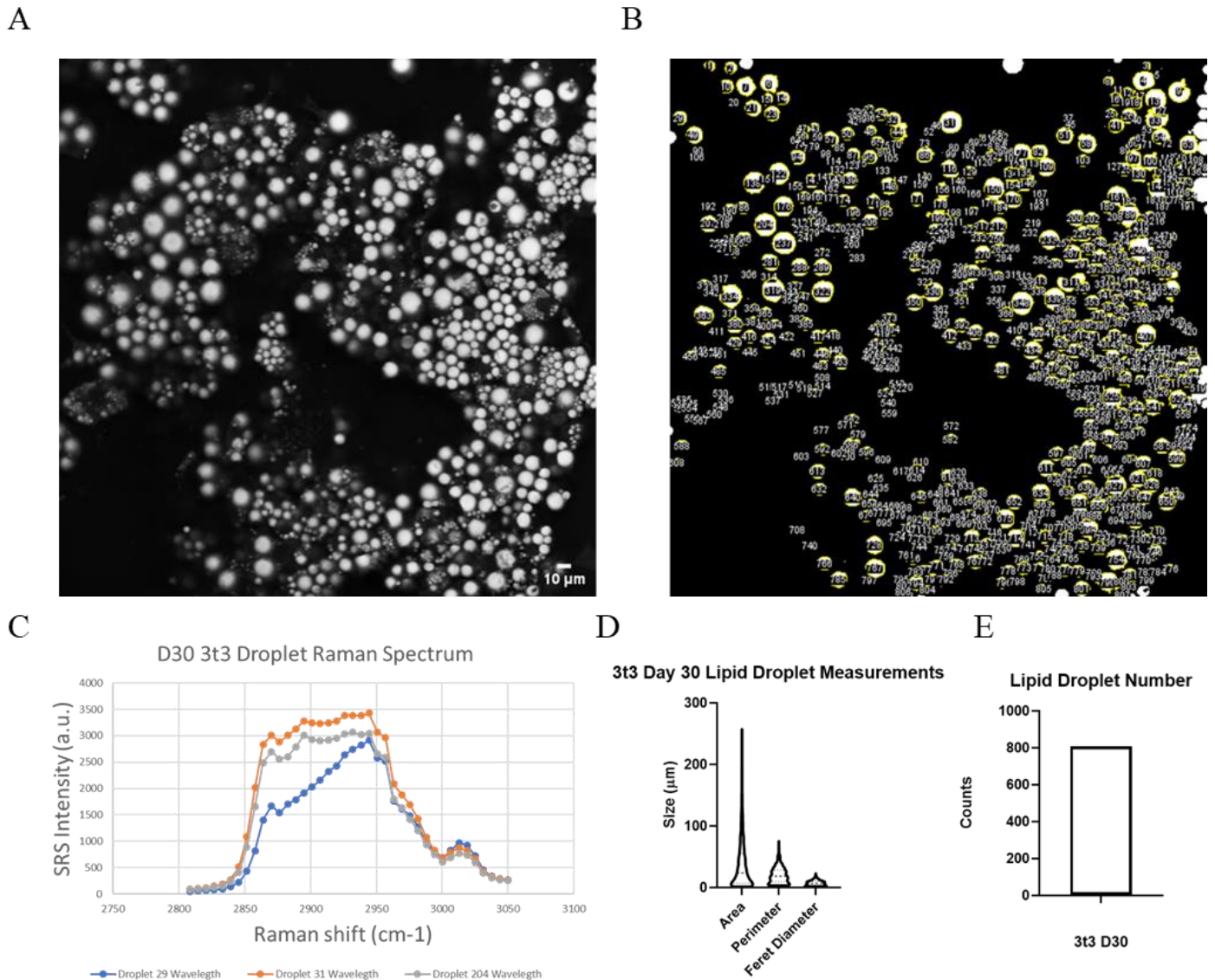


Figure 5.20. Bottleneck for High Throughput on Lipid Composition

The SRS workflow described in this chapter (above) demonstrates label-free images of adipocytes can be acquired (A), counted (B and E), measured (D) and Raman spectra can be plotted for individual droplets (C). However, the Raman profiling (C) has to be performed manually and by working through each individual droplet, presenting a bottleneck in the analysis. 3T3-L1 image processing (B) and data acquisition were performed with FIJI and data analysis on droplet measurements (B) Lipid Droplet Quantity (E), Diameter, Perimeter and Area (D) was performed using PRISM as outlined in **2.2.13 Data Analysis of Lipid Droplets**. Raman spectra generated for individual lipids in FIJI were plotted using Excel (C).

5.2.3 *Lots of Potential - Future Work*

Our work has utilized 3T3-L1 adipocytes that have been used in the field to study glucose metabolism and disease progression such as obesity and diabetes. It would be effective to treat the day 35 adipocytes with deuterated glucose and observe if the larger droplets *de novo* lipogenesis capacity has been affected by the size and difference in lipid composition observed in our studies. This could be further expanded by using a 3T3-L1 adipocyte line that has been genetically modified - for example a GLUT4 knock out model - and incubate adipocytes for the same duration. These could be used to study; (A) the effect impacted glucose uptake machinery has on *de novo* lipogenesis by utilizing the deuterated glucose, (B) the effect on lipid packaging over this extended period in absence of GLUT4. Are there varying rates of hyperplasia to hypertrophy to accommodate? Are the species of lipids different from the wild type adipocytes and are they stored differently/compositionally?

3T3-L1 adipocytes have been used as a model here due to their robustness to support our method development and proof of concept. However, now this is established, this could be extended to other cell types/models. The same experiments described above could be expanded to adipose tissue derived from mice and obesity models like the C57BL/6 mouse (Simon et al., 2013) to compare lipid droplet compositional differences and also a lipodystrophy model such as a BSCL2 knock out mouse for seipin (Dollet et al., 2014) and perform the same analysis. The lipid identification potentials of this method observed between healthy and unhealthy on both ends of the spectra could provide great insight to the machinery utilized in adipocytes with possible metabolic activity differences correlating with droplet size vs disease progression.

Lipid loading has been used to study adipogenesis in HEK293 cells as mentioned (Listenberger et al., 2007). Saturated and unsaturated lipid species have impacts on disease progression with saturated fats contributing to poor health (Phillips et al., 2012). 3T3-L1 adipocytes could be lipid loaded with an unsaturated fatty acid like oleic acid and a saturated fatty acid such as

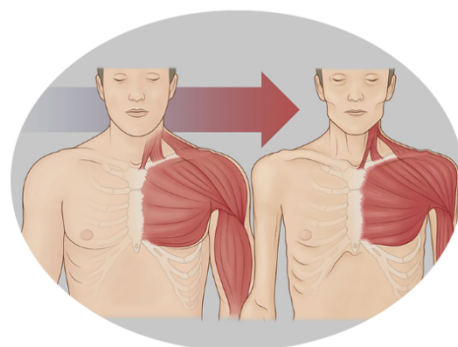
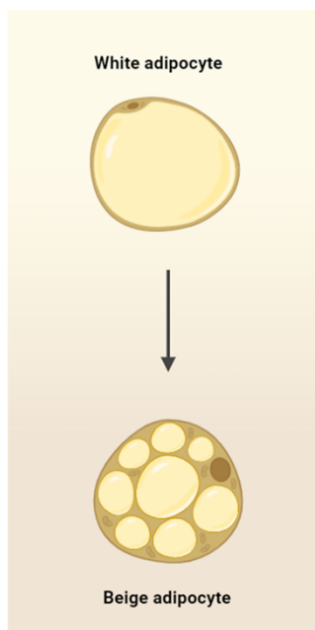
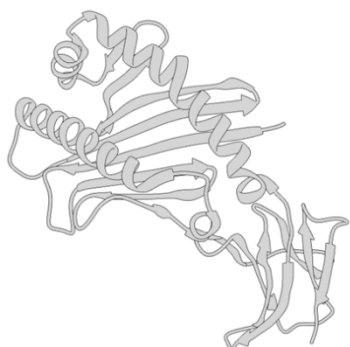
palmitic acid and observe the way these are packaged by all models of adipocytes mentioned and then furthermore introduce d7 glucose to observe the effect diet is impacting our adipocytes capabilities in storing lipids and the lead on effects in disease progression. Deuterated fatty acids are also available in varying levels of deuteration (Egoshi et al., 2022) which would allow distinctions from the glucose and could be paired and observed to see if they are stored differently spatially in the droplet.

This current work has taken images of adipocytes in one plane. The present workflow has demonstrated that Raman spectra can be generated for individual lipid droplets and segmented using the spectral phasor tool. With refinement in this technique, it would be possible to take a Z-stack of droplets of different sizes and segment the Raman spectra to build an image of droplets by layering and composing these segmentations together. This would result in a detailed 3D image of droplets comprising of their compositional differences and would give us an understanding in the lipid orientation and packing as a droplet expands.

Lastly, the majority of this work presented here was performed in fixed cells, but as an optical technique Raman microscopy is ideally suited for live-cell imaging. The use of near infrared laser sources can help to minimise sample damage and improve tissue penetration depth for imaging in complex sample types. All of the above could be performed in real time and progress towards kinetic studies such as monitoring the rate in which glucose is incorporated by these models.

Chapter 6

Investigating the Impact of Zinc Alpha 2-Glycoprotein in Adipose Browning Biology



6.0 Investigating the Impact of Zinc Alpha 2-Glycoprotein in Adipose Browning Biology

6.1.1 Introduction

The Relationship Between ZAG and Adipose Browning

This mechanism of adipose browning in cachexia is introduced in **1.2 Adipocyte Biology and Their Role in Metabolism** and the effects of ZAG treatment on mouse models influencing browning of adipose tissue and regulating components of the same pathway have been covered in **1.3 Zinc Alpha 2-Glycoprotein**. With this in mind, the intention of this work was to test the biological action of recombinant ZAG produced as outlined in **4.0 ZAG Expression Methodology** and investigate if ZAG affected these signalling pathways (β_3 -adrenergic receptor, PPAR γ , UCP-1), if it influences changes in cell metabolism such as glucose uptake and lipolysis (the latter observed in **4.1.8 Testing the Biological Activity of ZAG** and **4.1.11 Testing the Biological Activity of Mammalian ZAG**) and if any impacts are observed in mitochondrial biology such as mitochondrial biogenesis or their distribution in association with lipid droplets.

6.1.2 Examining Mitochondrial Distribution in 3T3-L1 Adipocytes

As outlined in this chapter, mitochondria play a critical role in regulating adipocyte metabolism, with their functions adapting based on the adipocyte phenotype, particularly by their spatial association with lipid droplets, which is increasingly recognized as a key regulatory factor (Benador et al., 2018; Veliova et al., 2020).

Mitochondria in adipocytes can be broadly categorized into two distinct subpopulations: cytosolic mitochondria (CM) and peridroplet mitochondria (PDM) (Benador et al., 2018; Veliova et al., 2020). CM are distributed within the cytoplasm and are primarily involved in the oxidation of FFAs to generate heat (Benador et al., 2018; Veliova et al., 2020). In contrast, PDM are physically associated with lipid droplets through interactions with proteins such as perilipin 5 (PLIN5) (Benador et al., 2019) and mitofusin 2 (MFN2) (Boutant et al., 2017). PDM are pivotal for lipid handling, facilitating processes like lipogenesis and TAG synthesis (Benador et al., 2018; Veliova et al., 2020). These mitochondria demonstrate enhanced pyruvate oxidation, augmented electron transport chain activity, and increased ATP synthesis capacity, but display reduced rates of β -oxidation relative to CM (Benador et al., 2018; Veliova et al., 2020). During adipocyte browning, a metabolic reprogramming occurs whereby PDM dissociate from lipid droplets, coinciding with mitochondrial biogenesis and a shift towards a thermogenic phenotype (Benador et al., 2018; Wikstrom et al., 2014). This transition underscores the dynamic plasticity of mitochondrial function in response to alterations in adipocyte metabolic demands.

By isolating mitochondria from adipocytes into these two groups, we can investigate the relationship between mitochondria and lipid droplet biology. Mitochondria were isolated from 3T3-L1 adipocytes at day 10 and day 30 as outlined in **2.2.11 Mitochondrial Isolation** to allow comparison between smaller and expanding droplet sizes. As shown in **Figure 5. 19. Glucose Uptake with Increasing 3T3-L1 Adipocyte Incubation Periods**, increasing droplet size did not

impact insulin-stimulated glucose uptake. However, as PDM are closely associated with droplets and participate in adipose lipogenesis (Benador et al., 2018), it was hypothesized that as the droplets are expanding in our model, there may be differences observed in the PDM concentrations between Day 10 and Day 30 3T3-L1 adipocytes. Mitochondria markers of voltage-dependent-anion-channel 1/3 (VDAC1/3) and UCP-1 were chosen to quantify mitochondria protein levels. VDAC 1/3 are proteins involved in metabolite exchange across the mitochondrial membrane (Varughese et al., 2021) whilst UCP-1 has been discussed above and will allow for distinction in thermogenic activity (Nedergaard et al., 2001). Although droplet expansion has been observed with increased adipocyte culture (**5.1.4 3T3-L1 Adipocytes Undergo Hypertrophy with Increased Incubation**), we observed no significant difference in mitochondria populations between Day 10 and Day 30 samples, despite a trend of PDM numbers appearing to fall, rather than increase, with lipid droplet size (Figure 6. 1). As discussed, ZAG appears to exhibit its browning effects through the β_3 -adrenrgic receptor (Collins & Surwit, 2001; Russell et al., 2002; Russell & Tisdale, 2012), which then with the cold exposure studies has shown upregulation in UCP-1 expression in mitochondria (Tabuchi & Sul, 2021). Therefore, we treated Day 10 3T3-L1 adipocytes with bacterially-expressed recombinant ZAG and isolated mitochondria. Again, there is no significant difference in mitochondria protein distribution after ZAG treatments was observed with either protein (Figure 6. 2 and Figure 6. 3).

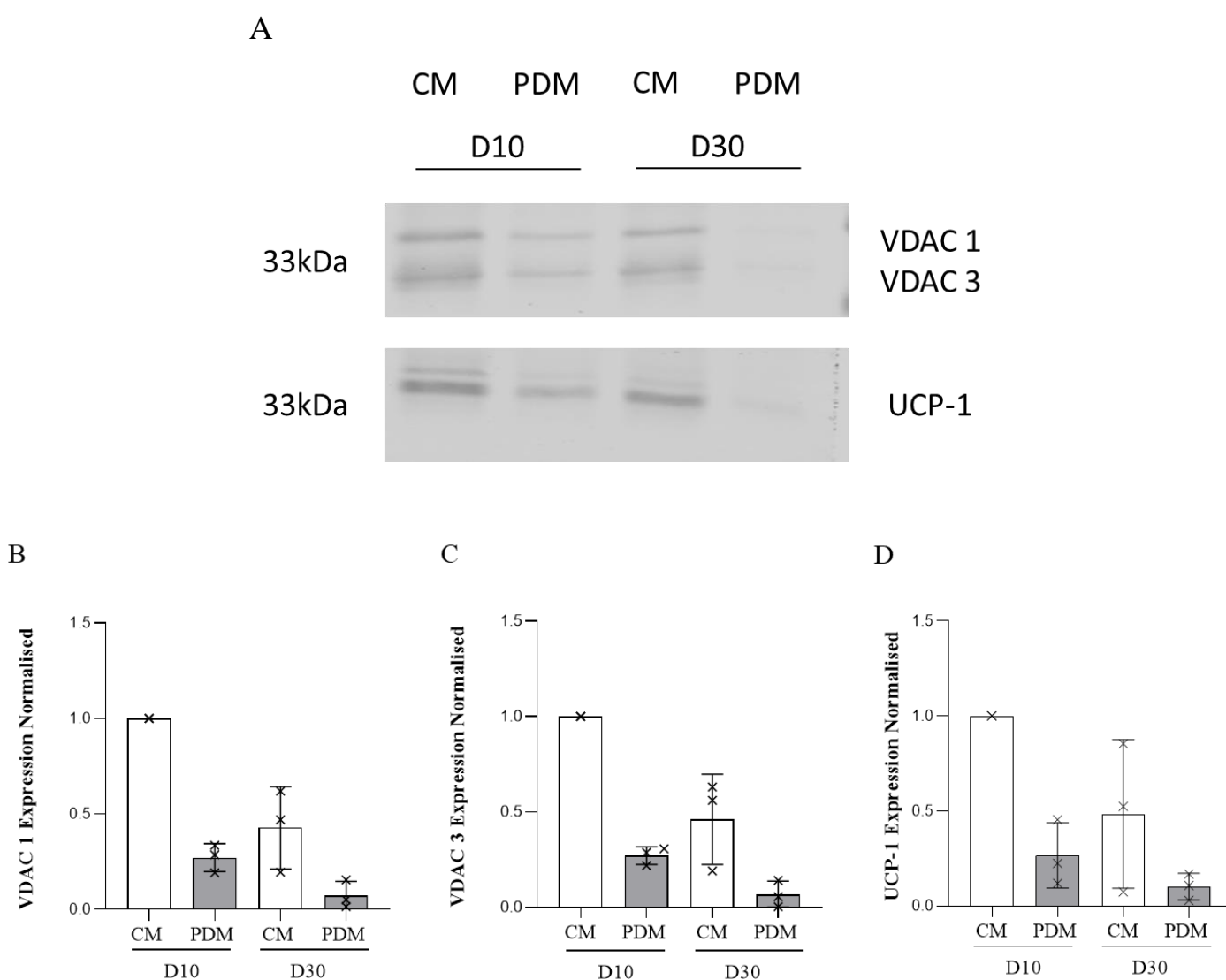


Figure 6. 1 Mitochondrial Protein Expression in Adipocytes at Varied Cultured Periods

3T3-L1 adipocytes were incubated for 10 and 30 days (D10 and D30) and cytosolic mitochondria (CM) and peridroplet mitochondria (PDM) were isolated as outlined in 2.2.11. Western blot analysis was performed for VDAC 1/3 and UCP-1 and a representative immunoblot is shown in Panel A which contains equal protein loads in each lane. Data were normalised and mean and SD of $n = 3$ independent experiments are shown in B, each 'x' on the graph is data from a separate biological replicate (B, C and D). Unpaired t-tests were performed to compare each mitochondrial sub-group at Day 10 and Day 30. No statistical significance was observed, despite the apparent trend towards lower levels of PDM in day 30 cells.

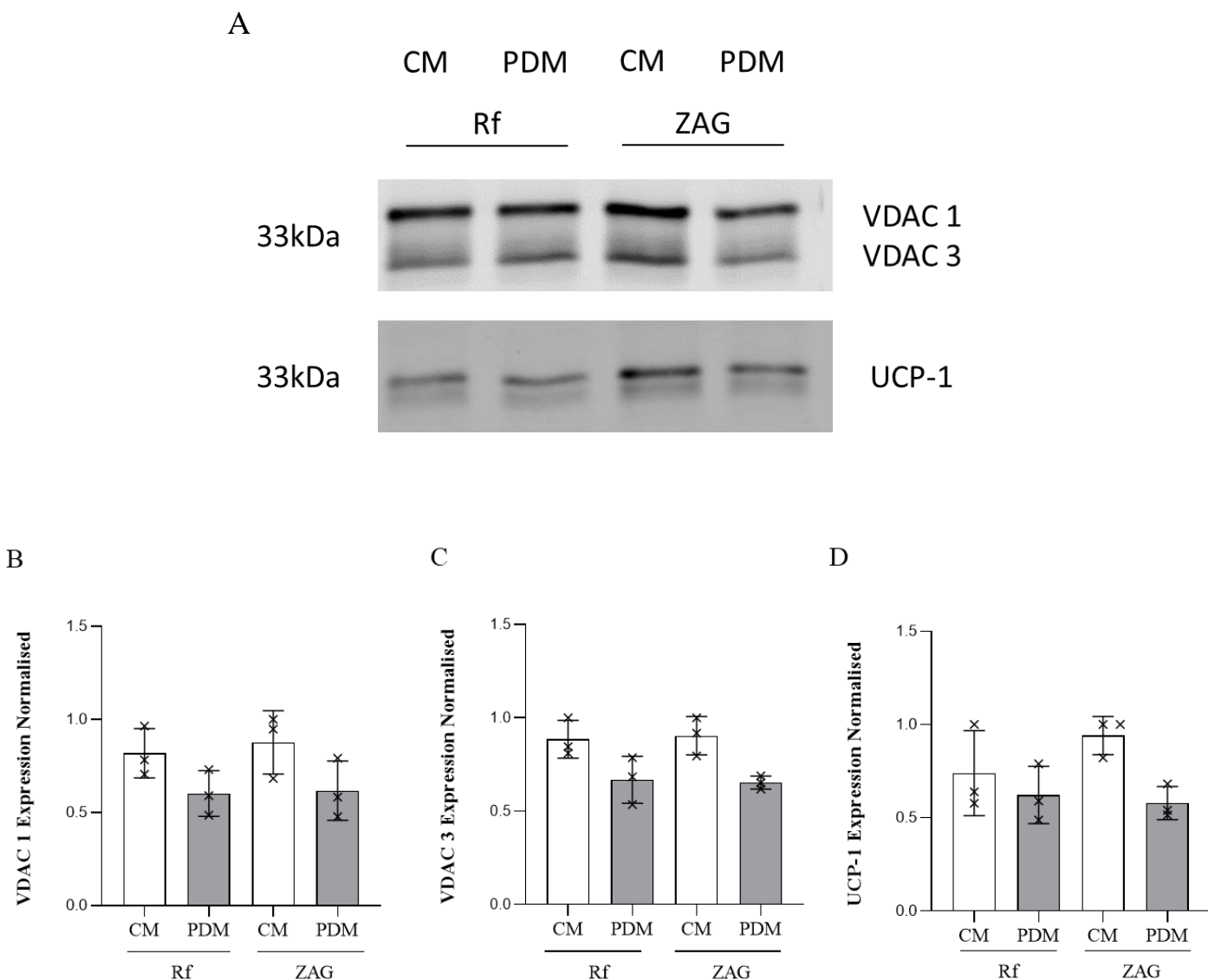


Figure 6. 2 Mitochondrial Protein Expression After Recombinant ZAG Stimulation

3T3-L1 adipocytes were treated with Refolding Buffer (Rf) as a control or ZAG (27 μ M) for 4 hours and mitochondria were isolated as described in 2.2.II. Western blot analysis was performed for VDAC 1/3 and UCP-1 with a represent immunoblot shown in panel (A); equal protein was loaded on each lane. Data were normalised and mean and SD of n = 3 independent experiments are shown in Panel. B-D, each 'x' on the graph is data from a separate biological replicate. Statistical analysis of unpaired t-tests were performed to compare each mitochondrial sub-group before and after ZAG treatment. No statistical significance was observed.

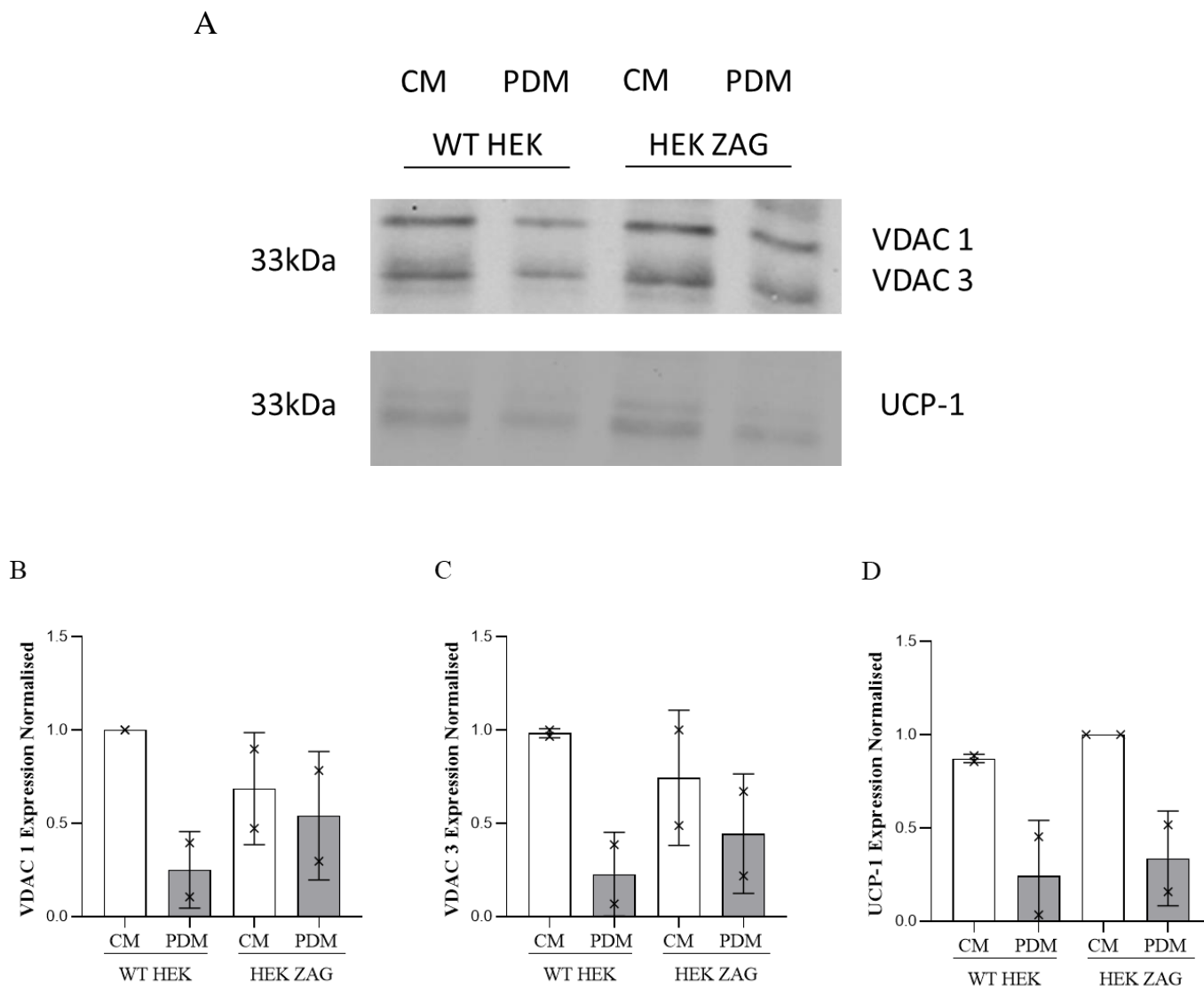


Figure 6. 3 Mitochondrial Protein Expression After Mammalian ZAG Stimulation

3T3-L1 adipocytes were treated with ZAG expressed in HEK cells or media from control cells as outlined previously. Mitochondria were isolated and immunoblotted to quantify levels of VDAC 1/3 and UCP-1 with a typical data set shown in Panel A. Data were normalised and Mean and SD of $n = 2$ independent experiments are shown, each 'x' on the graph is data from a separate biological replicate (B, C and D). As only two experiments were performed, statistical analysis was not undertaken, but there do not appear to be major differences between control and ZAG-treated cells.

6.1.3 Assessing Adipocyte Metabolic Rate with ZAG Stimulation.

As outlined, beige and brown adipocytes differ in their metabolic activity compared to white, with an upregulated rate of lipolysis and glucose uptake occurring to support the thermogenic demands of the cell (Rosell et al., 2014). Glucose uptake experiments were performed to investigate ZAGs acute and long-term effects on adipocyte glucose transport. Increasing concentrations of mammalian ZAG (27 μ M) (5, 10 and 20ul) and wild type HEK293 media-serving as a control- resulted in no significant upregulation of glucose in comparison to basal adipocytes after 1 hour treatments (A). 3T3-L1 adipocytes were pre-treated with ZAG for 1 hour and then insulin (100 nM) stimulated for 30 mins to observe if exposure before glucose introduction would stimulate up take. There was no significant difference observed (B). Incubation times were increased to 24 and 48 hours (C and D) with 3T3-L1 adipocytes being exposed to wild type HEK293 media and mammalian ZAG (27 μ M) (C) and recombinant ZAG (5 μ g/ml) expressed in insects (BioBench ShiJiaZhuang Quan Jing Biotechnology co., ltd) (1 and 5 μ g/ml) only in (D) paired with increasing insulin concentrations (1, 10 and 100 nM). No significant differences were observed.

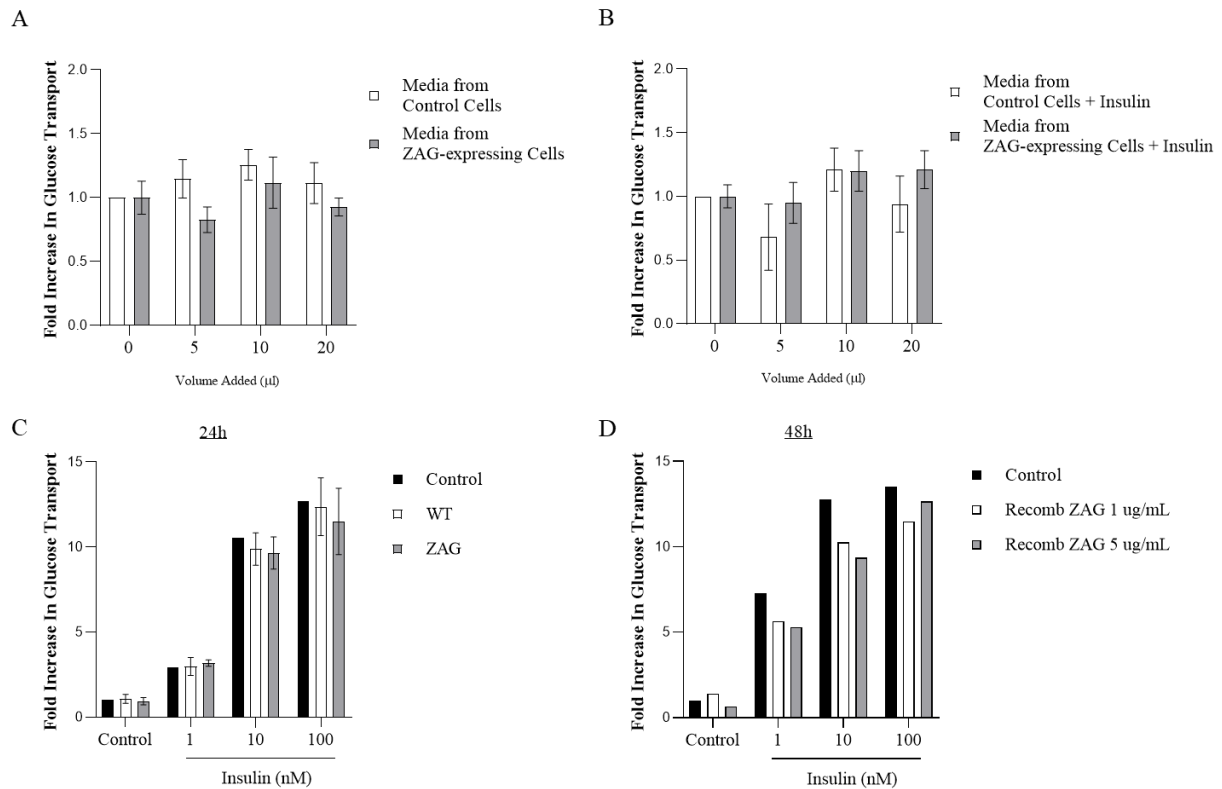


Figure 6. 4 Investigating Metabolic Activity Changes in 3T3-L1 Adipocytes via Glucose Uptake After ZAG Stimulation.

A. Glucose transport in Day 10 3T3-L1 adipocytes was measured after 60 minute incubation with increasing ZAG-containing media from HEK cells (27 μ M), or control media, as indicated. Data from a typical experiment is shown, repeated twice with similar results. Each bar is expressed relative to the no-addition measurement set to =1. Note there was no difference in absolute rates observed at any condition

B. Cells were treated exactly as shown in panel A, except after 60 minutes with ZAG or control, 100 nM Insulin was added for 30 minutes prior to 2-deoxy-D-glucose assay. Values were normalised to set no addition =1. No statistical difference was observed between control and treated cells at any condition.

C. 3T3-L1 adipocytes were incubated with ZAG-containing media from HEK cells (ZAG 27 μ M), or control media (WT) for 24 hours. 2-deoxy-D-glucose uptake was then assayed 30 minutes after the addition of no insulin ('Basal') or insulin at 1, 10 or 100 nM for 30 minutes.

D. As C, except cells were pre-treated with recombinant baculovirus expressed cell ZAG purchased from commercial sources (1 and 5 µg/ml) or controls for 48h prior to assay.

Data in panels A, B and C are the mean and SD of $n = 3$ independent experiments, with data from a sperate biological replicate and is the mean of triplicate technical replicates. Data in panel D is of one experiment with two technical replicates. Expense and limited supply precluded further experiments. Statistical analysis of two-way ANOVA was performed and no statistical significance was found in any comparison of control and treated cells.

6.1.4 Investigating Adipocyte Browning Signalling Pathways

Given the absence of changes in mitochondrial population distribution and glucose uptake following ZAG stimulation, the β 3-adrenergic receptor pathway and its associated metabolic markers were examined in greater detail. This pathway, which is known to be involved in adipocyte browning and enhanced lipolysis (Tabuchi & Sul, 2021), was identified as a potential area for further investigation. As previously discussed, the β 3-adrenergic pathway is activated during cold exposure (McNeill et al., 2021), leading to downstream upregulation of PPAR γ (Liang & Ward, 2006). Since lipolysis is a contributing factor in cachexia (Kenneth et al., 2012) and was observed following ZAG treatment, we hypothesized that lipogenesis-associated proteins would be downregulated in response to ZAG stimulation, given that adipocytes would likely be breaking down lipids rather than synthesizing or storing them. To test this, we measured the levels of two key enzymes in the lipogenesis pathway: fatty acid synthase (FAS) and acetyl-CoA carboxylase (ACC) (Ojha et al., 2014). Following 2, 24, and 48 hours of ZAG stimulation, no change in expression was observed for either browning markers, such as the β 3-adrenergic receptor or PPAR γ , nor in expression of the lipogenic proteins FAS or ACC. These findings suggest that ZAG stimulation does not modulate these pathways in the manner initially expected.

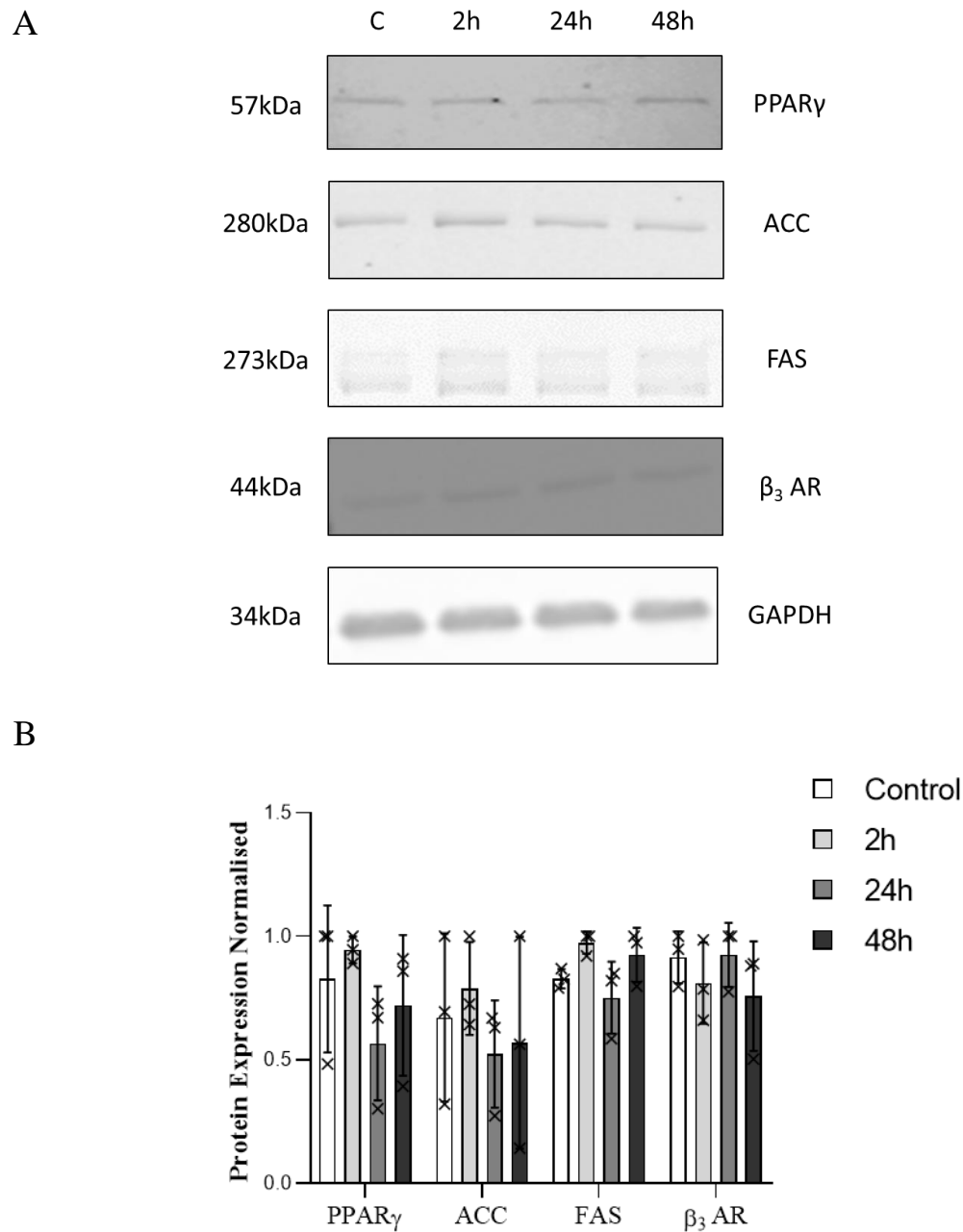


Figure 6. 5 Browning Protein Expression in ZAG Treated 3T3-L1 Adipocytes

3T3-L1 adipocytes were treated with 20 μ l mammalian ZAG (27 μ M) for 2, 24 and 48 hours as indicated and representative western blots (A) of peroxisome proliferator-activated receptor gamma (PPAR γ), acetyl-CoA carboxylase (ACC), fatty acid synthase (FAS) and β_3 -adrenergic receptor (β_3 AR) are shown. Glyceraldehyde-3-phosphate dehydrogenase (GAPDH) has been used as a loading control. Blots are representative of 3 independent experiments. BCA assay was performed on samples to ensure equal loading for each well. Data were normalised and Mean and SD of n = 3 independent experiments

are shown, each 'x' on the graph is data from a separate biological replicate (B). Statistical analysis of one-way ANOVA was performed to compare each mitochondrial sub-group before and after ZAG treatment. No statistical significance was observed.

6.2 Discussion

6.2.1 *No change observed ...*

It has been discussed that mitochondria can participate in both lipogenesis and lipolysis depending on the metabolic activity requirements of the adipocytes and that the distinction of two sub-groups reflect this activity (Benador et al., 2018; Veliova et al., 2020). Work has previously been done to isolate mitochondria in these sub-groups using murine primary adipose tissue (Benador et al., 2018) and this method has been adapted here for the use in 3T3-L1 adipocytes. From protocol, primary adipose tissue results in a solid fat body through centrifugation spins and allows for easier segmentation of mitochondria. Using 3T3-L1 adipocytes -especially as you increase incubation- the fat body is loose and greater care has been required to isolate mitochondria into two sub-groups. However, successful adaption of this protocol is evident with the mitochondria work shown in **6.1.2 Examining Mitochondrial Distribution in 3T3-L1 Adipocytes Under Increased Incubation and ZAG Treatments**, even if no significant differences were detected between Day 10 and Day 30 adipocytes. Despite observing upregulated lipolysis with both recombinant and mammalian ZAG, no changes in mitochondrial distribution, glucose uptake or related metabolic cell signalling were observed after stimulation. ZAG protein was purchased to repeat glucose uptake experiments to provide clarity on this lack of impact on glucose uptake, but this did not induce this activity either. Going back to what was discussed in **4.2.1 Optimizing ZAG Expression and Purification**, our approaches to detect proper folding and activity have been using fluorescence spectroscopy and measuring activity with lipolysis assays. This approach still lacks the capacity to provide us information at what capacity ZAG is properly folded. With a commercial ZAG, the protein provided should be folded and functional, but this did not induce metabolic activity. Adipocytes

should have been treated with positive controls of either isoproterenol to remove doubt between lack of change and cell response within the experiments, but time precluded this.

A limitation of this chapter is having 3T3-L1 adipocytes as the solitary cell line to assess mitochondrial populations and ZAG activity. Introducing a second cell line such as mouse embryonic fibroblasts (MEFs) or murine adipocyte tissue would aid in expanding this study. Single cell line studies are restrictive due to variations in gene expression and responsiveness to treatments between cell lines. Positive controls of isoproterenol or forskolin performed alongside ZAG would again improve robustness and clarity in identifying ZAGs effect on changes in mitochondrial populations and adipocyte metabolic activity. Further experiments with commercially purchased ZAG to increase biological replicates would also improve this study, but cost and limited availability precluded this.

Chapter 7

Discussions and Conclusions

7.0 Discussion and Conclusion

7.1 Key Work and Conclusions

Shown in Chapter 3.0 **Investigating Zinc Alpha 2-Glycoprotein Ligand Binding Through Computational Techniques**, we have validated the docking program PLANTS with previous crystallography work using the fluorescent probe DAUDA and allowed for *in silico* simulations to identify ligand binding partners that are further supported by changes in docking conformations after mutation of these key residues. Palmitic and Stearic acid were identified to be upregulated in lipid serum analysis of cachexia patients (Riccardi et al., 2020) and by using these as starting points, further ligands have been identified that dock with high affinity alongside the P6G and DAUDA that have been previously been crystallised in ZAGs binding pocket. Referring to **Table 3.1. Candidate Ligands for Docking Simulations in ZAG** lists 5 other lipids that have matching or exceeding ligand docking scores; 8,11-Eicosadiynoic acid (-115.276), Arachidic acid(-112.568), 9,12-Octadecadiynoic acid (-110.941), Stearic acid (-106.141), Hexadecanedioic acid (-104.965). As these are based on identified lipids in samples, these could be a ‘native’ ligand for ZAG. Through post-docking analysis in the UCSF Chimera software, key residues interacting with these ligands were identified; Tryptophan ¹⁴⁸, Threonine ⁸⁰, Tyrosine ¹¹⁷, Arginine ⁷³, Phenylalanine ¹⁰¹, Isoleucine ⁷⁶ and Glutamic acid ⁷⁹ (**Table 3.2. Common Residues That are Interacting with Successful Ligand Candidates**) which align with residues and pocket identified in previous work with ZAG (Kennedy et al., 2001; Silvia L. Delker, 2004) and mutations of these residues result in poor docking reflected by the high RMSD scoring (>2.5 is a significant change in ligand docking formation) shown in **Table 3.3. RMSD Scores of Candidate Ligands Docked in Native and Mutated ZAG**. Developing this *in silico* method for ZAG allowed for the investigation into claims of a novel binding site in ZAGs groove (Zahid et al., 2022), with our dockings conflicting with the proposed work as the

BODIPY probe docked in the same pocket as DAUDA (**Figure 3. 13. Proposed Binding Site of BODIPY C16**). Taken together this work has allowed for the identification of new candidate ligands to be investigated with fluorescence spectroscopy techniques discussed in **4.1.7 Validating the Refolding Procedure of ZAG**, which allow for the investigation of competitive ligand binding using the fluorescent probes and tracking their displacement with shifts in fluorescent light *in vitro*. Another investigative route for ZAGs ligand binding partners would be to implement protein immobilisation (Rusmini et al., 2007). Immobilisation embeds a protein to a bead -similar to the nickel beads mentioned in **4.1.6 Evaluating Methods for Purifying ZAG-** and can now be fitted to a column. Candidate ligands could then be passed through the column and their capacity and affinity to bind to ZAG could be measured.

As well as binding studies, by introducing these ligands into assays with wild-type and mutant ZAG, the affects these ligands induce on metabolic activity can be measured. Our work provides evidence that our recombinant and mammalian ZAG is inducing lipolysis (**Figure 4. 7. Glycerol is Released from 3T3-L1 Adipocytes After ZAG Stimulation** and **Figure 4. 12. Glycerol is Released from 3T3-L1 Adipocytes After Mammalian ZAG Stimulation**) and therefore introducing ligands in conjunction with ZAG treatments would allow for effects to be measured. For example, by incorporating candidate ligands -identified with the PLANTS docking studies- into these *in vitro* lipolysis assays, biological effects could be observed. This pairing of the studies would allow identification of the ligand's effects on inhibiting or promoting ZAG's lipolytic activity. With more time, these ZAG-ligand pairings could be compared with known lipolysis inducers such as Isoproterenol. Isoproterenol is a beta-adrenergic receptor agonist and with ZAGs reported involvement with beta-3 adrenergic receptor signalling and lipolysis activity, this would be an appropriate positive control to compare against. In our experiments, ZAG was able to induce lipolysis by measurement of

glycerol release in our lipolysis assay. A main focus of this work is the identification of a native ligand that would interact with ZAG and mediate its effect. Lipolysis was induced without the addition of ligands in our assay, suggesting either that a ligand does not need to be present for ZAG activity, or there are endogenous ligands present. The following work does not provide clarity on this point. However, the aim was to progress the initial identification of a hydrophobic molecule in ZAGs pocket, its involvement in cachexia and the fatty acids identified in cachexia patient's lipid serum analysis. Areas for comparison in a method of action would be with pharmaceuticals that interact with adrenergic receptors such as epinephrine or drugs like beta blockers. The size of these molecules allow for interaction directly on the receptor. The size of ZAG ~40kDa- promotes a hypothesis that it wouldn't interact with the receptor directly but would present a ligand as a way of activating or inhibiting the receptor in the same vain as the MHC class 1 molecules as discussed. These ligands identified from the *in silico* study are similar in size to the hormone epinephrine -C₉H₁₃NO₃- (Table 3.1) and support this as opposed to direct ZAG-adrenergic receptor interaction. There is no data to support ZAG is inducing glucose uptake or browning (**6.0 Investigating the Impact of Zinc Alpha 2-Glycoprotein in Adipose Browning Biology**) and therefore would be advised for future work to initiate with the lipolysis experiments before examination of cell signalling, changes in glucose uptake and browning cell signalling.

Work in **4.0 ZAG Expression Methodology** has addressed the procedures performed to generate stable cell lines in both bacterial and mammalian cells for ZAG protein production. The experimental procedures have addressed the complications of protein like ZAG that is expressed and packaged in inclusion bodies- which require further denaturing and refolding steps for experimentation- and the differences in cell transfection and transduction. By exploring different options in protein production, the benefits and restrictions in each system have shown each approach has their suitable applications. The ease of transformation and

protein expression in the bacterial systems allow for quick production, but the denaturing and refolding procedures have made this a difficult and heavy work load option. On the other hand, mammalian systems having higher demands on cell culture and selection process at the beginning result in slower access to protein, but after stable cell line generation has led to effective protein collection. The generation of cell lines for protein production has allowed for cell signalling, adipocyte metabolic activity and mitochondrial population studies which wouldn't be possible with the high price point of commercial protein.

Oil Red O staining has been utilised during this work to evaluate the effect ZAG has on adipocyte droplet size but had shown no evidence of change when the stain was eluted and absorbance measured (data not shown). Although possible, it was difficult to measure 3T3-L1 adipocyte characteristics such as lipid droplet size and cell size and the opportunity to implement raman imaging techniques to our adipocytes presented a technique that could strengthen our experimental work with its capacity for imaging lipids (Hislop et al., 2022; Renzonnet et al., 2024). Chapter **5.0 Developing a Workflow to Study Adipocyte Heterogeneity Using Stimulated Raman Spectroscopy** therefore has demonstrated a label-free methodology that can be used to study adipocyte biology by laying out its capabilities through single wavelength and lambda scan image generation, determining heterogeneity with post image spectral phasor analysis and segmentation techniques to begin identifying the composition of lipid droplets. To display its potential, a model of adipocyte hypertrophy has been implemented through increased incubation periods for 3T3-L1 adipocytes. Without the capacity to acquire primary tissue from murine or mammalian samples, the change from multi-ocular to monocular has possible use of studying droplet biology through mechanisms like fusion and represent lipid storage closer to primary tissue size and architecture.

Solely on the Raman technique developed, future work has been discussed in **5.2.3 Lots of Potential - Future Work**. However, this technique could be paired with other work in this thesis. For example, the mitochondria isolation experiments in **6.1.2 Examining Mitochondrial Distribution in 3T3-L1 Adipocytes Under Increased Incubation and ZAG Treatments** were performed to study the association between mitochondria, browning and metabolic activity. By pairing this work with the mitokyne introduced in **5.1.7 Using Chemical Probes to Study Adipocyte Biology**, these experiments to study mitochondria distribution in relation to metabolic activity could be performed in real time. For example, experiments in **Figure 6. 1 Mitochondrial Protein Expression in Adipocytes at Varied Cultured Periods** attempt to demonstrate differences in population distribution with increasing droplet size. By culturing 3T3-L1 adipocytes to Day 10 and Day 35 as shown in **5.1.9 Investigating Differences in the Adipocyte Life Cycle** and incorporating the mitokyne would allow for visual and spatial distribution differences to be observed and to pair with the western blot data. This could be expanded to introducing ZAG and ligand candidates as discussed and monitor their effects on mitochondria distribution in real time.

Lastly work in **6.0 Investigating the Impact of Zinc Alpha 2-Glycoprotein in Adipose Browning Biology** looked to investigate ZAGs effect on adipose browning biology by investigating expression changes in browning and lipogenesis protein markers, whilst also covering the glucose uptake capacity of 3T3-L1 adipocytes. Initial plans were to treat 3T3-L1 adipocytes knock out models of β -adrenergic receptors (1,2 and 3) and perform all the experiments performed here, but these cell lines became unobtainable as a result of collaborators failing to deliver these. However, experiments with these cells would be desirable as they would provide insight into β -adrenergic receptor signalling outlined in that chapter.

Again, with the ZAG-ligand pairings, these could be paired and observe if differences would have been examined in their signalling.

To conclude this work, it has been demonstrated that *in silico* studies have been successful in being implemented as a ligand screening technique and has resulted in the identification of novel ligands for ZAG. Secondly, cell lines have been established for the production of both recombinant and mammalian ZAG which has been shown to be functional through fluorescence spectroscopy and lipolysis assay techniques. Furthermore, a method has been developed to study adipocytes using SRS. This allows for label-free, high throughput, single cell analysis to investigate the heterogeneric metabolic activity of our samples with the system allowing for measuring lipid droplet numbers and size, quantifying glucose metabolism and where this glucose is being metabolised all within the same sample set. Pairing with this method development, a novel approach with 3T3-L1 adipocytes has been utilized by prolonging their regular cell culture periods, showing that these adipocytes undergo lipid droplet expansion. Lastly the adaption of a mitochondrial isolation technique -initially used for primary adipose tissue from murine models- was used in 3T3-L1 adipocytes and showed that mitochondria could be isolated into sub-groups of cytosolic and peridroplet mitochondria. When all combined, this study has provided further tools and insight to help progress the knowledge and understanding of cancer cachexia browning mechanisms and also for the investigation into both phenotypic and metabolic adipocyte heterogeneity.

Chapter 8

References

8.0 References

- Adams, E. J., & Luoma, A. M. (2013). The Adaptable Major Histocompatibility Complex (MHC) Fold: Structure and Function of Nonclassical and MHC Class I–Like Molecules. *Annual Review of Immunology*, 31(Volume 31, 2013), 529-561. <https://doi.org/https://doi.org/10.1146/annurev-immunol-032712-095912>
- Ameer, F., Scandiuizzi, L., Hasnain, S., Kalbacher, H., & Zaidi, N. (2014). De novo lipogenesis in health and disease. *Metabolism*, 63(7), 895-902. <https://doi.org/10.1016/j.metabol.2014.04.003>
- Angell, T. E., Vyas, C. M., Medici, M., Wang, Z., Barletta, J. A., Benson, C. B., Cibas, E. S., Cho, N. L., Doherty, G. M., Doubilet, P. M., Frates, M. C., Gawande, A. A., Heller, H. T., Kim, M. I., Krane, J. F., Marqusee, E., Moore, F. D., Nehs, M. A., Zavacki, A. M.,...Alexander, E. K. (2017). Differential Growth Rates of Benign vs. Malignant Thyroid Nodules. *The Journal of Clinical Endocrinology & Metabolism*, 102(12), 4642-4647. <https://doi.org/10.1210/jc.2017-01832>
- Anna, Geiser, A., Kamilla, Morris, S., Marie, Stirrat, L., Gadegaard, N., Boles, E., Hannah, Nia, & Gwyn. (2022). EFR3 and phosphatidylinositol 4-kinase III α regulate insulin-stimulated glucose transport and GLUT4 dispersal in 3T3-L1 adipocytes. *Bioscience Reports*, 42(7). <https://doi.org/10.1042/bsr20221181>
- Askari, M., Heshmati, J., Shahinfar, H., Tripathi, N., & Daneshzad, E. (2020). Ultra-processed food and the risk of overweight and obesity: a systematic review and meta-analysis of observational studies. *International Journal of Obesity*, 44(10), 2080-2091. <https://doi.org/10.1038/s41366-020-00650-z>
- Baba, A. I., & Cătoi, C. (2007). In *Comparative Oncology*. The Publishing House of the Romanian Academy

Copyright © 2007, The Publishing House of the Romanian Academy.

- Backdahl, J., Franzen, L., Massier, L., Li, Q., Jalkanen, J., Gao, H., Andersson, A., Bhalla, N., Thorell, A., Ryden, M., Stahl, P. L., & Mejhert, N. (2021). Spatial mapping reveals human adipocyte subpopulations with distinct sensitivities to insulin. *Cell Metab*, 33(11), 2301. <https://doi.org/10.1016/j.cmet.2021.10.012>
- Banaszak, M., Górna, I., & Przysławski, J. (2021). Zinc and the Innovative Zinc- α -Glycoprotein Adipokine Play an Important Role in Lipid Metabolism: A Critical Review. *Nutrients*, 13(6). <https://doi.org/10.3390/nu13062023>
- Bartlett, K., & Eaton, S. (2004). Mitochondrial β -oxidation. *European Journal of Biochemistry*, 271(3), 462-469. <https://doi.org/10.1046/j.1432-1033.2003.03947.x>
- Benador, I. Y., Veliova, M., Liesa, M., & Shirihai, O. S. (2019). Mitochondria Bound to Lipid Droplets: Where Mitochondrial Dynamics Regulate Lipid Storage and Utilization. *Cell Metabolism*, 29(4), 827-835. <https://doi.org/10.1016/j.cmet.2019.02.011>
- Benador, I. Y., Veliova, M., Mahdavian, K., Petcherski, A., Wikstrom, J. D., Assali, E. A., Acín-Pérez, R., Shum, M., Oliveira, M. F., Cinti, S., Sztalryd, C., Barshop, W. D., Wohlschlegel, J. A., Corkey, B. E., Liesa, M., & Shirihai, O. S. (2018). Mitochondria Bound to Lipid Droplets Have Unique Bioenergetics, Composition, and Dynamics that Support Lipid Droplet Expansion. *Cell Metabolism*, 27(4), 869-885.e866. <https://doi.org/10.1016/j.cmet.2018.03.003>
- Bennett, M. J., Lebrón, J. A., & Bjorkman, P. J. (2000). Crystal structure of the hereditary haemochromatosis protein HFE complexed with transferrin receptor. *Nature*, 403(6765), 46-53. <https://doi.org/10.1038/47417>
- Benson, S., De Moliner, F., Tipping, W., & Vendrell, M. (2022). Miniaturized Chemical Tags for Optical Imaging. *Angewandte Chemie International Edition*, 61(34). <https://doi.org/10.1002/anie.202204788>

- Bhatwa, A., Wang, W., Hassan, Y. I., Abraham, N., Li, X.-Z., & Zhou, T. (2021). Challenges Associated With the Formation of Recombinant Protein Inclusion Bodies in *Escherichia coli* and Strategies to Address Them for Industrial Applications. *Frontiers in Bioengineering and Biotechnology*, 9. <https://doi.org/10.3389/fbioe.2021.630551>
- Bing, C., Bao, Y., Jenkins, J., Sanders, P., Manieri, M., Cinti, S., Tisdale, M. J., & Trayhurn, P. (2004). Zinc- α 2-glycoprotein, a lipid mobilizing factor, is expressed in adipocytes and is up-regulated in mice with cancer cachexia. *Proceedings of the National Academy of Sciences*, 101(8), 2500-2505. <https://doi.org/10.1073/pnas.0308647100>
- Bing, C., Mracek, T., Gao, D., & Trayhurn, P. (2010). Zinc- α 2-glycoprotein: an adipokine modulator of body fat mass? *Int J Obes (Lond)*, 34(11), 1559-1565. <https://doi.org/10.1038/ijo.2010.105>
- Blondin, D. P., Labbé, S. M., Tingelstad, H. C., Noll, C., Kunach, M., Phoenix, S., Guérin, B., Turcotte, É. E., Carpentier, A. C., Richard, D., & Haman, F. (2014). Increased Brown Adipose Tissue Oxidative Capacity in Cold-Acclimated Humans. *The Journal of Clinical Endocrinology & Metabolism*, 99(3), E438-E446. <https://doi.org/10.1210/jc.2013-3901>
- Borén, J., Taskinen, M. R., Olofsson, S. O., & Levin, M. (2013). Ectopic lipid storage and insulin resistance: a harmful relationship. *Journal of Internal Medicine*, 274(1), 25-40. <https://doi.org/10.1111/joim.12071>
- Boutant, M., Kulkarni, S. S., Joffraud, M., Ratajczak, J., Valera-Alberni, M., Combe, R., Zorzano, A., & Cantó, C. (2017). Mfn2 is critical for brown adipose tissue thermogenic function. *The EMBO Journal*, 36(11), 1543-1558. <https://doi.org/10.15252/emboj.201694914>
- Braddick, H. J., Tipping, W. J., Wilson, L. T., Jaconelli, H. S., Grant, E. K., Faulds, K., Graham, D., & Tomkinson, N. C. O. (2023). Determination of intracellular esterase

- activity using ratiometric Raman sensing and spectral phasor analysis. *Analytical Chemistry*, 95(12), 5369-5376. <https://doi.org/10.1021/acs.analchem.2c05708>
- Bremner, S. K., Al Shammari, W. S., Milligan, R. S., Hudson, B. D., Sutherland, C., Bryant, N. J., & Gould, G. W. (2022). Pleiotropic effects of Syntaxin16 identified by gene editing in cultured adipocytes. *Frontiers in Cell and Developmental Biology*, 10. <https://doi.org/10.3389/fcell.2022.1033501>
- Bremner, S. K., Berends, R., Kaupisch, A., Roccisana, J., Sutherland, C., Bryant, N. J., & Gould, G. W. (2023). Phosphorylation of the N-terminus of Syntaxin-16 controls interaction with mVps45 and GLUT4 trafficking in adipocytes. *PeerJ*, 11, e15630. <https://doi.org/10.7717/peerj.15630>
- Burmeister, W. P., Gastinel, L. N., Simister, N. E., Blum, M. L., & Bjorkman, P. J. (1994). Crystal structure at 2.2 Å resolution of the MHC-related neonatal Fc receptor. *Nature*, 372(6504), 336-343. <https://doi.org/10.1038/372336a0>
- Butler, H. J., Ashton, L., Bird, B., Cinque, G., Curtis, K., Dorney, J., Esmonde-White, K., Fullwood, N. J., Gardner, B., Martin-Hirsch, P. L., Walsh, M. J., McAinsh, M. R., Stone, N., & Martin, F. L. (2016). Using Raman spectroscopy to characterize biological materials. *Nature Protocols*, 11(4), 664-687. <https://doi.org/10.1038/nprot.2016.036>
- Byrne, C. D., & Targher, G. (2014). Ectopic Fat, Insulin Resistance, and Nonalcoholic Fatty Liver Disease. *Arteriosclerosis, Thrombosis, and Vascular Biology*, 34(6), 1155-1161. <https://doi.org/10.1161/atvbaha.114.303034>
- Carpentier, A. C. (2021). 100th anniversary of the discovery of insulin perspective: insulin and adipose tissue fatty acid metabolism. *American Journal of Physiology-Endocrinology and Metabolism*, 320(4), E653-E670. <https://doi.org/10.1152/ajpendo.00620.2020>

- Chadt, A., & Al-Hasani, H. (2020). Glucose transporters in adipose tissue, liver, and skeletal muscle in metabolic health and disease. *Pflügers Archiv - European Journal of Physiology*, 472(9), 1273-1298. <https://doi.org/10.1007/s00424-020-02417-x>
- Cifone, M. A. (1982). In vitro growth characteristics associated with benign and metastatic variants of tumor cells. *Cancer and Metastasis Review*, 1(4), 335-347. <https://doi.org/10.1007/bf00124216>
- Collins, S., & Surwit, R. S. (2001). The beta-adrenergic receptors and the control of adipose tissue metabolism and thermogenesis. *Recent Prog Horm Res*, 56, 309-328. <https://doi.org/10.1210/rp.56.1.309>
- Cusi, K. (2010). The Role of Adipose Tissue and Lipotoxicity in the Pathogenesis of Type 2 Diabetes. *Current Diabetes Reports*, 10(4), 306-315. <https://doi.org/10.1007/s11892-010-0122-6>
- Darby, N., & Creighton, T. E. Disulfide Bonds in Protein Folding and Stability. In (pp. 219-252). Humana Press. <https://doi.org/10.1385/0-89603-301-5:219>
- De Backer, I., Hussain, S. S., Bloom, S. R., & Gardiner, J. V. (2016). Insights into the role of neuronal glucokinase. *American Journal of Physiology-Endocrinology and Metabolism*, 311(1), E42-E55. <https://doi.org/10.1152/ajpendo.00034.2016>
- Dewal, R. S., & Wolfrum, C. (2023). Master of disguise: deconvoluting adipose tissue heterogeneity and its impact on metabolic health. *Current Opinion in Genetics & Development*, 81, 102085. <https://doi.org/https://doi.org/10.1016/j.gde.2023.102085>
- Di Girolamo, D., & Tajbakhsh, S. (2022). Pathological features of tissues and cell populations during cancer cachexia. *Cell Regeneration*, 11(1). <https://doi.org/10.1186/s13619-022-00108-9>

- Dollet, L., Magré, J., Cariou, B., & Prieur, X. (2014). Function of seipin: New insights from Bsc12/seipin knockout mouse models. *Biochimie*, 96, 166-172. <https://doi.org/https://doi.org/10.1016/j.biochi.2013.06.022>
- Dowling, P., & Clynes, M. (2011). Conditioned media from cell lines: A complementary model to clinical specimens for the discovery of disease-specific biomarkers. *PROTEOMICS*, 11(4), 794-804. <https://doi.org/https://doi.org/10.1002/pmic.201000530>
- Du, J., Su, Y., Qian, C., Yuan, D., Miao, K., Lee, D., Ng, A. H. C., Wijker, R. S., Ribas, A., Levine, R. D., Heath, J. R., & Wei, L. (2020). Raman-guided subcellular pharmacometabolomics for metastatic melanoma cells. *Nature Communications*, 11(1). <https://doi.org/10.1038/s41467-020-18376-x>
- Duan, G., & Walther, D. (2015). The Roles of Post-translational Modifications in the Context of Protein Interaction Networks. *PLOS Computational Biology*, 11(2), e1004049. <https://doi.org/10.1371/journal.pcbi.1004049>
- Duerre, D. J., & Galmozzi, A. (2022). Deconstructing Adipose Tissue Heterogeneity One Cell at a Time. *Frontiers in Endocrinology*, 13. <https://doi.org/10.3389/fendo.2022.847291>
- Duncan, R. E., Ahmadian, M., Jaworski, K., Sarkadi-Nagy, E., & Sul, H. S. (2007). Regulation of Lipolysis in Adipocytes. *Annual Review of Nutrition*, 27(1), 79-101. <https://doi.org/10.1146/annurev.nutr.27.061406.093734>
- Dunnington, E. L., Wong, B. S., & Fu, D. (2024). Innovative approaches for drug discovery: quantifying drug distribution and response with Raman imaging. *Analytical Chemistry*, 96(20), 7926-7944. <https://doi.org/10.1021/acs.analchem.4c01413>
- Durrant, J. D., & McCammon, J. A. (2011). Molecular dynamics simulations and drug discovery. *BMC Biology*, 9(1), 71. <https://doi.org/10.1186/1741-7007-9-71>

- Egoshi, S., Dodo, K., & Sodeoka, M. (2022). Deuterium Raman imaging for lipid analysis. *Current Opinion in Chemical Biology*, 70, 102181. <https://doi.org/https://doi.org/10.1016/j.cbpa.2022.102181>
- Elattar, S., Dimri, M., & Satyanarayana, A. (2018). The tumor secretory factor ZAG promotes white adipose tissue browning and energy wasting. *The FASEB Journal*, 32(9), 4727-4743. <https://doi.org/10.1096/fj.201701465rr>
- Eynaudi, A., Díaz-Castro, F., Bórquez, J. C., Bravo-Sagua, R., Parra, V., & Troncoso, R. (2021). Differential Effects of Oleic and Palmitic Acids on Lipid Droplet-Mitochondria Interaction in the Hepatic Cell Line HepG2. *Frontiers in Nutrition*, 8. <https://doi.org/10.3389/fnut.2021.775382>
- Faulconnier, Y., Bobby, C., Pires, J., Labonne, C., & Leroux, C. (2019). Effects of *Azgp1*^{−/−} on mammary gland, adipose tissue and liver gene expression and milk lipid composition in lactating mice. *Gene*, 692, 201-207. <https://doi.org/https://doi.org/10.1016/j.gene.2019.01.010>
- Felberbaum, R. S. (2015). The baculovirus expression vector system: A commercial manufacturing platform for viral vaccines and gene therapy vectors. *Biotechnology Journal*, 10(5), 702-714. <https://doi.org/10.1002/biot.201400438>
- Fenzl, A., & Kiefer, F. W. (2014). Brown adipose tissue and thermogenesis. *Hormone Molecular Biology and Clinical Investigation*, 19(1), 25-37. <https://doi.org/10.1515/hmbci-2014-0022>
- Fliedl, L., Grillari, J., & Grillari-Voglauer, R. (2015). Human cell lines for the production of recombinant proteins: on the horizon. *New Biotechnology*, 32(6), 673-679. <https://doi.org/https://doi.org/10.1016/j.nbt.2014.11.005>
- Freudiger, C. W., Min, W., Saar, B. G., Lu, S., Holtom, G. R., He, C., Tsai, J. C., Kang, J. X., & Xie, X. S. (2008). Label-Free Biomedical Imaging with High Sensitivity by

- Stimulated Raman Scattering Microscopy. *Science*, 322(5909), 1857-1861.
<https://doi.org/10.1126/science.1165758>
- Fritsche, K. L. (2015). The science of fatty acids and inflammation. *Adv Nutr*, 6(3), 293s-301s.
<https://doi.org/10.3945/an.114.006940>
- Fryk, E., Olausson, J., Mossberg, K., Strindberg, L., Schmelz, M., Brogren, H., Gan, L.-M., Piazza, S., Provenzani, A., Becattini, B., Lind, L., Solinas, G., & Jansson, P.-A. (2021). Hyperinsulinemia and insulin resistance in the obese may develop as part of a homeostatic response to elevated free fatty acids: A mechanistic case-control and a population-based cohort study. *EBioMedicine*, 65, 103264.
<https://doi.org/10.1016/j.ebiom.2021.103264>
- Fu, D., & Xie, X. S. (2014). Reliable Cell Segmentation Based on Spectral Phasor Analysis of Hyperspectral Stimulated Raman Scattering Imaging Data. *Analytical Chemistry*, 86(9), 4115-4119. <https://doi.org/10.1021/ac500014b>
- Fujioka, H., Shou, J., Kojima, R., Urano, Y., Ozeki, Y., & Kamiya, M. (2020). Multicolor Activatable Raman Probes for Simultaneous Detection of Plural Enzyme Activities. *Journal of the American Chemical Society*, 142(49), 20701-20707.
<https://doi.org/10.1021/jacs.0c09200>
- Fus-Kujawa, A., Prus, P., Bajdak-Rusinek, K., Teper, P., Gawron, K., Kowalczyk, A., & Sieron, A. L. (2021). An Overview of Methods and Tools for Transfection of Eukaryotic Cells in vitro. *Frontiers in Bioengineering and Biotechnology*, 9.
<https://doi.org/10.3389/fbioe.2021.701031>
- Ganeva, I., Lim, K., Boulanger, J., Hoffmann, P. C., Muriel, O., Borgeaud, A. C., Hagen, W. J. H., Savage, D. B., & Kukulski, W. (2023). The architecture of Cidec-mediated interfaces between lipid droplets. *Cell Reports*, 42(2), 112107.
<https://doi.org/10.1016/j.celrep.2023.112107>

- Gao, M., Huang, X., Song, B.-L., & Yang, H. (2019). The biogenesis of lipid droplets: Lipids take center stage. *Progress in Lipid Research*, 75, 100989. <https://doi.org/https://doi.org/10.1016/j.plipres.2019.100989>
- Gao, S. X., Guo, J., Fan, G. Q., Qiao, Y., Zhao, R. Q., & Yang, X. J. (2018). ZAG alleviates HFD-induced insulin resistance accompanied with decreased lipid depot in skeletal muscle in mice. *J Lipid Res*, 59(12), 2277-2286. <https://doi.org/10.1194/jlr.M082180>
- Geiser, A., Foylan, S., Peter, N., & Gwyn. (2023). GLUT4 dispersal at the plasma membrane of adipocytes: a super-resolved journey. *Bioscience Reports*, 43(10). <https://doi.org/10.1042/bsr20230946>
- Germain, R. N. (1994). MHC-dependent antigen processing and peptide presentation: Providing ligands for T lymphocyte activation. *Cell*, 76(2), 287-299. [https://doi.org/https://doi.org/10.1016/0092-8674\(94\)90336-0](https://doi.org/https://doi.org/10.1016/0092-8674(94)90336-0)
- Gong, F. Y., Zhang, S. J., Deng, J. Y., Zhu, H. J., Pan, H., Li, N. S., & Shi, Y. F. (2009). Zinc-alpha2-glycoprotein is involved in regulation of body weight through inhibition of lipogenic enzymes in adipose tissue. *Int J Obes (Lond)*, 33(9), 1023-1030. <https://doi.org/10.1038/ijo.2009.141>
- Grabner, G. F., Xie, H., Schweiger, M., & Zechner, R. (2021). Lipolysis: cellular mechanisms for lipid mobilization from fat stores. *Nature Metabolism*, 3(11), 1445-1465. <https://doi.org/10.1038/s42255-021-00493-6>
- Gregor, M. F., & Hotamisligil, G. S. (2007). Thematic review series: Adipocyte Biology. Adipocyte stress: the endoplasmic reticulum and metabolic disease. *Journal of Lipid Research*, 48(9), 1905-1914. <https://doi.org/10.1194/jlr.r700007-jlr200>
- Greig, J. C., Tipping, W. J., Graham, D., Faulds, K., & Gould, G. W. (2024). New insights into lipid and fatty acid metabolism from Raman spectroscopy. *The Analyst*, 149(19), 4789-4810. <https://doi.org/10.1039/d4an00846d>

- Gustafson, B., Gogg, S., Hedjazifar, S., Jenndahl, L., Hammarstedt, A., & Smith, U. (2009). Inflammation and impaired adipogenesis in hypertrophic obesity in man. *American Journal of Physiology-Endocrinology and Metabolism*, 297(5), E999-E1003. <https://doi.org/10.1152/ajpendo.00377.2009>
- Han, H.-S., Kang, G., Kim, J. S., Choi, B. H., & Koo, S.-H. (2016). Regulation of glucose metabolism from a liver-centric perspective. *Experimental & Molecular Medicine*, 48(3), e218-e218. <https://doi.org/10.1038/emm.2015.122>
- Hargreaves, M., & Spriet, L. L. (2020). Skeletal muscle energy metabolism during exercise. *Nature Metabolism*, 2(9), 817-828. <https://doi.org/10.1038/s42255-020-0251-4>
- Hirai, K., Hussey, H. J., Barber, M. D., Price, S. A., & Tisdale, M. J. (1998). Biological evaluation of a lipid-mobilizing factor isolated from the urine of cancer patients. *Cancer Res*, 58(11), 2359-2365.
- Hislop, E. W., Tipping, W. J., Faulds, K., & Graham, D. (2022). Label-Free Imaging of Lipid Droplets in Prostate Cells Using Stimulated Raman Scattering Microscopy and Multivariate Analysis. *Analytical Chemistry*, 94(25), 8899-8908. <https://doi.org/10.1021/acs.analchem.2c00236>
- Hislop, E. W., Tipping, W. J., Faulds, K., & Graham, D. (2023). Label-free cytometric evaluation of mitosis via stimulated Raman scattering microscopy and spectral phasor analysis. *Analytical Chemistry*, 95(18), 7244-7253. <https://doi.org/10.1021/acs.analchem.3c00212>
- Horwitz, A., & Birk, R. (2023). Adipose Tissue Hyperplasia and Hypertrophy in Common and Syndromic Obesity—The Case of BBS Obesity. *Nutrients*, 15(15), 3445. <https://doi.org/10.3390/nu15153445>
- Houten, S. M., Violante, S., Ventura, F. V., & Wanders, R. J. A. (2016). The Biochemistry and Physiology of Mitochondrial Fatty Acid β -Oxidation and Its Genetic Disorders. *Annual*

- Review of Physiology*, 78(Volume 78, 2016), 23-44.
<https://doi.org/https://doi.org/10.1146/annurev-physiol-021115-105045>
- Hu, H., Wei, Y., Wang, D., Su, N., Chen, X., Zhao, Y., Liu, G., & Yang, Y. (2018). Glucose monitoring in living cells with single fluorescent protein-based sensors. *RSC Advances*, 8(5), 2485-2489. <https://doi.org/10.1039/c7ra11347a>
- Huang, K.-C., Li, J., Zhang, C., Tan, Y., & Cheng, J.-X. (2020). Multiplex stimulated Raman scattering imaging cytometry reveals lipid-rich protrusions in cancer cells under stress conditions. *iScience*, 23(3), 100953.
<https://doi.org/https://doi.org/10.1016/j.isci.2020.100953>
- Jensen, M. D. (2006). Adipose tissue as an endocrine organ: implications of its distribution on free fatty acid metabolism. *European Heart Journal Supplements*, 8(suppl_B), B13-B19. <https://doi.org/10.1093/eurheartj/sul003>
- Jumper, J., Evans, R., Pritzel, A., Green, T., Figurnov, M., Ronneberger, O., Tunyasuvunakool, K., Bates, R., Židek, A., Potapenko, A., Bridgland, A., Meyer, C., Kohl, S. A. A., Ballard, A. J., Cowie, A., Romera-Paredes, B., Nikolov, S., Jain, R., Adler, J.,...Hassabis, D. (2021). Highly accurate protein structure prediction with AlphaFold. *Nature*, 596(7873), 583-589. <https://doi.org/10.1038/s41586-021-03819-2>
- Kalantar-Zadeh, K., Rhee, C., Sim, J. J., Stenvinkel, P., Anker, S. D., & Kovesdy, C. P. (2013). Why cachexia kills: examining the causality of poor outcomes in wasting conditions. *Journal of Cachexia, Sarcopenia and Muscle*, 4(2), 89-94.
<https://doi.org/10.1007/s13539-013-0111-0>
- Karim, S., Adams, D. H., & Lalor, P. F. (2012). Hepatic expression and cellular distribution of the glucose transporter family. *World J Gastroenterol*, 18(46), 6771-6781.
<https://doi.org/10.3748/wjg.v18.i46.6771>

- Kawai, T., Autieri, M. V., & Scalia, R. (2021). Adipose tissue inflammation and metabolic dysfunction in obesity. *Am J Physiol Cell Physiol*, 320(3), C375-c391. <https://doi.org/10.1152/ajpcell.00379.2020>
- Kennedy, M. W., Heikema, A. P., Cooper, A., Bjorkman, P. J., & Sanchez, L. M. (2001). Hydrophobic Ligand Binding by Zn- α 2-glycoprotein, a Soluble Fat-depleting Factor Related to Major Histocompatibility Complex Proteins. *Journal of Biological Chemistry*, 276(37), 35008-35013. <https://doi.org/10.1074/jbc.c100301200>
- Kenneth, David, & Denis. (2012). Cancer Cachexia: Mediators, Signaling, and Metabolic Pathways. *Cell Metabolism*, 16(2), 153-166. <https://doi.org/10.1016/j.cmet.2012.06.011>
- Kershaw, E. E., & Flier, J. S. (2004). Adipose tissue as an endocrine organ. *J Clin Endocrinol Metab*, 89(6), 2548-2556. <https://doi.org/10.1210/jc.2004-0395>
- Kim, J. I., Huh, J. Y., Sohn, J. H., Choe, S. S., Lee, Y. S., Lim, C. Y., Jo, A., Park, S. B., Han, W., & Kim, J. B. (2015). Lipid-overloaded enlarged adipocytes provoke insulin resistance independent of inflammation. *Mol Cell Biol*, 35(10), 1686-1699. <https://doi.org/10.1128/mcb.01321-14>
- Koester, A. M., Geiser, A., Bowman, P. R. T., Van De Linde, S., Gadegaard, N., Bryant, N. J., & Gould, G. W. (2022). GLUT4 translocation and dispersal operate in multiple cell types and are negatively correlated with cell size in adipocytes. *Scientific Reports*, 12(1). <https://doi.org/10.1038/s41598-022-24736-y>
- Korb, O., Stützle, T., & Exner, T. E. (2007). An ant colony optimization approach to flexible protein–ligand docking. *Swarm Intelligence*, 1(2), 115-134. <https://doi.org/10.1007/s11721-007-0006-9>

- Koshland, D. E. (1995). The Key–Lock Theory and the Induced Fit Theory. *Angewandte Chemie International Edition in English*, 33(23-24), 2375-2378.
<https://doi.org/10.1002/anie.199423751>
- Kwok, K. H. M., Lam, K. S. L., & Xu, A. (2016). Heterogeneity of white adipose tissue: molecular basis and clinical implications. *Experimental & Molecular Medicine*, 48(3), e215-e215. <https://doi.org/10.1038/emm.2016.5>
- Langin, D. (2021). Adipocyte heterogeneity revealed by spatial transcriptomics of human adipose tissue: Painting and more. *Cell Metabolism*, 33(9), 1721-1722.
<https://doi.org/10.1016/j.cmet.2021.08.011>
- Lass, A., Zimmermann, R., Oberer, M., & Zechner, R. (2011). Lipolysis - a highly regulated multi-enzyme complex mediates the catabolism of cellular fat stores. *Prog Lipid Res*, 50(1), 14-27. <https://doi.org/10.1016/j.plipres.2010.10.004>
- Lau, A. M., Zahid, H., Gor, J., Perkins, S. J., Coker, A. R., & McDermott, L. C. (2019). Crystal structure of zinc- α 2-glycoprotein in complex with a fatty acid reveals multiple different modes of protein-lipid binding. *Biochemical Journal*, 476(19), 2815-2834.
<https://doi.org/10.1042/bcj20190354>
- Lee, K. Y., Luong, Q., Sharma, R., Dreyfuss, J. M., Ussar, S., & Kahn, C. R. (2019). Developmental and functional heterogeneity of white adipocytes within a single fat depot. *EMBO J*, 38(3), 10.15252/emboj.2021108206.
<https://doi.org/10.15252/emboj.201899291>
- Lee, P., Swarbrick, M. M., & Ho, K. K. Y. (2013). Brown Adipose Tissue in Adult Humans: A Metabolic Renaissance. *Endocrine Reviews*, 34(3), 413-438.
<https://doi.org/10.1210/er.2012-1081>

- Li, Y., Zhang, W., Fung, A. A., & Shi, L. (2021). DO-SRS imaging of metabolic dynamics in aging *Drosophila*. *The Analyst*, 146(24), 7510-7519. <https://doi.org/10.1039/d1an01638e>
- Liang, H., & Ward, W. F. (2006). PGC-1 α : a key regulator of energy metabolism. *Advances in Physiology Education*, 30(4), 145-151. <https://doi.org/10.1152/advan.00052.2006>
- Lichtenthaler, F. W. (1995). 100 Years “Schlüssel-Schloss-Prinzip”: What Made Emil Fischer Use this Analogy? *Angewandte Chemie International Edition in English*, 33(23-24), 2364-2374. <https://doi.org/10.1002/anie.199423641>
- Listenberger, L. L., Ostermeyer-Fay, A. G., Goldberg, E. B., Brown, W. J., & Brown, D. A. (2007). Adipocyte differentiation-related protein reduces the lipid droplet association of adipose triglyceride lipase and slows triacylglycerol turnover. *Journal of Lipid Research*, 48(12), 2751-2761. <https://doi.org/10.1194/jlr.m700359-jlr200>
- Liu, J., Han, H., Fan, Z., El Beaino, M., Fang, Z., Li, S., & Ji, J. (2018). AZGP1 inhibits soft tissue sarcoma cells invasion and migration. *BMC Cancer*, 18(1). <https://doi.org/10.1186/s12885-017-3962-5>
- Liu, K., Zhou, S., Kim, J.-Y., Tillison, K., Majors, D., Rearick, D., Lee, J. H., Fernandez-Boyanapalli, R. F., Barricklow, K., Houston, M. S., & Smas, C. M. (2009). Functional analysis of FSP27 protein regions for lipid droplet localization, caspase-dependent apoptosis, and dimerization with CIDEA. *American Journal of Physiology-Endocrinology and Metabolism*, 297(6), E1395-E1413. <https://doi.org/10.1152/ajpendo.00188.2009>
- Liu, M., Zhu, H., Dai, Y., Pan, H., Li, N., Wang, L., Yang, H., Yan, K., & Gong, F. (2018). Zinc- α 2-Glycoprotein Is Associated with Obesity in Chinese People and HFD-Induced Obese Mice. *Frontiers in Physiology*, 9. <https://doi.org/10.3389/fphys.2018.00062>

- Luo, L., & Liu, M. (2016). Adipose tissue in control of metabolism. *Journal of Endocrinology*, 231(3), R77-R99. <https://doi.org/10.1530/joe-16-0211>
- Maassen, J. A., Romijn, J. A., & Heine, R. J. (2007). Fatty acid-induced mitochondrial uncoupling in adipocytes as a key protective factor against insulin resistance and beta cell dysfunction: a new concept in the pathogenesis of obesity-associated type 2 diabetes mellitus. *Diabetologia*, 50(10), 2036-2041. <https://doi.org/10.1007/s00125-007-0776-z>
- Maker, P. D., & Terhune, R. W. (1965). Study of optical effects due to an induced polarization third order in the electric field strength. *Physical Review*, 137(3A), 801-818. <http://link.aps.org/doi/10.1103/PhysRev.137.A801>
- Maki, K. C., Dicklin, M. R., & Kirkpatrick, C. F. (2021). Saturated fats and cardiovascular health: Current evidence and controversies. *Journal of Clinical Lipidology*, 15(6), 765-772. <https://doi.org/https://doi.org/10.1016/j.jacl.2021.09.049>
- Maljaars, J., Romeyn, E. A., Haddeman, E., Peters, H. P., & Masclee, A. A. (2009). Effect of fat saturation on satiety, hormone release, and food intake. *Am J Clin Nutr*, 89(4), 1019-1024. <https://doi.org/10.3945/ajcn.2008.27335>
- Martínez-Reyes, I., & Chandel, N. S. (2020). Mitochondrial TCA cycle metabolites control physiology and disease. *Nature Communications*, 11(1). <https://doi.org/10.1038/s41467-019-13668-3>
- McKenzie, E. A., & Abbott, W. M. (2018). Expression of recombinant proteins in insect and mammalian cells. *Methods*, 147, 40-49. <https://doi.org/https://doi.org/10.1016/j.ymeth.2018.05.013>
- McNeill, B. T., Suchacki, K. J., & Stimson, R. H. (2021). MECHANISMS IN ENDOCRINOLOGY: Human brown adipose tissue as a therapeutic target: warming

- up or cooling down? *European Journal of Endocrinology*, 184(6), R243-R259.
<https://doi.org/10.1530/eje-20-1439>
- McPherson, S., Hardy, T., Henderson, E., Burt, A. D., Day, C. P., & Anstee, Q. M. (2015). Evidence of NAFLD progression from steatosis to fibrosing-steatohepatitis using paired biopsies: Implications for prognosis and clinical management. *Journal of Hepatology*, 62(5), 1148-1155. <https://doi.org/10.1016/j.jhep.2014.11.034>
- Mehlem, A., Hagberg, C. E., Muhl, L., Eriksson, U., & Falkevall, A. (2013). Imaging of neutral lipids by oil red O for analyzing the metabolic status in health and disease. *Nature Protocols*, 8(6), 1149-1154. <https://doi.org/10.1038/nprot.2013.055>
- Mensink, R. P., & Katan, M. B. (1989). Effect of a Diet Enriched with Monounsaturated or Polyunsaturated Fatty Acids on Levels of Low-Density and High-Density Lipoprotein Cholesterol in Healthy Women and Men. *New England Journal of Medicine*, 321(7), 436-441. <https://doi.org/10.1056/nejm198908173210705>
- Merrett, J. E., Xie, J., Psaltis, P. J., & Proud, C. G. (2020). MAPK-interacting kinase 2 (MNK2) regulates adipocyte metabolism independently of its catalytic activity. *Biochemical Journal*, 477(14), 2735-2754. <https://doi.org/10.1042/bcj20200433>
- Morigny, P., Boucher, J., Arner, P., & Langin, D. (2021). Lipid and glucose metabolism in white adipocytes: pathways, dysfunction and therapeutics. *Nat Rev Endocrinol*, 17(5), 276-295. <https://doi.org/10.1038/s41574-021-00471-8>
- Morzel, M., Chabanet, C., Schwartz, C., Lucchi, G., Ducoroy, P., & Nicklaus, S. (2014). Salivary protein profiles are linked to bitter taste acceptance in infants. *European Journal of Pediatrics*, 173(5), 575-582. <https://doi.org/10.1007/s00431-013-2216-z>
- Mracek, T., Ding, Q., Tzanavari, T., Kos, K., Pinkney, J., Wilding, J., Trayhurn, P., & Bing, C. (2010). The adipokine zinc- α 2-glycoprotein (ZAG) is downregulated with fat mass

- expansion in obesity. *Clinical Endocrinology*, 72(3), 334-341.
<https://doi.org/10.1111/j.1365-2265.2009.03658.x>
- Mracek, T., Stephens, N. A., Gao, D., Bao, Y., Ross, J. A., Rydén, M., Arner, P., Trayhurn, P., Fearon, K. C., & Bing, C. (2011). Enhanced ZAG production by subcutaneous adipose tissue is linked to weight loss in gastrointestinal cancer patients. *Br J Cancer*, 104(3), 441-447. <https://doi.org/10.1038/sj.bjc.6606083>
- Murphy, N., Tipping, W. J., Braddick, H. J., Wilson, L. T., Tomkinson, N. C. O., Faulds, K., Graham, D., & Farràs, P. (2023). Expanding the range of bioorthogonal tags for multiplex stimulated Raman scattering microscopy. *Angewandte Chemie International Edition*, 62(48), e202311530. <https://doi.org/https://doi.org/10.1002/anie.202311530>
- Nagarajan, S. R., Cross, E., Sanna, F., & Hodson, L. (2022). Dysregulation of hepatic metabolism with obesity: factors influencing glucose and lipid metabolism. *Proceedings of the Nutrition Society*, 81(1), 1-11.
<https://doi.org/10.1017/s0029665121003761>
- Nedergaard, J., Golozoubova, V., Matthias, A., Asadi, A., Jacobsson, A., & Cannon, B. (2001). UCP1: the only protein able to mediate adaptive non-shivering thermogenesis and metabolic inefficiency. *Biochimica et Biophysica Acta (BBA) - Bioenergetics*, 1504(1), 82-106. [https://doi.org/https://doi.org/10.1016/S0005-2728\(00\)00247-4](https://doi.org/https://doi.org/10.1016/S0005-2728(00)00247-4)
- Neuhaus, M., Fryklund, C., Taylor, H., Borreguero-Muñoz, A., Kopietz, F., Ardalani, H., Rogova, O., Stirrat, L., Bremner, S. K., Spéjel, P., Bryant, N. J., Gould, G. W., & Stenkula, K. G. (2023). EHD2 regulates plasma membrane integrity and downstream insulin receptor signaling events. *Molecular Biology of the Cell*, 34(12).
<https://doi.org/10.1091/mbc.e23-03-0078>
- Ojha, S., Budge, H., & Symonds, M. E. (2014). Adipocytes in Normal Tissue Biology. In L. M. McManus & R. N. Mitchell (Eds.), *Pathobiology of Human Disease* (pp. 2003-

- 2013). Academic Press. [https://doi.org/https://doi.org/10.1016/B978-0-12-386456-7.04408-7](https://doi.org/10.1016/B978-0-12-386456-7.04408-7)
- Olzmann, J. A., & Carvalho, P. (2019). Dynamics and functions of lipid droplets. *Nature Reviews Molecular Cell Biology*, 20(3), 137-155. <https://doi.org/10.1038/s41580-018-0085-z>
- Onal, G., Kutlu, O., Gozuacik, D., & Dokmeci Emre, S. (2017). Lipid Droplets in Health and Disease. *Lipids in Health and Disease*, 16(1). <https://doi.org/10.1186/s12944-017-0521-7>
- Patel, A. (2020). Benign vs Malignant Tumors. *JAMA Oncology*, 6(9), 1488. <https://doi.org/10.1001/jamaoncol.2020.2592>
- Pati, S., Irfan, W., Jameel, A., Ahmed, S., & Shahid, R. K. (2023). Obesity and Cancer: A Current Overview of Epidemiology, Pathogenesis, Outcomes, and Management. *Cancers*, 15(2), 485. <https://doi.org/10.3390/cancers15020485>
- Peres Valgas Da Silva, C., Hernández-Saavedra, D., White, J. D., & Stanford, K. I. (2019). Cold and Exercise: Therapeutic Tools to Activate Brown Adipose Tissue and Combat Obesity. *Biology*, 8(1), 9. <https://doi.org/10.3390/biology8010009>
- Perola, E. (2010). An Analysis of the Binding Efficiencies of Drugs and Their Leads in Successful Drug Discovery Programs. *Journal of Medicinal Chemistry*, 53(7), 2986-2997. <https://doi.org/10.1021/jm100118x>
- Petruzzelli, M., Schweiger, M., Schreiber, R., Campos-Olivas, R., Tsoli, M., Allen, J., Swarbrick, M., Rose-John, S., Rincon, M., Robertson, G., Zechner, R., & Erwin. (2014). A Switch from White to Brown Fat Increases Energy Expenditure in Cancer-Associated Cachexia. *Cell Metabolism*, 20(3), 433-447. <https://doi.org/10.1016/j.cmet.2014.06.011>

- Pettersen, E. F., Goddard, T. D., Huang, C. C., Couch, G. S., Greenblatt, D. M., Meng, E. C., & Ferrin, T. E. (2004). UCSF Chimera—A visualization system for exploratory research and analysis. *Journal of Computational Chemistry*, 25(13), 1605-1612. <https://doi.org/10.1002/jcc.20084>
- Pham, D.-V., Nguyen, T.-K., & Park, P.-H. (2023). Adipokines at the crossroads of obesity and mesenchymal stem cell therapy. *Experimental & Molecular Medicine*, 55(2), 313-324. <https://doi.org/10.1038/s12276-023-00940-2>
- Phillips, C. M., Kesse-Guyot, E., McManus, R., Herberg, S., Lairon, D., Planells, R., & Roche, H. M. (2012). High dietary saturated fat intake accentuates obesity risk associated with the fat mass and obesity-associated gene in adults. *J Nutr*, 142(5), 824-831. <https://doi.org/10.3945/jn.111.153460>
- Poti, J. M., Braga, B., & Qin, B. (2017). Ultra-processed Food Intake and Obesity: What Really Matters for Health—Processing or Nutrient Content? *Current Obesity Reports*, 6(4), 420-431. <https://doi.org/10.1007/s13679-017-0285-4>
- Qiu, S., Wu, Q., Wang, H., Liu, D., Chen, C., Zhu, Z., Zheng, H., Yang, G., Li, L., & Yang, M. (2024). AZGP1 in POMC neurons modulates energy homeostasis and metabolism through leptin-mediated STAT3 phosphorylation. *Nature Communications*, 15(1). <https://doi.org/10.1038/s41467-024-47684-9>
- Ramazi, S., & Zahiri, J. (2021). Post-translational modifications in proteins: resources, tools and prediction methods. *Database*, 2021. <https://doi.org/10.1093/database/baab012>
- Rensonnet, A., Tipping, W. J., Malherbe, C., Faulds, K., Eppe, G., & Graham, D. (2024). Spectral fingerprinting of cellular lipid droplets using stimulated Raman scattering microscopy and chemometric analysis. *The Analyst*, 149(2), 553-562. <https://doi.org/10.1039/d3an01684f>

- Riccardi, D. M. D. R., Das Neves, R. X., De Matos-Neto, E. M., Camargo, R. G., Lima, J. D. C. C., Radloff, K., Alves, M. J., Costa, R. G. F., Tokeshi, F., Otoch, J. P., Maximiano, L. F., De Alcantara, P. S. M., Colquhoun, A., Laviano, A., & Seelaender, M. (2020). Plasma Lipid Profile and Systemic Inflammation in Patients With Cancer Cachexia. *Frontiers in Nutrition*, 7. <https://doi.org/10.3389/fnut.2020.00004>
- Riccardi, G., Giacco, R., & Rivellese, A. A. (2004). Dietary fat, insulin sensitivity and the metabolic syndrome. *Clin Nutr*, 23(4), 447-456. <https://doi.org/10.1016/j.clnu.2004.02.006>
- Richter, E. A., & Hargreaves, M. (2013). Exercise, GLUT4, and Skeletal Muscle Glucose Uptake. *Physiological Reviews*, 93(3), 993-1017. <https://doi.org/10.1152/physrev.00038.2012>
- Rigsby, R. E., & Parker, A. B. (2016). Using the <sc>P</sc>y<sc>MOL</sc> application to reinforce visual understanding of protein structure. *Biochemistry and Molecular Biology Education*, 44(5), 433-437. <https://doi.org/10.1002/bmb.20966>
- Rivera-De-Torre, E., Rimbault, C., Jenkins, T. P., Sørensen, C. V., Damsbo, A., Saez, N. J., Duhoo, Y., Hackney, C. M., Ellgaard, L., & Laustsen, A. H. (2022). Strategies for Heterologous Expression, Synthesis, and Purification of Animal Venom Toxins. *Frontiers in Bioengineering and Biotechnology*, 9. <https://doi.org/10.3389/fbioe.2021.811905>
- Roep, B. O., Thomaidou, S., Van Tienhoven, R., & Zaldumbide, A. (2021). Type 1 diabetes mellitus as a disease of the β -cell (do not blame the immune system?). *Nature Reviews Endocrinology*, 17(3), 150-161. <https://doi.org/10.1038/s41574-020-00443-4>
- Romauch, M. (2020). Zinc- α 2-glycoprotein as an inhibitor of amine oxidase copper-containing 3. *Open Biology*, 10(4), 190035. <https://doi.org/10.1098/rsob.190035>

- Rosell, M., Kaforou, M., Frontini, A., Okolo, A., Chan, Y. W., Nikolopoulou, E., Millership, S., Fenech, M. E., MacIntyre, D., Turner, J. O., Moore, J. D., Blackburn, E., Gullick, W. J., Cinti, S., Montana, G., Parker, M. G., & Christian, M. (2014). Brown and white adipose tissues: intrinsic differences in gene expression and response to cold exposure in mice. *Am J Physiol Endocrinol Metab*, 306(8), E945-964. <https://doi.org/10.1152/ajpendo.00473.2013>
- Rubio-Cabezas, O., Puri, V., Murano, I., Saudek, V., Semple, R. K., Dash, S., Hyden, C. S. S., Bottomley, W., Vigouroux, C., Magré, J., Raymond-Barker, P., Murgatroyd, P. R., Chawla, A., Skepper, J. N., Chatterjee, V. K., Suliman, S., Patch, A. M., Agarwal, A. K., Garg, A.,...Savage, D. B. (2009). Partial lipodystrophy and insulin resistant diabetes in a patient with a homozygous nonsense mutation in *CIDEA*. *EMBO Molecular Medicine*, 1(5), 280-287. <https://doi.org/10.1002/emmm.200900037>
- Ruiz-Ojeda, F., Rupérez, A., Gomez-Llorente, C., Gil, A., & Aguilera, C. (2016). Cell Models and Their Application for Studying Adipogenic Differentiation in Relation to Obesity: A Review. *International Journal of Molecular Sciences*, 17(7), 1040. <https://doi.org/10.3390/ijms17071040>
- Rusmini, F., Zhong, Z., & Feijen, J. (2007). Protein Immobilization Strategies for Protein Biochips. *Biomacromolecules*, 8(6), 1775-1789. <https://doi.org/10.1021/bm061197b>
- Russell, S. T., Hirai, K., & Tisdale, M. J. (2002). Role of beta3-adrenergic receptors in the action of a tumour lipid mobilizing factor. *Br J Cancer*, 86(3), 424-428. <https://doi.org/10.1038/sj.bjc.6600086>
- Russell, S. T., & Tisdale, M. J. (2011a). Studies on the anti-obesity activity of zinc- α 2-glycoprotein in the rat. *Int J Obes (Lond)*, 35(5), 658-665. <https://doi.org/10.1038/ijo.2010.193>

- Russell, S. T., & Tisdale, M. J. (2011b). Studies on the antiobesity effect of zinc- α 2-glycoprotein in the ob/ob mouse. *International Journal of Obesity*, 35(3), 345-354. <https://doi.org/10.1038/ijo.2010.150>
- Russell, S. T., & Tisdale, M. J. (2012). Role of β -adrenergic receptors in the anti-obesity and anti-diabetic effects of zinc- α 2-glycoprotein (ZAG). *Biochimica et Biophysica Acta (BBA) - Molecular and Cell Biology of Lipids*, 1821(4), 590-599. <https://doi.org/10.1016/j.bbalip.2011.12.003>
- Saltiel, A. R. (2021). Insulin signaling in health and disease. *Journal of Clinical Investigation*, 131(1). <https://doi.org/10.1172/jci142241>
- Sanders, P. M., & Tisdale, M. J. (2004). Effect of zinc- α 2-glycoprotein (ZAG) on expression of uncoupling proteins in skeletal muscle and adipose tissue. *Cancer Letters*, 212(1), 71-81. <https://doi.org/https://doi.org/10.1016/j.canlet.2004.03.021>
- Santoro, A., & Kahn, B. B. (2023). Adipocyte Regulation of Insulin Sensitivity and the Risk of Type 2 Diabetes. *N Engl J Med*, 388(22), 2071-2085. <https://doi.org/10.1056/NEJMr2216691>
- Santoro, A., McGraw, T. E., & Kahn, B. B. (2021). Insulin action in adipocytes, adipose remodeling, and systemic effects. *Cell Metabolism*, 33(4), 748-757. <https://doi.org/10.1016/j.cmet.2021.03.019>
- Schütz, A., Bernhard, F., Berrow, N., Buyel, J. F., Ferreira-da-Silva, F., Hastraete, J., van den Heuvel, J., Hoffmann, J.-E., de Marco, A., Peleg, Y., Suppmann, S., Unger, T., Vanhoucke, M., Witt, S., & Remans, K. (2023). A concise guide to choosing suitable gene expression systems for recombinant protein production. *STAR Protocols*, 4(4), 102572. <https://doi.org/https://doi.org/10.1016/j.xpro.2023.102572>

- Sheka, A. C., Adeyi, O., Thompson, J., Hameed, B., Crawford, P. A., & Ikramuddin, S. (2020). Nonalcoholic Steatohepatitis. *JAMA*, 323(12), 1175. <https://doi.org/10.1001/jama.2020.2298>
- Silvia L. Delker, A. P. W. J., Lindsay McDermott, Malcolm W. Kennedy, and Pamela J. Bjorkmana,. (2004). Crystallographic studies of ligand binding by Zn-a2-glycoprotein. *Journal of Structural Biology*, 148, 205–213.
- Simon, M. M., Greenaway, S., White, J. K., Fuchs, H., Gailus-Durner, V., Wells, S., Sorg, T., Wong, K., Bedu, E., Cartwright, E. J., Dacquin, R., Djebali, S., Estabel, J., Graw, J., Ingham, N. J., Jackson, I. J., Lengeling, A., Mandillo, S., Marvel, J.,...Brown, S. D. (2013). A comparative phenotypic and genomic analysis of C57BL/6J and C57BL/6N mouse strains. *Genome Biology*, 14(7), R82. <https://doi.org/10.1186/gb-2013-14-7-r82>
- Sohn, J. W. (2015). Network of hypothalamic neurons that control appetite. *BMB Rep*, 48(4), 229-233. <https://doi.org/10.5483/bmbrep.2015.48.4.272>
- Spangenburg, E. E., Pratt, S. J. P., Wohlers, L. M., & Lovering, R. M. (2011). Use of BODIPY (493/503) to Visualize Intramuscular Lipid Droplets in Skeletal Muscle. *BioMed Research International*, 2011(1), 1-8. <https://doi.org/10.1155/2011/598358>
- Stenkula, K. G., & Erlanson-Albertsson, C. (2018). Adipose cell size: importance in health and disease. *American Journal of Physiology (Regul Integr Comp Physiol)*, 315(2), R284-R295. <https://doi.org/10.1152/ajpregu.00257.2017>
- Swiatlowska, P., Tipping, W., Marhuenda, E., Severi, P., Fomin, V., Yang, Z., Xiao, Q., Graham, D., Shanahan, C., & Iskratsch, T. (2024). Hypertensive pressure mechanosensing alone triggers lipid droplet accumulation and transdifferentiation of vascular smooth muscle cells to foam cells. *Advanced Science*, 11(n/a), 2308686. <https://doi.org/https://doi.org/10.1002/advs.202308686>

- Tabuchi, C., & Sul, H. S. (2021). Signaling Pathways Regulating Thermogenesis. *Frontiers in Endocrinology*, 12. <https://doi.org/10.3389/fendo.2021.595020>
- Takebe, T., Imai, R., & Ono, S. (2018). The Current Status of Drug Discovery and Development as Originated in <scp>United States</scp> Academia: The Influence of Industrial and Academic Collaboration on Drug Discovery and Development. *Clinical and Translational Science*, 11(6), 597-606. <https://doi.org/10.1111/cts.12577>
- Tan, Y., Li, J., Zhao, G., Huang, K.-C., Cardenas, H., Wang, Y., Matei, D., & Cheng, J.-X. (2022). Metabolic reprogramming from glycolysis to fatty acid uptake and beta-oxidation in platinum-resistant cancer cells. *Nature Communications*, 13(1). <https://doi.org/10.1038/s41467-022-32101-w>
- Tchkonian, T., Thomou, T., Zhu, Y., Karagiannides, I., Pothoulakis, C., Michael, & James. (2013). Mechanisms and Metabolic Implications of Regional Differences among Fat Depots. *Cell Metabolism*, 17(5), 644-656. <https://doi.org/10.1016/j.cmet.2013.03.008>
- Thomas, J. A., Kendall, B. J., El-Serag, H. B., Thrift, A. P., & Macdonald, G. A. (2024). Hepatocellular and extrahepatic cancer risk in people with non-alcoholic fatty liver disease. *The Lancet Gastroenterology & Hepatology*, 9(2), 159-169. [https://doi.org/https://doi.org/10.1016/S2468-1253\(23\)00275-3](https://doi.org/https://doi.org/10.1016/S2468-1253(23)00275-3)
- Thorens, B. (2015). GLUT2, glucose sensing and glucose homeostasis. *Diabetologia*, 58(2), 221-232. <https://doi.org/10.1007/s00125-014-3451-1>
- Tipping, W. J., Wilson, L. T., Tomkinson, N. C. O., Faulds, K., & Graham, D. (2024). Label-Free Screening of Drug-Induced Liver Injury Using Stimulated Raman Scattering Microscopy and Spectral Phasor Analysis. *Analytical Chemistry*, 96(26), 10639-10647. <https://doi.org/10.1021/acs.analchem.4c01285>
- UK, D. (2023). *Differences between type 1 and type 2 diabetes*.

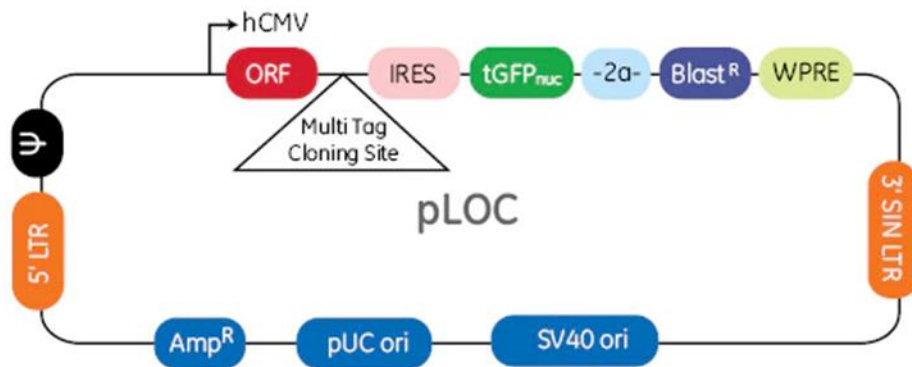
- Unamuno, X., Gómez-Ambrosi, J., Rodríguez, A., Becerril, S., Frühbeck, G., & Catalán, V. (2018). Adipokine dysregulation and adipose tissue inflammation in human obesity. *European Journal of Clinical Investigation*, 48(9), e12997. <https://doi.org/https://doi.org/10.1111/eci.12997>
- Varughese, J. T., Buchanan, S. K., & Pitt, A. S. (2021). The Role of Voltage-Dependent Anion Channel in Mitochondrial Dysfunction and Human Disease. *Cells*, 10(7), 1737. <https://doi.org/10.3390/cells10071737>
- Veliova, M., Petcherski, A., Liesa, M., & Shirihai, O. S. (2020). The biology of lipid droplet-bound mitochondria. *Seminars in Cell & Developmental Biology*, 108, 55-64. <https://doi.org/10.1016/j.semcdb.2020.04.013>
- Verboven, K., Wouters, K., Gaens, K., Hansen, D., Bijnen, M., Wetzels, S., Stehouwer, C. D., Goossens, G. H., Schalkwijk, C. G., Blaak, E. E., & Jocken, J. W. (2018). Abdominal subcutaneous and visceral adipocyte size, lipolysis and inflammation relate to insulin resistance in male obese humans. *Scientific Reports*, 8(1). <https://doi.org/10.1038/s41598-018-22962-x>
- Verma, S., Giagnocavo, S. D., Curtin, M. C., Arumugam, M., Osburn-Staker, S. M., Wang, G., Atkinson, A., Nix, D. A., Lum, D. H., Cox, J. E., & Hilgendorf, K. I. (2024). Zinc Alpha-2-Glycoprotein (ZAG/AZGP1) secreted by triple-negative breast cancer promotes tumor microenvironment fibrosis. Cold Spring Harbor Laboratory. <https://dx.doi.org/10.1101/2024.03.04.583349>
- Villanueva-Carmona, T., Cedó, L., Núñez-Roa, C., Maymó-Masip, E., Vendrell, J., & Fernández-Veledo, S. (2023). Protocol for the in vitro isolation and culture of mature adipocytes and white adipose tissue explants from humans and mice. *STAR Protocols*, 4(4), 102693. <https://doi.org/https://doi.org/10.1016/j.xpro.2023.102693>

- Wang, C., Wang, M., & Han, X. (2015). Applications of mass spectrometry for cellular lipid analysis. *Molecular BioSystems*, 11(3), 698-713. <https://doi.org/10.1039/c4mb00586d>
- Wang, Z., & Dong, C. (2019). Gluconeogenesis in Cancer: Function and Regulation of PEPCK, FBPase, and G6Pase. *Trends Cancer*, 5(1), 30-45. <https://doi.org/10.1016/j.trecan.2018.11.003>
- Wei, M., Shi, L., Shen, Y., Zhao, Z., Guzman, A., Kaufman, L. J., Wei, L., & Min, W. (2019). Volumetric chemical imaging by clearing-enhanced stimulated Raman scattering microscopy. *Proceedings of the National Academy of Sciences (USA)*, 116(14), 6608-6617. <https://doi.org/doi:10.1073/pnas.1813044116>
- Wei, X., Liu, X., Tan, C., Mo, L., Wang, H., Peng, X., Deng, F., & Chen, L. (2019). Expression and Function of Zinc- α 2-Glycoprotein. *Neuroscience Bulletin*, 35(3), 540-550. <https://doi.org/10.1007/s12264-018-00332-x>
- Wen, R. M., Qiu, Z., Marti, G. E. W., Peterson, E. E., Marques, F. J. G., Bermudez, A., Wei, Y., Nolley, R., Lam, N., Polasko, A. L., Chiu, C.-L., Zhang, D., Cho, S., Karageorgos, G. M., McDonough, E., Chadwick, C., Ginty, F., Jung, K. J., Machiraju, R.,...Brooks, J. D. (2024). AZGP1 deficiency promotes angiogenesis in prostate cancer. *Journal of Translational Medicine*, 22(1). <https://doi.org/10.1186/s12967-024-05183-x>
- Wikstrom, J. D., Mahdavian, K., Liesa, M., Sereda, S. B., Si, Y., Las, G., Twig, G., Petrovic, N., Zingaretti, C., Graham, A., Cinti, S., Corkey, B. E., Cannon, B., Nedergaard, J., & Shirihai, O. S. (2014). Hormone-induced mitochondrial fission is utilized by brown adipocytes as an amplification pathway for energy expenditure. *The EMBO Journal*, n/a-n/a. <https://doi.org/10.1002/embj.201385014>
- Wong, B., Zhao, X., Su, Y., Ouyang, H., Rhodes, T., Xu, W., Xi, H., & Fu, D. (2023). Characterizing silicone oil-induced protein aggregation with stimulated Raman

- scattering imaging. *Molecular Pharmaceutics*, 20(8), 4268-4276.
<https://doi.org/10.1021/acs.molpharmaceut.3c00391>
- Woodbury, E. J., & Ng, W. K. (1962). Ruby laser operation in the near IR. *Proceedings of the Institute of Radio Engineers*, 50, 2347-2348.
- Xu, Z., You, W., Zhou, Y., Chen, W., Wang, Y., & Shan, T. (2019). Cold-induced lipid dynamics and transcriptional programs in white adipose tissue. *BMC Biology*, 17(1).
<https://doi.org/10.1186/s12915-019-0693-x>
- Yang, A., & Mottillo, E. P. (2020). Adipocyte lipolysis: from molecular mechanisms of regulation to disease and therapeutics. *Biochemical Journal*, 477(5), 985-1008.
<https://doi.org/10.1042/bcj20190468>
- Yang Loureiro, Z., Solivan-Rivera, J., & Corvera, S. (2022). Adipocyte heterogeneity underlying adipose tissue functions. *Endocrinology*, 163(1), 10.1210/endo/bqab1138.
<https://doi.org/10.1210/endo/bqab138>
- Zahid, H., Lau, A. M., Kelly, S. M., Karu, K., Gor, J., Perkins, S. J., & McDermott, L. C. (2022). Identification of diverse lipid-binding modes in the groove of zinc α_2 glycoprotein reveals its functional versatility. *The FEBS Journal*, 289(7), 1876-1896. <https://doi.org/10.1111/febs.16293>
- Zatterale, F., Longo, M., Naderi, J., Raciti, G. A., Desiderio, A., Miele, C., & Beguinot, F. (2020). Chronic Adipose Tissue Inflammation Linking Obesity to Insulin Resistance and Type 2 Diabetes. *Frontiers in Physiology*, 10.
<https://doi.org/10.3389/fphys.2019.01607>
- Zebisch, K., Voigt, V., Wabitsch, M., & Brandsch, M. (2012). Protocol for effective differentiation of 3T3-L1 cells to adipocytes. *Analytical Biochemistry*, 425(1), 88-90.
<https://doi.org/https://doi.org/10.1016/j.ab.2012.03.005>

Zhu, Y., Ge, X., Ni, H., Yin, J., Lin, H., Wang, L., Tan, Y., Prabhu Dessai, C. V., Li, Y., Teng, X., & Cheng, J.-X. (2023). Stimulated Raman photothermal microscopy toward ultrasensitive chemical imaging. 9(43), eadi2181.
<https://doi.org/doi:10.1126/sciadv.adi2181>

Supplementary Material



Vector Element	Utility
hCMV	Human cytomegalovirus promoter drives strong transgene expression
ORF	Full-length human ORFs from the ORFeome Collaboration Collection
Multi Tag Cloning Site	Convenient cloning site for the addition of a purification or tracking tag
IRES	Internal ribosomal entry site allows expression of TurboGFP™ and Blasticidin S resistance genes in a single transcript
tGFP _{nuc}	TurboGFP reporter expressed in the cell nucleus to facilitate visual tracking of transduction and expression
Blast ^R	<i>Blasticidin S</i> resistance permits antibiotic-selective pressure and propagation of stable integrants
2a	2a self-cleaving peptide allows simultaneous expression of tGFP _{nuc} and Blasticidin S resistance proteins from a single transcript
5' LTR	5' long terminal repeat
3' SIN LTR	3' self-inactivating long terminal repeat for increased lentivirus safety
Ψ	Psi packaging sequence allows viral genome packaging using lentiviral packaging systems
WPRE	Woodchuck hepatitis posttranscriptional regulatory element enhances transgene expression in the target cells

Supplementary Data 1:Lenti-ORF Plasmid Map

List of genes listed by Horizon for their Lenti-ORF construct. Contains the Blasticidin S resistance gene to allow for cell selection and the turbo GFP that is viewed to confirm transduction success.

Supplementary Table 1: List of Candidate Ligands for Docking Experiments

Table contains candidate ligand names, their chemical formula and their Protein Data Bank (PDB) links for access to molecular models used in UCSF Chimera and ligand docking experiments.

Candidate	Chemical Formula	Protein Data Bank (PDB) Link
8,11-Eicosadiynoic acid	$C_{20}H_{32}O_2$	https://pubchem.ncbi.nlm.nih.gov/compound/8_11-Eicosadiynoic-acid .
Arachidic acid	$C_{20}H_{40}O_2$	https://pubchem.ncbi.nlm.nih.gov/compound/Arachidic-Acid .
DAUDA	$C_{23}H_{34}N_2O_4S$	https://pubchem.ncbi.nlm.nih.gov/compound/11-Dansylamino-undecanoic-acid .
9,12-Octadecadiynoic acid	$C_{18}H_{28}O_2$	https://pubchem.ncbi.nlm.nih.gov/compound/9_12-Octadecadiynoic-acid .
Stearic acid	$C_{18}H_{36}O_2$	https://pubchem.ncbi.nlm.nih.gov/compound/Stearic-Acid .
Hexadecanedioic acid	$C_{16}H_{30}O_4$	https://pubchem.ncbi.nlm.nih.gov/compound/Hexadecanedioic-acid .
P6G	$C_{12}H_{26}O_7$	https://pubchem.ncbi.nlm.nih.gov/compound/Hexaethylene-glycol .
Heptadecanoic acid	$C_{17}H_{34}O_2$	https://pubchem.ncbi.nlm.nih.gov/compound/Heptadecanoic-acid .
16-Hydroxyhexadecanoic acid	$C_{32}H_{64}O_6$	https://pubchem.ncbi.nlm.nih.gov/compound/16-hydroxyhexadecanoic-acid .
2-fluoropalmitic acid	$C_{16}H_{31}FO_2$	https://pubchem.ncbi.nlm.nih.gov/compound/2-Fluoropalmitic-acid .
Palmitic acid	$C_{16}H_{32}O_2$	https://pubchem.ncbi.nlm.nih.gov/compound/Palmitic-Acid .

Myristic acid	C ₁₄ H ₂₈ O ₂	https://pubchem.ncbi.nlm.nih.gov/compound/Myristic-Acid .
Lauric acid	C ₁₂ H ₂₄ O ₂	https://pubchem.ncbi.nlm.nih.gov/compound/Lauric-Acid .
Undecanoic acid	C ₁₁ H ₂₂ O ₂	https://pubchem.ncbi.nlm.nih.gov/compound/Undecanoic-Acid .
Decanoic acid	C ₁₀ H ₂₀ O ₂	https://pubchem.ncbi.nlm.nih.gov/compound/Capric-Acid .
Nonanoic acid	C ₉ H ₁₈ O ₂	https://pubchem.ncbi.nlm.nih.gov/compound/Nonanoic-Acid .
Octanoic acid	C ₈ H ₁₆ O ₂	https://pubchem.ncbi.nlm.nih.gov/compound/Octanoic-Acid .